The chemistry and magnetism of some rhenium and rhodium perovskite oxides

---

Nijat Hasanli

Somerville College

October 2019



UNIVERSITY OF OXFORD

A thesis submitted to the Board of the Faculty of Physical Sciences in partial fulfilment of the requirements for the degree of Doctor of Philosophy

The chemistry and magnetism of some rhenium and rhodium perovskite oxides

This work focuses on synthesis and characterisation of novel 4*d* and 5*d* materials with attention given to spin, orbital and lattice effects seen in metal oxides with heavy transition-metals.

The first half of the work is devoted to topochemical reduction of rhenium-containing perovskites following from the work on double perovskites with the composition $Sr_2BB'O_6$ (B = 4*d*/5*d;* B' = 3*d*), that exhibit spin-polarisation and ferromagnetism. An attempt was made to make $Re^{5+/6+}$ phases via low temperature methods to overcome synthetic challenges of cited phases. Treatment of Sr_2ReLiO_6 with 5%/95% H_2/N_2 gas resulted in formation of $Sr_2Re^{6+}LiO_{5.5}$, a cation ordered double perovskite with partial oxygen vacancy ordering localised on alternate layers of a tetragonal perovskite unit cell. The phase showed extensive crystallographic twinning to minimize lattice strain built as a result of unusual vacancy positions. The phase showed high spin-orbit coupling effects despite the breakage of local Re symmetry. Following this, B'-site doped $Sr_2ReLi_{0.64}Co_{0.36}O_6$ was treated with dilute hydrogen gas to form $Sr_2ReLi_{0.64}Co_{0.36}O_{5.5}$, a solid-solution of Re^{5+}, Re^{6+}, Co^{2+}, and Li^{1+} with oxygen vacancies distributed across the lattice in a disordered manner. This experiment confirmed that inclusion of Li can stabilise the 5*d*-3*d* metal oxide systems for topochemical reduction.

The second half is devoted to the study of electric transport and magnetic properties of mixed-metal rhodium perovskite oxides. It is shown that $La_{0.5}Sr_{0.5}Mn_{0.5}Rh_{0.5}O_3$ crystallizes in the *Pnma* space group with Rh and Mn distributed evenly in the B-site to form a solid-solution. Electric transport measurements show Mott's Variable Range Hopping behavior across the whole temperature range but magnetic measurements show a transition to a ferromagnetic state at T_C = 55 K suggesting ferromagnetic insulator type behavior. A study of structural and physical properties concludes the cations are found in Mn^{3+} and Rh^{4+} oxidation states and the ferromagnetism is a result of superexchange interactions between Mn^{3+} – Mn^{3+} centers with Rh^{4+} cations not involved in ferromagnetic exchange. A'-site doping with Ca^{2+} to make $La_{0.5}Sr_{0.5-x}Ca_xMn_{0.5}Rh_{0.5}O_3$ (x = 0.15, 0.25) shows expected changes to unit cell parameters including decrease in volume, bending of the B-O-B angle, and a decrease in T_C. The synthesis of the Ruddlesden-Popper analogue $La_{0.5}Sr_{1.5}Mn_{0.5}Rh_{0.5}O_4$ is studied in detail and shown to crystallize in the *I4/mmm* space group when made in air but with phase separation due to oxygen inhomogeneity. Treating the anion deficient phases under flowing oxygen gas restores the stoichiometry. Finally the synthesis and characterisation of B-site disordered spin-glass $La_{0.5}Sr_{0.5}Fe_{0.5}Rh_{0.5}O_3$ with the Fe^{3+} and Rh^{4+} oxidation state combination confirms the relative stability of Rh^{4+} over the generally accepted Rh^{3+} oxidation state.

Declaration

The work described in this thesis was carried out at the Inorganic Chemistry Laboratory at the University of Oxford between October 2015 and September 2019 under the supervision of Professor Michael A. Hayward. All the work presented in this thesis is my own except where I have either acknowledged help from a named person or given reference to a published source. None of this work has been submitted by the author for any other degree at any other university.

Nijat Hasanli

October 2019

To my family.

Acknowledgements

First, I would like to thank my supervisor Professor Michael A. Hayward, for offering me the incredible opportunity to take up a doctoral position in his research group. His unwavering dedication to research and support for his students are lessons of character and integrity that I will carry with me forever. I am grossly indebted to your brilliant mind.

Second, I would like to thank all the members of the MAH research group I have worked with over the years. In particular, Dr. Tong Zhu for being a great friend since the day he arrived; Dr. Zheying Xu for her support, positivity, and kindness at all times; Dr. Jacob Page and Dr. Midori E. Amano Patiño for helping me settle in and teaching all the laboratory techniques I would need.

Finally, I would like to thank the Government of Azerbaijan for the scholarship that made this research work possible. Likewise, I want to thank all the researchers who contributed to this work: Joke Hadermann and Maria Batuk for the TEM study; Paul A. Bingham for the Mössbauer spectroscopy study; members of the Clarke, Battle and Goodwin groups, and the I11 beam scientists at Diamond Light Source for helping to collect the neutron and synchrotron X-ray powder diffraction data.

Table of Contents

Abstract……I

Declaration……III

Acknowledgements……VIII

Table of Contents……IX

Chapter 1 Introduction……1

1.1 Complex Transition-Metal Oxides……1

1.2 Perovskites……2

1.2.1 The Perovskite Structure……2

1.2.2 Cation Ordering and Double Perovskites……4

1.2.3 Disordered Perovskites……6

1.2.4 Ruddlesden-Popper Structure……6

1.3 Electronic Structure of Metal Oxides……7

1.3.1 Electronic Band Structure……7

1.3.2 Mott-Hubbard Considerations……9

1.3.3 Conduction Mechanisms in Disordered Systems……11

1.4 Correlated Magnetic Behaviour……12

1.4.1 Magnetism in Solids……12

1.4.2 Mechanisms for Correlated Magnetic Behaviour……13

1.5 Control of Spin Currents……14

1.5.1 Half-Metallic Ferromagnetism……15

1.5.2 Colossal Magnetoresistance……16

1.6 General Considerations……18

1.6.1 Spin-Orbit Coupling in 4*d*/5*d* Transition-Metal Oxides……18

1.6.2 Spin-Orbit Coupling in Rhenium……19

1.6.3 Jahn-Teller Distortions……20

1.7 Synthesis and Reactions of Transition-Metal Oxides……22

1.7.1 Traditional and Soft Chemistry……22

1.7.2 Topochemical Reduction……23

Chapter 2 Experimental Methods and Techniques 25
2.1 Synthesis Methods 25
2.1.1 Ceramic Synthesis 25
2.1.2 Pechini Method 25
2.2 Glove Box 26
2.3 Flowing-Gas Reactions 27
2.4 Thermogravimetric Analysis 27
2.5 X-ray Powder Diffraction 28
2.5.1 Bruker D8 Advance Eco Diffractometer 30
2.5.2 PANalytical X'Pert and Empyrean Diffractometers 31
2.5.3 Synchrotron X-ray Powder Diffraction 32
2.6 Neutron Powder Diffraction 33
2.6.1 GEM Diffractometer 35
2.6.2 D2B Diffractometer 37
2.7 Rietveld Refinement 38
2.8 Bond Valence Sums (BVS) 39
2.9 ^{57}Fe Mössbauer Spectroscopy 40
2.10 Transmission Electron Microscopy 43
2.10.1 Electron Energy Loss Spectroscopy 44
2.11 Superconducting Quantum Interference Device (SQUID) 45
2.11.1 Standard Measurement 46
2.11.2 Ferrosubtraction Measurements 46
2.12 Magnetism 47
2.12.1 The Curie-Weiss Law 48
2.12.2 Correlated Magnetic Behaviour 50
2.13 Conductivity Measurements 50
Chapter 3 Topochemical Reduction of Sr_2ReLiO_6 to $Sr_2ReLiO_{5.5}$ 51
3.1 Introduction 51
3.2 Synthesis 52
3.2.1 Synthesis of Sr_2ReLiO_6 52
3.2.2 Synthesis of $Sr_2ReLiO_{5.5}$ 52
3.3 Results 53
3.3.1 Reactivity 53
3.3.2 Thermogravimetric Analysis 55
3.3.3 Electron Energy Loss Spectroscopy 56

3.3.4 Magnetic Characterisation 57
3.3.5 Structural Characterisation 60
3.4 Discussion 69
3.4.1 Anion Deintercalation Chemistry 69
3.4.2 Structural Characterisation 70
3.4.3 Cation Coordination Polyhedra 71
3.4.4 Composition-Structure Relations 74
3.4.5 Magnetic and Electronic Properties 76
3.5 Conclusions 78
Chapter 4 Synthesis and Characterisation of $Sr_2ReLi_{0.64}Co_{0.36}O_6$ 80
4.1 Introduction 80
4.2 Synthesis 80
4.3 Results 81
4.3.1 Structural Characterisation 81
4.3.2 Magnetic Characterisation 87
4.4 Discussion 90
4.4.1 Structural Characterisation 90
4.4.2 Magnetic Characterisation 90
4.5 Conclusion 92
Chapter 5 A Topochemical Reduction of $Sr_2ReLi_{0.64}Co_{0.36}O_6$ 93
5.1 Introduction 93
5.2 Synthesis 93
5.3 Results 94
5.3.1 Reactivity of $Sr_2ReLi_{0.64}Co_{0.36}O_6$ 94
5.3.2 Thermogravimetric Analysis 95
5.3.3 Structural Characterisation of $Sr_2ReLi_{0.64}Co_{0.36}O_{5.5}$ 96
5.3.4 Magnetic Characterisation 101
5.4 Discussion 104
5.4.1 Reduction Chemistry 104
5.4.2 Structural Characterisation 105
5.4.3 Magnetic Characterisation 105
5.5 Conclusion 108
Chapter 6 Synthesis and Characterisation of $La_{0.5}Sr_{0.5-x}Ca_xMn_{0.5}Rh_{0.5}O_3$ 109
6.1 Introduction 109
6.2 Synthesis 109

6.2.1 Synthesis of $La_{0.5}Sr_{0.5-x}Ca_xMn_{0.5}Rh_{0.5}O_3$, (x = 0.125, 0.25) 109
6.3 Results 110
6.3.1 Structural Characterisation 110
6.3.2 Magnetic Characterisation 118
6.3.3 Conductivity Measurements 121
6.4 Discussion 123
6.4.1 Structural Characterisation 123
6.4.2 Oxidation States 124
6.4.3 Unit-cell and Jahn-Teller Distortion 126
6.4.4 Magnetic Characterisation 128
6.4.5 Transport Properties 131
6.4.6 Effects of A-site Doping 132
6.5 Conclusions 135
Chapter 7 Oxygen Non-Stoichiometry in $La_{0.5}Sr_{1.5}Mn_{0.5}Rh_{0.5}O_4$ 137
7.1 Introduction 137
7.2 Synthesis 137
7.3 Structural Characterisation 138
7.3.1 Synchrotron X-ray Powder Diffraction of Sample A 139
7.3.2 Synchrotron X-ray Powder Diffraction of Sample B 140
7.3.3 Synchrotron X-ray Powder Diffraction of Sample C 141
7.3.4 Structural Characterisation of Sample B 143
7.3.5 Structural Characterisation of Sample A 147
7.3.6 Thermogravimetric Analysis 150
7.4 Magnetic Characterisation 152
7.4.1 Magnetisation Plots 153
7.4.2 Magnetic Characterisation of Sample C, $La_{0.5}Sr_{1.5}Mn_{0.5}Rh_{0.5}O_4$ 156
7.4.3 Magnetic Characterisation of Samples A and B 156
7.5 Conductivity Measurements 158
7.6 Discussion 160
7.6.1 Structural Characterisation of $La_{0.5}Sr_{1.5}Mn_{0.5}Rh_{0.5}O_4$, Sample C 160
7.6.2 Two-Phase Split in Oxygen Deficient Samples A and B 162
7.7 Conclusions 163
Chapter 8 Synthesis and Characterisation of $La_{0.5}Sr_{0.5}Fe_{0.5}Rh_{0.5}O_3$ 164
8.1 Introduction 164
8.2 Synthesis 164

8.3 Results 165
8.3.1 Structural Characterisation 165
8.3.2 ^{57}Fe Mössbauer Spectroscopy 167
8.3.3 Magnetic Characterisation 169
8.3.4 Conductivity Measurements 171
8.4 Discussion 173
8.4.1 Structural Characterisation 173
8.4.2 Oxidation State Determination 173
8.4.3 Magnetic Characterisation 176
8.4.4 Rhodium Coordination Chemistry 180
8.5 Conclusions 182
Chapter 9 Conclusions 183
Appendix 1 List of Figures 187
Appendix 2 Bibliography 192

Chapter 1 Introduction

1.1 Complex Transition-Metal Oxides

Complex metal-oxides that contain transition-metals with variable oxidation states have been a focus of investigation across many research disciplines. The ability of these materials to exhibit a wide range of different physical properties has been the main motivating factor for researchers[1, 2]. Materials in this class of compounds have unique electric transport and magnetic properties that continue to motivate the discovery and synthesis of functional new phases. Transition-metal oxides have shown physical properties including long-range magnetic order[3], superconductivity[4], spin-polarised conductivity[5, 6], multiferroicity[7, 8] and photocatalytic behaviour[9]. The adoption of these materials into conventional devices has made significant contributions to a wide range of industries like energy storage[10], data processing[11], photovoltaics[12] and catalysis[13].

These properties arise from cooperative behaviour of the electrons localised at transition-metal centres and the surrounding anion environment. In solid-state oxides, metal centres are organised into regular arrays via shared anion junctions. Transition-metals can adopt variable oxidation states as the partial filling of the *d*-orbitals can result in multiple stable electronic configurations. These partially filled orbitals can interact with neighbouring anion *p*-orbitals that act as bridges and enable cooperative electronic behaviour between the metal centres. These interactions are normally enhanced when they propagate through the material and lead to electronic states that subsequently lead to macroscopic properties. These properties are typically sensitive to small variations in transition-metal oxidation states and anion environments. Fine-tuning the compositional chemistry of

perovskites has been utilised to design materials with new and previously unknown electrical transport and magnetic properties[14].

1.2 Perovskites

1.2.1 The Perovskite Structure

The perovskite structure is one of the most widely explored transition-metal oxide frameworks. The wide interest began in 1950's when Na_xWO_3 was discovered to be metallic[15] and grew rapidly when $La_{0.5}Sr_{0.5}MO_3$, M = Mn, Co were discovered to be ferromagnetic conductors via complex exchange coupling mechanisms[16, 17].

The aristotype perovskite structure has the ABX_3 composition. 'A' is a large electropositive cation, usually a Group I/II metal or a lanthanide. 'B' is a smaller electropositive cation, usually a transition-metal and 'X' is an electronegative anion, usually oxygen. The A-cation sits in the middle of a simple-cubic array of B-cations where the anions act as (180° - φ) B-X-B bridges. The B-cations sit in an array of BX_6 corner-sharing octahedra and the larger A-cation sit in a 12-fold anion coordination. The structure is very flexible as the BX_6 octahedra are free to twist, expand, and distort. This allows a large variety of A/B-cation combinations to be accommodated into the framework without breaking the integrity of the structure.

The perfect ABO_3 cubic perovskite is rare as the difference in A-O and B-O bond lengths introduces strain, forcing the B-O-B bond to bend to 180° - φ and twisting the octahedra to preserve connectivity. These twisting distortions propagate through the structure to accommodate for the mismatch in the radii of the A- and B-cations. The Goldsmith tolerance factor[18] is used to quantify the degree of twisting:

Tolerance Factor

$$t = \frac{< A - O >}{\sqrt{2} < B - O >} = \frac{r_A + r_O}{\sqrt{2}(r_B + r_O)} \qquad 1.1$$

Where '*t*' is the tolerance factor, '<A - O>' and '<B - O>' are respective bond lengths, and 'r_A', 'r_B' and 'r_O' terms represent respective ionic radii. The ideal cubic perovskite, has a tolerance factor of 1 as the size of A- and B-cations are related by the appropriate factor. A typical example is $SrTiO_3$[19] where the ionic radii of Sr^{2+} and Ti^{4+} are such that the tolerance factor is equal to 1.

The ABO_3 network accommodates $t >> 1$ by forming hexagonal polytypes[20] when the A-site cation is too large for the respective site and t < 1 by cooperative rotation of the BO_6 octahedra. The bending angle φ decreases discontinuously from cubic to rhombohedral to an orthorhombic *Pbnm* symmetry. For example, rotation of the octahedra along the [110] axis results in an orthorhombic *Pnma* ($b/a < \sqrt{2}$) space group, which is one of the most common symmetries perovskites adopt.

The flexibility of the perovskite structure is primarily a result of its ability to cooperatively twist and form <180° B-O-B bond angles. Controlled manipulation of the tolerance factor is a prominent technique in solid-state synthesis as the tolerance factor can be correlated to physical properties. The ability to adjust to $t < 1$ allows for cation substitution through conventional synthetic methods, opening pathways for new cooperative magnetic and electronic behaviour mechanisms. Substitutions or other chemical alterations can be made onto all three sites. A-site doping primarily affects the cooperative twisting regime and the formal oxidation state of the B-site cations and has been shown to influence physical properties of many materials[21]. Substitutions on the B-site are more significant as cations with differing orbital energies, spin states and electron configurations can open

or break cooperative exchange pathways. Finally, the anion sites can accommodate a range of anions including oxides, fluorides and nitrides[22, 23]. The effects of A-site and B-site doping can be observed in the study of manganese oxides with configuration $A_xA'_{1-x}B'_xMn_{1-x}O_3$ (A, A' = alkali metals, lanthanides; B' = 3*d*-4*d*-5*d* transition-metals) where properties like magnetoresistance, magnetic ordering temperature, electrical resistivity have been controlled[24-26].

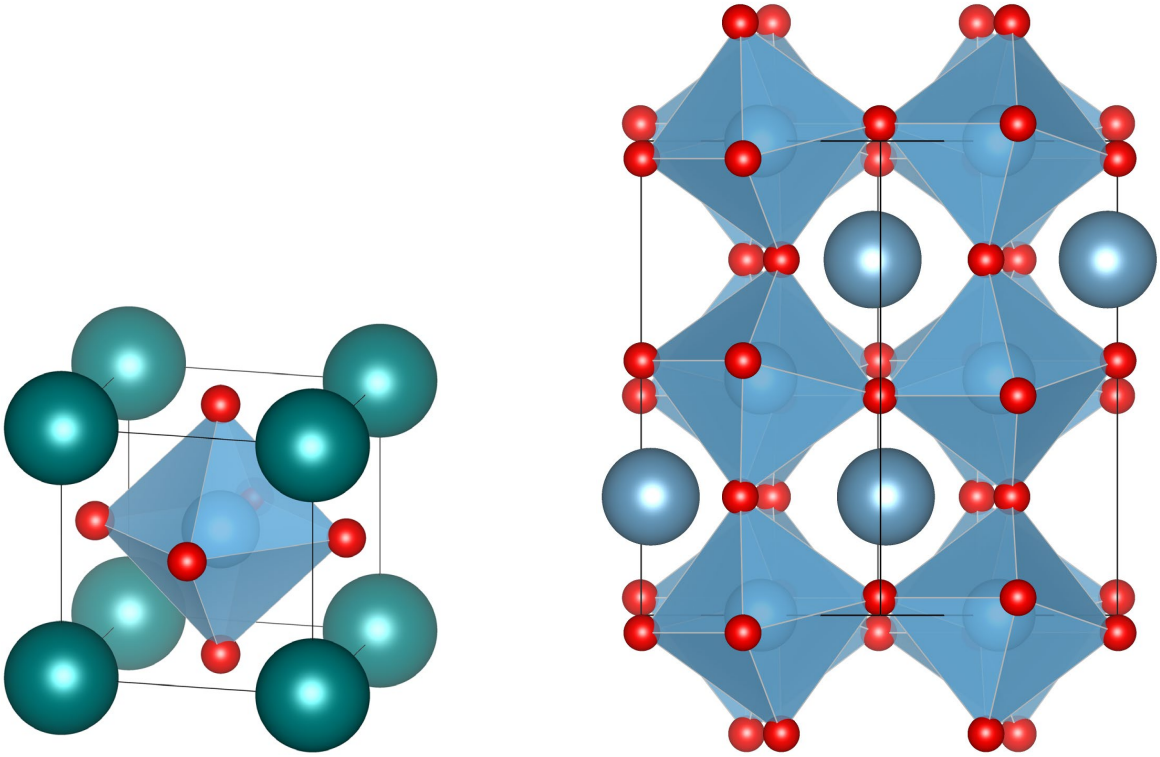


Figure 1.1 Left: Aristotype ABX_3 *Pm*-3*m* (221) $SrTiO_3$[19]; Right: *Pbnm* (62) $CaTiO_3$[27]

1.2.2 Cation Ordering and Double Perovskites

The aristotype ABX_3 can be doped at both A- and B-sites to make an ordered double perovskite. When cations are substituted into the perovskite structure there is a possibility they will order, especially when the composition has elements in ratios like $A_2BB'O_6$ or $AA'B_2O_6$. Ordered double perovskites have a 1:1 ratio of the substituent cation in their atomic site, giving rise to periodic ordering. Cations tend to order when the

difference in oxidation states is >2 and/or when their sizes differ by more than 0.10 Å. When these conditions are met, the cations adopt a periodic order to minimize the structural stress arising from localised clusters of high Coulombic charges. The unit-cell of an ordered double perovskite is expanded relative to a disordered phase. Woodward *et al*[28] had conducted thorough analysis on types of ordering and the properties that arise from cation ordering. The three ordering types are 'rock-salt', 'layered', and 'columnar'. Due to electrostatic considerations, the rock-salt formation is the most common and symmetric form as the two cations occupy a geometry equivalent to the standard rock-salt structure. The other forms result in connectivity of the octahedra in one or more dimensions but are rare.

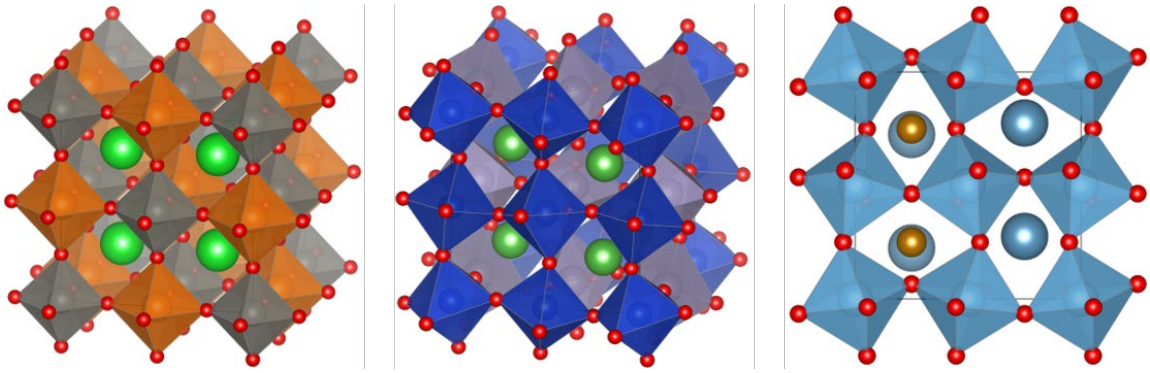


Figure 1.2 Left: B-site rock-salt ordered Ba_2MgWO_6[29] Middle: B-stie layered ordered La_2CuSnO_6[30] Right: A-site columnar ordereed $CaFeTi_2O_6$[31]

Cation ordering is an important consideration as it has drastic implications for physical properties. The half-metallic ferromagnet Sr_2FeMoO_6[6] is highly sensitive to the B/B' order and spin polarisation of this compound decreases rapidly as the cation ordering is broken.

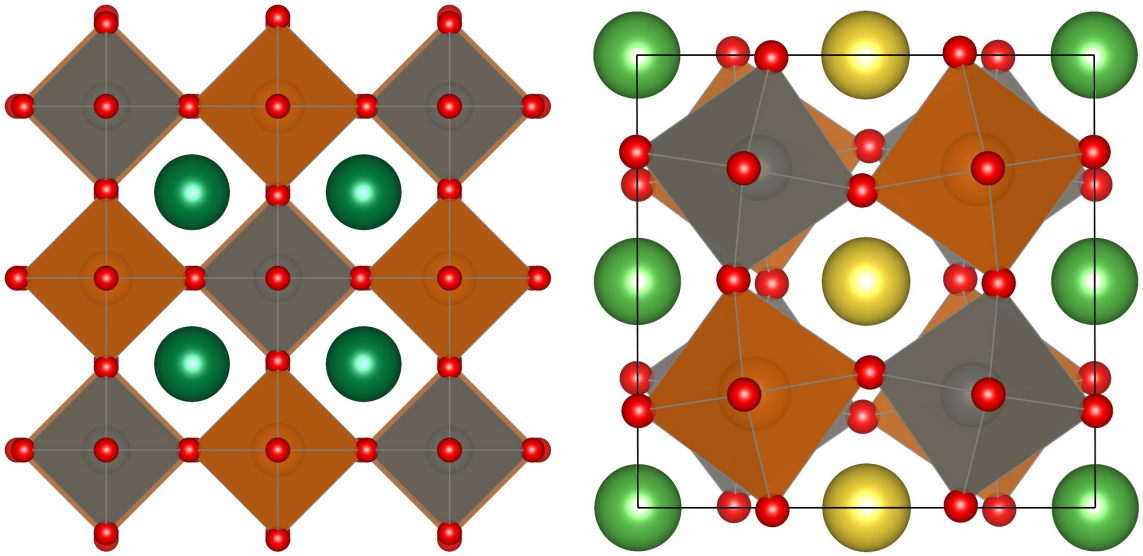


Figure 1.3 Left: *Fm*-3*m* (225) B-site ordered Sr_2WMnO_6[28] Right: *C2/m* (12) doubly ordered $NaLaMgWO6_6$[32]

1.2.3 Disordered Perovskites

If the cations in A- or B-site are similar in size or have a <2 difference in oxidation states, they will tend to be randomly distributed across that site, resulting in a disordered chemical formula $AB_{0.5}B'_{0.5}O_3$. Materials with this composition are called 'solid-solutions' and are more likely to be insulating. This is because any formation of bands is disfavoured when cation periodicity is absent or bands form with narrow bandwidth.

1.2.4 Ruddlesden-Popper Structure

Ruddlesden-Popper structure has the general formula $A_{n+1}B_nO_{3n+1}$ and can be regarded as an intergrowth of regular perovskite blocks and AO rock-salt layers[33, 34]. Interest in these structures was primarily inspired by the discovery of high-T_c cuprate superconductors with mixed valent Cu^{3+}/Cu^{2+} in $La_{2-x}A'_xCu^{3+/2+}O_4$ (A' = Sr^{2+}, Ba^{2+}, x = 0.10 – 0.22). The rock-salt layer breaks the connectivity of regular perovskites along the c-axis reducing the dimensionality of the system. The consequences are two-fold. Firstly, this breaks the orbital overlap along c-axis, inhibiting exchange interactions in that direction. The physical properties are therefore largely defined by intraplanar interactions.

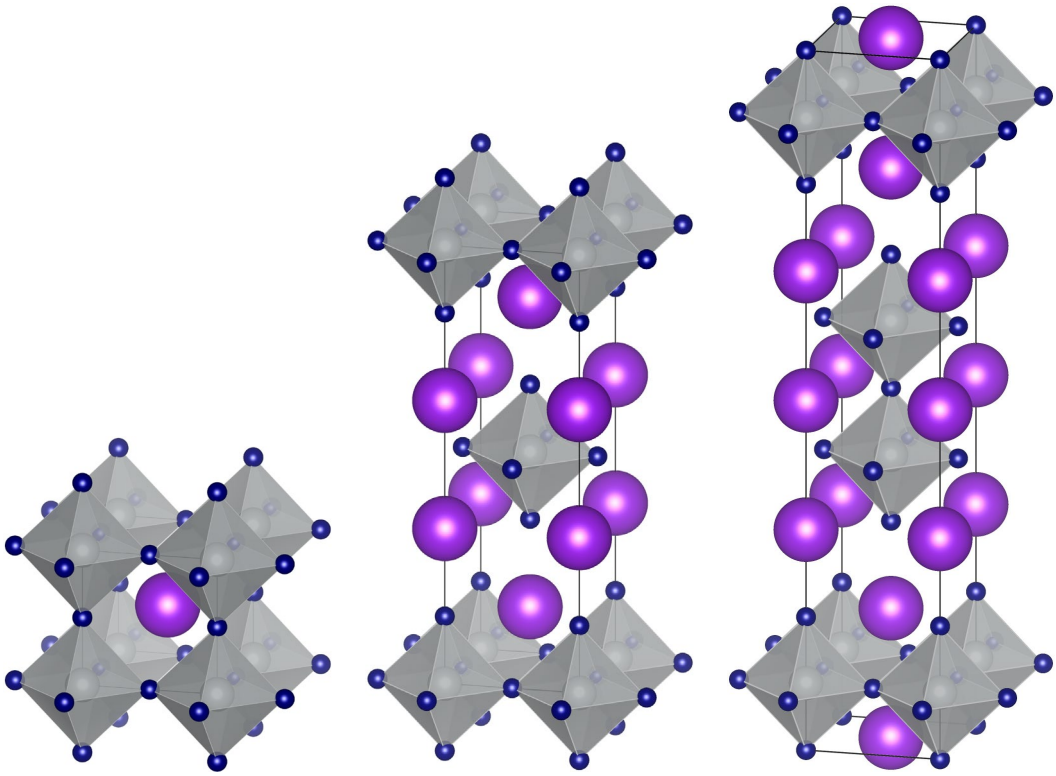


Figure 1.4 Left: The perovskite $KNiF_3$. Centre: The aristotype $KNiF_4$, n = 1 Ruddlesden-Popper structure. Right: $K_3Ni_2F_7$, n = 2 Ruddlesden-Popper structure[35].

1.3 Electronic Structure of Metal Oxides

1.3.1 Electronic Band Structure

Electrons of a single atom occupy atomic orbitals with a discreet energy level. In solid-state chemistry, extended solids are made up of chains of individual ions whose orbitals overlap to form molecular orbitals with distinct energy states. When these molecular orbitals propagate through the entire solid, the energy spacing between them can become small enough to be regarded as negligible. If the spacing is taken to be negligible, the network of orbitals can be considered as one continuous 'band' of energy states. These bands can be found filled, partially filled, or empty depending on the occupancy of the molecular orbitals and hence depend on oxidation states of cations that make up the band. The extent to which atomic orbitals overlap determines the 'bandwidth' (W) – small

orbital overlap results in narrow bandwidths and large orbital overlap results in wide bands[36].

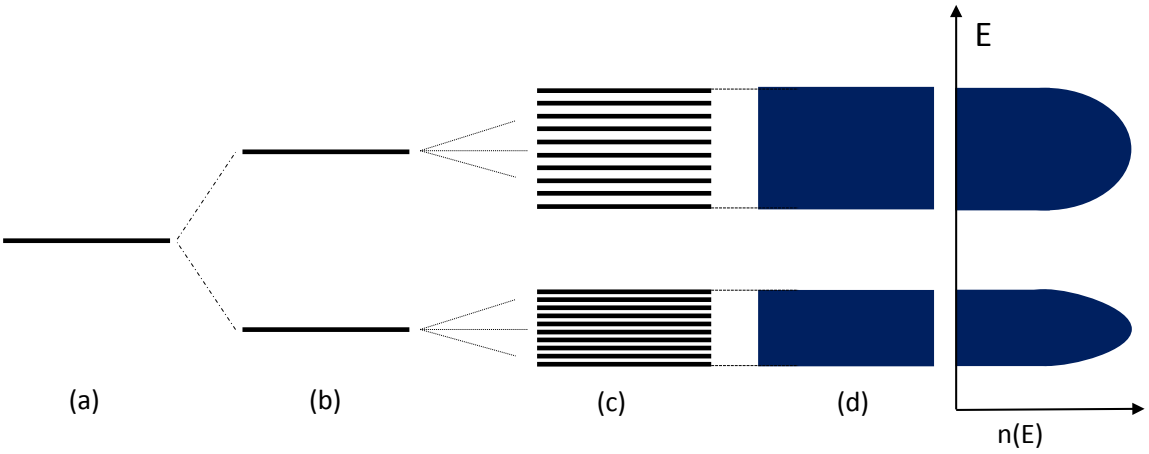


Figure 1.5 Illustrations of (a) atomic orbital, (b) molecular orbitals, (c) a large molecule, (d) distinct bands[36]

The bands are primarily a result of valence electrons and these are the ones involved in chemical bonding and conductivity. The core orbitals do not overlap strongly so these bands are typically very narrow and core electrons are generally localised.

The occupancy of the bands are determined by the occupancy of atomic orbitals and the energy of the highest occupied level is known as the *Fermi Level.* In a filled band, the net motion of electrons are cancelled out by electrons moving in opposite directions. Therefore a solid with filled bands and a band gap to the next empty band will be an insulator. When bands are made up of partially occupied orbitals, the electrons in highest occupied energy level (valence band) can be excited into the lowest unoccupied level (conduction band) and become itinerant. In non-metallic solids, the energy gap between these bands is wide and is called the band gap.

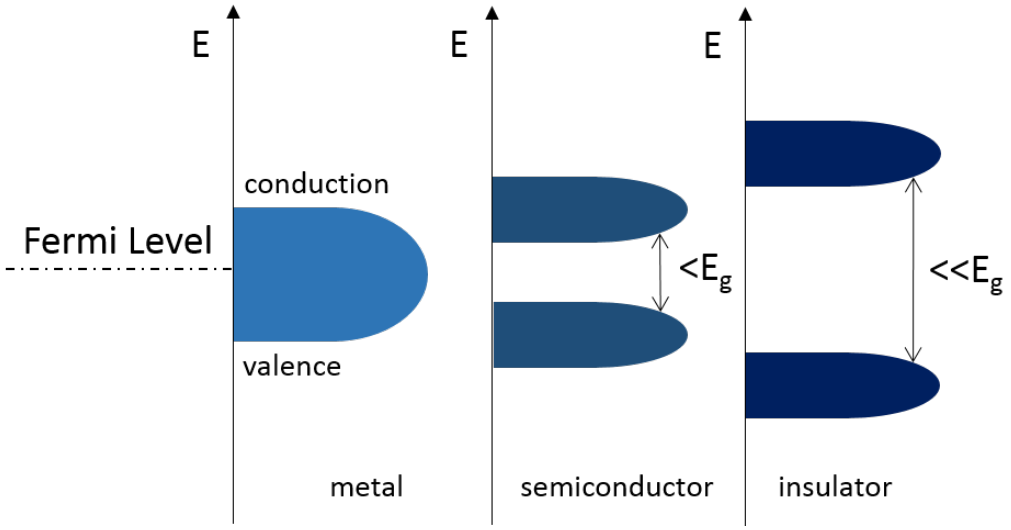


Figure 1.6 Illustrations for different electronic behaviour. E_g is the bang gap in electron volts (eV)

1.3.2 Mott-Hubbard Considerations

Many materials which are predicted to be metals by simple band theory calculations are in fact insulating due to electron-electron interactions and are called Mott-Hubbard Insulators[37]. The Hubbard model[36, 38] builds on band theory by describing the electron-electron correlations in insulating narrow bands. The *Hubbard Hamiltonian* consists of two terms: a kinetic term that describes the tunnelling (hopping) of electrons between sites (t) and the potential energy term (U) that describes the repulsion energy between two electrons on the same atom.

The Hubbard model assumes that the intra-atomic electron-electrons interactions are the only important repulsion effect in a solid. Even if atoms overlap to form a band in accordance with band theory, the energy of electrons in these bands will not be uniform. The positively charged nuclei create potential wells that need to be overcome for an electron to move freely. This is why there is an energy cost for electron delocalisation. The energy required to move an electron to another atomic orbital is the ionisation energy 'I'. When the electron is placed on a site already occupied, some of the energy gained to

ionisation is lost in the form of electron affinity *'A'*. Therefore the energy cost of interatomic electron movement is the difference between ionisation energy an energy affinity, defined as '*U*'. The effect of this electron repulsion can make a half-filled band to be insulating when the interatomic interaction is small. For example, if the atomic orbital overlap is small, the ground state will have electrons localised on each atom unable to jump to other atoms. Therefore the Hubbard model accounts for the competition between chemical bonding (t) favouring itinerant electrons and localised Coulombic repulsion (U).

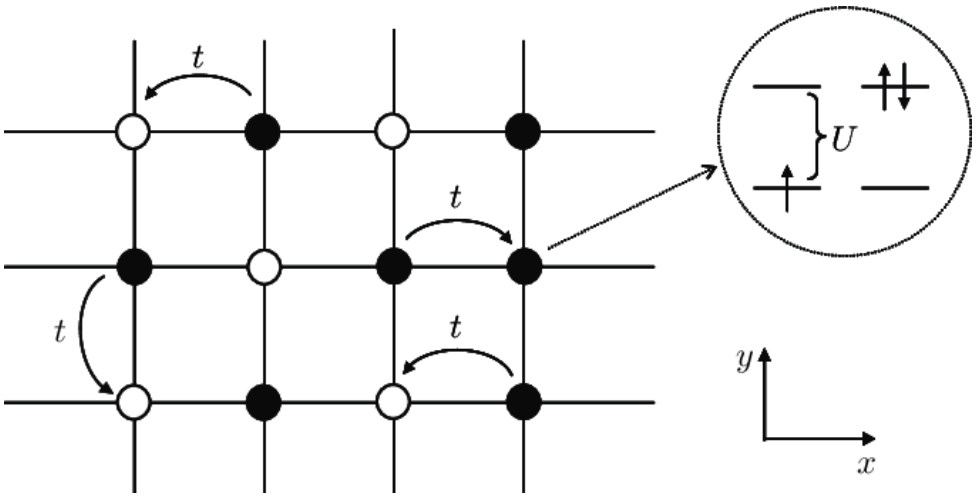


Figure 1.7 The Hubbard model: Electron hopping from filled (black) to empty sites (white). Hopping to a filled site has an on-site Coulomb interaction, *U*, penalty.[39]

There is typically an important interplay between Hubbard '*U*' and bandwidth '*W*' described in Section 1.3.1. Figure 1.8 illustrates this relationship. When *W* = 0, the *–I* denotes the energy of single occupied orbitals and *–A* denotes energy for an extra electron to be added. The gap between these is *U*. When *U* > *W* on-site repulsions dominate the electronic behaviour. The equilibrium point when *U* = *W* is called the Mott-Hubbard transition. When U < W there is no energy gap and on-site repulsions can be overcome for electrons to delocalise through the material. In this region band theory applies. These

factors make the study of 'band engineering' an important field for solid-state chemists. For example, simple band theory predicts NiO should be a metallic conductor but it is observed to be an insulator. This is because the bands in NiO have poor orbital overlap resulting in narrow bands and a much large *U* than *W*.

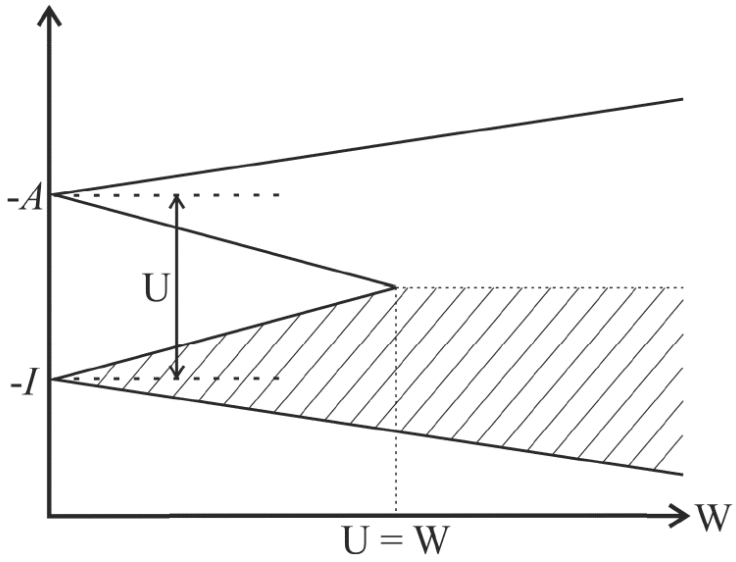


Figure 1.8 Hubbard sub-bands as a function of bandwidth, *W*.

1.3.3 Conduction Mechanisms in Disordered Systems

Transition-metal oxide materials show a wide range of electrical transport behaviours and these are primarily characterised using resistivity-temperature plots to model the temperature dependence of carrier transport. Semiconductors typically follow the thermal activation model where conductivity follows an Arrhenius pathway[36]. In disordered transition-metal oxides the conventional conduction behaviours sometimes don't apply where carrier transport mechanisms change to a localised medium. In these systems carrier transport depends on the probability of hopping to closely neighbouring atoms denoted as 'hopping conduction'. The two possible models of temperature dependence are small-polaron hopping and variable range hopping. The three temperature dependence models are[40]:

Thermal Activation	$\rho = \rho_o \exp\left(\frac{E_A}{kT}\right)$	1.2
Small Polaron	$\rho = \rho_o T \exp\left(\frac{E_A}{kT}\right)$	1.3
Variable Range Hopping	$\rho = \rho_o \exp\left(\frac{T_0}{kT}\right)^{\frac{1}{4}}$	1.4

Where 'ρ' is resistivity, 'ρ_o' is the pre-exponential term, 'E_A' is the activation energy and 'T_o' is the characteristic hopping temperature.

1.4 Correlated Magnetic Behaviour

1.4.1 Magnetism in Solids

The electrical transport properties of solids are often correlated to magnetic behaviour in an external field[41]. Many materials show strong interactions between unpaired electron spins that propagate through the lattice creating net magnetic response in an external field.

A material without unpaired electrons is 'diamagnetic'. The presence of unpaired electrons in transition-metal oxides results in non-zero magnetic susceptibilities. Materials with unpaired electrons are 'paramagnetic' when an external field aligns the individual magnetic moments to lower the energy of the system. Materials that have individual magnetic moments aligned parallel to the external field below an intrinsic Curie temperature, 'T_c', are 'ferromagnetic'. In 'antiferromagnetic' materials, the spins align anti-parallel to each other and cancel out the external field below the critical Néel Temperature, 'T_N'.

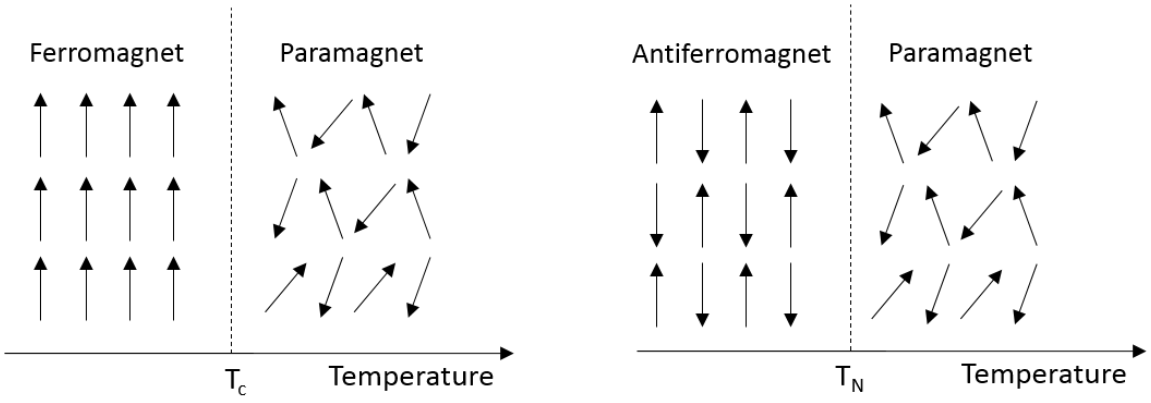


Figure 1.9 Spin alignment in an external field

1.4.2 Mechanisms for Correlated Magnetic Behaviour

The simplest type of magnetic coupling is 'direct exchange' of electrons via orbital overlaps. However, interatomic separation between cation centres in transition-metal oxides is often too strong for direct exchange. The other coupling mechanism is 'superexchange' that predicts electron hopping between metal centres via anion orbitals that bridge the gap between them. Superexchange coupling assumes high *d-p* orbital hybridisation to mediate spin delocalisation and so the effects are strong in materials where *B-O-B* angles approach 180°. The Goodenough-Kanomori[26] rules describe the conditions for magnetic coupling mechanisms via superexchange. Ferromagnetism is predicted when a half-filled orbital is coupled to a filled or an empty orbital. Antiferromagnetism can occur between two half-filled orbitals or a filled and an empty orbital. Superexchange therefore depends strongly on the symmetry of the overlapping orbitals as it is the orbital covalence that extends the wave-function to allow for superexchange electron transfer. The rules depend on whether the orbitals are at 180° or orthogonal relative to each other and the outcomes vary between weak/strong antiferromagnetic or ferromagnetic interactions. Superexchange interactions can be 'σ-

type' or 'π-type' depending on orbital symmetry with the former being significantly stronger due to symmetry allowed orbital overlaps.

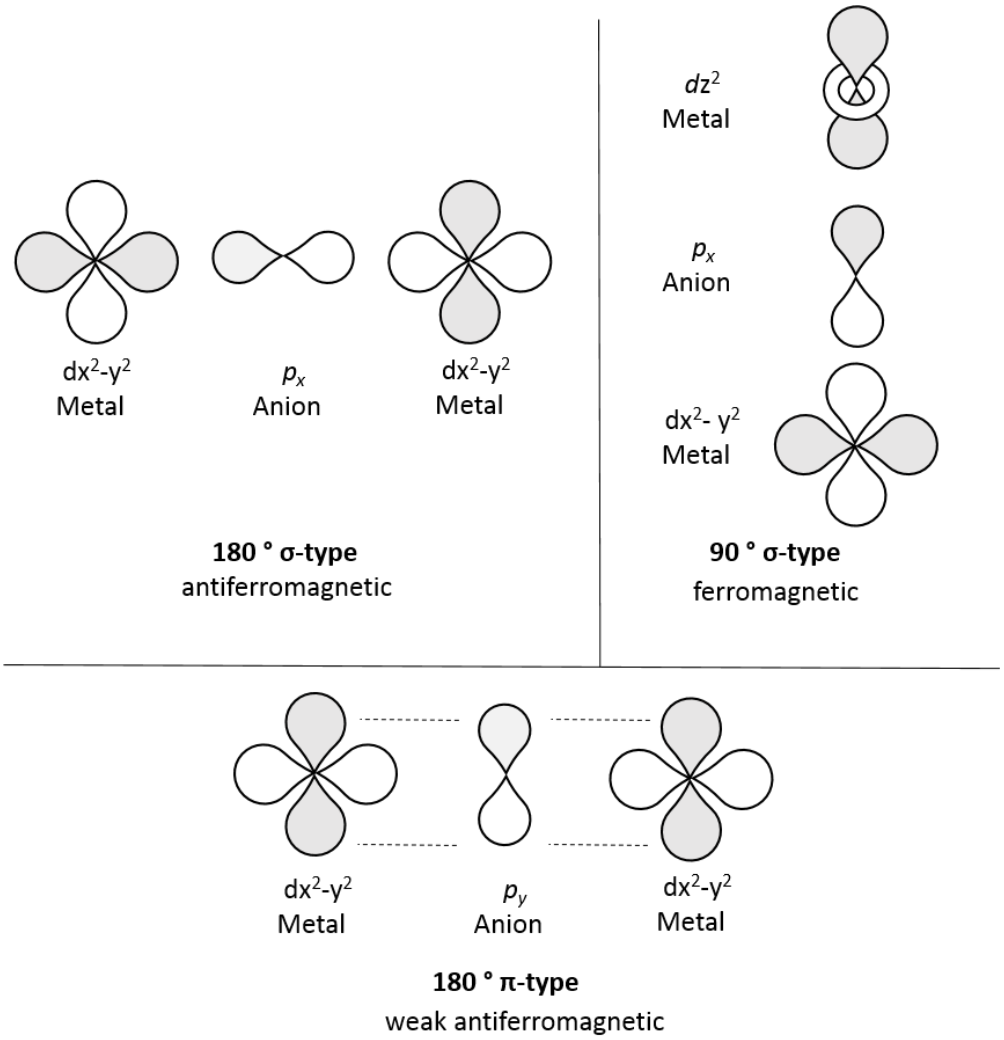


Figure 1.10 Standard superexchange mechanisms in transition-metal oxides

1.5 Control of Spin Currents

In order to synthesise and deploy complex technological solutions, it is important to design and synthesise materials that exhibit a combination of different physical properties like ferromagnetism, magnetoresistance, and pyro-electricity among others. This is an effective way to maximise the efficiency and minimize raw materials used in conventional devices. Likewise, materials that show unconventional property pairs such as

ferromagnetic insulators help understand the underlying complex mechanisms of correlated physical behaviour.

Spintronics is an area of research that depends heavily on synthesis of such materials. Spintronics devices are being designed to use spin currents in the same way conventional devices use charge currents, the difference being that in spin current devices electrons are not transported via any medium so ohmic resistivity is suppressed[42]. These materials are rare and difficult to make but the magneto-electronic properties of half-metallic ferromagnets and colossal magnetoresistance observed in manganese oxides have been strongly considered.

1.5.1 Half-Metallic Ferromagnetism

The concept of half-metallic ferromagnetism was introduced by Groot *et al* who described a class of materials with an energy gap (band gap) between valence and conduction bands on one spin polarisation and a continuous band at the Fermi level on the other spin polarisation was described[43]. Density of states plots show a band gap at the Fermi level in one direction ($N_{\downarrow}(E_f) \sim 0$) and high electron cloud density at the Fermi level on the opposite channel, resulting in 100% spin polarisation. The material is therefore an insulator in one spin direction and a ferromagnetic metal in the opposite spin direction. Materials with half-metallic ground states are very few in nature. Design of half-metals requires very specific set of conditions and polarisation is highly sensitive to perturbations in spin flip scattering and atomic positions and is therefore considered a 'serious challenge' for solid-state chemists[42].

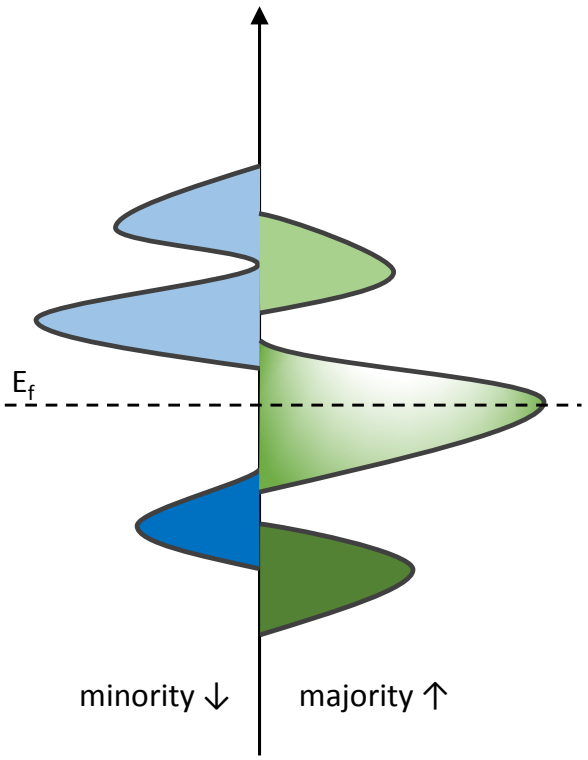


Figure 1.11 Schematic DOS for 100% spin-polarisation. The minority spin is insulating and majority spin is metallic

The first perovskite half-metallic ferromagnet Sr_2FeMoO_6 was reported by Kobayashi *et al*[44] who described a double perovskite that showed tunnelling type magnetoresistance. Since then, other materials like Sr_2FeReO_6 (T_c = 420 K)[5] and Sr_2CrReO_6 (T_C = 635 K)[45] have been prepared. The inclusion of 4*d*/5*d* in cations with greater radial extensions and previously unexplored oxidation states has been the deciding factor. In an attempt to design half-metallic ferromagnets, a topochemical study on rhenium double perovskites has been herein described.

1.5.2 Colossal Magnetoresistance

Perovskite manganese oxides were originally used by Jonker *et al*[16] to describe strong correlation between magnetism and electrical transport. When all-Mn^{3+} antiferromagnetic insulator $LaMnO_3$ is 30% A-site doped with Ca, the material undergoes ferromagnetic ordering and a sign change in resistivity-temperature slope at the Curie

temperature indicating a metal-insulator transition (positive temperature-resistance slope) at the onset of ferromagnetic order. Zener *et al*[46] and consequent work by Goodenough *et al*[26] have thoroughly described the interactions using the 'double-exchange' mechanism. In $La_{1-x}Ca_xMnO_3$, x ≈ 0.2 - 0.5, oxidation of sufficient concentration of Mn^{3+} to Mn^{4+} allows for electron exchange mechanism between the half-filled e_g orbitals in Mn^{3+} ($t_{2g}^3e_g^1$) and empty e_g orbitals in Mn^{4+} ($t_{2g}^3e_g^0$) via the 2*p* O orbitals. It was consequently discovered by Sealer and Wang *et al*[47] that the resistivity-temperature curves were highly sensitive to the frequency of external magnetic fields. This effect is now called colossal-magnetoresistance. The phase diagram for $La_{1-x}Ca_xMnO_3$ is shown in Figure 1.12. Consequently, researchers have built on manganese oxide chemistry by A-site and B-site doping. A study of rhodium-manganese oxides has been herein described.

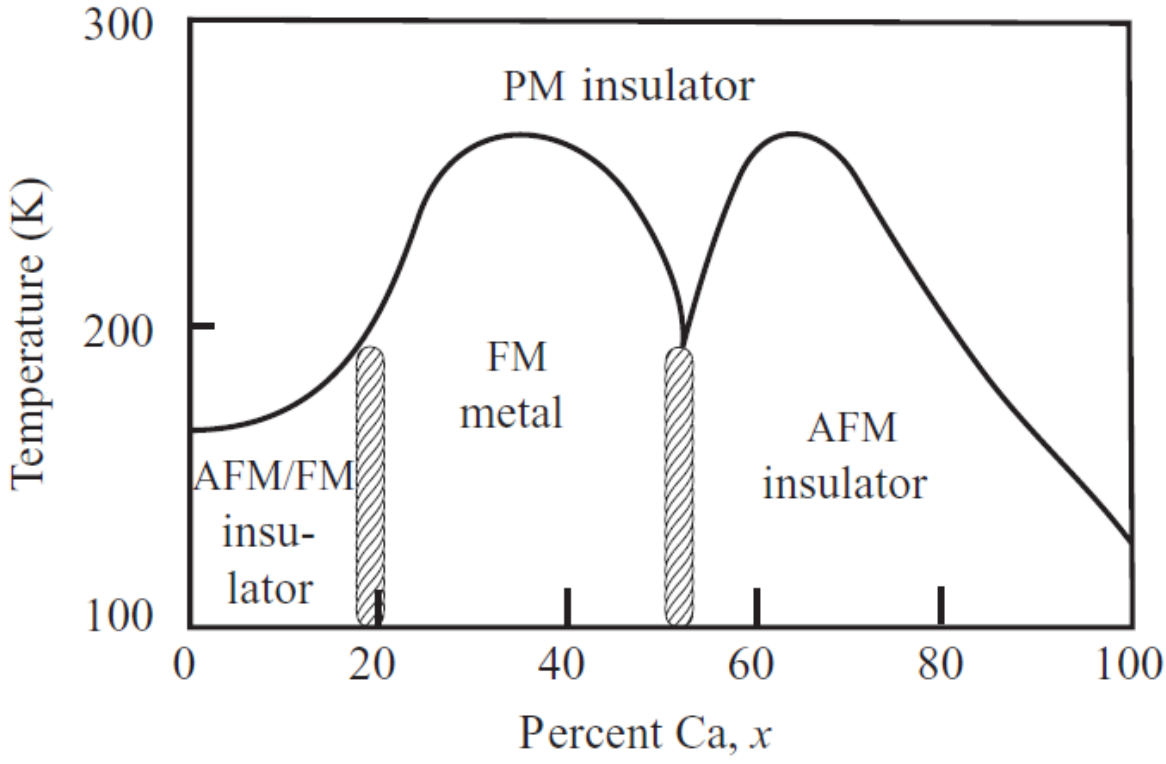


Figure 1.12 Simplified phase diagram of $La_{1-x}Ca_xMnO_3$[3]

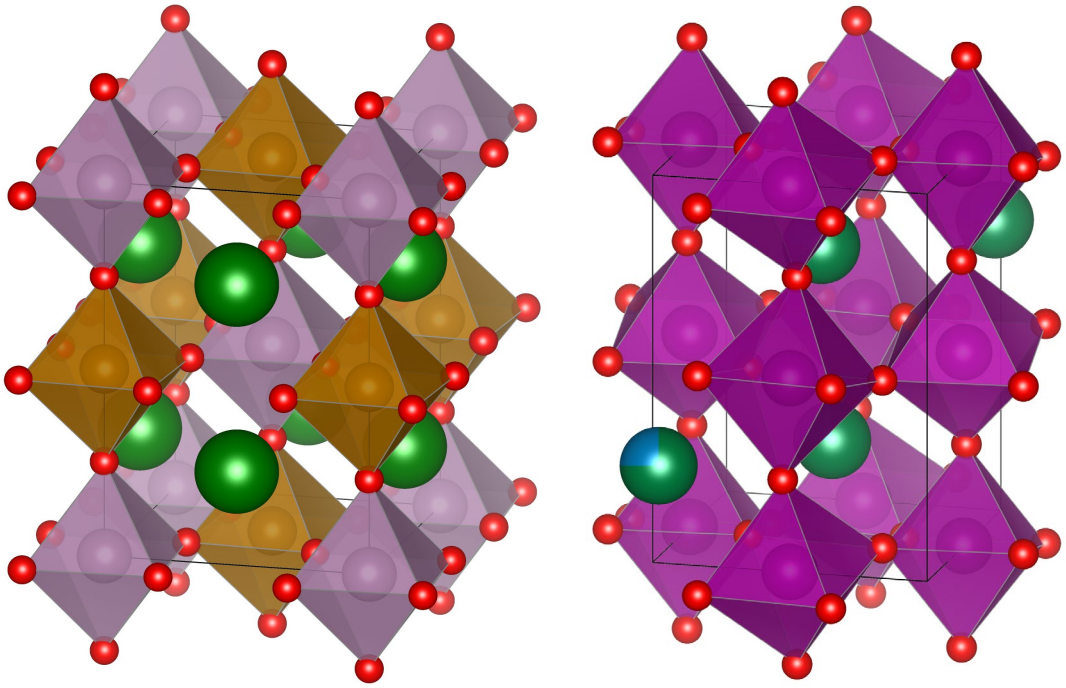


Figure 1.13 Left: I4/*m* (87) Sr_2ReFeO_6[48]; Right: *Pnma* (62) $La_{0.7}Ca_{0.3}MnO_3$[49]

1.6 General Considerations

1.6.1 Spin-Orbit Coupling in 4*d*/5*d* Transition-Metal Oxides

When considering the atomic structure of conventional elements, the spin angular momentum and orbital angular momentum are interpreted separately and sometimes assumed uncorrelated. Russell-Saunders[50] coupling scheme can accurately be used to determine the electronic structure of 'light' elements but it ignores the interactions between angular momenta. These assumptions cease to apply when large atom are being considered.

The electrons with an orbital angular momentum (*l*) act like electrical circuits. The electron itself possesses a magnetic moment with an associated magnetic field described by the spin angular momentum (*s*). The electron's magnetic moment interacts with the magnetic

field from its orbital motion and the resulting effect is called spin-orbit coupling[3]. The energy of this spin-orbit interaction is directly proportional to Z^4, where Z is the atomic number. This is determined by solving the Hamiltonian for spin-orbit coupling. Consequently, spin-orbit coupling has significant effects on the energy levels of cations. The atomic number and the radial extension of 3*d* elements is small so the spin-orbit effect is likewise negligible. Going down from 4*d* to 5*d* elements spin-orbit coupling effect increases and Russell-Saunders coupling scheme no longer applies. When Russell-Saunders coupling scheme does not apply the *j-j* coupling regime is considered. In the *j-j* regime, the total angular momentum (*J*) is the sum of the momentum of each spin-orbit (*l*+*s*) interaction[51].

j-j Coupling $$j_i = l_i + s_i \quad (1.5)$$

Total Angular Momentum $$J = \sum_i l_i + \sum_i s_i \quad (1.6)$$

1.6.2 Spin-Orbit Coupling in Rhenium

Rhenium is a 5*d* transition-metal with an atomic number of 75. Given the high radial expansion and high atomic number, Re materials are expected to undergo high degree of spin-orbit coupling.

Spin-orbit effects can have significant effects on the structural, magnetic, and electrical transport properties of materials. In an octahedral field, Re 5*d* orbitals are expected to split into one set of t_{2g} and one set of e_g orbitals. Spin-orbit coupling effects further split the t_{2g} to a low energy state and a higher energy state.

The magnetic moment of an atom and therefore a material is determined by the total angular momentum of the unpaired electrons. The spin-orbit effects can either quench or enhance observed moment depending on the electronic configuration of the element. When the *d*-orbital is more than half-full, the total angular momentum is $J = L + S$ so the observed magnetic moment is larger than calculated. This is observed in d^7 Co^{2+} [51]. When the orbital is less than half-full, the total angular momentum is $J = |L - S|$. The lifting of t_{2g} degeneracy is strongly expected for a Re^{6+} ($t_{2g}^1 e_g^0$) system and this has been observed to different extents in a number of materials[52, 53].

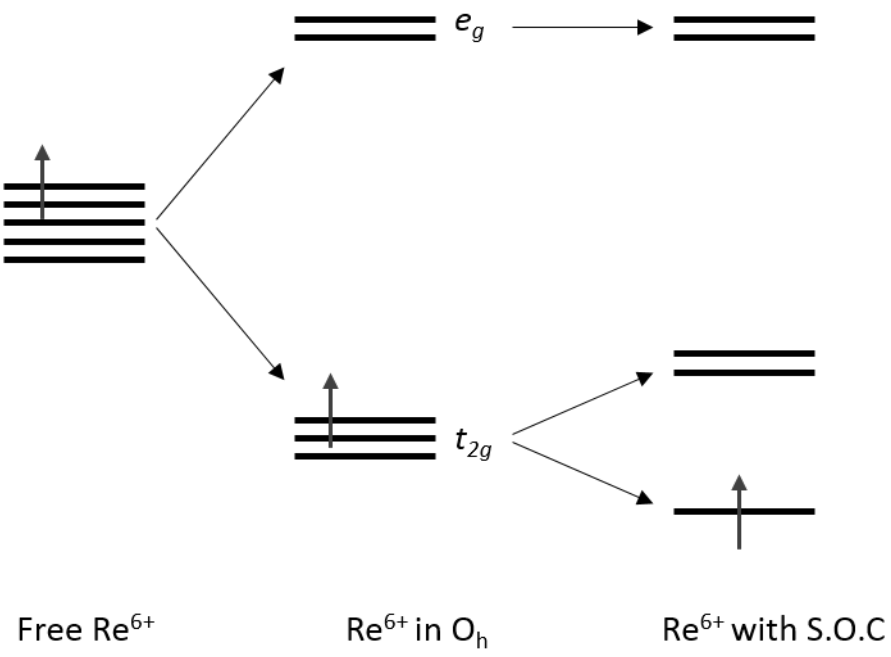


Figure 1.14 An illustration of orbital arrangements of Re^{6+} in free ion, octahedral coordination and in spin-orbit coupling regimes

1.6.3 Jahn-Teller Distortions

Transition-metal oxides with partially filled *d* orbitals can undergo a large energetic stabilisation via preferential occupation of orbitals. In materials that contain octahedrally

coordinated Jahn-Teller cations like Mn^{3+} ($t_{2g}^3e_g^1$) or Cu^{2+} ($t_{2g}^6e_g^3$), the octahedral geometry is broken by removing the electronic degeneracy of the highest occupied molecular orbitals[54]. Energetic stabilisation can be realised by the elongation of two bonds *trans* to each other and contraction of the remaining four or contraction of *trans* bonds and elongation of the remaining four with former leading to greater energy minimisation[55]. Multiple neutron and electron diffraction techniques have been deployed to study the charge and spin configurations and describe the influence of octahedral tilting and cation on orbital ordering in J-T materials[56]. Figure 1.15 shows the two general Jahn-Teller distortion types as seen in Cu^{2+} complexes but applicable to all J-T distorted transition-metal oxides.

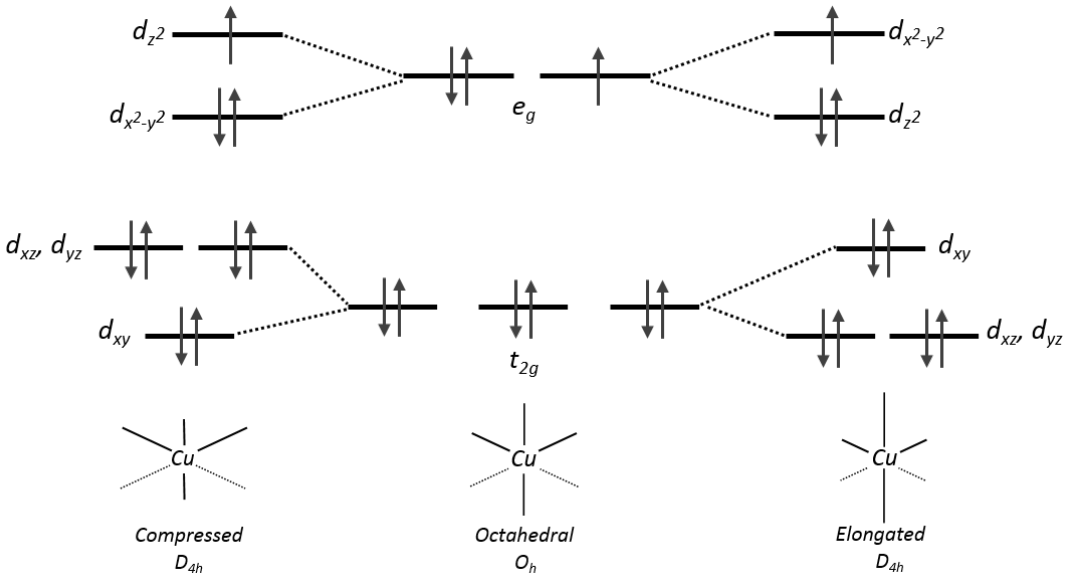


Figure 1.15 The most common Jahn-Teller distortions of an octahedral Cu^{2+} complex[56].

This effect can lead to the development of long range orbital ordering of occupied orbitals called 'cooperative Jahn-Teller distortions'. Lufaso *et al* have given a comprehensive study of J-T distortions found in manganese oxides and cation ordered double perovskites and described how ionic effects and lattice strains often stabilise less symmetric distortions[21].

Ternary materials like $LaMn^{3+}O_3$ undergo a '*Q2*' type distortion where two Mn – O_{eq} bonds shorten and two Mn – O_{eq} bonds lengthen resulting in short, medium and long bonds. Changing the symmetry and the identity of cations leads to a change in J-T distortion parameters and is correlated to bulk physical properties. A quantitative distortion parameter, '*Δd*', is often used to measure and compare the magnitude of J-T distortions[21]:

Distortion Parameter

$$\Delta d = \left(\frac{1}{6}\right) \sum_{n=1,6} \left[\left(\frac{d_n - d}{d}\right)\right]^2 \qquad 1.7$$

1.7 Synthesis and Reactions of Transition-Metal Oxides

1.7.1 Traditional and Soft Chemistry

Making crystalline solids requires heating metal oxide constituents to very high temperatures. This is to ensure high mobility of ions to overcome the strict barriers to diffusion between solid grains. High temperature synthesis leads to the 'thermodynamic' product that is most stable under the synthesis conditions. The ceramic synthesis is a rigid synthesis method so various 'soft-chemistry' methods have been developed. Pechini method[57] polymerises the cations into an organic framework which minimizes the interatomic separation between atoms and speeds up the synthesis. A major drawback of these methods is the limited range of possible oxidation state combinations and coordination geometries that minimize the total energy of the system. Most of synthesis leading up to 2000's has been conducted at very high temperatures or non-ambient pressures. In response to these limitations, Hayward *et al*[58] have developed a series of synthetic methods that allow for the formation of the 'kinetic' phase and the capture of metastable phases made under low temperatures (200-500 °C). These techniques have been termed 'topochemical'. Topochemical reactions exploit the mobility of individual

ions in a solid to modify the parent phase while keeping its structural integrity intact. These methods have led to the preparation of a range of metastable phases[23, 58-60].

1.7.2 Topochemical Reduction

Topochemical reduction is a process intended to modify the oxidation states of the cations via oxygen deintercalation. As oxygen-vacancies are introduced, to maintain the charge neutrality and structural integrity, materials are forced to adopt unusual oxidation states. This results in metastable 'kinetic' phases that would otherwise be impossible to make.

These reactions are performed at relatively low temperatures (180 < T / °C < 630) and have been utilised to make a range of anion-deficient phases[61-63]. A good example of this process is the formation of $SrFe_{0.5}Ru_{0.5}O_3$ to $SrFe_{0.5}Ru_{0.5}O_2$ using CaH_2 as a reducing agent as shown in Figure 1.16 [59].

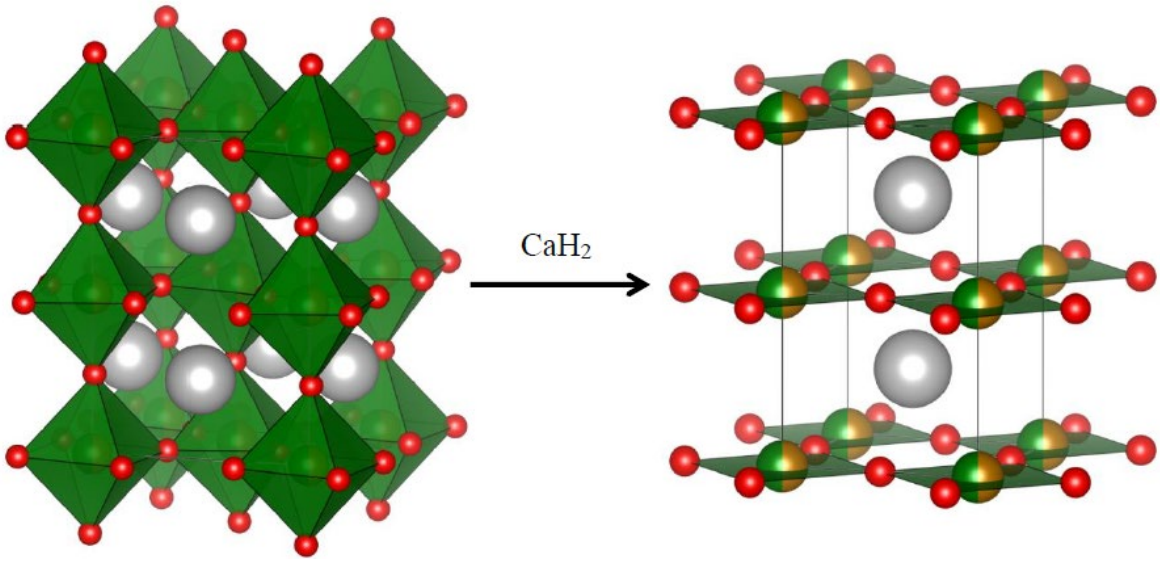


Figure 1.16 Topochemical reduction of $SrFe_{0.5}Ru_{0.5}O_3$ to $SrFe_{0.5}Ru_{0.5}O_2$

Group I/II hydrides have extensively been used to perform topochemical reductions but their reducing strength is very strong which sometimes results in decomposition of the parent phase. Dilute hydrogen gas is a softer reducing agent and has been using

extensively to introduce oxygen vacancies to metal-oxides as well as form double perovskites with novel magnetic and electronic properties like square-planar Ir^{2+} Sr_2FeIrO_4[64].

The use of flowing H_2 gas to perform oxygen-deintercalation on complex transition-metal oxides has been widely studied. A good example is the topochemical reduction of $CaMnO_3$ to yield a cation-vacancy ordered phase $CaMnO_{2.5}$ in the reaction[65]:

$$CaMnO_3 + xH_{2(g)} \rightarrow CaMnO_{3-x} + xH_2O$$

The driving force of reactions like these is typically water-vapour that forms as a by-product and the level of oxide ion deintercalation can be controlled by managing the pressure of water to make a range of compounds with the composition $CaMnO_{3-x}$ ($0 \leq x \leq 0.5$)[66]. This reduction is notable as the $Mn^{4+}O_6$ octahedra are converted to $Mn^{3+}O_5$ square-based pyramids as illustrated in Figure 1.17. Reductions like these have shown that while flowing H_2 gas reactions have limited reducing ability due to the strong H-H bond, they have a strong reduction potential.

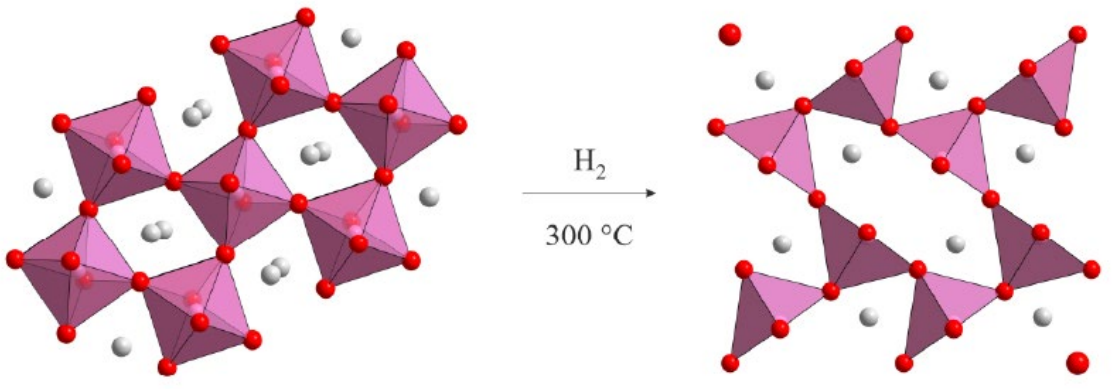


Figure 1.17 Topochemical reduction of $CaMnO_3$ to $CaMnO_{2.5}$ under H_2 gas[66]

Chapter 2 Experimental Methods and Techniques

2.1 Synthesis Methods

2.1.1 Ceramic Synthesis

Ceramic synthesis is the most widely employed synthesis method for making crystalline solids at high temperatures. In a standard ceramic synthesis cycle, suitable stoichiometric quantities of starting materials such as oxides, carbonates, and elemental metals are weighed out and thoroughly ground using an agate mortar and pestle. The use of metal carbonates requires overnight heating at 900 °C to decompose carbonates into equivalent oxides before proceeding to high-temperature synthesis. The resulting powders are pressed into 13 mm diameter pellets under five tonnes of force to minimise the diffusion distance within the solid and facilitate the formation of the target phase. Heating cycles are normally 24 h or 48 h periods, and resulting powders in every cycle are characterised with X-ray powder diffraction to monitor reaction progress. If incomplete, the powders are pressed into a pellet and re-heated under same or modified thermodynamic conditions. When the reaction is judged to be complete, the pellets are ground to fine powder and stored in vials for further characterisation.

2.1.2 Pechini Method

Ceramic synthesis is a reliable method for preparing crystalline solids at high-temperatures but this method can fall short of perfect particle homogeneity even when thermal diffusion is maximised by pressing powders into pellets. Ionic diffusion in the solid-state is slow and relatively large distances have to be overcome.

The Pechini method[57], known conventionally as the citrate method is an alternative to ceramic synthesis that overcomes some of these issues using wet chemistry. In citrate synthesis the metals which make up the target phase are trapped within a gel of polymerised citric acid. This precursor phase contains a closely mixed array of the metal cations, meaning that long range cation diffusion is not required to from the target phase.

In a typical citrate synthesis, the metals are weighed out and dissolved in a 1:1 distilled water and concentrated HNO_3 solution with intermittent heating to facilitate dissolution. The resulting solution is heated to 300 °C after adding an appropriate amount of citric acid monohydrate to balance out the metal charges. Ethylene glycol is added dropwise to coordinate tridentate citric acid ligands to cations and facilitate polymerisation. The solution is heated until nitric acid is expended in NO_x form and dried at 300 °C for an hour until an anhydrous solid organic polymer is fully deposited in the beaker. The polymerised solid product is ground in an agate mortar and pestle and heated to 1000 °C at 1 °C min^{-1} overnight to combust undesired organic compounds. The resulting powders are pressed into 13 mm pellets and heated at required synthesis conditions to make the target phase.

2.2 Glove Box

Air-sensitive compounds in this research work were handled exclusively in an inert atmosphere. Anion deficient phases can react with air resulting in re-oxidation to the parent phase so an argon-filled glove box was used to store and process air-sensitive materials. The oxygen level in the glove box was maintained at a partial pressure of <10 ppm by constantly circulating the internal atmosphere over a copper catalyst. The glove box was unpack venting apparatus for topochemical reactions and prepare X-ray powder diffraction slides.

2.3 Flowing-Gas Reactions

Topochemical reduction of complex oxides were attempted by heating samples under flowing 5%/95% H_2/N_2 gas. The reaction set-up is shown in Figure 2.1.

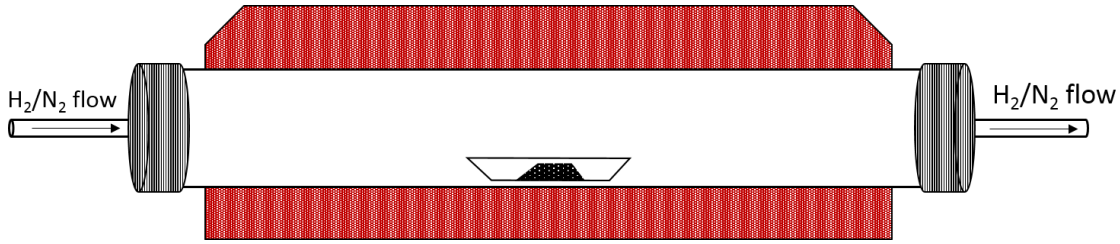


Figure 2.1 Set-up for the flowing hydrogen gas reaction.

In a standard flowing-gas reaction, the powder is placed in an alumina boat crucible and sealed within a quartz tube capped on both ends with brass T-junction taps. The assembled apparatus is placed inside a clam-shell furnace and connected to a gas cylinder via a T-junction tap on one end and an exit to a fume-hood on the other. The clam-shell furnace is set up with a program that gradually heats up and cools down at 2 °C min^{-1}. The sample is heated over several cycles with intermittent X-ray powder diffraction measurements. Once the reaction is considered complete, the tube is sealed, removed from the furnace, evacuated and transferred into an argon-filled glove box for storing and characterisation.

2.4 Thermogravimetric Analysis

A Mettler Toledo TGA/DSC 1 STARe system was used to determine the composition of parent materials and reduced substituents. A TGA apparatus can be used to record the change in mass of a sample as a function of temperature in a given gaseous environment. The sample can be heated under flowing gas of choice to trigger a chemical change characterised by analysing the change in mass.

Reductive TGA measurements were carried out under 5% H_2/N_2 environment to decompose a sample to its constituent elements or to simulate a topochemical reduction under a controlled environment. Reoxidative TGA measurements were carried out under flowing O_2 gas to recover oxygen in a sample under a controlled environment. X-ray powder diffraction and graphing tools were used to characterise before-after products and anion content.

Re-Oxidative $\mathrm{ABO_{3-x} + O_{2(g)} \rightarrow ABO_3}$

Decomposition $\mathrm{ABO_{3-x} + H_{2(g)} \rightarrow AO + B + H_2O}$

Reduction $\mathrm{ABO_3 + H_{2(g)} \rightarrow ABO_{3-x} + H_2O}$

2.5 X-ray Powder Diffraction

X-ray powder diffraction is an essential tool for structural characterisation of materials in solid state chemistry. From laboratory diffractometers to industrial scale beam sources, X-ray powder diffraction is one of the most important characterisation tools that chemists have at their disposal.

X-ray powder diffraction relies on the fact that electrons coherently scatter electromagnetic radiation whereby each atom acts as a coherent point scatterer. Crystalline solids diffract X-ray radiation due to the presence of periodic arrangement of scattering atoms that form an array of lattice planes. Each plane acts as a scattering obstacle for radiating waves and planes diffract radiation when the separation between them is of comparable to the wavelength of the incident radiation. X-ray scattering is elastic meaning the kinetic energy of the propagating wave is conserved but its propagation direction is altered as each point in the array is detected as an individual

secondary wave. In most directions these waves will cancel out through destructive interference. In a few specific directions, these scattered waves will undergo constructive interference and appear on a Fourier space transformed diffraction pattern as distinguishable signals known as diffraction peaks. Lawrence Bragg first proposed this model of diffraction and described it by formulating the nominal Bragg's Law that calculates the angle where constructive interference from X-rays scattered by parallel planes of atoms will produce a diffraction peak[67]. The Bragg's Law is:

Bragg's Law $$n\lambda = 2d_{hkl}sin(\theta)$$ 2.1

Where '*n*' is an integer, 'λ' is the wavelength of incident radiation, 'd_{hkl}' is the inter-planar distance, and 'θ' is the angle of incidence.

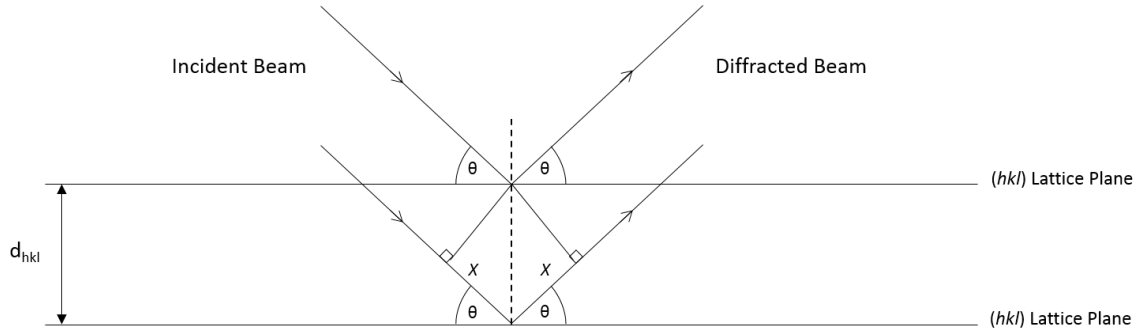


Figure 2.2 A depiction of Bragg's Law of diffraction

The interplanar distance d_{hkl}, is defined as the distance between planes of atoms that give rise to diffraction peaks. The position of a given reflection in a diffraction pattern is defined by its *d*-spacing, which can be used to describe unit cell dimensions. The following relationship defines the intensity of reflections:

Intensity of Reflections $$I_{hkl} \propto LmA|F_{hkl}|^2$$ 2.2

Where '*L*' is the Lorentz-polarisation factor, '*m*' is the reflection multiplicity, '*A*' is the absorption factor, and 'F_{hkl}' is the structure factor.

The structure factor describes how individual contents of the unit cell affect the intensity of reflections[68]. X-rays diffraction depends heavily on electron density at the point of scattering, and therefore the scattering factor 'f_n' is proportional to the atomic number '*Z*':

$$F_{hkl} = \sum_n f_n(\theta)\, exp[2\pi i(hx_n + ky_n + lz_n)]\, exp\left[\frac{-8\pi^2 U_{iso_n}\, sin^2\, \theta_{hkl}}{\lambda^2}\right] \qquad 2.3$$

Where 'f_n' is the atomic scattering factor, 'x_n', 'y_n' and 'z_n' are fractional coordinates of the atoms in the unit cell, and 'U_{iso}' is the isotropic thermal displacement factor. The second exponential term describes the reduction in intensity of reflections as a function of scattering angle θ.

X-ray powder diffraction was ubiquitously used in this research work to characterise materials thanks to the ready availability of multiple X-ray radiation sources at hand.

2.5.1 Bruker D8 Advance Eco Diffractometer

The Bruker D8 Eco diffractometer was used to track the progress of reactions in short and systematic measurements. The Bruker diffractometer operates at 40 kV and 25 mA, is equipped with a Bragg-Brentano focusing geometry, a LYNXEYE detector and a copper X-ray source producing Cu $K_{\alpha1}$ and Cu $K_{\alpha2}$ radiation. Bruker data have spectral contamination, but a high signal-to-noise ratio which allows fast collection of data at the expense of precision.

The Bruker was primarily used to track reaction progress by sprinkling the sample on plastic powder specimen holders covered with Dow-Corning high vacuum grease. The holders were tightened at the instrument on a spinning stage and mounted on the machine for measurement.

2.5.2 PANalytical X'Pert and Empyrean Diffractometers

The PANalytical X'Pert and Empyrean diffractometers were used to collect high precision data for Rietveld refinement. PANalytical instruments use a Bragg-Brentano focusing geometry and generate monochromatic Cu K_{a1} radiation by blocking Cu K_{a2} radiation using a Ge (111) monochromator. Here the divergent and diffracted beams focus at a fixed radius from the sample leading to both to good resolution and peak intensities. Both instruments were used to track the progress of reactions and confirm final structures. The Empyrean was the most frequently used instrument for both air sensitive and non-air sensitive samples at measurement times ranging from 30 minutes to overnight scans. The X'Pert diffractometer is equipped with an angle sensitive detector and the beam optics could be adjusted by the choice of beam mask, anti-scatter and Soller slits to control divergence.

Both instruments have the same type of sample holders and sample mounting procedures. Non-air sensitive samples were sprinkled on Dow-Corning high vacuum greased silicon wafers and mounted on spinner stage holders. Air sensitive samples were sprinkled on thin glass slides covered with Dow-Corning high vacuum grease and loaded on air-sensitive X-ray holders, as depicted in Figure 2.3, in an argon-filled glove box. These holders were secured with brass caps that press on rubber O-Rings to create an air-tight seal and mounted on flat-stage holders on the diffractometers.

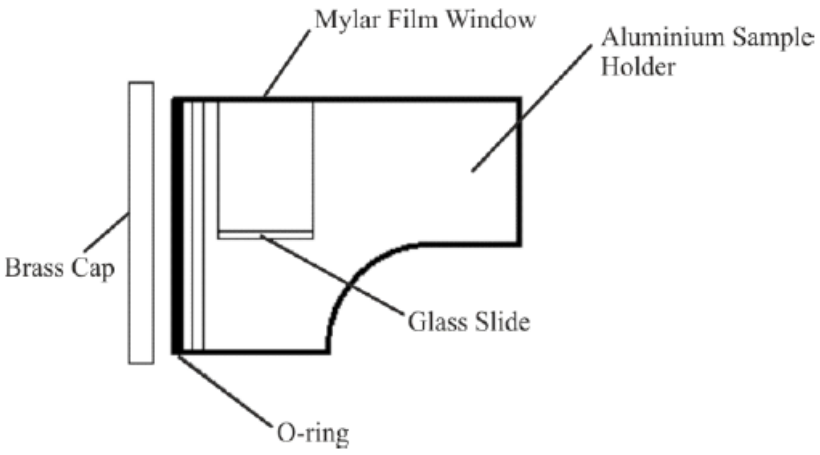


Figure 2.3 Air sensitive X-ray slide holder

2.5.3 Synchrotron X-ray Powder Diffraction

The Diamond Light Source Facility in Didcot, Oxfordshire manages an I11 beamline that was used to collected X-ray powder diffraction data using synchrotron radiation. The I11 beamline produces X-rays at energies from 5 keV to 30 keV by accelerating electrons to near speed of light around a curved path using powerful magnets. Electrons circulate at a constant speed due to the conservation of angular momentum. This generates a constant X-ray radiation that is diverted to the diffractometers as required. The I11 beamline uses a double crystal monochromator and harmonic rejection mirrors to deliver extremely high brightness and low bandpass X-ray beams to the sample and is equipped with 45 Si [111] crystals and detectors to provide rapid data collection[69, 70].

The diffractometer is equipped with a wide-angle (2θ = 0 - 150°) position sensitive detector (PSD) that uses the MYTHEN-II silicon microchip technology. PSD was used for standard measurements lasting <1 s at a very high resolution to collect data that could be analysed using Rietveld refinement techniques. For higher precision and resolution

measurements, a single-axis instrument called the multi-analysing crystal (MAC) assembly of 40 to 50 crystals with pre-aligned angular offsets was used.

The samples were loaded into 0.3 mm or 0.5 mm borosilicate capillaries, secured on brass holders with a magnetic base and mounted onto the diffractometer by a robotic arm.

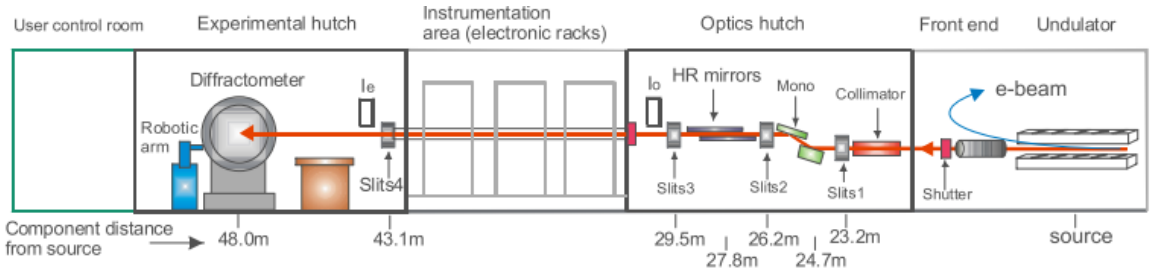


Figure 2.4 Schematic representation of I11 X-ray source and the diffractometer[69].

2.6 Neutron Powder Diffraction

Complex transition-metal oxides studied in this research work consist of light and heavy elements with a wide range of atomic numbers. The X-ray scattering factor of elements follows a linear relationship with atomic number, and reflections from lighter elements are often thoroughly undetectable on the diffraction pattern in the presence of heavier elements. Neutron radiation interacts with nuclei of atoms and unpaired spins, offering a new dimension for characterising structures of crystalline materials.

Neutron scattering factors of atomic nuclei do not follow a linear relationship with atomic number. A knowledge of scattering lengths and absorption cross sections of elements (the effective area of a nucleus exposed to an incident beam) is usually able to differentiate between lighter, heavy and isoelectronic elements. X-ray powder diffraction scattering intensity also rapidly drops with the increase of scattering angle unlike in neutron diffraction from nuclei where there is no fall-off in intensity. Nuclear scattering factor is

not dependent on the scattering angle so diffraction peaks at high angles don't lose intensity. Materials investigated in this research work included combinations of very heavy and very light elements and low-temperature magnetic ordering that could only be characterised using a neutron source.

Neutron powder diffraction can also be used to describe the magnetic ordering present in the material. Neutrons are ½ spin elementary particles and therefore couple with unpaired electrons to scatter neutron radiation. This scattering appears in the form of weak magnetic reflections in the diffraction pattern and can be fitted to a magnetic structure using the Rietveld method. The magnetic scattering factor for an unpolarised neutron source is expressed as follows:

Scattering factor

$$F_{hkl}^{mag} = \sum_{j} q_j p_j e^{2\pi i h x_j} \qquad 2.4$$

Where 'q_j' is the magnetic interaction vector, 'p_j' is the magnetic scattering length, 'h' is the magnetic scattering vector, and 'x_j' is the position vector of the magnetic atoms in the unit cell. The intensity of reflections is proportional to the square of the projection of the magnetic structure factor onto the scattering vector:

Intensity of reflections

$$I_{hkl}^{mag} = \left|F_{hkl}^{mag}\right|^2 \cos^2 \alpha \qquad 2.5$$

Where 'α' is the angle between the lattice place and the magnetic spin vector. Compared to nuclear scattering, the form factor of magnetic scattering has angular dependence so the intensity of scattering decays even stronger than in X-ray powder diffraction.

A disadvantage is that neutron scattering intensity of nuclei is relatively weak and most neutron diffraction experiments require comparably large samples weighing up to 4 g.

Neutron powder diffraction samples were loaded into vanadium cans which has a negligible contribution to a neutron diffraction pattern due to its low coherent scattering length of -0.3825 fm[71]. Neutron powder diffraction measurements presented in this research work were all collected at the ISIS Neutron and Muon Source in Didcot, Oxfordshire and the Institut Laue-Langevin (ILL) neutron source in Grenoble, France. The ISIS neutron facility uses a spallation source i.e. neutrons are generated by hitting a heavy metal target with pulses of accelerated high-energy protons. The ILL facility uses a nuclear reactor source where neutron radiation is generated via a fission process.

2.6.1 GEM Diffractometer

The ISIS neutron source at the Rutherford Appleton Laboratory in Didcot, Oxfordshire uses a spallation neutron source where proton pulses are accelerated to 800 MeV in a synchrotron and fired at a tantalum target. The resulting intranuclear cascade results in a stream of neutrons. These neutron pulses have very high energies and are slowed down with a hydrogenous moderator to achieve an appropriate wavelength for time-of-flight measurements. Time-of-flight diffractometers use fixed angle detectors to collect diffraction patterns as a function of wavelength. The de Broglie relationship describes how the wavelength of the neutron source is related to the velocity of neutrons:

de Broglie relationship

$$\lambda = \frac{h}{m} \times \frac{t}{L} \qquad 2.6$$

Where 'λ' is wavelength, 'h' is Planck's constant, 'm' is the neutron mass, and 't' is the time taken to travel a distance 'L' from to source to the detector via the sample[72]. Samples were loaded into vanadium cans and measured at temperatures 5 K to 300 K. Vanadium has a relatively low scattering length of -0.3824 fm, making its contribution to the

diffraction pattern detectable and negligible[73]. Time-of-flight Instrument used in this research was GEM.

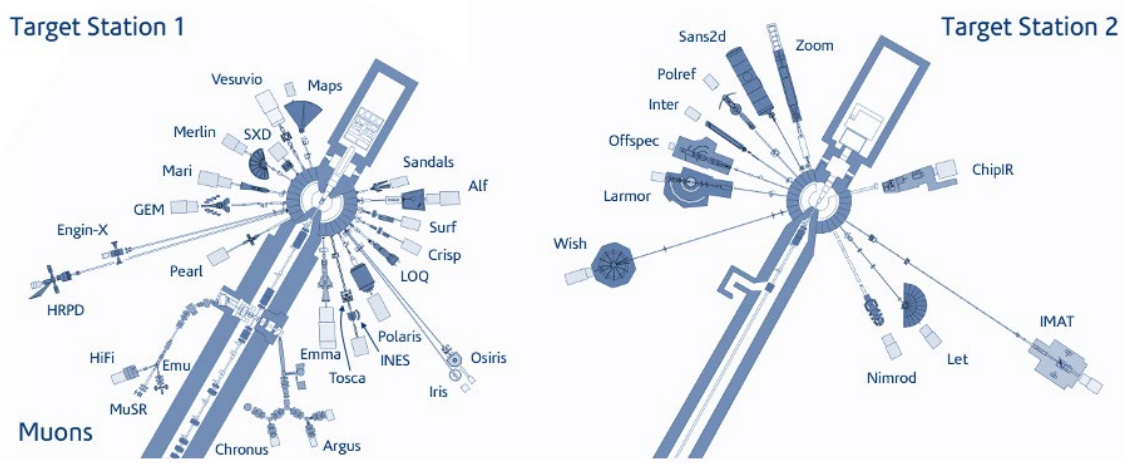


Figure 2.5 ISIS neutron and Muon facility schematic

The General Materials Diffractometer (GEM) is a high intensity, high-resolution neutron diffractomer at the ISIS facility. Its detectors cover a scattering angle range from 1.1° to 169.3° and is used routinely to study the structure of crystalline powders and amorphous materials. In this research work, a cryostat was used to cool down samples to be measured at low temperatures[71].

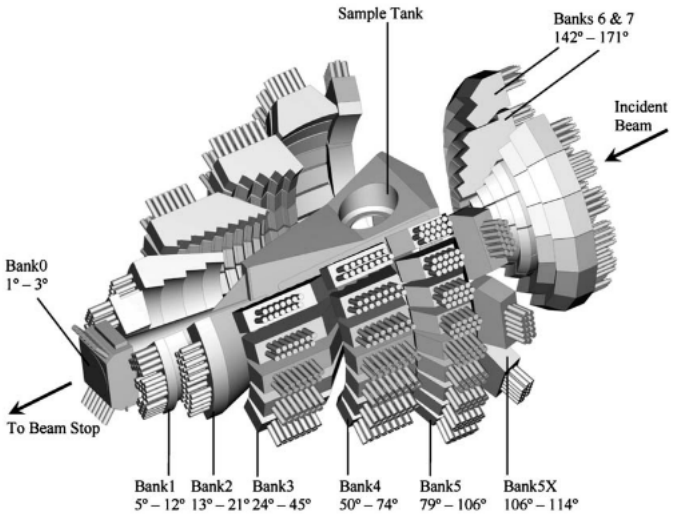


Figure 2.6 GEM Instrument at the ISIS Facility[71]

2.6.2 D2B Diffractometer

The D2B instrument at the ILL neutron source in Grenoble, France generates neutrons using a nuclear reactor source that generates radiation via fission. It is a high-resolution diffractometer that generates high-intensity neutrons in the meV range from fission of ^{235}U moderated with D_2O. The generated neutrons are of constant wavelength (maximum flux at 1.2 Å) and are of suitable energies for diffraction measurement. The wavelengths can be further discriminated using a crystal monochromator at each instrument[74]. The D2B instrument perform scans over the $5 < 2\theta /° < 160$ range and sums several scans to generate a pattern with great signal-to-noise ratio. The instrument can be set-up with a specific wavelength by rotating a Ge crystal monochromator within the *hkl* plane. The wavelength of the incident beam used in this research work was 1.5943 Å.

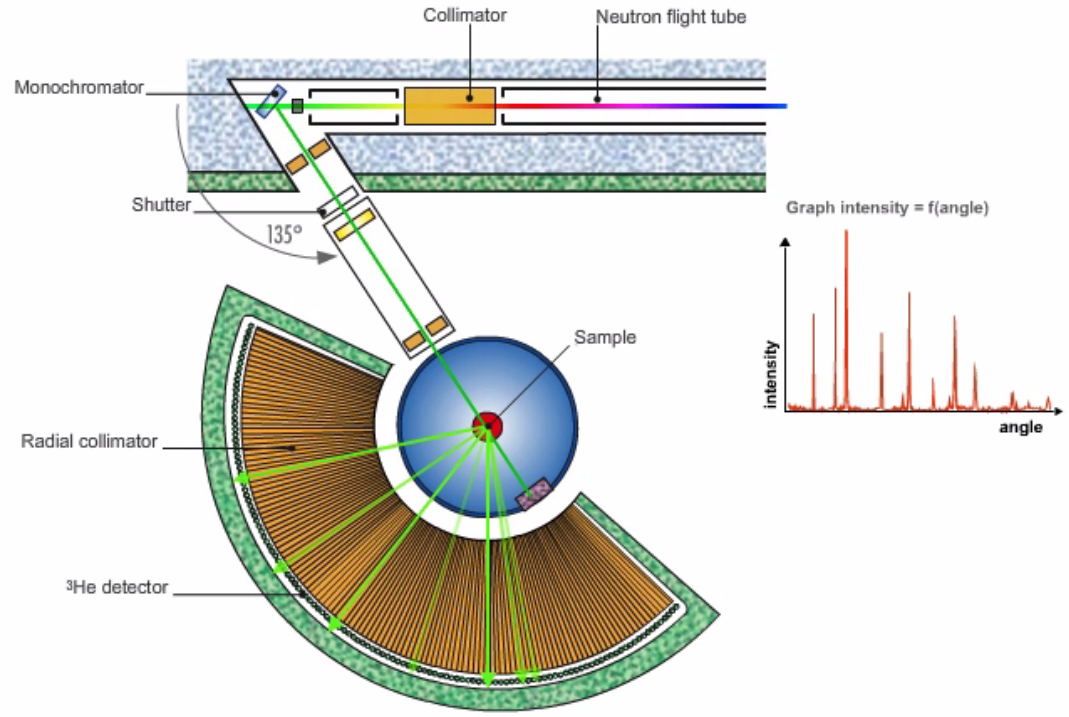


Figure 2.7 D2B diffractometer at ILL, Grenoble, France[74]

2.7 Rietveld Refinement

Extracting information from diffraction data is an important part of crystallographic characterisation and can be approached in a number of ways. A major challenge is that when a diffraction pattern is generated, planes that have the same or similar *d*-spacing but different *hkl* values have reflections that are transformed on a 1-dimensional pattern at the similar 2θ. These reflections all contribute to a peak intensity at comparable angles resulting in peak overlap and loss of significant 3D information. Rietveld refinement is a structure refinement method used for characterisation of crystalline materials from powder diffraction data that overcomes this challenge[75]. Rietveld refinement uses the least-squares method to refine the crystallographic parameters of a simulated theoretical model until it matches the measured profile of the material. It compares the intensity of a given point calculated from the theoretical model with the measured intensity and iteratively updates various parameters until the model converges with the measured peak profile.

Least squares

$$S = \sum w_i \{y_i^{obs} - y_i^{calc}\}^2 \qquad 2.7$$

Weighting factor

$$w_i = \frac{1}{\sigma^2[y_i^{obs}]} \qquad 2.8$$

Where '*S*' is the difference between calculated and experimental intensities, 'w_i' is the weighing factor, 'y_i^{obs}' is the observed intensity of step '*i*' and 'y_i^{calc}' is the calculated intensity of step '*i*'. The objective of a refinement is to minimise '*S*'.

General Structure Analysis System (GSAS) suite of programs was used to conduct Rietveld refinements[76]. The fit of a model at each refinement iteration to the data was assessed based on three parameters:

Profile factor

$$R_p = \frac{\sum |y_i^{obs} - y_i^{calc}|}{\sum y_i^{obs}} \quad (2.9)$$

Weighted profile factor

$$wR_p = \sqrt{\frac{\sum w_i \left(y_i^{obs} - y_i^{calc}\right)^2}{\sum w_i y_i^{2(obs)}}} = \sqrt{\frac{S}{\sum w_i y_i^{2(obs)}}} \quad (2.10)$$

Goodness of fit

$$\chi^2 = \frac{\sum w_i \left(y_i^{obs} - y_i^{calc}\right)^2}{n_{obs} - n_{var}} = \frac{S}{n_{obs} - n_{var}} \quad (2.11)$$

Where 'R_p' is the profile factor, 'wR_p' is the weighed profile factor, and 'χ^2' is the goodness of fit, 'n_{obs}' is the number of observations in histograms and 'n_{var}' is the number of variables in the least squares refinement. Lattice parameters, atomic positions, site occupancies, and peak profiles among other variables were obtained using the Rietveld method.

2.8 Bond Valence Sums (BVS)

Bond Valence Sum (BVS) is a method used to estimate the valence of ions based on bond lengths and the nature of atoms in their coordination environment. Various sources show a strong linear correlation exists between cation and anion bond parameters that allow us to extrapolate bond-valance parameters of coordinated metal centres in complex oxides[77].

BVS calculations define the total valence of an ion in a coordination environment as the sum of valence contributions of individual bonds between atoms '*i*' and '*j*'. The method

can be used to predict bond lengths for a given bond valence set or be used to confirm the reliability of a determined structure. Two following equations govern BVS calculations:

Bond Valence Sum $$V_i = \sum_j v_{ij} \quad (2.12)$$

The valence of a bond $$v_{ij} = e^{(R_{ij} - d_{ij})/b} \quad (2.13)$$

Where 'V_i' is total valence of an ion, 'v_{ij}' is valence contributions of individual bonds, 'R_{ij}' is the bond-valence parameter, 'd_{ij}' is the individual bond length and 'b' is an empirical constant equalling 0.37 Å. The equations above were used by Brese and O'Keefe to predict unique bond-valence parameters for many sets of cation-anion pairs[78].

2.9 ^{57}Fe Mössbauer Spectroscopy

Nuclei undergo a constant series of energy level transitions that are associated with emission or absorption of gamma rays. These nucleonic transitions can provide essential information about local energy level environments in atoms as they are governed by the electronic and magnetic properties of the material. In the gas phase, these nucleonic interactions with local environments are of significantly small magnitudes and suffer from nuclei recoil due to the conservation of momentum during emission that has associated recoil energy comparable or larger than the energy of gamma-ray emission.

In solids nuclei are more tightly bound to their environment and therefore do not move as freely during absorption-emission making nuclei recoil effects less significant. The energy of an emitted gamma ray is nevertheless lessened by quantised lattice vibrations characterised by phonon emissions. The magnitude of lattice vibrations is random, so when zero phonons are emitted, the event is considered 'recoil-free'. In a recoil-free

event, gamma ray energy loss is negligible as individual recoil energies are comparable to the bulk recoil energy. Therefore the absorption-emission energies overlap strongly enough to create a measurable resonance of gamma radiation. This is called the Mössbauer effect.

^{57}Fe Mössbauer Spectroscopy is the most common technique that utilises the Mössbauer effect to detect gamma-ray resonance and study the local environment of atoms or ions in iron-containing materials. It uses a ^{57}Co source that decays by electron capture to a ^{57}Fe excited state which further decays to its ground state thereby emitting gamma rays. The energy of these gamma rays propagate through and are modified via the Doppler Effect. A detector can measure the transmission of these rays as they propagate through the sample with sharp dips in the spectra indicating absorption at energies where resonance occurs.

In ^{57}Fe Mössbauer Spectroscopy the local environment of the atoms or ions modify the energies at which transitions occur. Three parameters that can be identified from these interactions are isomer shifts, quadrupole splitting, and magnetic splitting. These parameters can inform the experimenter about valence and spin-states of all iron species in a given sample, irrespective of what charge and valence state iron is in or if the sample is diamagnetic, paramagnetic, or undergoes a magnetic coupling.

Isomer shifts occur due to a non-zero volume of nuclei and energy density levels of *s* electrons around them. When electron charge density is observed within the nuclei, the net Coulomb interactions lead to a shift in nuclear energy levels. The differences between *s* electron density at the source and the detector cause a shift in the resonance energy. These shifts, being directly related to electron charge density, can be used to determine

the oxidation state of iron. The most common experiment is the differentiation of ferrous and ferric systems where the oxidation state of iron ambiguous. Ferrous Fe^{3+} experiences weaker screening of *d* electrons compared to ferric Fe^{2+}, resulting in a relative difference in *s* electron charge density at the nucleus and is represented by a lower chemical shift on a spectrum[79, 80].

A nuclear quadrupole moment is observed when an asymmetrical electric field splits the nuclear energy levels. This is seen in nuclei with an angular momentum quantum number $I > ½$ that have non-spherical charge distribution. In the case of the ^{57}Fe isotope, the excited state is split into $m_I = \pm 1/2$ and $m_I = \pm 3/2$ and these transitions create a quadrupole effect as seen in Figure 2.8.

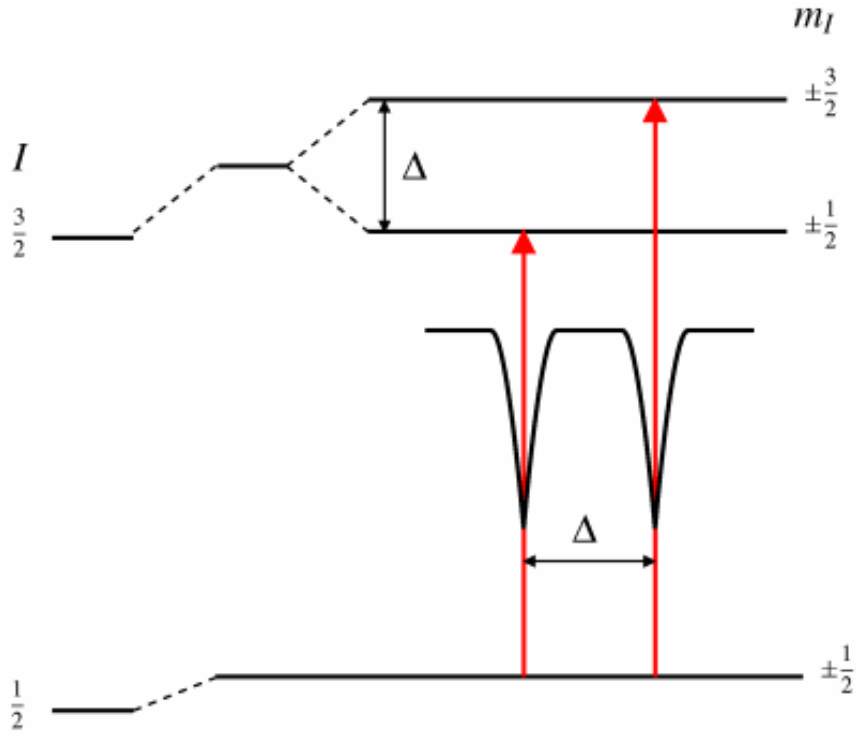


Figure 2.8 Quadrupole splitting from a 3/2 to 1/2 transition. Δ is the magnitude of quadrupole splitting.

Spectra presented in this research were collected and fitted by Dr Paul A. Bingham and Dr Susan D. Forder at Sheffield Hallam University. Samples were diluted with graphite and

sealed in airtight holders. ^{57}Fe Mössbauer Spectroscopy data were collected relative to α-Fe standard using a 36 mCi ^{57}Co in Rh source. All spectra were recorded over a ± 5 mms^{-1} velocity range.

2.10 Transmission Electron Microscopy

Transmission Electron Microscopy (TEM) uses a concentrated electron beam to project an electron diffraction pattern of crystalline materials. TEM is the strongest microscope and produces high-resolution, two-dimensional images used to collect compositional and crystallographic information[81, 82].

In TEM, the sample is deposited onto a thin film and stored in a vacuum chamber. An electron gun generates a stream of electrons that are re-focused onto the sample chamber by a condenser. The electron source is usually a cathode composed of heated tungsten filaments or lanthanum rods. A condenser converges the electron beam on the sample chamber providing a concentrated exposure of the sample to the electron source and generating high-resolution images which are recorded on a monochromatic detector with a point resolution of 0.24 nm.

Electron diffraction patterns were taken on Philips CM20 and FEI Tecnai microscopes and dark field images were obtained on the Tecnai microscope. Samples for all TEM techniques were prepared in a glove box filled with inert argon by crushing the powder and dispersing it in ethanol. A few drops of this solution were deposited on a copper grid covered with a holey carbon film. The samples were exposed to air for a few minutes at insertion into the microscope.

2.10.1 Electron Energy Loss Spectroscopy

Scanning transmission electron microscopy - electron energy loss spectroscopy (STEM-EELS) is an alternative electron microscopy method that combines the principles of transmission electron microscopy and scanning electron microscopy but also allows to take electron energy loss spectroscopy measurements. Having both electron diffraction, transmission imaging and X-ray emission spectroscopy, all in one set-up make STEM-EELS apparatus very useful for studying materials.

Electron energy loss spectroscopy measures the energy lost by electrons after they have interacted with the sample under the microscope. It provides information about the interacting atoms and can be used to collect information on the elemental identity, chemical bonding and valence of atoms[83, 84].

STEM-EELS is effective in determining oxidations states of transition-metals in cases of ambiguity. Most early investigations have focused on the L_2 and L_3 edges of transition-metals that exhibit prominent features called white lines due to transitions from the $2p_{3/2}$ and $2p_{1/2}$ levels to the un-occupied 3d states or the chemical shift method that relies on the observation that the excitation edges shift to a higher energy-loss for higher oxidation states[85, 86]. Over time a consolidated database of reference edge spectra has been built[87]. In a standard STEM-EELS measurement the measured near-edge energy loss is qualitatively compared to reference energy loss spectra allowing a judgement to be made about the oxidation state of the element being investigated.

STEM-EELS in this research was performed on a Titan 80–300 microscope equipped with an aberration corrector for the probe forming lens and an electron monochromator yielding an energy resolution of 100 meV with a Gatan Quantum spectrometer.

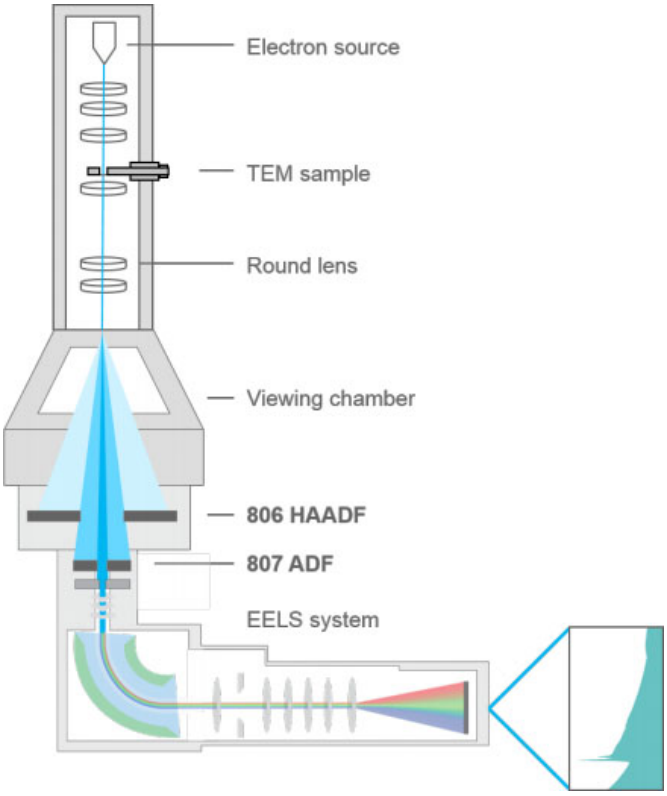


Figure 2.9 Schematic of a STEM-EELS[30]

2.11 Superconducting Quantum Interference Device (SQUID)

Magnetisation data were routinely collected using a Quantum Design MPMS SQUID magnetometer. A Superconducting Quantum Interference Device can measure the magnetisation of materials with high precision by making use of the Josephson Effect[88]. A SQUID is equipped with two Josephson junctions made of a thin layer of insulating material that separate a superconducting coil.

These junctions quantise the current in the ring allowing Cooper pairs to maintain coherence in the absence of a magnetic field and tunnel freely when operational[89]. In the presence of an external magnetic field, the superconductivity current breaks when a magnetic field is produced to counter it. The voltage of the new current is recorded and it is proportional to the magnetic moment of the sample being measured.

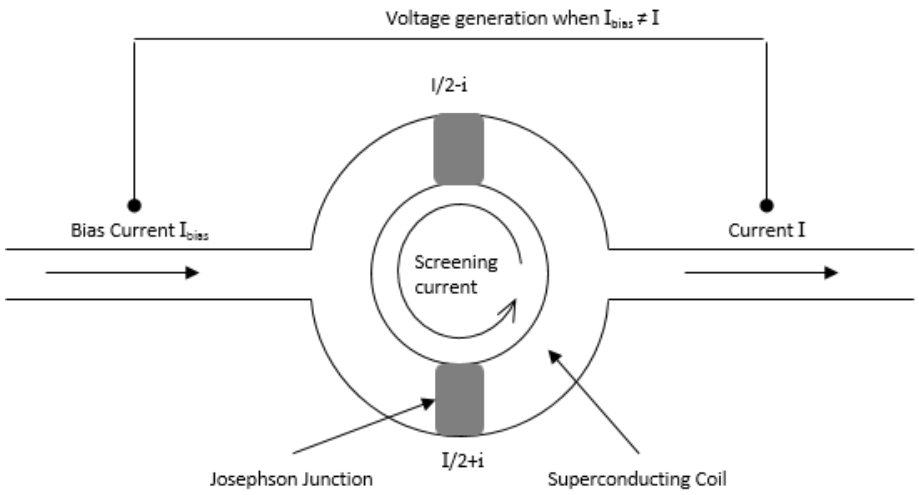


Figure 2.10 Principal component of a Superconducting Quantum Interference Device magnetometer[88]

For all SQUID measurements, a small amount of sample (15 mg to 30 mg) was trapped inside gelatine capsules and suspended by empty capsules either side inside a plastic straw. The capsules at the top and bottom edges were wrapped in diamagnetic tape to ensure the integrity of the sample holder. The straws were attached on a sample stick, evacuated through small holes pierced with a syringe needle and lowered into the SQUID for measurement.

2.11.1 Standard Measurement

Standard SQUID measurements were ubiquitously used in this research work to characterise the magnetic behaviour of synthesised materials. Zero-field-cooled (ZFC) and field-cooled (FC) measurements were collected in a 100 Oe or 1000 Oe field over a temperature range of $5 < T / K < 300$. Magnetisation measurements as a function of field were conducted at in the $-5 < H / T < 5$ field range.

2.11.2 Ferrosubtraction Measurements

Some samples contained ferromagnetic impurities that had to be factored out of the bulk phase magnetisation readings. In these cases the samples were exposed to a large

magnetic field that saturated the ferromagnetic susceptibility of the impurity, allowing the paramagnetic susceptibility of the bulk phase to be discerned. Field-cooled isotherms were collected every 5 K over the range 10 < T / K < 300 and magnetisation was measured at every temperature interval every 0.5 T over the range 3 < H / T < 5. For each temperature interval, the magnetisation was measured as a function of the field which gave a straight line where slope equalled the paramagnetic susceptibility at that temperature, and the intercept equalled the saturated ferromagnetic impurity moment.

2.12 Magnetism

The presence of unpaired electrons in crystalline material results in a net magnetic moment that fundamentally arises from the intrinsic property of the electrons defined by the spin quantum number and the orientation of the orbitals defined by the orbital quantum number. In the presence of an external field, the $|S|$ spin angular momentum and $|L|$ orbital angular momentum is quantised and both have associated magnetic quantum numbers m_s and m_l. These quantum numbers define the orientation of the angular moment relative to the magnetic field. The spin angular momentum can only take values ½ and -½, while orbital angular momentum depends on the orbital quantum number *l*. The magnetic dipole moments that arise as a result of orbital and spin angular momenta can be described with the following equations:

Spin Magnetic Moment

$$m = g_e \mu_B \sqrt{s(s+1)} \qquad 2.14$$

Where $g_e = 2.002319$ is the g-factor of the electron and $\mu_B = e\hbar/2m_e$ is the Bohr magneton, the elementary unit of the orbital magnetic moment in an atom. Therefore, in the presence of an external field, the spin and orbital angular momenta that describe an

electron in an atomic orbital influence the energy of that electron and cause an energy splitting via the Zeeman Effect[3]. The term g-factor can be taken as $g_e = 2$ so that the spin magnetic moment of a single electron is 1 Bohr magneton as it simplifies the qualitative analysis of magnetic behaviour.

The quantum numbers outlined above are the fundamental principles that describe the atomic origins of magnetism in materials. This research work was interested in synthesising and studying materials with unpaired electrons and focused primarily on complex oxides with partially occupied 4*d* and 5*d* orbitals.

2.12.1 The Curie-Weiss Law

All materials measured in this research work showed non-diamagnetic behaviour due to the presence of unpaired electrons. In the presence of an external field, the unpaired electrons experience a force that aligns the electrons in the direction of the field.

In an external field, paramagnetic materials have electron spins aligned to different extents and directions giving rise to paramagnetic susceptibility. Paramagnetic susceptibility is inversely proportional to temperature in the scenario where total magnetic field acting on the material is external, and the Curie Law describes this relationship:

Curie Law

$$\chi_m = \frac{C}{T} \qquad 2.15$$

Where 'χ_m' is magnetic susceptibility, 'C' is the Curie constant and 'T' is temperature. Paramagnetic materials often do not fully obey the Curie law when they experience correlated magnetic behaviour. The Curie Law is expanded upon by the inclusion of the Weiss molecular field constant as the total magnetic field acting on the electrons is not

reserved to the applied external field but includes the internal magnetic field that arises from correlated electron-electron Coulombic exchange interactions. The Curie-Weiss Law describes this:

Curie-Weiss Law

$$\chi_m = \frac{C}{T - \theta} \tag{2.16}$$

Where 'θ' is the Weiss molecular field. Curie Law assumes that individual magnetic moments do not interact while in reality most complex magnetic systems have additional interactions. Systems like ferromagnetic materials cannot be described by the Curie Law alone above their T_C but can be explained well using the Curie-Weiss law. An extra term is often incorporated onto the Curie-Weiss law where:

CW law with *K*

$$\chi_m = \frac{C}{T - \theta} + K \tag{2.17}$$

Where '*K*' is the temperature-independent paramagnetic contribution. By plotting the inverse magnetic susceptibility data against temperature to determine the Weiss constant and the Curie constant which is subsequently proportional to the square of the effective magnetic moment of the measured material:

Inverse Susceptibility

$$1/\chi_m = \frac{T}{C} - \frac{\theta}{C} \tag{2.18}$$

Curie Constant

$$C = \frac{N_A \mu_B g^2 S(S+1)}{3k_B} \approx \frac{1}{8}\mu_{eff}^2 \tag{2.19}$$

Spin only Moment

$$\mu_{eff} = g_e\sqrt{S(S+1)} \tag{2.20}$$

Where 'N_A' is the Avogadro's number, 'μ_B' is the Bohr magneton, 'g' is the gyrometric ratio, 'S' is the spin quantum number of the magnetic ion, 'k_B' is the Boltzmann's constant and 'μ_{eff}' is the effective magnetic moment.

2.12.2 Correlated Magnetic Behaviour

The Weiss molecular field is used to describe the various forms of correlated magnetic behaviour that deviate from paramagnetism. Normally, when $\theta > 0$, the molecular field generated by electron-electron correlated behaviour is acting in the same direction as the applied external field leading to ferromagnetism. The transition from paramagnetic to ferromagnetic behaviour happens at the Curie temperature 'T_C' below which the molecular field is strong enough to align the spins. Weiss molecular field theory further expands to explain the antiferromagnetism property of materials where $\theta < 0$ and the negative molecular field aligns the spins anti-parallel to each other where the bulk net-magnetic moment is cancelled out[3].

2.13 Conductivity Measurements

Conductivity measurements were performed on a custom-made system built internally. The setup uses an Oxford Instruments helium flow cryostat and a custom probe. The powders were pressed into 13 mm pellets and a ~2 mm – 5 mm bar was cut off using an automated saw. Refrigerated silver paste and copper wire was soldered to create a four-probe. The probe was installed into the cryostat and the resistance of the sample was measured as a function of temperature.

Chapter 3 Topochemical Reduction of Sr_2ReLiO_6 to $Sr_2ReLiO_{5.5}$

3.1 Introduction

The synthesis and reactivity of novel mixed-metal double perovskites presents an interesting challenge for solid-state chemists. Low-temperature chemistry has made this area of research more expansive and has opened a pathway for the preparation of a multitude of new materials. A wide range of metastable materials with unusual oxidation state metal centres such as Mn^{1+} [90], Ni^{1+} [91], Co^{1+} [92] and Fe^{2+} [93] have been made in recent years using Group I/II metal-hydrides like NaH and CaH_2 as reducing agents in topochemical reactions. Research on late 4*d* transition-metals has been productive with a notable example being the preparation of an extended oxide $LaSrNiRuO_4$ phase made up of infinite sheets of apex-linked, square-planar Ni^{1+} and Ru^{2+} [94]. Some systems are comparatively fragile to heavily reducing metal hydrides with an energetic preference for reduction to elemental metals so softer reduction methods have been applied. Notably, an iridium compound Sr_2FeIrO_6 was treated under dilute hydrogen to make Sr_2FeIrO_4, an Ir^{2+} square-planar infinite layer phase[64].

Rhenium oxide chemistry has been relatively unexplored due to the rarity and high cost of the element but, there has been considerable progress marked by the discovery of spin-polarised ferromagnetism in Sr_2ReFeO_6[5] and a spin-singlet state in La_2LiReO_6[95]. Many rhenium double perovskite parent materials have been made since then, often using elaborate synthetic conditions to reach the lower oxidation states contrary to the preferred d^0 Re^{7+} state[96-99]. In an attempt to stabilise lower oxidation states that prove challenging to make under thermodynamic conditions, the topochemical reduction of

Re^{7+} to $Re^{5+/6+}$ using dilute hydrogen gas is described. The parent material for this study was Sr_2ReLiO_6, a diamagnetic cubic double perovskite reported by Loye *et al* [100].

3.2 Synthesis

3.2.1 Synthesis of Sr_2ReLiO_6

Samples of Sr_2ReLiO_6 were prepared using the ceramic synthesis method previously described by Zur Loye *et al*[100]. Suitable stoichiometric ratios of $SrCO_3$ (99.994%), Re metal (99.99%) and Li_2CO_3 (99.998%) were finely ground together using an agate mortar and pestle and transferred into an alumina crucible. The mixture was heated at a rate of 5 °C min^{-1} to 1000 °C to decompose the carbonates. The resulting powder was reground with an agate mortar and pestle and pressed into a 13 mm pellet. The pellet was heated in a muffle furnace in air at 900 °C for 24 hours.

The resulting material was confirmed to be phase pure using X-ray powder diffraction data with systematic absences consistent with the *I*4*/m* space group and lattice parameters of *a* = 5.54722(4) Å, *c* = 7.91827(7) Å. This was in good agreement with the literature values of *a* = 5.5467(2) Å, *c* = 7.9197(4) Å[100]. The synthetic method applied in this research work deviated from the published method whereby Li_2CO_3 was used in 25% excess given its volatility. All attempts to use stoichiometric amounts resulted in impurities.

3.2.2 Synthesis of $Sr_2ReLiO_{5.5}$

Samples of $Sr_2ReLiO_{5.5}$ were made by reacting Sr_2ReLiO_6 under flowing hydrogen gas as described in Chapter 2, Section 2.3. The sample analysed and presented in this chapter was made by reacting 1.5 g of Sr_2ReLiO_6 under flowing 5% H_2/N_2 gas at 475 °C for four periods of 4 hours. X-ray powder diffraction data collected between heating periods

showed a change in lattice parameters (expansion in *a* and *c*) and no further changes were observed in the diffraction data collected after the third heating period.

3.3 Results

3.3.1 Reactivity

The reduction behaviour was initially tested on the TGA device by heating a small amount of material under flowing 5% H_2/N_2 gas but the products of TGA experiments were found to be incompletely reduced or containing impurities from gradual decomposition.

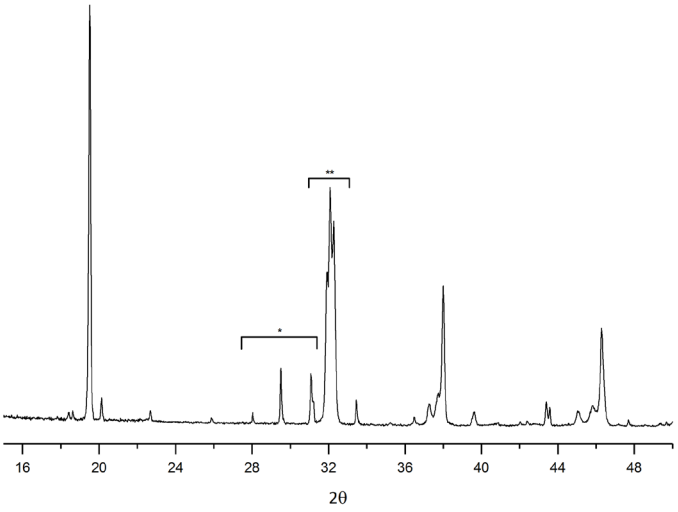


Figure 3.1 X-ray powder diffraction data collected from Sr_2ReLiO_6 heated up to 800 °C 5% H_2 in N_2. (* = impurity peaks) (= signs of reduction)**

The starting material was heated under flowing dilute hydrogen gas in a clamshell furnace at a temperature chosen based on the TGA data. Consecutive heatings at 475 °C, with laboratory X-ray powder diffraction measurements at each step, showed that the reduction follows in a continuous manner with a gradual lattice expansion after each heating. X-ray powder diffraction data showed continued splitting of peaks signalling a change in lattice parameters, and the emergence of new peaks such as the [001] peak signalling a change from a body-centred to a primitive cell.

In the search for the most reduced sample, the starting material was kept at 475 °C for four days. X-ray powder diffraction showed that during the synthesis of the reduced sample, there was a general broadening of peaks and emergence of impurity peaks. For the final product, the reaction conditions were controlled as described in Section 3.2.2.

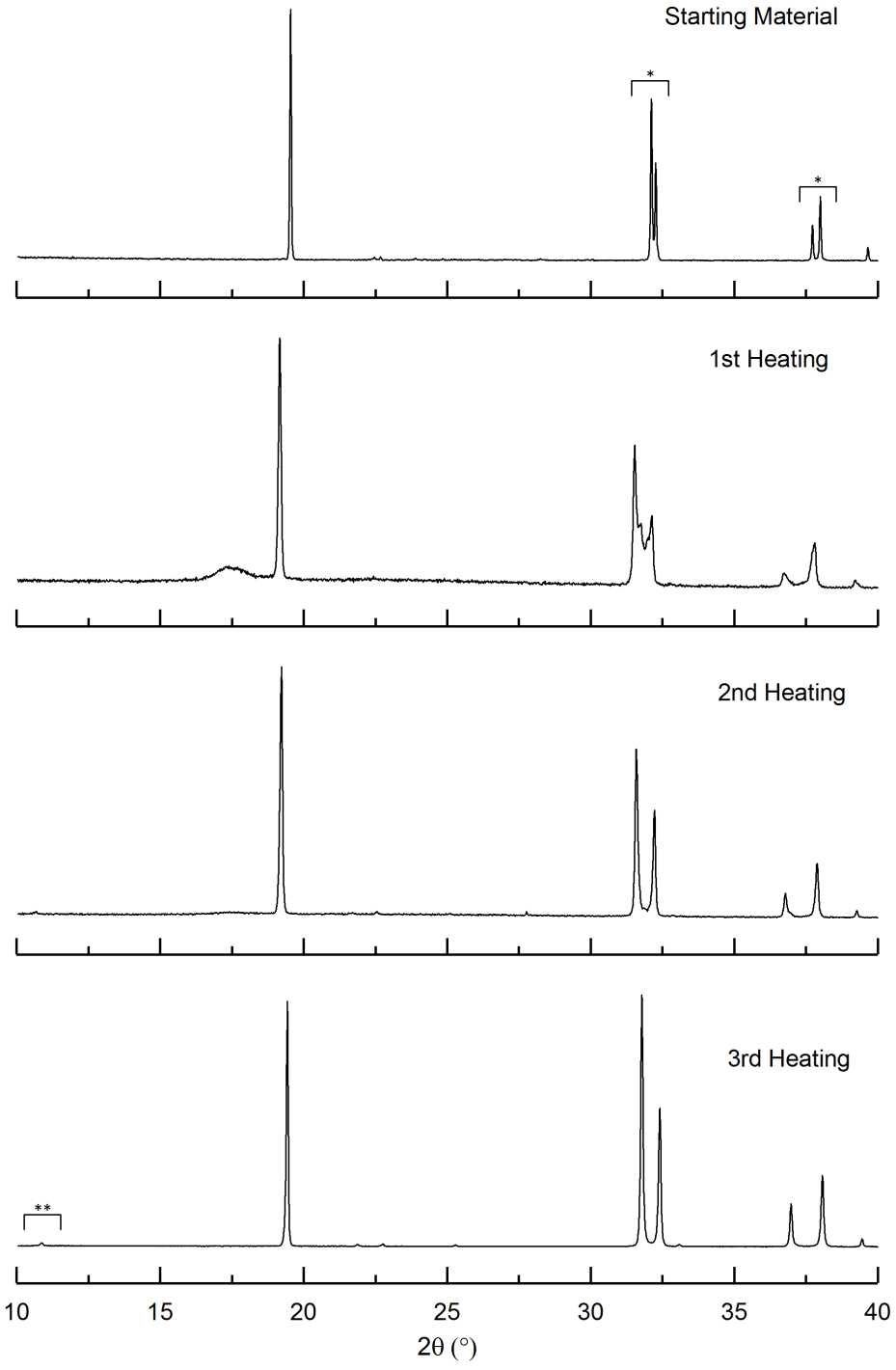


Figure 3.2 Progression of reduction of Sr_2ReLiO_6 at consecutive heatings (* = splitting peaks, ** = [001] peak)

3.3.2 Thermogravimetric Analysis

Thermogravimetric analysis was conducted to determine the composition of the reduced material. Reoxidative TGA experiments described in Chapter 2, Section 2.4 were used to recover the lost oxygen and solve for the difference. A small amount of the reduced sample was heated at 800 °C and held at this temperature for 6 hours under flowing oxygen. The resulting powder was confirmed to be Sr_2ReLiO_6 using X-ray powder diffraction. During this heating, a 1.99% increase in mass was observed indicating that the composition of the reduced material was $Sr_2ReLiO_{5.47(4)}$. This stoichiometry can be confidently rounded up to $Sr_2ReLiO_{5.5}$ as it is within the error margin and a convenient way of describing the new material.

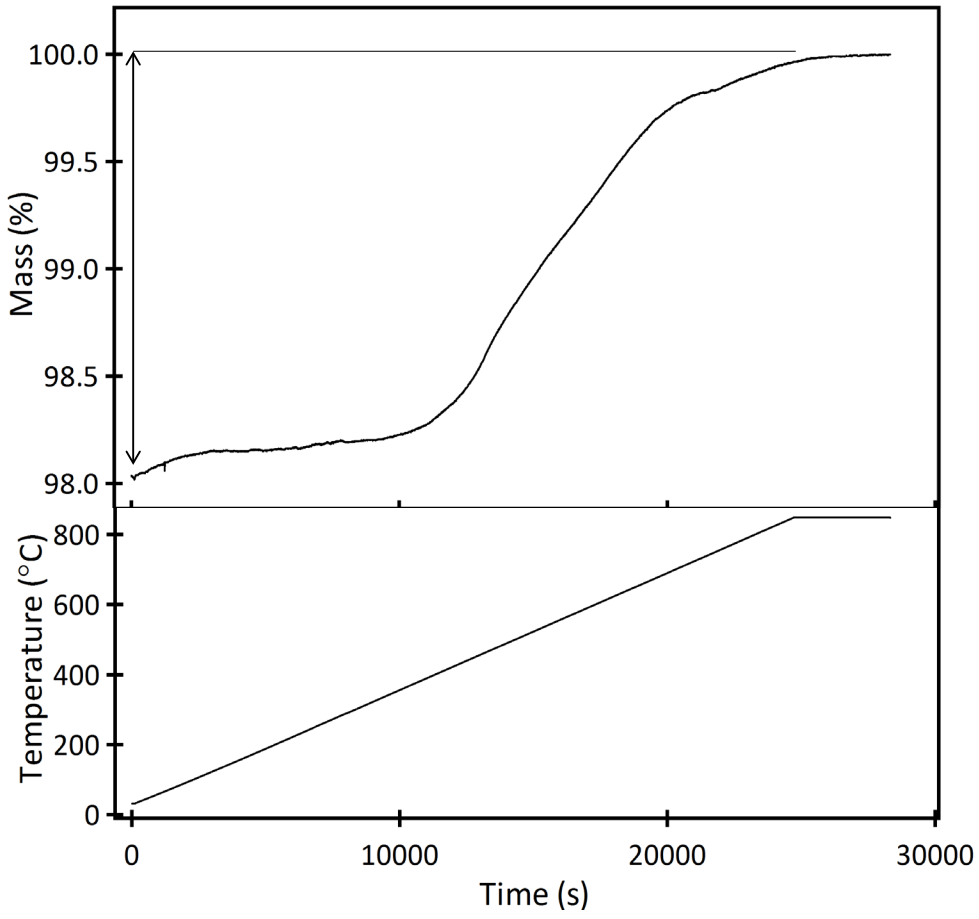


Figure 3.3 Thermogravimetric data collected during the reoxidation of $Sr_2ReLiO_{5.47(4)}$ to Sr_2ReLiO_6

3.3.3 Electron Energy Loss Spectroscopy

TGA analysis described in Section 3.3.2 indicated that the composition of the reduced material was $Sr_2ReLiO_{5.5}$. However, solving for the oxidation state of rhenium in the new material posed a level of ambiguity, as will be described in structural characterisation sections, which necessitated a more rigorous method of determining oxidation states. The final product was sent to the University of Antwerp for STEM-EELS measurements as described in Chapter 2, Section 2.10.1 together with reference Re^{5+}, Re^{6+} and Re^{7+} samples. Results are shown in Figure 3.4.

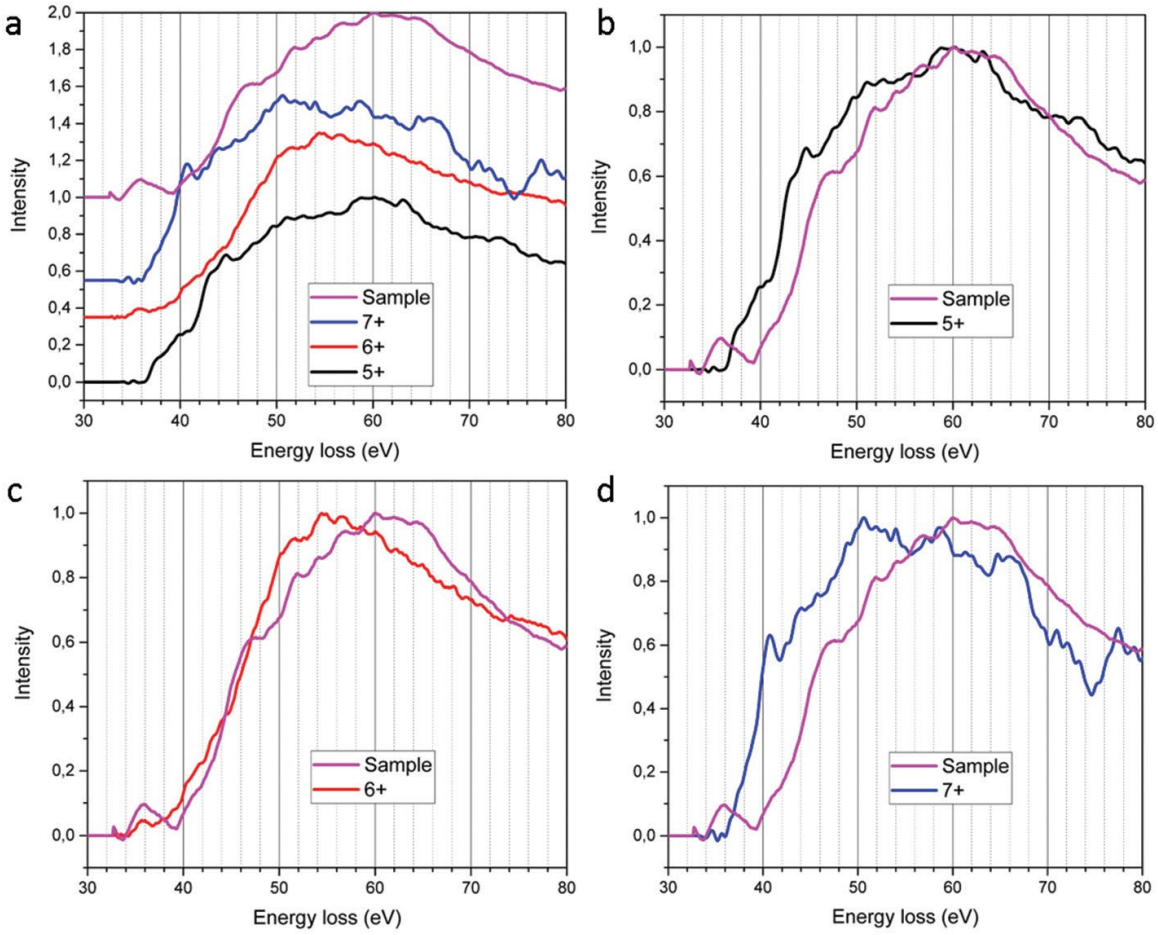


Figure 3.4 (a) EELS measurement of the Re $O_{2,3}$ edge of $Sr_2ReLiO_{5.5}$ (sample) compared with La_2ReLiO_6 (Re^{5+}), Sr_2ReCoO_6 (Re^{6+}) and Sr_2ReLiO_6 (Re^{7+}). For better visualisation, the reference patterns for Re^{5+}, Re^{6+} and Re^{7+} were compared separately to the sample spectrum in (b), (c) and (d).

Figure 3.4 shows the EELS spectra of the Re $O_{2,3}$ edge of the reduced $Sr_2ReLiO_{5.5}$ (magenta) sample compared with reference spectra for La_2ReLiO_6 (Re^{5+})[101], Sr_2ReCoO_6 (Re^{6+})[96] and Sr_2ReLiO_6 (Re^{7+})[100]. The Re $O_{2,3}$ edge was used because it was not possible to use the sharp Re $M_{4,5}$ edge at 1883 eV due to the strong overlap with the Sr^{2+} $L_{2,3}$ edge at 1940 eV in Sr-containing compounds. This edge has never been measured for different valences of Re, and no reference data were available in literature. Thus, the compounds mentioned above were synthesised and sent for measurement. Visual comparison of the shape of the Re $O_{2,3}$ edge, implied that the Re oxidation state in $Sr_2ReLiO_{5.5}$ appears to be a solid-solution of Re^{6+} and Re^{5+}, with Re^{6+} being the majority. The discrepancy of the spectrum for the $Sr_2ReLiO_{5.5}$ compound with the Re^{6+} reference is due to the absence of the Li K edge at 55 eV for Sr_2ReCoO_6. A linear least squares fitting using the EELSModel software[102] yields a ratio of 80 ± 5% Re^{6+} in $Sr_2ReLiO_{5.5}$. These findings are in good agreement with the TGA data, further indicating that the composition of the reduced material can be approximated as $Sr_2ReLiO_{5.5}$ with an average Re^{6+} oxidation state across the material. The implications of Re coordination to composition-structure relations will be covered later.

3.3.4 Magnetic Characterisation

Magnetisation data were collected from a sample of $Sr_2ReLiO_{5.5}$ on an MPMS SQUID magnetometer in the temperature range $5 < T / K < 300$ (Chapter 2, Section 2.11). Zero-field-cooled (ZFC) and field-cooled (FC) magnetisation data in an applied field of 1000 Oe, Curie-Weiss fit to inverse magnetisation data and magnetisation-field isotherms collected are shown in Figure 3.5, Figure 3.6 and Figure 3.7 respectively.

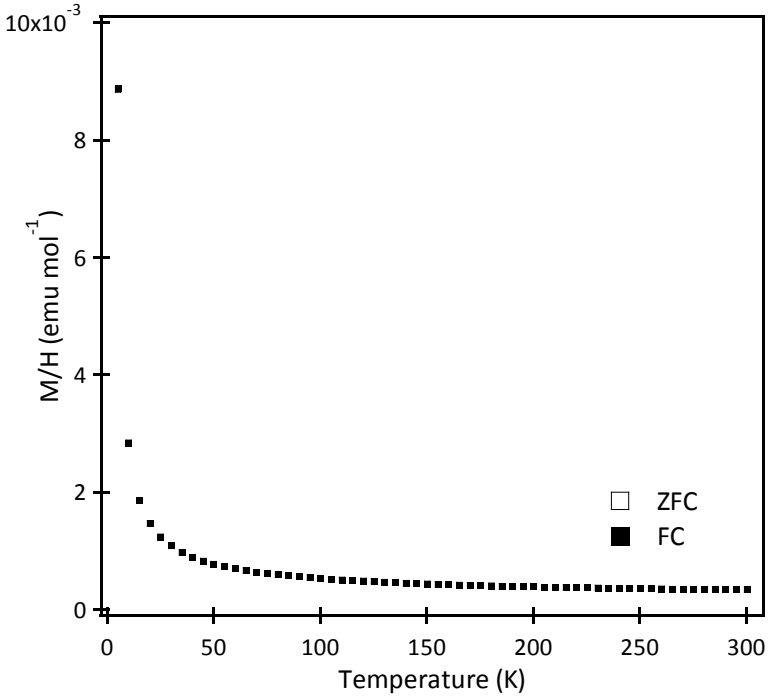


Figure 3.5 Zero-field and field cooled magnetisation data collected from $Sr_2ReLiO_{5.5}$ in an applied field of 1000 Oe

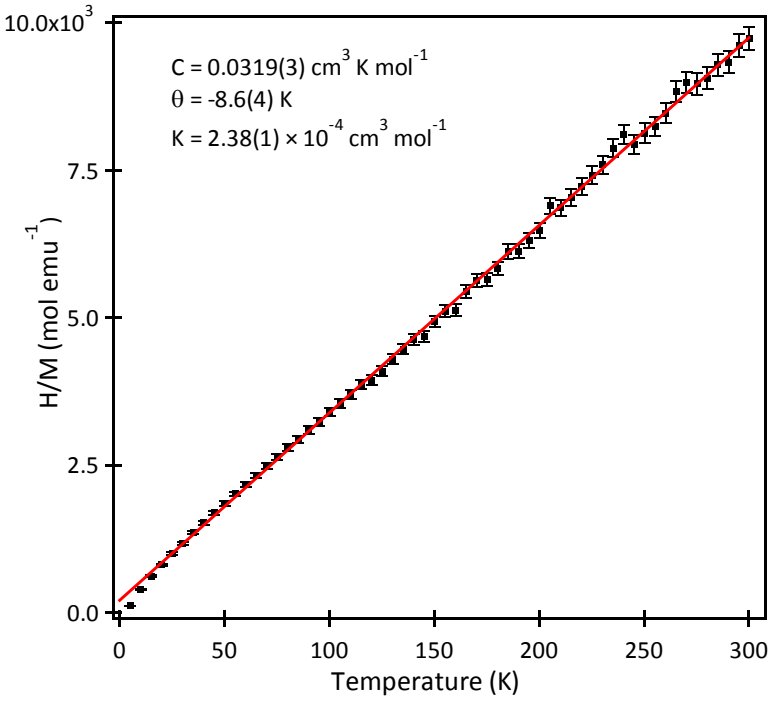


Figure 3.6 Curie–Weiss law linear fit in the temperature range 50 < T / K < 300 to data collected from $Sr_2ReLiO_{5.5}$

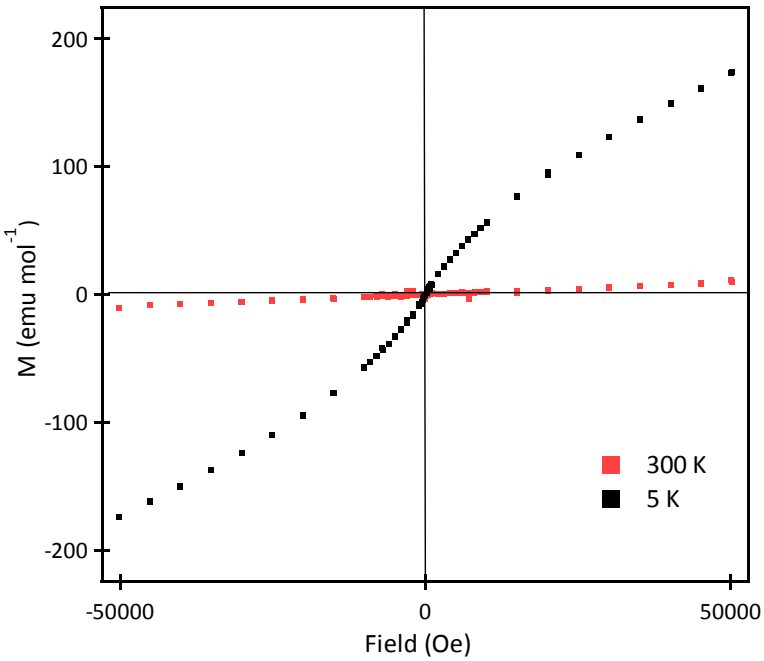


Figure 3.7 Magnetisation-field isotherms collected from $Sr_2ReLiO_{5.5}$

The zero-field cooled and field cooled magnetisation are exactly coincident at all temperatures except 5 K, where there is a very weak divergence. The divergence is difficult to identify and characterise, but it is clear that the material does not undergo any significant magnetic ordering at low temperatures. Magnetisation-field isotherms confirm this, as the field dependence at 5 K deviates mildly from linearity but does not suggest significant long-range ordering. The data can be fit by the Curie–Weiss law in the temperature range $20 < T / K < 300$ to yield values of $C = 0.0319(3)$ cm^3 K mol^{-1}, $\theta = -8.6(4)$ K and $K = 2.38(1) \times 10^{-4}$ cm^3 K mol^{-1}.

Upon reduction, the system goes from a d^0 Re^{7+} to an average d^1 Re^{6+} with one unpaired electron on average for each rhenium site. The observed Curie constant is only 8.5% of the value expected for a spin-only, $S = ½$ system, and corresponds to an effective rhenium moment of $\mu_{eff} = 0.505$ μ_B. The temperature-independent moment ($2.38(1) \times 10^{-4}$ cm^3 mol^{-1}) corresponds to ~70% of the measured magnetisation at 300 K. The data were fitted over different temperature intervals to test the robustness of the fit to the Curie–Weiss

law. It was observed that the fitting range did not influence the values of the extracted parameters, which appear independent of the temperature range fitted. Deviation from the Curie–Weiss law at temperatures below T ≈ 20 K could indicate the onset of magnetic order. However, neutron diffraction data collected at 2 K show no additional features compared to the corresponding data collected at 300 K and can be fit to a good statistical agreement by the crystallographic model refined at 300 K.

3.3.5 Structural Characterisation

3.3.5.1 Room Temperature Synchrotron X-ray Powder Diffraction

A qualitative study of reflections in the laboratory and synchrotron X-ray powder diffraction (Chapter 2, Section 2.5.3) data collected from $Sr_2ReLiO_{5.5}$ shows the parent material undergoing a structural transformation from a body-centred to a primitive tetragonal structure. From a list of candidate primitive tetragonal space groups, the only space group in agreement with the reflections conditions was the *P*4/*m* space group. The published structural data for Sr_2ReLiO_6[100] was used to construct a structural model.

Collected diffraction data could be readily indexed using a primitive tetragonal unit cell, with extinction conditions consistent with the *P*4/*m* space group and lattice parameters of a = 5.5213(1) Å and c = 8.1133(1) Å. Final refinement statistics of χ^2 = 43.2, wRp = 3.24%, and Rp = 2.41% suggested a good fit to the collected data. The model could account for all the observed peaks but several discrepancies were observed in peak intensities. The discrepancy was expected as X-ray powder diffraction data is not good at detecting lighter atoms (in this case Li) and anion vacancies with high precision in the presence of heavy atoms like Re and Sr. Observed, calculated, and difference plots from Rietveld refinement

against synchrotron X-ray data are presented in Figure 3.8. This refinement does not account for the oxygen vacancies found in the material.

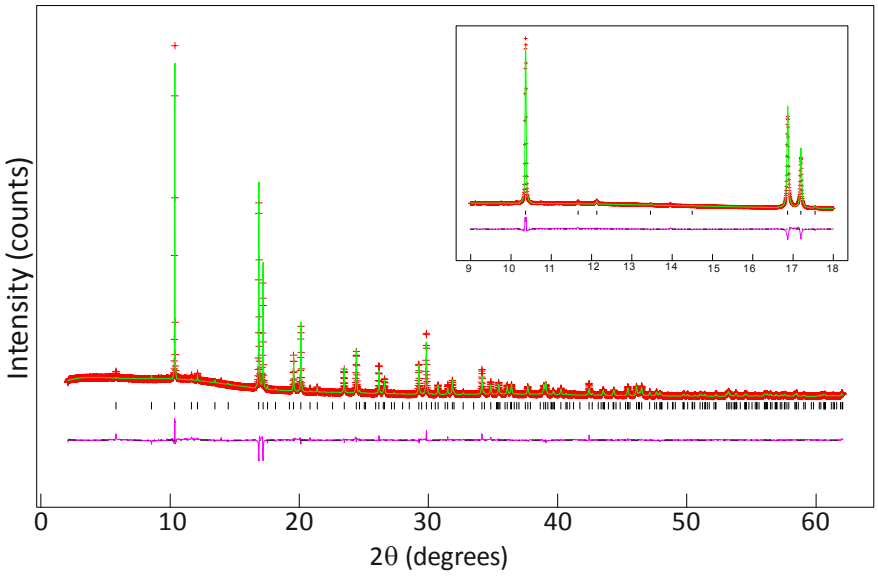


Figure 3.8 Observed, calculated, and difference plots from the refinement of the *P4/m* structural model of $Sr_2ReLiO_{5.5}$ against synchrotron X-ray powder diffraction data (λ = 0.82626(1) Å)

3.3.5.2 Room Temperature Neutron Powder Diffraction Data

Neutron powder diffraction data were collected from $Sr_2ReLiO_{5.5}$ at 298 K using the GEM instrument at ISIS neutron source (Chapter 2, Section 2.6.1). The neutron diffraction data were refined against the *P*4/*m* model in the same Rietveld refinement file as the synchrotron data, but the fit was not as good until anion occupancy variables were refined. All oxygen sites were allowed to refine and all but one site refined to the full occupancy. The refinement led to a dramatic improvement in the fit to the data, when the oxygen vacancies were located in the 'equatorial' anion sites in alternate layers, such that the following stacking sequence could describe the overall structure: Sr_2O_2 – $ReLiO_3$ –Sr_2O_2 –$ReLiO_4$.

However, upon close inspection it was discovered that the intensities of some diffraction peaks were not accounted for satisfactorily. The discrepancy only revealed itself upon closest inspection of low *d*-spacing reflections at which point it became apparent these mismatches were present in most reflections as can be observed in Figure 3.10 (top). Several possibilities were proposed for the discrepancy such as magnetic order or impurity peaks, but all were ruled out since the discrepancy was not a single event such as an unaccounted peak, a split peak or a poor refinement parameter but rather a feature of the entire data set. The existence of a larger unit cell would be the next reasonable hypothesis so to investigate if these intensity mismatches were due to anion-vacancy order the sample was sent for electron microscopy measurements.

3.3.5.3 Transmission Electron Microscopy

A series of electron diffraction patterns were taken from several crystals (Chapter 2, Section 2.10), rotating the crystal to many different zones. All obtained patterns could be indexed using the *P*4*/m* primitive tetragonal cell obtained from the X-ray and neutron diffraction data, showing that the intensity mismatches are not due to a supercell.

Results showed a high amount of twinning in all crystals. Representative patterns along some main zones are shown in Figure 3.9. The $[1\bar{1}0]$ pattern (Figure 3.9c) shows that the twinning occurs on the (112) plane, and involves a rotation of 90° around the $[1\bar{1}0]$ direction. This is schematically shown in Figure 3.9d. The same twin law also generates the combination [001] / [110] shown in Figure 3.9b. The twinning occurs on a fine scale, as seen in Figure 3.9e, showing a dark field image using only the 201 reflections (a white circle indicates the approximate size of the aperture), in the zone $[11\bar{2}]$ twinned with $[2\bar{2}1]$. Unfortunately, in the main zones, the reflections were too close together to select

individual reflections with the available apertures. The twin domain sizes varied from crystal to crystal but were on average between 50 – 200 nm.

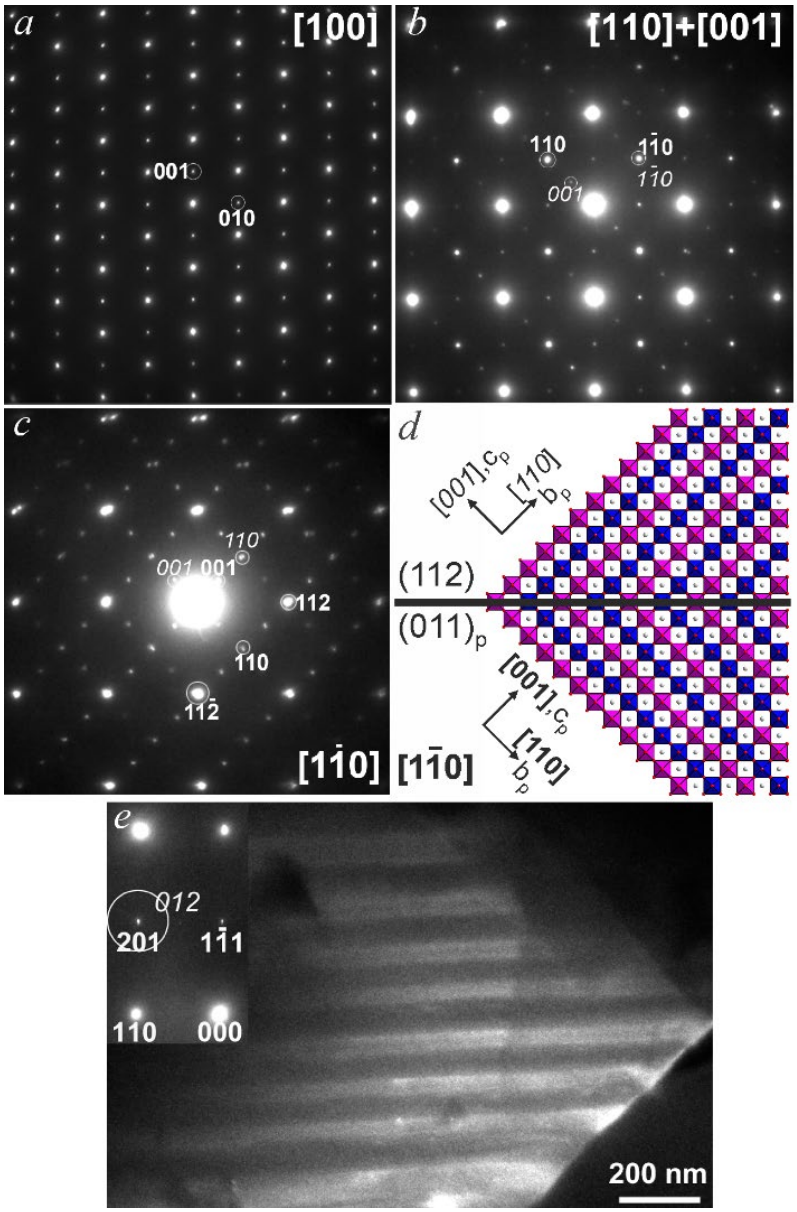


Figure 3.9 Electron diffraction patterns (a–c) and dark field TEM image (e) showing extensive twinning of $Sr_2ReLiO_{5.5}$ particles. Indices of the different twin components are given in bold versus italic. The schematic representation (d) visualises the twins as seen along the $[1\bar{1}0]$ zone as in (c), blue and purple layers represent stoichiometric $ReLiO_4$ and reduced $ReLiO_3$ layers respectively. Indices with subscript 'p' indicate the lattice vectors of the 'single perovskite' lattice. Light and dark bands in (e) indicate domains related by 90° rotation around the $[1\bar{1}0]$ axis, imaged by selecting only the 201 reflection in a $[11\bar{2}]/[\,2\bar{2}1]$ electron diffraction pattern (inset).

3.3.5.4 Improved Neutron Diffraction Data Fitting

Given the absence of an expanded unit cell, the neutron diffraction data were refined against a lower symmetry model to add variability to the refinement. Neutron powder diffraction data were fitted to a *Pmmm* model while keeping the unit cell metrically tetragonal. The fit dramatically improved from the metrically identical tetragonal analogue where the reflection intensities were in better agreement with the calculated parameters while all other structural parameters were kept constant. There was no splitting or shoulders observed anywhere in the pattern which suggested that while the lattice parameters of $Sr_2ReLiO_{5.5}$ are metrically tetragonal, on average the structure has orthorhombic inclinations.

It was further observed that the displacement parameters of the oxide ions were significantly larger than those of the cations. All the anion displacements were changed to an anisotropic description. Refinement of these parameters led to the partially occupied anion site at position (x, y, 0.5) being described by a displacement ellipsoid which was highly elongated in a direction perpendicular to the Re–O–Li bond vector. This suggested that a disordered rotation of the ReO_x and LiO_x polyhedra around the z-axis is present in the alternating layers of oxygen vacancies. Thus, this anion site was split into two separate (x, y, 0.5) sites with half the occupancy of the original site, and with the new sites described using isotropic displacement parameters.

The results from one bank are shown in Figure 3.10 where it can be seen that this model converged smoothly to give a good statistical fit (χ^2 = 2.97), a marked improvement from the *P*4*/m* model.

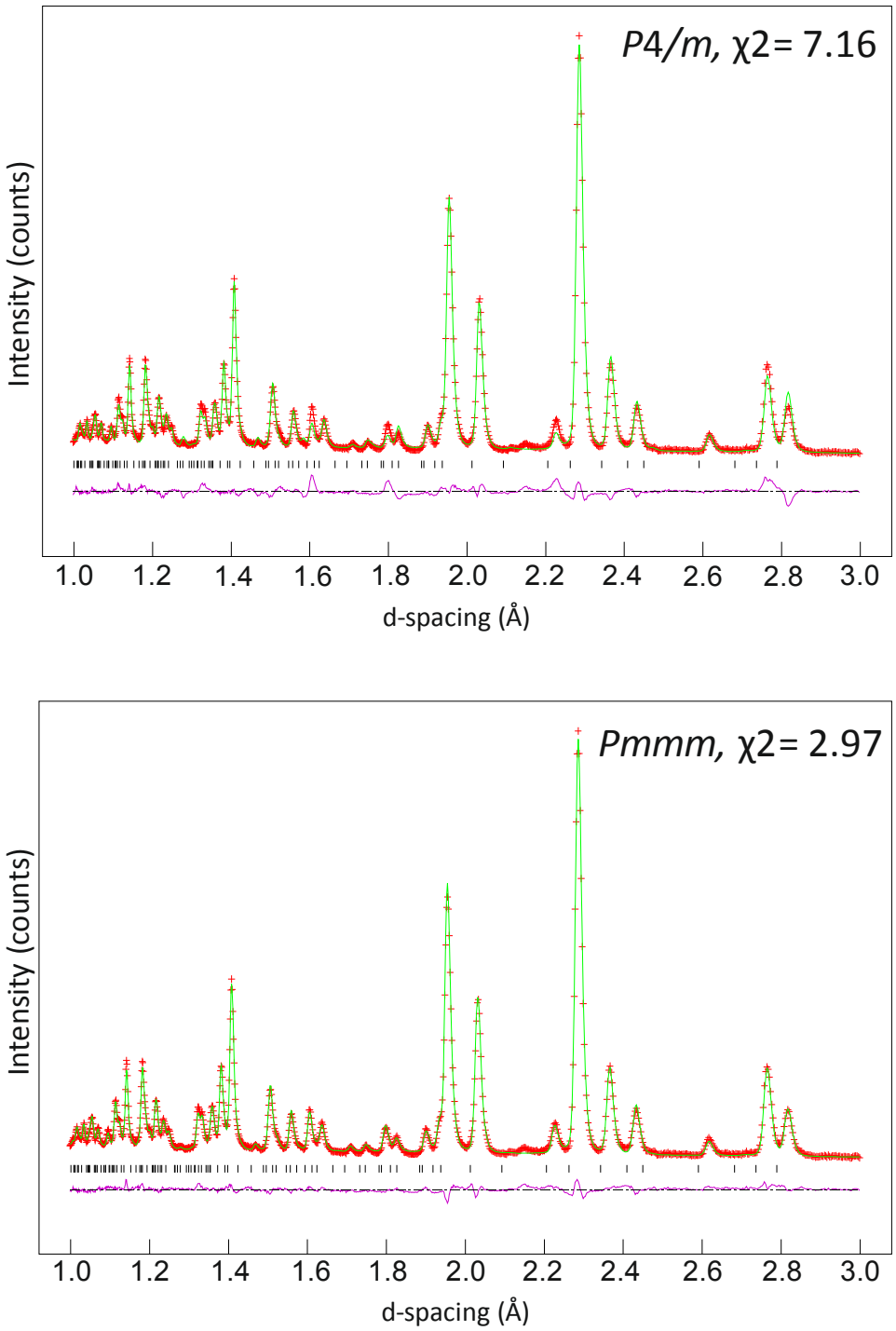
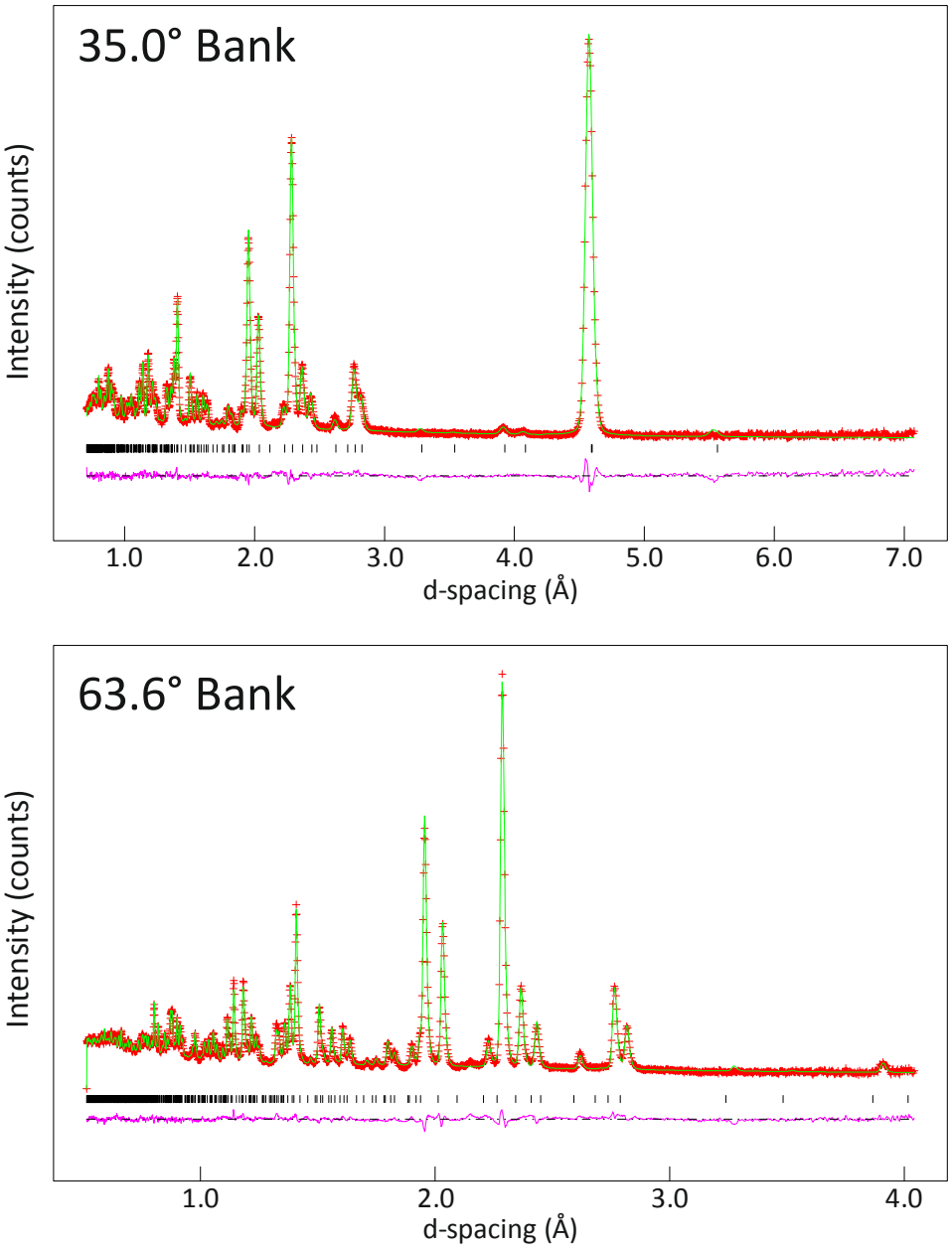


Figure 3.10 Observed, calculated, and difference plots from the refinement of *P4/m* and *Pmmm* models (bottom) against neutron powder diffraction data collected from $Sr_2ReLiO_{5.5}$ at 300 K.

The occupancy of the O(4) and O(5) sites was constrained to maintain the composition determined by thermogravimetric analysis. A full description of the refined structure of $Sr_2ReLiO_{5.5}$ is given in Table 3.1, with selected bond lengths given in Table 3.2. Neutron

powder diffraction data confirm the absence of any long-range order of anion vacancies, which would result in high *d*-spacing peaks. The refined plots are shown in Figure 3.11.



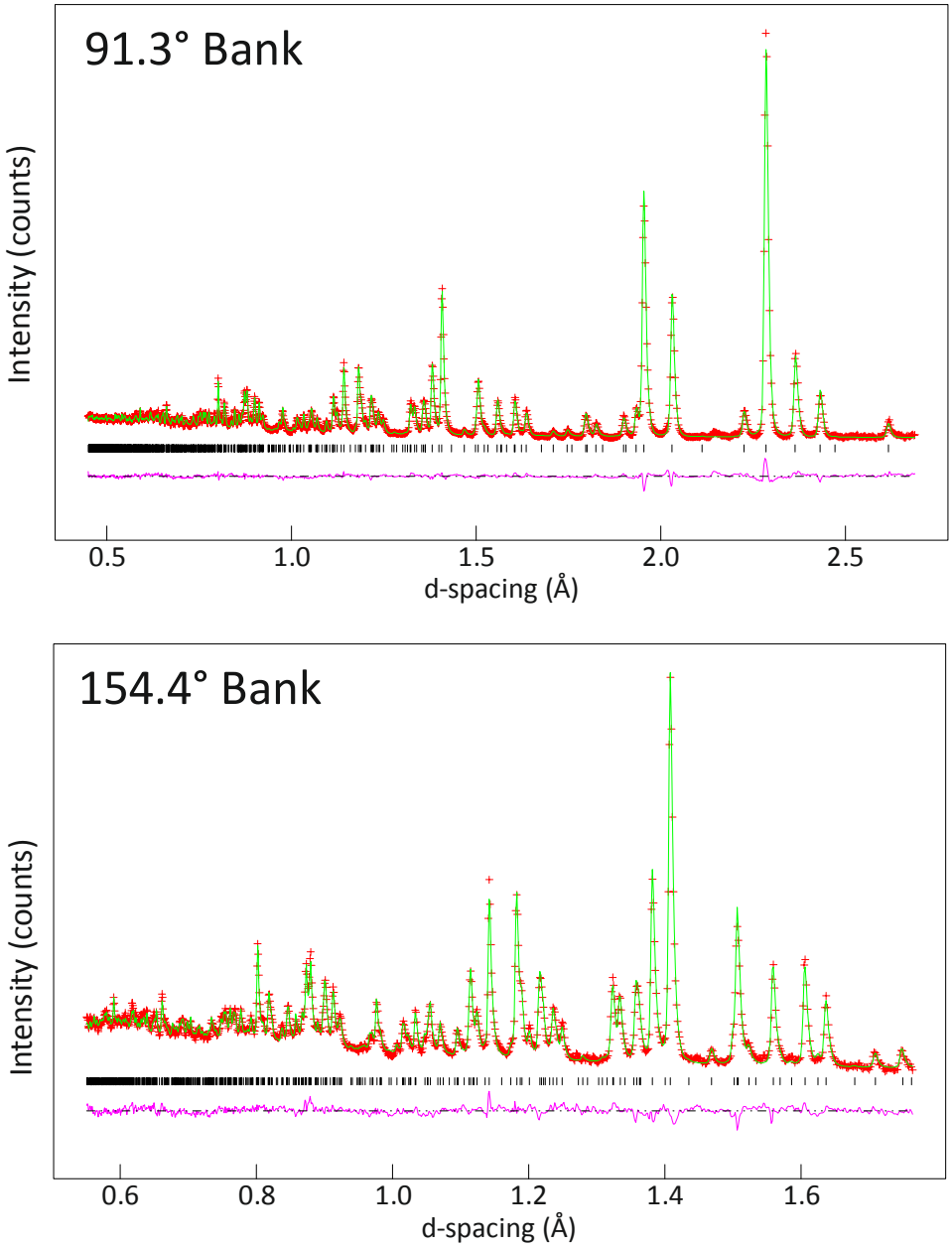


Figure 3.11 Observed, calculated, and difference plots from the of the *Pnma* structural model of $Sr_2ReLiO_{5.5}$ against neutron powder diffraction data collected at 300 K using the GEM instrument.

Atom	*x*	*y*	*z*	Multiplicity	Fraction	U_{iso} (Å^2)
Sr(1)	0.5	0	0.2298(4)	2	1	0.0117(3)
Sr(2)	0	0.5	0.2232(4)	2	1	0.0117(3)
Re(1)	0	0	0	1	1	0.0059(1)
Re(2)	0.505(1)	0.5	0.5	2	1	0.0059(1)
Li(1)	0.553(2)	0.5	0	2	0.5	0.0136(14)
Li(2)	0	0	0.5	1	1	0.0136(14)
O(1)	0.2514(4)	0.2291(3)	0	4	1	
O(2)	0.5	0.5	0.2725(2)	2	1	
O(3)	0	0	0.2414(2)	2	1	
O(4)	0.2955(9)	0.2415(9)	0.5	2	0.376(2)	0.0242(8)
O(5)	0.1795(9)	0.3875(9)	0.5	2	0.374(2)	0.0242(8)

Atom	U_{11}	U_{22}	U_{33}	U_{12}
O(1)	0.0061(3)	0.0090(3)	0.0196(6)	0.0063(2)
O(2)	0.0191(4)	0.0183(4)	0.0109(7)	-
O(3)	0.0191(4)	0.0183(4)	0.0109(7)	-

$Sr_2ReLiO_{5.5}$ – Space group *Pmmm* (#47)

Formula mass = 456.37 gmol^{-1}

a = 5.5207(5) Å, b = 5.5216(5) Å, c = 8.1144(7)

Radiation source: Time-of-flight neutrons (GEM, ISIS)

Temperature: 298 K

χ^2 = 2.978; wRp = 4.51%; Rp = 4.18%

Table 3.1 Parameters from the structural refinement of $Sr_2ReLiO_{5.5}$ against neutron powder diffraction data collected at 219 K

Cation	Anion	Length (Å)
Re(1)	O(1) x4	1.878(2)
	O(3) x2	1.959(2)
Re(2)	O(2) x2	1.846(2)
	O(4) x1	1.820(5)
	O(4) x2	1.875(5)
Li(1)	O(1) x2	1.854(7)
	O(1) x2	2.238(8)
	O(2) x2	2.230(2)
Li(2)	O(3) x2	2.098(2)
	O(4) x1	2.107(5)
	O(5) x2	2.358(5)
Sr(1)	O(1) x4	2.638(3)
	O(2) x2	2.782(1)
	O(3) x2	2.762(1)
	O(4) x4	2.804(4)
	O(5) x4	3.538(4)
Sr(2)	O(1) x4	2.728(3)
	O(2) x2	2.789(1)
	O(3) x2	2.765(1)
	O(4) x3	3.121(4)
	O(5) x4	2.532(4)

Table 3.2 Selected bond lengths from the refined structure of $Sr_2ReLiO_{5.5}$

3.4 Discussion

3.4.1 Anion Deintercalation Chemistry

Anion deintercalation can be used to prepare many meta-stable materials with transition-metals in unusual oxidation and coordination states, and the examples are plenty. Most reported cases have been made using metal-hydrides, metal getters or dilute hydrogen gas reactions as long as the agent had sufficient reduction potential and anion

deintercalation was exploitable[65, 103, 59]. When it comes to 4*d*/5*d* materials, topochemical chemistry becomes more challenging as a complete reduction to 4*d* and 5*d* transition-metals to elements becomes more kinetically stable. For example, $SrRuO_3$ decomposes to form SrO + Ru under conditions where $SrFeO_3$ is topochemically reduced to $SrFeO_2$[59]. Similarly, Sr_2IrO_4 is reduced to SrO + Ir under conditions where $LaSrCoO_4$ is reduced to $LaSrCoO_{3.38}$[104].

The topochemical reduction of Sr_2ReLiO_6 to the Re^{6+} material $Sr_2ReLiO_{5.5}$ results in oxygen deintercalation from alternating layers resulting in a $–Sr_2O_2–ReLiO_3–Sr_2O_2–ReLiO_4–$ stacking sequence. Literature findings suggest that 3*d* transition-metals have been shown to stabilise the reduced lattice framework and promote topochemical behaviour. For example, the introduction of iron can help to stabilise Ru^{2+} and Ir^{2+} in $SrFe_{0.5}Ru_{0.5}O_2$ and Sr_2FeIrO_4 respectively[59, 64]. In $Sr_2ReLiO_{5.5}$, Li appears to be a stabilising force for a multitude of structural transformations such as extensive twinning. Absence of a long-range vacancy order is particularly challenging to characterise, but it explains insulating behaviour and lack of long-range magnetic ordering.

3.4.2 Structural Characterisation

The topochemical reduction of Sr_2ReLiO_6 to the Re^{6+} material $Sr_2ReLiO_{5.5}$ follows a previously unobserved pathway. The reduction results in a highly anisotropic 5.2% increase in the volume of the material with only a 0.3% increase of *a* and *b* lattice parameters, but a 4.6% increase in *c*. As a result, the 'tetragonality' of the material, defined as $c/(\sqrt{2} \times a)$ changes from 0.996 for Sr_2ReLiO_6 to 1.039 for $Sr_2ReLiO_{5.5}$. This highly anisotropic expansion potentially explains the extensive crystallographic twinning observed in $Sr_2ReLiO_{5.5}$. As seen in Figure 3.9 the material undergoes a 90° rotation around

the [110] axis to presumably compensate for the high-energy barrier of stabilising the radical broadening. The transformation seems to be driven by the inter-particle strain that is reduced when the twin domains align themselves in a way as to create isotropy along 1 μm domains. This division of particles into small domains is consistent with the apparent mismatch between the orthorhombic crystal symmetry of the material and the metrically tetragonal lattice parameters of the material and the lack of long-range anion-vacancy order in the material.

Refinement of oxygen sites shows that the reduced material contains alternating oxygen stoichiometric $ReLiO_4$ layers and anion-deficient $ReLiO_3$ layers. While this was expected to result in long-range anion-vacancy order, neutron diffraction data and electron microscopy data showed no evidence of long-range vacancy ordering. The way a partially vacancy-ordered material could be described is proposed herein.

3.4.3 Cation Coordination Polyhedra

Both X-ray and neutron diffraction data showed that oxygen vacancies were localised to alternating layers which suggests the anion-deficient structure of $Sr_2ReLiO_{5.5}$ consists of alternating oxygen-stoichiometric $ReLiO_4$ layers and anion-deficient $ReLiO_3$ layers, stacked with Sr_2O_2 sheets. Figure 3.12 shows the various possible structures considered.

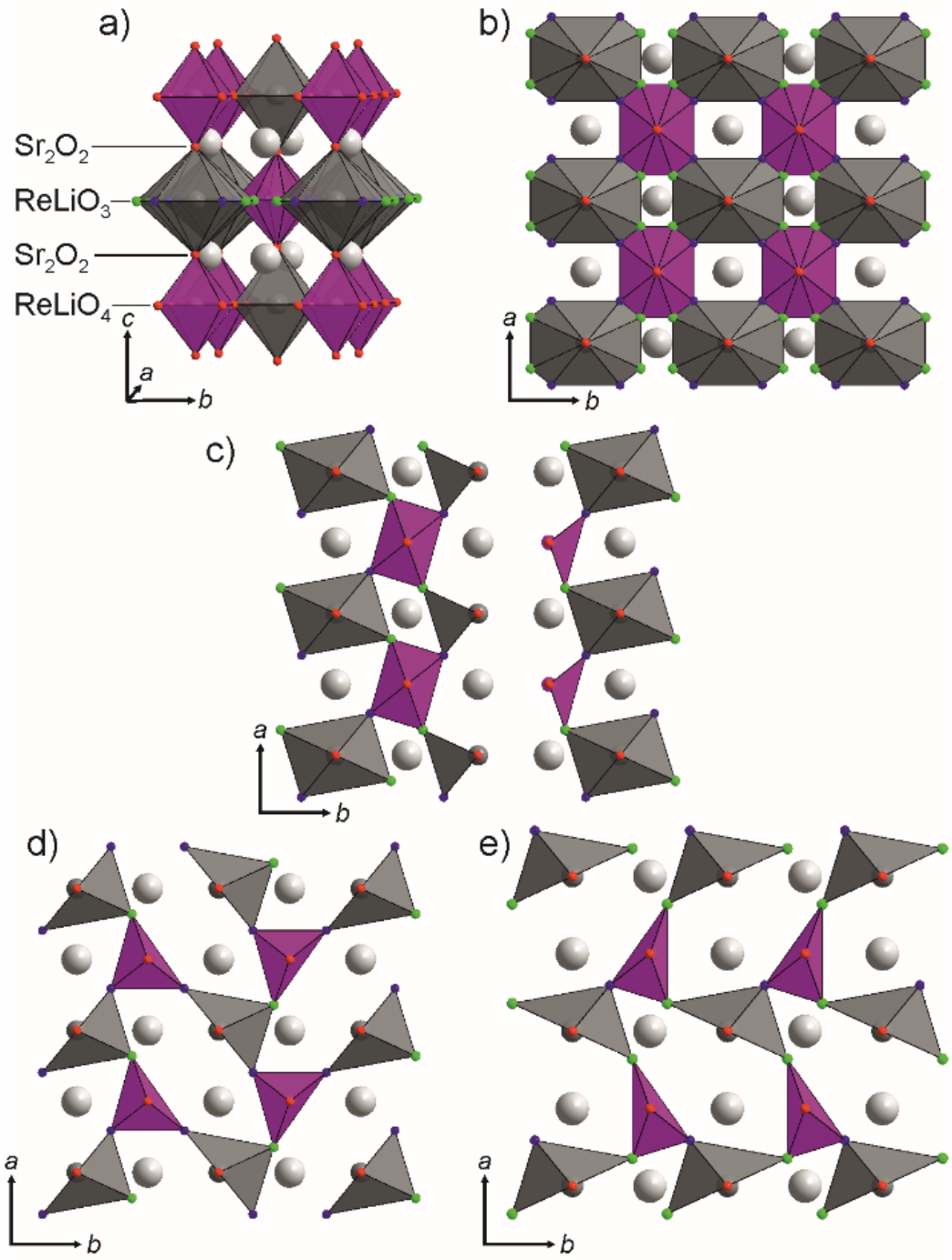


Figure 3.12 (a) the refined structure of $Sr_2ReLiO_{5.5}$ viewed in projection approximately along [100]. (b) The anion-deficient $ReLiO_3$ layered viewed down [001]. Anion-vacancy ordered arrangements of the $ReLiO_3$ layer with (c) 4- and 6-fold coordinate metal cations, (d) and (e) 5-fold coordinate metal cations. Light grey, dark grey and purple spheres represent Sr, Li and Re cations respectively. Red spheres represent fully occupied anion sites (O(1) O(3)), blue and green spheres represent partially occupied O(4) and O(5) anion sites respectively.

Figure 3.12 (a) and Figure 3.12 (b) show different viewpoints of the least-squares result extracted from Rietveld refinement. The anisotropy of the oxygen sites allows for the best statistical fit to the data but is not a sufficiently rigorous characterisation. Instead, locally ordered structures can be constructed which would describe plausible local coordination polyhedra for the Re and Li cations from the partially occupied oxygen site positions within the oxygen-deficient layers. The $ReLiO_3$ stoichiometry and disposition of the partially occupied oxide ions sites within the anion-deficient layers gives two plausible coordination possibilities for the rhenium and lithium *B*-site cations. Either the *B*-site cations are in a 1:1 ratio of 6- and 4-fold coordinate sites, as shown in Figure 3.12 (c), or all cations are in 5-fold coordinate sites as shown in Figure 3.12 (d) and Figure 3.12 (e).

Bond-valence sum calculations were conducted to test the validity of these structures. Calculating bond valence sums (BVS) for the B-site cations[77, 78], values +7.792 and +5.196 for the 6- and 4-fold coordination rhenium cations are observed respectively. Such a large difference in BVS for the two Re coordination sites would imply the average Re^{6+} oxidation state had disproportionated into a Re^{5+}/Re^{7+} combination, which is inconsistent with the EELS data. Thus structural models of this type can be discarded, 5-fold coordination for rhenium and lithium frameworks are considered.

It is possible to construct two sets of plausible five-fold coordination polyhedra for the Re and Li cations which reside on the $ReLiO_3$ anion-deficient layers. The metal cations can either reside within an $M[O^{(2)}]_2[O^{(4)}]_2[O^{(5)}]_1$ coordination as seen in Figure 3.12 (e), which gives BVS values of Re +6.596 and Li +0.764. Alternatively, $M[O^{(2)}]_2[O^{(4)}]_1[O^{(5)}]_2$ arrangement seen Figure 3.12 (d) gives BVS values of Re +6.398 and Li +0.681. The BVS

values for the stoichiometric layer of ReO_6 and LiO_6 are Re +6.215 and Li +1.139 respectively, which is in agreement with EELS data

Given that neither neutron or electron diffraction show any evidence for long-range anion-vacancy order, the proposed structure of $Sr_2ReLiO_{5.5}$ consists of a long-range disordered array of these coordination's connected into apex-linked sheets which respect the Re/Li cation order of the parent material. It is likely that short-range order of small regions of anion vacancy exists but only locally within the twinned domains. The nanoscale twinning means this short-range order cannot be probed.

Refinements against the obvious models like Brownmillerite type structure were inconclusive. The described structure is reminiscent and in some ways resembles compounds like $Ca_2MnO_{3.5}$ with MO_5 square pyramids[105], $Sr_2MnO_{3.5}$ with corner-sharing tetrameters[106] or $Ho_{0.2}Sr_{0.8}CoO_{2.75}$[107] with alternating vacancy sites.

3.4.4 Composition-Structure Relations

The reduction of Sr_2ReLiO_6 to $Sr_2ReLiO_{5.5}$ leads to dramatic changes to the cation coordination polyhedra. The cation polyhedra in the 'oxygen stoichiometric' layer expand in a highly anisotropic manner on reduction which extends the axial Re – O bond by 7.9%, compared to a much more modest 2.2% expansion of the equatorial Re – O bonds. This anisotropic expansion changes the tetragonal distortion parameter of the Re polyhedra from a 0.92% compression to a 4.3% expansion.

The immediate explanation for this anisotropic expansion could be an emergence of a Jahn–Teller distortion associated with the change from d^0 Re^{7+} to d^1 Re^{6+}. However, it is well understood that d^1 configurations are more likely to break the degeneracy of orbitals

to undergo tetragonal compression. The $(d_{xy})_1(d_{xz}/d_{yz})_0$ electronic configuration is more likely than an expansion $(d_{xz}/d_{yz})_1(d_{xy})_0$ state where degeneracy of the electronic configuration makes it an energetically unfavourable outcome. The large axial elongation of both the $Re^{(1)}O_6$ and $Li^{(1)}O_6$ is proposed to be a crystal packing effect which arises from the need to simultaneously satisfy the coordination 'requirements' of the rhenium cations which are being reduced, and the lithium and strontium cations which are not.

Many of the large-scale structural features of $Sr_2ReLiO_{5.5}$ can be attributed to such crystal packing effects. The optimum lattice configuration of the topochemically reduced material $Sr_2ReLiO_{5.5}$ will lower the BVS of the rhenium cation across both layers whilst maintaining the sums of the Sr^{2+} and Li cations, all while respecting the topochemical constraint that the overall topology of the lattice is retained – an effect which has been seen in other systems[108]. The ordering of anion vacancies into alternate anion-deficient and anion-stoichiometric layers means that, in contrast to Re(2) (located in the anion-deficient layers) which lowers its BVS by lowering its coordination number, the BVS value of Re(1) can only be lowered to a value consistent with reduction to Re^{6+} by expanding the $Re^{(1)}$–O bond lengths. An isotropic lengthening of all the $Re^{(1)}$–O bonds would lead to an isotropic expansion of the anion lattice which would also lower the BVS of the Sr^{2+} and Li cations – an undesirable outcome. Thus the observed anisotropic distortion of the $ReLiO_4$ layers appears to be a compromise which lowers the BVS of Re without significantly affecting those of Li and Sr. In the case of lithium, off-centring of the cation mitigates the expansion of the $Li^{(1)}O_6$ resulting in slightly larger BVS of Li(1).

When it comes to coordination of anion-nonstoichiometric cations, the disorder present in the layer fundamentally limits analysis but it is evident that the expansion of this layer

is more isotropic than the $ReLiO_4$ layer. The highly anisotropic expansion of the bulk lattice characterised by a larger *c* and subsequently large-scale twining of the material is solely attributable to the anisotropic expansion of the stoichiometric layer. This solution agrees with highly convoluted set of observations made from various characterisation methods where all bond lengths, oxidation states, anion-vacancy properties are rationalised.

3.4.5 Magnetic and Electronic Properties

The magnetic susceptibility of $Sr_2ReLiO_{5.5}$ is only 8.5% of the expected S = ½ spin-only magnetic moment and this was initially attributed to spin-orbit coupling. In rhenium-based materials, it is assumed that the spin-only moment is no longer sufficient as spin-orbit coupling effects become important. Spin-orbit coupling, however, is also dependant on the local symmetry of the material – its effects are stronger in cubic structures compared to low symmetry structures. This becomes relevant in the characterisation of $Sr_2ReLiO_{5.5}$ because its symmetry is further lowered from tetragonal to orthorhombic because of local Re-O coordination effects and thus it was expected that the orbital contributions to the magnetic moment of d^1 Re would be quenched.

Symmetry effects on spin-orbit coupling vary in magnitude and a literature review was conducted to find similar Re based structures to establish the degree of sensitivity to symmetry effects. A comparison was made between Ba_2CaReO_6[52], which adopts a cubic crystal structure, and thus retains O_h symmetry at ReO_6 centres, with Sr_2CaReO_6[53] and Sr_2MgReO_6[109] which adopt monoclinic and tetragonal structures respectively and thus have distorted ReO_6 centres. Table 3.3 lists the effective moments of these materials, extracted from high-temperature susceptibility data.

Material	Space Group	μ_{eff} (μ_B)	θ (K)	Re-O bond length (Å)	Ref.
Ba_2CaReO_6	$Fm\bar{3}m$	0.744(2)	-39	2.092(1)	[52]
Sr_2CaReO_6	$I4/m$	1.72(9)	-426	1.926(8)/1.9101(4)	[53]
Sr_2MgReO_6	$P21/n$	1.659(6)	-443	1.899(5)/1.908(4)/1.925(5)	[109]

Table 3.3 Magnetic behaviour and local symmetry of some rhenium double perovskites

First thing to note is unusually large θ values obtained from these materials so Curie-Weiss fits of these materials should be questioned. It is clear however that the low symmetry materials exhibit effective moments close to the calculated spin-only moment (1.73 μ_B), while the cubic phase exhibits an effective moment significantly smaller in contrast. Evidently, the spin-orbit coupling in low-symmetry materials is almost completely quenched while the cubic phase exhibits significant spin–orbit coupling. Even the modest local distortions present in the ReO_6 centres of the low symmetry materials appear to be sufficient to quench the orbital contribution. Table 3.3 lists the different Re – O bond lengths of these materials and it can be seen that the octahedral distortions are small compared to $Sr_2ReLiO_{5.5}$, which would further suggest that orbital contributions are expected to be quenched in the latter. However, a 91.5% suppression of the moment for the Re^{6+} cations in $Sr_2ReLiO_{5.5}$ suggests otherwise and demonstrates that Re^{6+} can exhibit strong spin–orbit effects even when residing in lower-symmetry coordination sites.

These and aforementioned observations indicate that the stoichiometric $Re^{(1)}O_6$ unit has D_{2d} symmetry which retains the degeneracy of the d_{xz} and d_{yz} orbitals enabling an orbital contribution to the moment of this centre to be retained. Likewise some of the possible $Re^{(2)}O_5$ centres could have a C_{4v} symmetry which also retains d_{xz}/d_{yz} degeneracy. These would explain the strong suppression of the expected magnetic moment but it is clear

that the influence of local symmetry on the spin–orbit interaction in Re^{6+} oxides is more complex than initially stated.

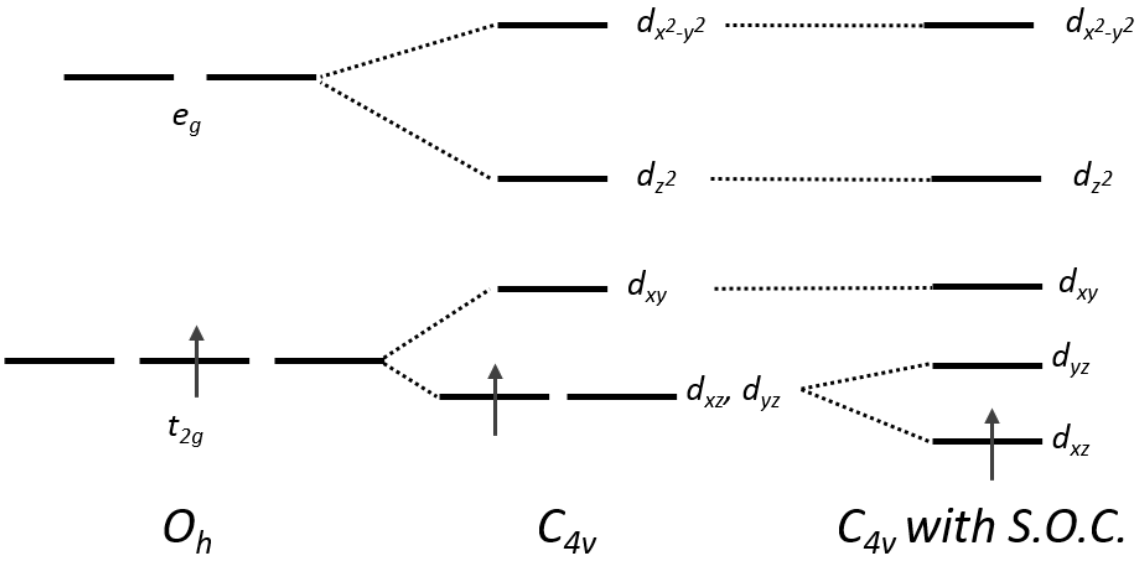


Figure 3.13 Possible crystal field splittings of Re 5-coordinate polyhedra

The anion-deficient $Sr_2ReLiO_{5.5}$ does not undergo long-range magnetic ordering and differs from other Re^{6+} materials studied above. Sr_2CaReO_6 and Sr_2MgReO_6 are observed to be spin glasses at low temperature (T_{order} = 50 K and 14 K respectively) while Ba_2CaReO_6 has an antiferromagnetic ground state (T_N = 15 K) and Ba_2MgReO_6 a ferromagnetic ground state (T_C = 18 K). It is proposed that the combination of uneven composition properties, large-scale crystallographic disorder, and localised anion-vacancy framework sets the reduced material apart from other Re^{6+} double perovskites

3.5 Conclusions

The reaction of Sr_2ReLiO_6 with 5%/95% H_2/N_2 results in the deintercalation of oxygen and formation of $Sr_2ReLiO_{5.5}$ which is believed to be the first reported example of heavily disordered and low symmetry Re^{6+} material with strong spin-orbital effects and a

suppressed magnetic moment. Refinement against X-ray and neutron diffraction data show that $Sr_2ReLiO_{5.5}$ is a cation ordered double perovskite material with partially ordered oxygen vacancies located in the equatorial anion sites in alternate layers, such that the overall structure could be described by the stacking sequence: $–Sr_2O_2–ReLiO_3–Sr_2O_2–ReLiO_4–$. The material can be accurately described using a tetragonal *P*4*/m* model but a Rietveld refinement against an orthorhombic *Pmmm* model yields a better statistical fit due to local disorder in the anion-vacant layers. Electron diffraction measurement show that the material undergoes extreme extensive microstructural twinning to minimize crystallographic strain caused by anisotropic broadening of polyhedra. EELS measurements strongly indicate Re^{6+} oxidation state for the majority of Re centres in the material. SQUID magnetometry measurements show that these Re^{6+} centres exhibit significantly reduced local paramagnetic moments, despite their location in reduced symmetry coordination sites, indicating spin–orbit coupling is not always quenched by small deviations from local O_h symmetry, contrary to widespread belief.

Chapter 4 Synthesis and Characterisation of $Sr_2ReLi_{0.64}Co_{0.36}O_6$

4.1 Introduction

Rhenium-containing mixed metal oxides are being investigated more frequently in search for functional materials like half-metallic ferromagnets. The previous chapter described the reduction chemistry of the d^0 ordered double perovskite Sr_2ReLiO_6. This chapter reports the synthesis and characterisation of a 3*d* transition-metal doped analogue, $Sr_2ReLi_{0.64}Co_{0.36}O_6$.

The synthesis of $Sr_2ReLi_{0.64}Co_{0.36}O_6$ was performed as a part of a wider study of rhenium mixed-metal oxides. Rhenium oxide chemistry has been challenging and the majority of oxides have been made under elaborate synthesis conditions such as using evacuated platinum crucibles[109] or high-pressure chemistry[48]. Soft chemistry methods were used to allow for accessible synthetic conditions and to reach rare oxidation states[96, 98]. The reported stoichiometry was achieved in an attempt to make the most reduced analogue of $Sr_2ReLi_xCo_{1-x}O_6$. The final composition is understood to be the theoretical limit of Co incorporation.

4.2 Synthesis

A sample of $Sr_2ReLi_{0.64}Co_{0.36}O_6$ was prepared using the Pechini method[57] (Chapter 2, Section 2.1.2). Suitable stoichiometric ratios of $SrCO_3$ (99.994%), Li_2Co_3 (99.998%), Co_3O_4 (99.999%) and Re metal (99.99%) to make the equivalent of $Sr_4Re_2CoLiO_{12}$ were dissolved in a 1:1 mixture of concentrated nitric acid and distilled water. The solution was stirred at 300 °C with citric acid and a few drops of ethylene glycol. The resulting gel was thoroughly dried and combusted in air. The subsequent product was ground into a powder using an

agate mortar and pestle, placed in an alumina crucible and heated to 1000 °C in air at a rate of 1 °C min^{-1} to combust the organic precursor. The resulting powder was pressed into a 13 mm diameter pellet and heated under inert gas flow for three cycles of 2 days at 1200 °C in the presence of a titanium rod acting as an oxygen getter.

The resulting powder was observed to be a mixture of $Sr_2ReLi_{0.64}Co_{0.36}O_6$ and CoO formed from non-incorporated Co confirmed by synchrotron X-ray and neutron diffraction methods. Refinement of neutron diffraction data showed CoO made up ~2.1% weight of the total which was consistent with the final refined stoichiometry of $Sr_2ReLi_{0.64}Co_{0.36}O_6$ for the final phase. The majority phase was indexed using a body-centred tetragonal *I*4*/m* model with lattice parameters *a* = 5.5574(3) Å, *c* = 7.9252(5) Å.

4.3 Results

4.3.1 Structural Characterisation

4.3.1.1 Synchrotron X-ray Powder Diffraction

Synchrotron X-ray powder diffraction (Chapter 2, Section 2.5.3) data collected from a sample of $Sr_2ReLi_{0.64}Co_{0.36}O_6$ could be readily indexed using a body-centred tetragonal, with extinction conditions consistent with the *I*4/*m* space group. The published structural data for Sr_2ReLiO_6[100] was used to construct a tetragonal cell with a split occupancy for the Li/Co site.

Synchrotron X-ray powder diffraction data collected from the sample could be readily indexed using the *I*4/*m* space group with lattice parameters *a* = 5.5574(3) Å, *c* = 7.9252(5) Å and fitting statistics χ^2 = 149.6, *wRp* = 5.69%, and *Rp* = 3.37%. While the χ^2 is relatively high, the more important *wRp* and *Rp* values were low. X-ray powder diffraction data

suggested the sample was a mixture with approximately 2.1% weight fraction of CoO. This was residue from the unincorporated CoO into the parent phase and contributed to the poor refinement fitting parameters of the X-ray measurement.

Compound	*a* / Å	*b* / Å	*c* / Å	Vol / Å^3	Ref
Sr_2ReLiO_6	5.5467(2)	5.5467(2)	7.9197(4)	244.29(1)	100
$Sr_2ReLi_{0.64}Co_{0.36}O_6$	5.5574(3)	5.5574(3)	7.9252(5)	244.77(4)	This work
Sr_2ReCoO_6	5.5631(1)	5.5631(1)	7.9516(2)	246.09(1)	96

Table 4.1 Unit cell parameter of $Sr_2ReLi_{0.64}Co_{0.36}O_6$ and ordered double perovskite analogues

Observed, calculated, and difference plots from Rietveld refinement against synchrotron X-ray powder diffraction data are presented in Figure 4.1. Full details of structural refinement parameters are given in Table 4.2. This Li/Co site occupancy was fixed in this refinement. This sites occupancy will be discussed in the next section on neutron powder diffraction.

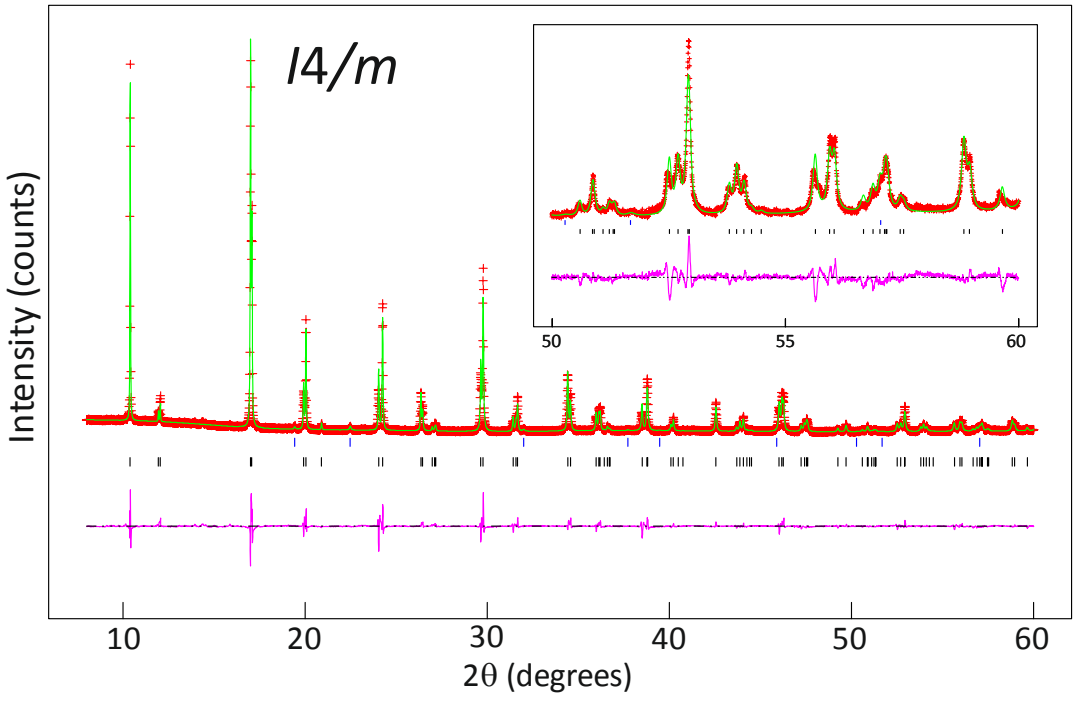


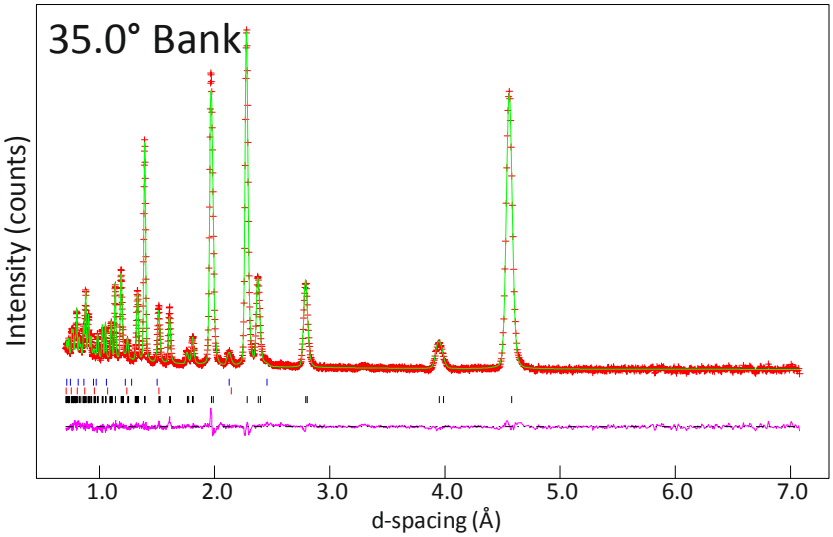
Figure 4.1 Observed, calculated, and difference plots from the refinement of the *I4/m* structural model of $Sr_2ReLi_{0.64}Co_{0.36}O_6$ against synchrotron X-ray powder diffraction data

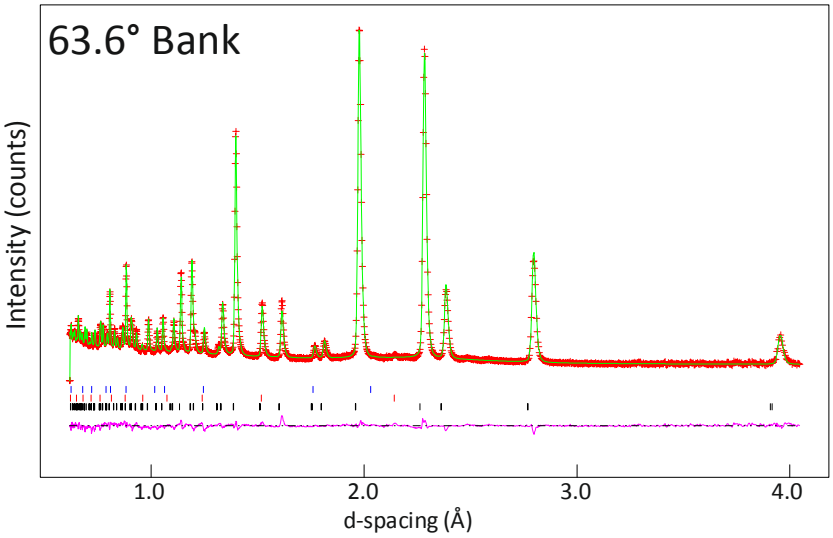
Atom	x	y	z	Fraction	U_{iso} (Å^2)
Sr	0	0.5	0.25	1	0.0131(3)
Re	0	0	0.5	1	0.0200(1)
Co/Li	0	0	0	0.36/0.64	0.0200(1)
O(1)	0	0	0.26664(7)	1	0.0121(2)
O(2)	0.288(1)	0.226(1)	0	1	0.0121(2)
$Sr_2ReLi_{0.64}Co_{0.36}O_6$ – Space group *I4/m* (#87) Formula mass = 483.10 gmol^{-1} *a* = 5.5574(3) Å, *c* = 7.9252(5) Å, Vol = 244.77(4) Å^3 Radiation source: Synchrotron X-ray, λ = 0.82626(1) Å Temperature: 298 K χ^2 = 149.6, *wRp* = 5.69%, and *Rp* = 3.37%					

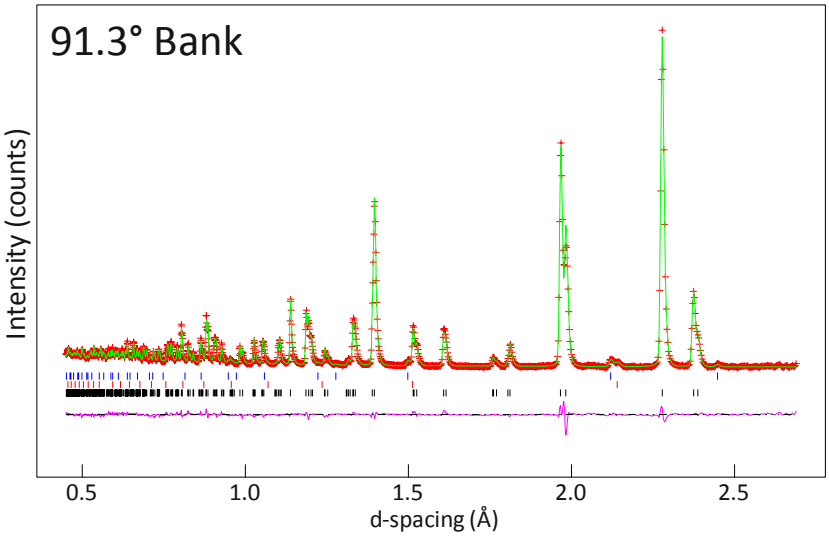
Table 4.2 Parameters from the structural refinement of $Sr_2ReLi_{0.64}Co_{0.36}O_6$ against synchrotron X-ray powder diffraction data

4.3.1.2 Room Temperature Neutron Diffraction Data

Neutron powder diffraction data were collected from a sample of $Sr_2ReLi_{0.64}Co_{0.36}O_6$ at 298 K using the GEM instrument at ISIS (Chapter 2, Section 2.6.1). An *I4/m* symmetry model was simultaneously refined against these neutron diffraction data and the synchrotron X-ray powder diffraction data. The fit greatly improved when the fractional occupancy of the Li/Co site was allowed to refine. The fit was improved with the introduction of vanadium metal and cobalt oxide as secondary phases. As seen in Figure 4.2**,** all the peaks and intensities are accounted for in the refinement. At T > 900 °C, Co_3O_4 decomposes to CoO[110] so the third phase was assigned to CoO. Rietveld refinement with CoO (χ^2 = 2.227, wRp = 3.82%, and Rp = 3.33%) gives better refinement statistics compared to Co_3O_4 (χ^2 = 2.540, wRp = 4.05%, and Rp = 3.44%). Observed, calculated, and difference plots for all data banks are shown in Figure 4.2. Full details of the structural parameters and selected bond lengths are given in Table 4.3 and Table 4.4 respectively.


35.0° Bank
Intensity (counts)
1.0
2.0
3.0
4.0
5.0
6.0
7.0
d-spacing (Å)


63.6° Bank
Intensity (counts)
1.0
2.0
3.0
4.0
d-spacing (Å)


91.3° Bank
Intensity (counts)
0.5
1.0
1.5
2.0
2.5
d-spacing (Å)

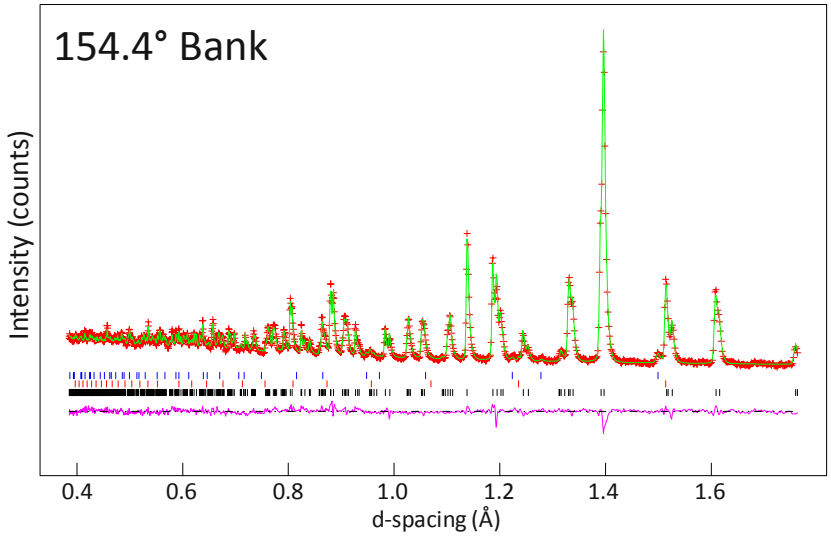


Figure 4.2 Observed, calculated, and difference plots from the refinement of $Sr_2ReLi_{0.64}Co_{0.36}O_6$ against neutron powder diffraction data collected at 298 K (black = $Sr_2ReLi_{0.64}Co_{0.36}O_6$, red = vanadium, blue = CoO)

Atom	***x***	***y***	***z***	**Fraction**	**U_{iso} (Å²)**
Sr	0	0.5	0.25	1	0.0101(3)
Re	0	0	0.5	1	0.0014(2)
Co/Li	0	0	0	0.361(5)/ 0.639(5)	0.0200(1)
O(1)	0	0	0.2621(2)	1	0.0134(2)
O(2)	0.2891(1)	0.2334(1)	0	1	0.0134(2)
$Sr_2ReLi_{0.64}Co_{0.36}O_6$ – Space group *I*4/*m* (#87) Formula mass = 483.10 gmol^{-1} *a* = 5.5574(3) Å, c = 7.9252(2), Vol = 244.77(4) Å^3 Temperature: 298 K Phase Fraction: 97.7 weight % ± 0.2 weight %					
Atom	***x***	***y***	***z***	**Fraction**	**U_{iso} (Å²)**
Co	0	0	0	1	0.00032(2)
O	0.5	0.5	0.5	1	0.00032(2)
CoO – Space group $Fm\bar{3}m$ (#225) *a* = 4.235763(3) Å Phase Fraction: 2.1 weight % ± 0.3 weight %					
Atom	***x***	***y***	***z***	**Fraction**	**U_{iso} (Å²)**
V	0	0	0	1	0.00250(1)
V – Space group $Im\bar{3}m$ (#229) *a* = 3.1337(3) Å					
Radiation source: Time-of-flight neutrons (GEM, ISIS) χ^2 = 2.275; *wRp* = 3.81%; *Rp* = 3.32%					

Table 4.3 Parameters from the structural refinement of $Sr_2ReLi_{0.64}Co_{0.36}O_6$ against neutron diffraction data at 298 K

Cation	Anion	Length (Å)
Re	O(1) x2	1.8854(16)
	O(2) x4	1.8887(6)
Li/Co	O(1) x2	2.0772(16)
	O(2) x4	2.0653(6)

Table 4.4 Selected bond lengths from the refined structure of $Sr_2ReLi_{0.64}Co_{0.36}O_6$

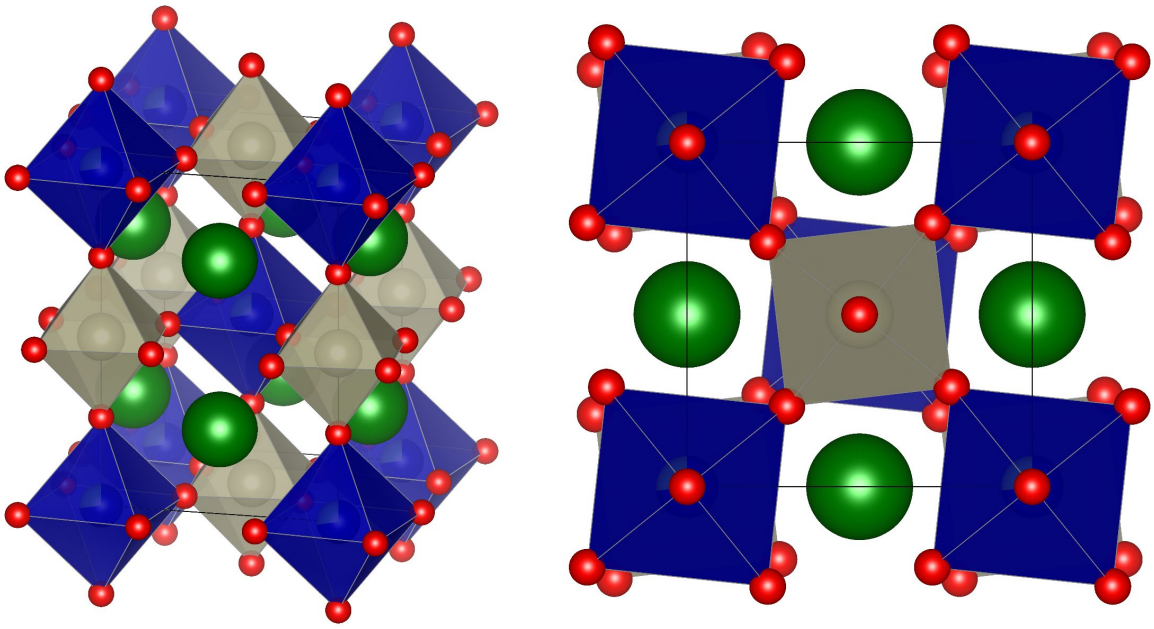


Figure 4.3 The structure $Sr_2ReLi_{0.64}Co_{0.36}O_6$ with *I4/m* space group symmetry viewed along [101] (left) and [010] (right) directions (blue octahedra = Co/Li, grey octahedra = Re, green spheres = Sr).

4.3.1.3 Low Temperature Neutron Diffraction Data

Low temperature neutron diffraction data (Chapter 2, Section 2.6.1) were collected from $Sr_2ReLi_{0.64}Co_{0.36}O_6$ to check for magnetic ordering reflections. Figure 4.4 shows the observed, calculated, and difference plots for one of the detector banks. The magnetic ordering peak observed at $d_{spacing} \approx 4.8$ Å is assigned to reflections from G-type antiferromagnetic order of CoO which has a Néel temperature of 291 K[111]. The magnetic model was refined to give an excellent fit and the ordered magnetic moments were

refined to be 2.03(1) μ_B per Co centre. There is no evidence of magnetic ordering peaks from the majority phase at 5 K.

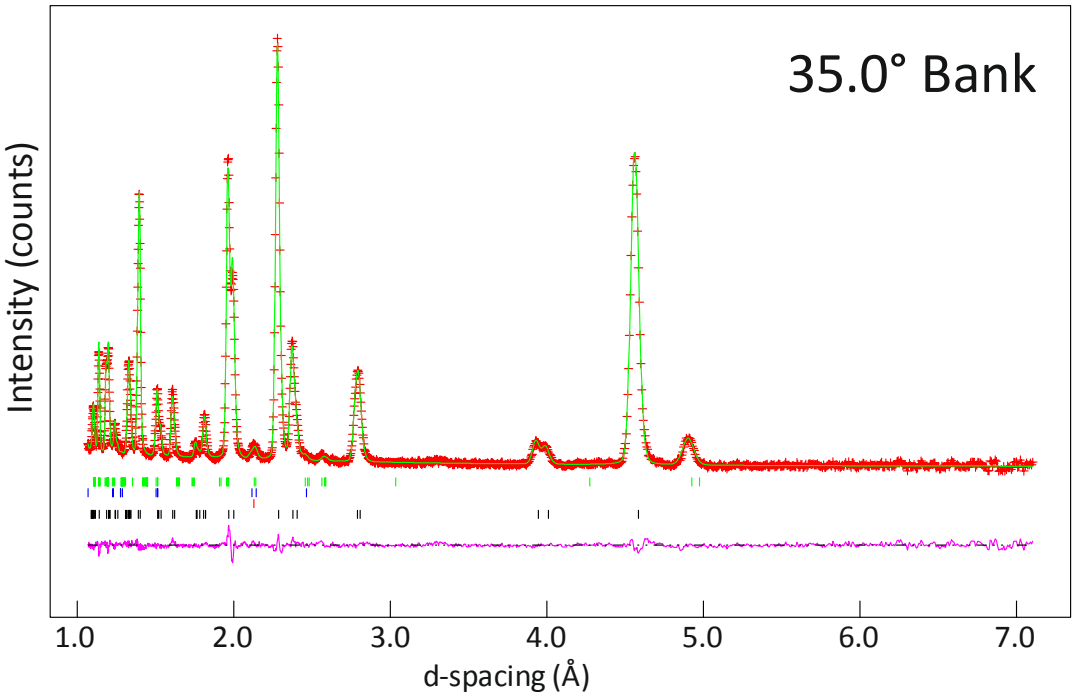


Figure 4.4 Neutron powder diffraction data collected from $Sr_2ReLi_{0.64}Co_{0.36}O_6$ at 5 K using the GEM Instrument (black = $Sr_2ReLi_{0.64}Co_{0.36}O_6$, red = vanadium; blue = CoO, green = CoO magnetic cell).

4.3.2 Magnetic Characterisation

Magnetisation data were collected from a sample of $Sr_2ReLi_{0.64}Co_{0.36}O_6$ on an MPMS SQUID magnetometer in an applied field of 100 Oe in the temperature range 5 < T / K < 300 (Chapter 2, Section 2.11). The zero-field cooled (ZFC) and field cooled (FC) data and magnetisation-field isotherms collected at 300 K and 5 K are shown in Figure 4.5 and Figure 4.6 respectively. The ZFC and FC curves are coincident at all temperatures above T ≈ 75 K where a minor divergence is seen. Remnant CoO with a T_N = 291 K likely had a minor contribution to the observed magnetic data but the relative contribution can be considered insignificant. At T ≈ 10 K the curves strongly diverge where a sharp drop in the ZFC curve and a decrease in the slope for FC curve is observed.

Magnetisation-field isotherms collected from $Sr_2ReLi_{0.64}Co_{0.36}O_6$ are shown in Figure 4.7. Field dependence of magnetism at 300 K is linear. Magnetisation-field isotherm collected in a field at 5 K shows a minor hysteresis but no signs of long-range magnetic order are observed. At 5 K field-dependence shows unusual splitting at strong negative field which has been attributed to an instrumental error and is not significant.

The inverse magnetisation data show non-linear behaviour at all temperatures with the temperature-independent part included. The temperature-independent moment corresponded to ~ 30% ($1.23(1) \times 10^{-3}$ cm^3 mol^{-1}) of the measured magnetisation at 300 K. With the temperature-independent part subtracted, a straight line could be fit to the most linear range of the data in the temperature range of $20 < T / K < 200$ as shown in Figure 4.7. Curie-Weiss fit to the data gives a Curie constant value $C = 0.592(2)$ cm^3 K mol^{-1} ($\mu^2 = 4.74(4)$ μ_B^2) and Weiss constant value $\theta = -10.42(9)$ K.

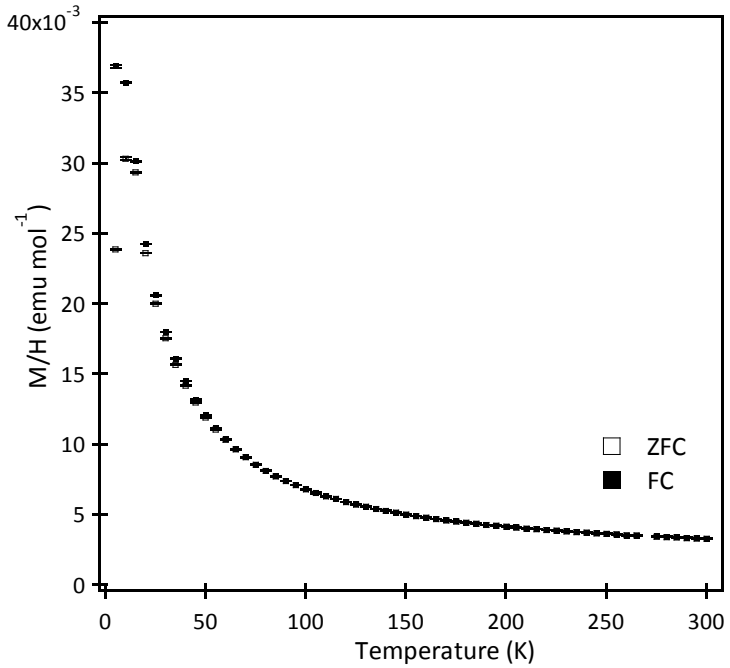


Figure 4.5 Zero-field cooled and field-cooled magnetisation data collected from $Sr_2ReLi_{0.64}Co_{0.36}O_6$

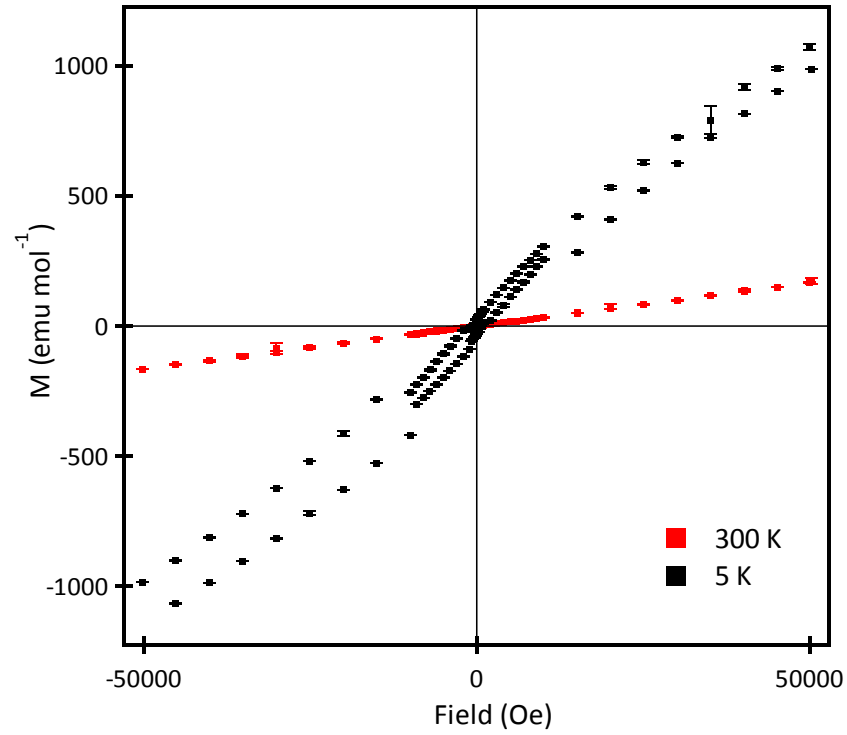


Figure 4.6 Magnetisation-field isotherms collected from $Sr_2ReLi_{0.64}Co_{0.36}O_6$

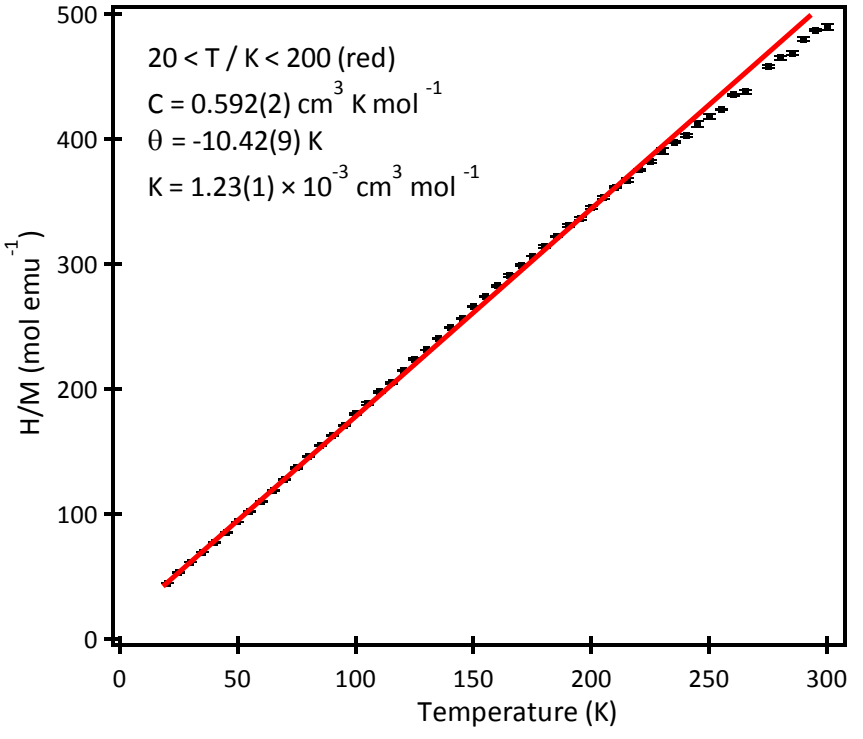


Figure 4.7 Fit to the Curie–Weiss law in the temperature range 20 < T / K < 200

4.4 Discussion

4.4.1 Structural Characterisation

Refinements of synchrotron powder X-ray powder diffraction data and neutron powder diffraction data (Section 4.3.1) show that the structure of $Sr_2ReLi_{0.64}Co_{0.36}O_6$ is best described by a body-centred tetragonal unit cell with *I*4*/m* space group symmetry (Figure 4.3) and lattice parameters of a = 5.5574(3) Å, c = 7.9252(5) Å. Rietveld refinement fitting statistics of χ^2 = 2.275; *wRp* = 3.81%; *Rp* = 3.32% suggest an excellent fit the collected diffraction data. The bond lengths listed in Table 3.2 suggest the octahedra retain a near-perfect O_h symmetry which is expected as none of the cations are J-T active ions.

The structure can be qualitatively described as an ordered double perovskite with Re on the B-site and Li/Co on the B'-site. Woodward *et al*[28] work on cation order suggests that B-site cation order occurs when there are significant differences in cation radius or charge between the two cations. Given the large size and charge difference between Re and Li/Co, its unsurprising to see Re fully occupying the B-site.

4.4.2 Magnetic Characterisation

Magnetisation data collected from $Sr_2ReLi_{0.64}Co_{0.36}O_6$ (Section 4.3.2) show that the zero-field-cooled and field-cooled measurements are coincident 75 < T / K < 300 temperature range below which a weak divergence is observed at T ≈ 75 K. At T = 20 K, the ZFC and FC curves diverge strongly signalling a change in magnetic behaviour. However given the scarcity of data points it is challenging to characterise the low-temperature magnetic state. Neutron powder diffraction data collected at 5 K show a magnetic ordering peak that has been assigned to the antiferromagnetic cell of CoO and no other features are

seen. The calculated Weiss constant is θ = −10.42(8) K which is consistent with the expected weakly antiferromagnetic interactions.

The reported material $Sr_2ReLi_{0.64}Co_{0.36}O_6$ has a complex oxidation state combination given its composition and the oxidation states of the different cations are not directly defined by any measurements. Consideration of the established oxide chemistries of Co and Re suggest there are two possible oxidation state combinations – $Co^{2+}/Re^{6.65+}$ or $Co^{3+}/Re^{6.38+}$ with the former combination preferred on chemical grounds.

The smaller observed moment is partially due expected spin-orbit coupling effects on the Re^{6+} ($t_{2g}^1e_g^0$) sites where the orbital degeneracy of the t_{2g} orbital is broken and the magnetic moment is quenched. Given the discussion of spin-orbit coupling effects in Re compounds discussed in Chapter 3, Section 3.4.5, there is very high likelihood that in $Sr_2ReLi_{0.64}Co_{0.36}O_6$ spin-orbit effects are strong with regards to Re centres.

Inverse magnetisation fit to the Curie–Weiss law in the temperature range 20 < T / K < 200 yields a Curie constant of C = 0.592(2) cm^3 K mol^{-1} (μ^2 = 4.736 μ_B^2). The expected spin-only Curie constant for $Co^{2+}/Re^{6.65+}$ combination is C = 0.818 cm^3 K mol^{-1} (μ^2 = 6.45 μ_B^2). Therefore, the observed moment is 72% of the expected spin-only moment for $Co^{2+}/Re^{6.65+}$ oxidations state combination. Alternatively, the expected spin-only Curie constant for a $Co^{3+}/Re^{6.38+}$ oxidation state combination is C = 1.84 cm^3 K mol^{-1} (μ^2 = 14.72 μ_B^2). Therefore, the observed moment is 32% of the expected spin-only moment for $Co^{3+}/Re^{6.38+}$ combination. The loss of 68% of the expected moment is unlikely so the former oxidation state combination is more likely.

However the observed moment is even smaller than the expected diluted spin-only moment of $\mu^2 = 5.4\ \mu_B^2$ for a Co^{2+} ($t_{2g}^5 e_g^2$) system (in this case 88% of as S = 3/2 system). Co^{2+} notably undergoes strong spin-orbit coupling to enhance the expected magnetic moment so the observed moment would be expected to be larger. It is apparent that the spin-orbit effects from Co^{2+} are quenched and this would be unsurprising given the high degree of local disorder on the B'-site in $Sr_2ReLi_{0.64}Co_{0.36}O_6$. There have been many reported examples, $LaRh^{4+}Co^{2+}O_6$[112] for example where the observed moment is only 86% of the expected spin only moment which is consistent with a 87% of diluted spin-only expected moment from Co^{2+} centres in $Sr_2ReLi_{0.64}Co_{0.36}O_6$.

4.5 Conclusion

The application of sol-gel chemistry allows for synthesis of $Sr_2ReLi_{0.64}Co_{0.36}O_6$. Refinements of synchrotron powder X-ray powder diffraction data and neutron powder diffraction data show that the structure of $Sr_2ReLi_{0.64}Co_{0.36}O_6$ is best described by a body-centred tetragonal unit cell with *I4/m* space group symmetry. Magnetisation data collected from $Sr_2ReLi_{0.64}Co_{0.36}O_6$ (Section 4.3.2) show that the zero-field-cooled and field-cooled measurements are coincident 75 < T / K < 300 temperature range below which a weak divergence is observed at T ≈ 75 K. At T = 20 K, ZFC and FC curves diverge strongly but neutron powder diffraction data do not suggest an antiferromagnetic unit cell. An analysis of Curie and the Weiss constants suggest $Sr_2ReLi_{0.64}Co_{0.36}O_6$ has the $Co^{2+}/Re^{6.65+}$ oxidation state combination.

Chapter 5 A Topochemical Reduction of $Sr_2ReLi_{0.64}Co_{0.36}O_6$

5.1 Introduction

Building on the rhenium chemistry described in previous chapters, the topochemical reduction of $Sr_2ReLi_{0.64}Co_{0.36}O_6$ is herein reported. The doping of Sr_2ReLiO_6 with a 3*d* metal changes the electronic configuration of the system with added *d*-electrons which in turn changes the reduction behaviour of the material. The reduction profile of $Sr_2ReLi_{0.64}Co_{0.36}O_6$ and characterisation of the topochemically reduced $Sr_2ReLi_{0.64}Co_{0.36}O_{5.5}$ is described.

5.2 Synthesis

Samples of $Sr_2ReLi_{0.64}Co_{0.36}O_{5.5}$ were made by reacting the $Sr_2ReLi_{0.64}Co_{0.36}O_6$ sample reported in Chapter 4 under flowing 5% H_2/N_2 gas in a flowing gas reaction described in Chapter 2, Section 2.3. The reported sample was made by reacting 2 g of $Sr_2ReLi_{0.64}Co_{0.36}O_6$ under flowing 5% H_2/N_2 gas at 550 °C for four periods of 4 hours. X-ray powder diffraction data collected between heating periods showed a change in lattice parameters, and no further changes were observed in the diffraction data after the third heating period. The resulting powder was observed to be a two-phase mixture of $Sr_2ReLi_{0.64}Co_{0.36}O_{5.5}$ and a small Co impurity. The resulting powder was characterised using synchrotron X-ray and neutron powder diffraction methods and thermogravimetric analysis.

5.3 Results

5.3.1 Reactivity of $Sr_2ReLi_{0.64}Co_{0.36}O_6$

The compound described here was made in a clam shell furnace in a controlled experiment. Consecutive reactions at 550 °C with laboratory X-ray powder diffraction measurements in between showed that the reduction follows in a continuous manner with a gradual lattice contraction after each heating. Examination of X-ray powder diffraction patterns at each step showed continued convergence of peaks, signalling a change in lattice parameters indicative of the compound become more metrically cubic.

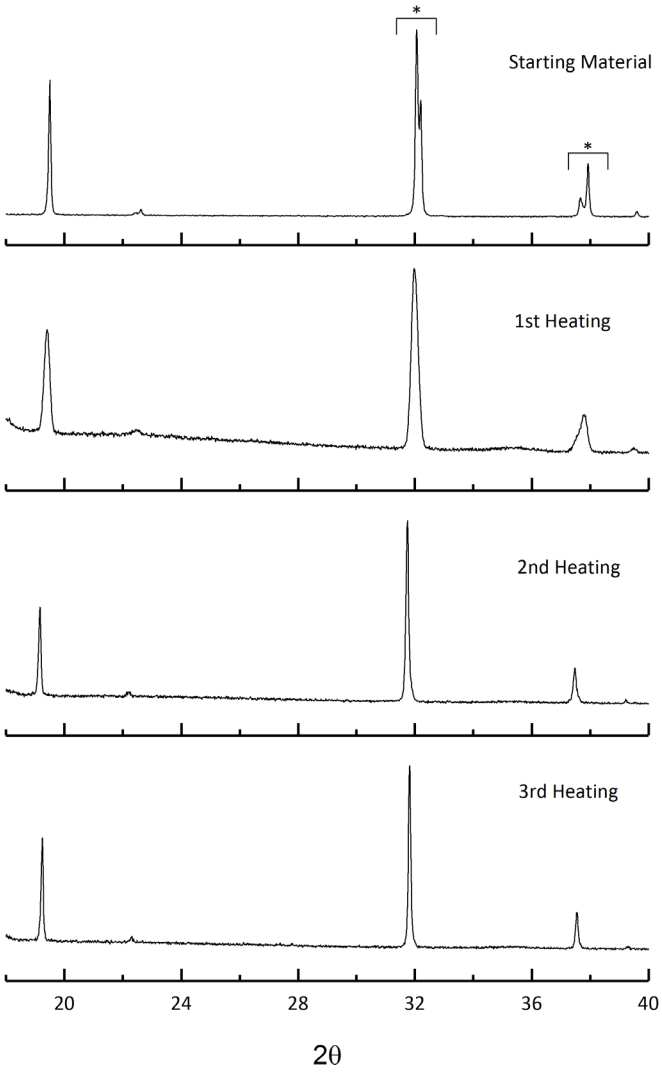


Figure 5.1 Progression of reduction of $Sr_2ReLi_{0.64}Co_{0.36}O_6$ during consecutive heatings. (* = converging peaks)

5.3.2 Thermogravimetric Analysis

Thermogravimetric analysis was conducted to determine the oxygen composition of the reduced material. Oxidative TGA experiment described in Chapter 2, Section 2.4 was used to recover the lost oxygen to the sample allowing the difference to be calculated. A small amount of the reduced sample was heated at 850 °C and held at this temperature for 1.5 hours under flowing oxygen gas. The resulting powder was confirmed to be $Sr_2ReLi_{0.64}Co_{0.36}O_6$ using X-ray powder diffraction. During this heating, a 1.57% increase in mass was observed indicating that the composition of the reduced phase was $Sr_2ReLi_{0.64}Co_{0.36}O_{5.52(3)}$. This composition can be rounded up to $Sr_2ReLi_{0.64}Co_{0.36}O_{5.5}$ for reference.

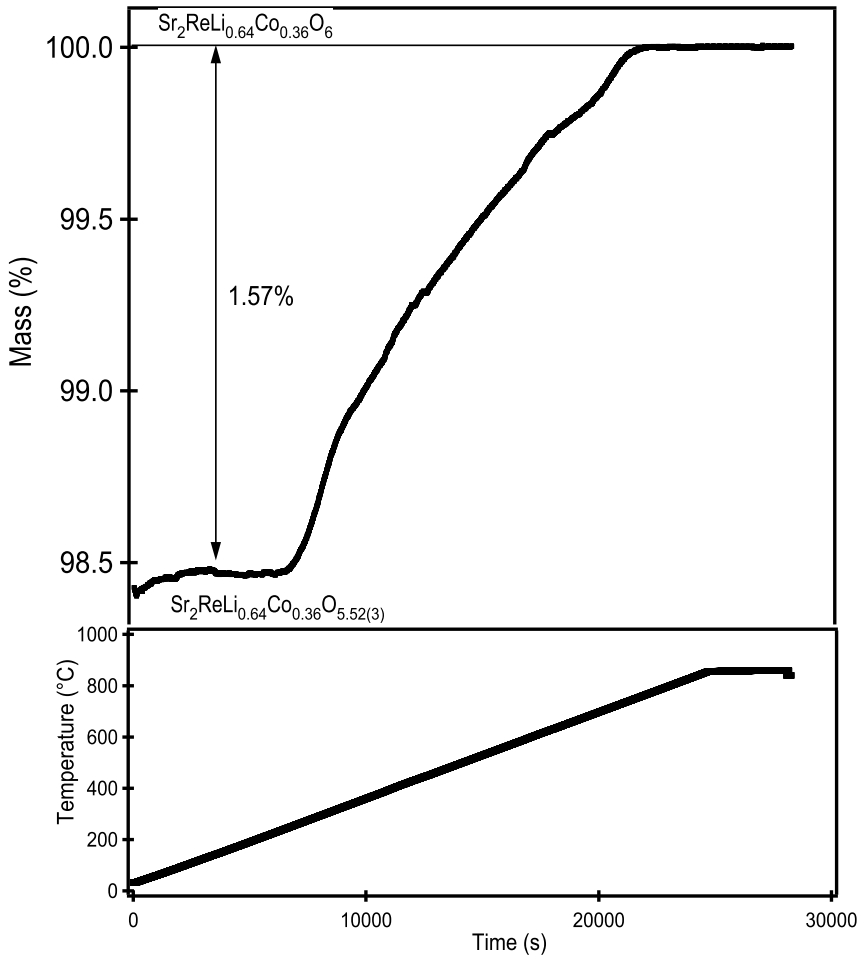


Figure 5.2 Thermogravimetric data collected during the reoxidation of $Sr_2ReLi_{0.64}Co_{0.36}O_6$ to $Sr_2ReLi_{0.64}Co_{0.36}O_{5.52(3)}$

5.3.3 Structural Characterisation of $Sr_2ReLi_{0.64}Co_{0.36}O_{5.5}$

5.3.3.1 Room Temperature Synchrotron X-ray Powder Diffraction

Synchrotron X-ray powder diffraction data were collected (Chapter 2, Section 2.5.3) from a sample of $Sr_2ReLi_{0.64}Co_{0.36}O_{5.5}$. The collected data could be readily indexed using a body-centred tetragonal *I*4/*m* space group. A structural model was constructed based on the refined structure of $Sr_2ReLi_{0.64}Co_{0.36}O_6$ described in Chapter 4. The model was refined against synchrotron X-ray powder diffraction data collected at room temperature. A single-phase refinement converged to a good statistical fit (χ^2 = 28.04, wRp = 2.99%, and Rp = 2.03%). The observed, calculated, and difference plots for the *I*4/*m* refinement are shown in Figure 5.3. The sample is known to have elemental Co as a secondary phase but its contribution to the X-ray powder diffraction pattern is not observable.

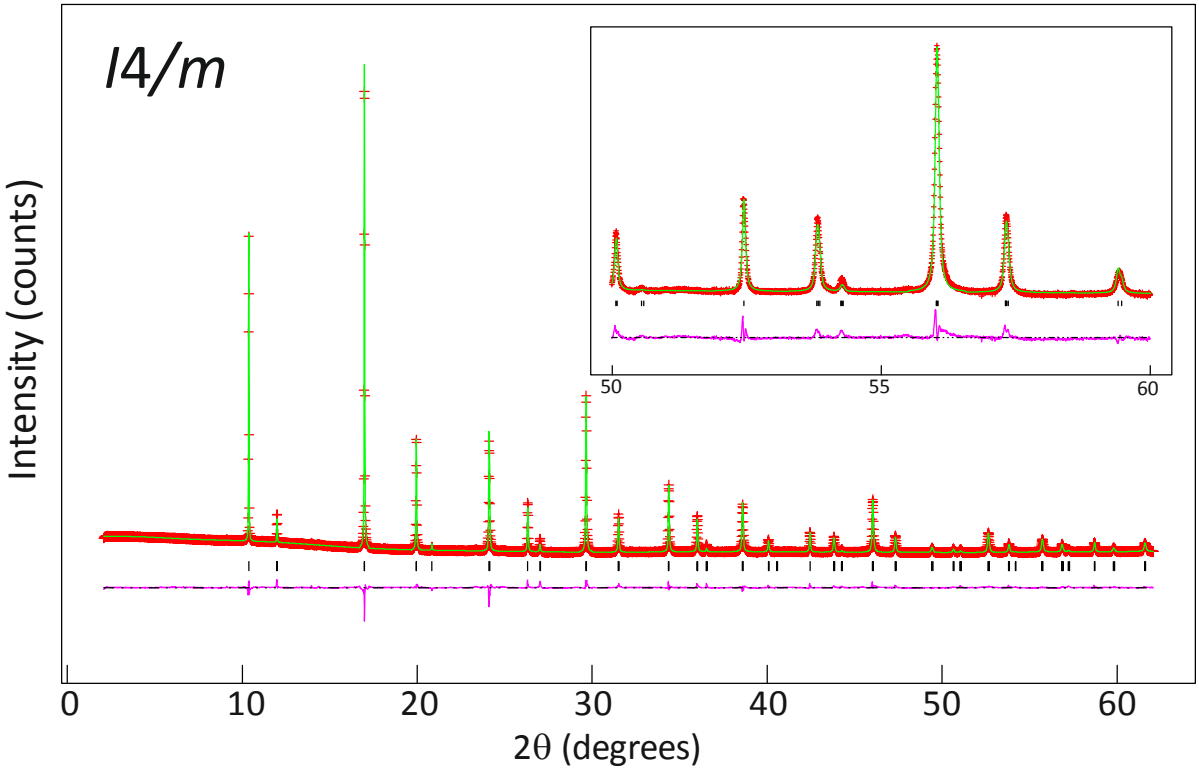
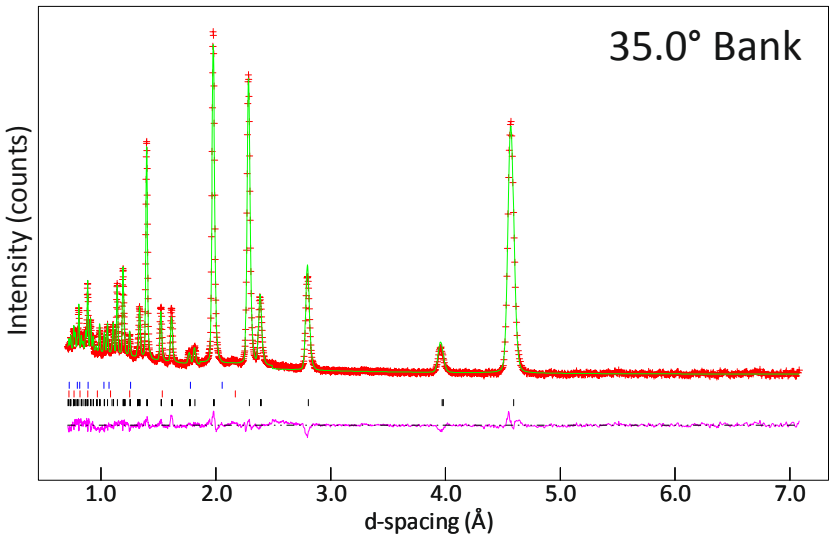


Figure 5.3 Observed, calculated, and difference plots from the refinement of the *I4/m* structural model of $Sr_2ReLi_{0.64}Co_{0.36}O_{5.5}$ against synchrotron X-ray powder diffraction data (λ = 0.82596(1) Å)

5.3.3.2 Room Temperature Neutron Diffraction Data

Neutron powder diffraction data were collected from $Sr_2ReLi_{0.64}Co_{0.36}O_{5.5}$ at 298 K using the GEM instrument at the ISIS Neutron and Muon centre (Chapter 2, Section 2.6.1). An *I4/m* symmetry model based on structure of $Sr_2ReLi_{0.64}Co_{0.36}O_6$ described in Chapter 4 was simultaneously refined against this neutron diffraction data and the synchrotron X-ray powder diffraction data where the fractional occupancy of the O atoms were allowed to refine freely and converged at a $Sr_2ReLi_{0.64}Co_{0.36}O_{5.5}$ stoichiometry. This stoichiometry agrees with the thermogravimetric analysis described in Section 5.3.2 and indicates that oxygen deintercalation happens in a disordered manner across two sites. The refinement was carried out with vanadium and cobalt structural files and the peaks across all banks were accounted for. The refinement converged to a good statistical fit with χ^2 = 4.203; wRp = 4.33%; Rp = 3.39%. The observed, calculated, and difference plots for all data banks are shown in Figure 5.4. Full details of the structural parameters and bond lengths are given in Table 5.1 and Table 5.2 respectively.



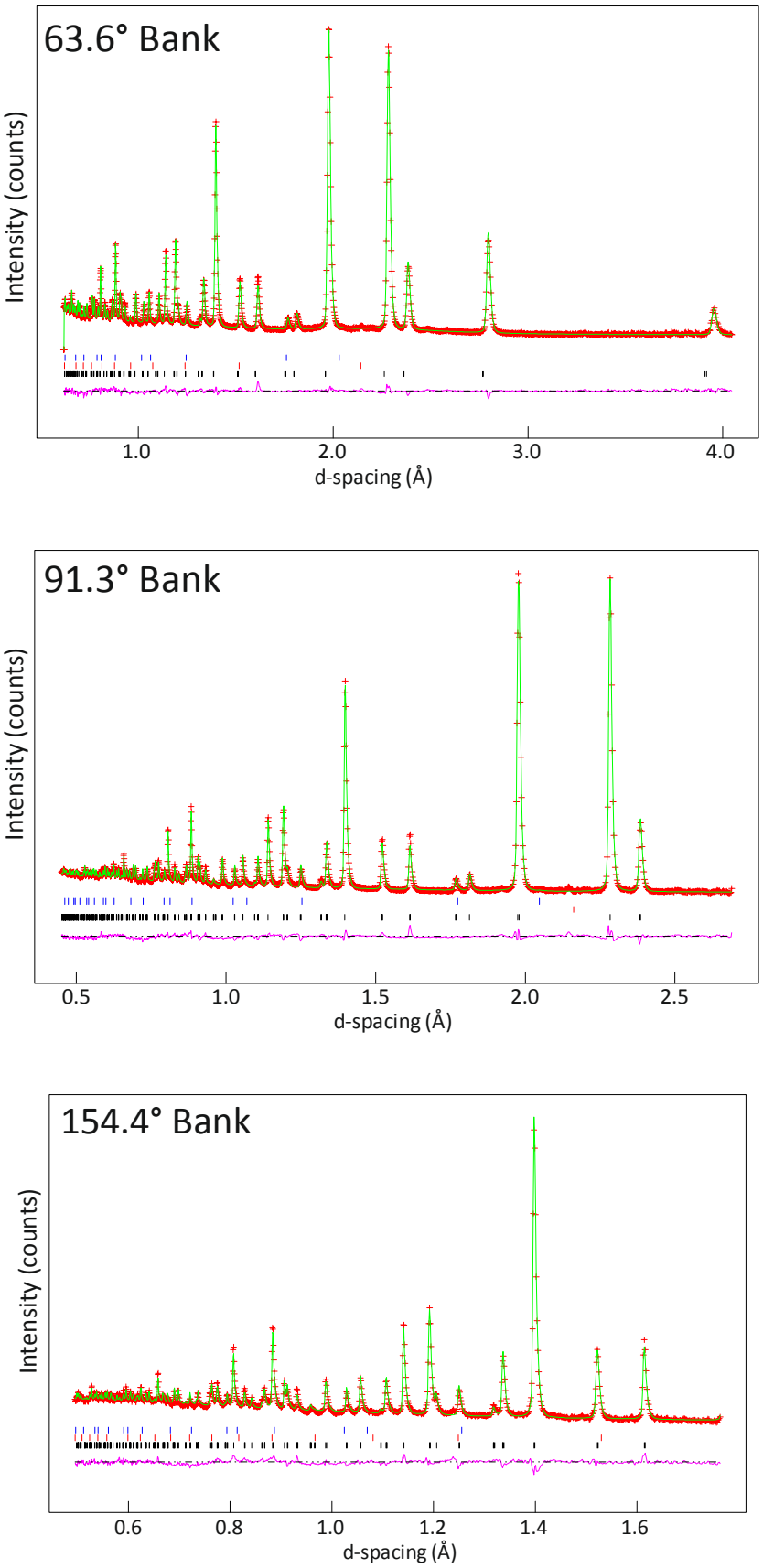


Figure 5.4 Observed, calculated, and difference plots from the refinement of $Sr_2ReLi_{0.64}Co_{0.36}O_{5.5}$ against neutron powder diffraction data collected at 298 K (black = $Sr_2ReLi_{0.64}Co_{0.36}O_{5.5}$, red = vanadium can, blue = cobalt)

Atom	*x*	*y*	*z*	Fraction	U_{iso} (Å^2)
Sr	0	0.5	0.25	1	0.0162(3)
Re	0	0	0.5	1	0.0148(2)
Co/Li	0	0	0	0.34(2)/ 0.65(1)	0.0203(2)
O(1)	0	0	0.2624(7)	0.939(9)	0.0256(2)
O(2)	0.2800(5)	0.2460(7)	0	0.917(9)	0.0052(2)
$Sr_2ReLi_{0.64}Co_{0.36}O_{5.5}$– Space group *I4/m* (#87)					
Formula mass = 475.10 gmol^{-1}					
a = 5.5831(3) Å, c = 7.9110(2) Å, Vol = 246.52(6) Å^3					
Temperature: 298 K					
Phase Fraction: 98.0(1) weight %					
Atom	***x***	***y***	***z***	**Fraction**	**U_{iso} (Å^2)**
Co	0	0	0	1	0.00032(2)
Co – Space group $Fm\bar{3}m$ (#225)					
a = 3.546073(3) Å					
Atom	***x***	***y***	***z***	**Fraction**	**U_{iso} (Å^2)**
V	0	0	0	1	0.00250(1)
V – Space group $Im\bar{3}m$ (#229)					
a = 3.1337(3) Å					
Radiation source: Time-of-flight neutrons (GEM, ISIS)					
χ^2 = 4.203; *wRp* = 4.33%; *Rp* = 3.39%					

Table 5.1 Parameters from the structural refinement of $Sr_2ReLi_{0.64}Co_{0.36}O_{5.5}$ against neutron powder diffraction data

Cation	Anion	Length (Å)
Re	O(1) x4	1.901(6)
	O(2) x2	1.875(3)
Co/Li	O(1) x4	2.081(3)
	O(2) x2	2.054(6)

Table 5.2 Selected bond lengths from the refined structure of $Sr_2ReLi_{0.64}Co_{0.36}O_{5.5}$

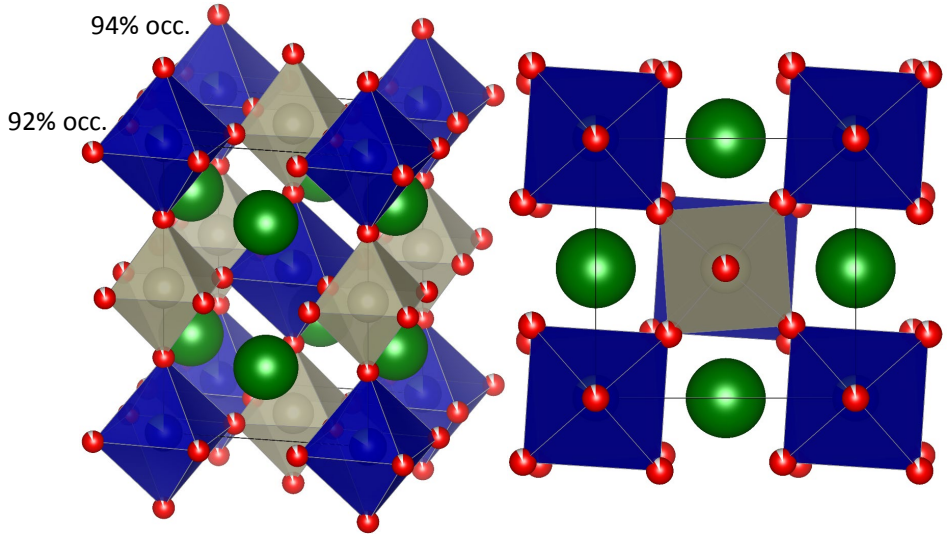


Figure 5.5 The averaged structure $Sr_2ReLi_{0.64}Co_{0.36}O_{5.5}$ with *I4/m* space group symmetry viewed along [101] (left) and [010] (right) directions. The blue octahedra = Co/Li site, grey octahedra = Re site, green spheres = Sr site. The oxygen positions are assigned occupancies consistent with the structural refinement

5.3.3.3 Low Temperature Neutron Diffraction Data

Low temperature neutron diffraction data (Chapter 2, Section 2.6.1) were collected from $Sr_2ReLi_{0.64}Co_{0.36}O_{5.5}$ to check for magnetic ordering reflections. The magnetic ordering peaks that were attributed to CoO in the neutron diffraction pattern of $Sr_2ReLi_{0.64}Co_{0.36}O_6$ as shown in Chapter 4, Section 4.3.1.3 are absent and no other ordering peaks are seen.

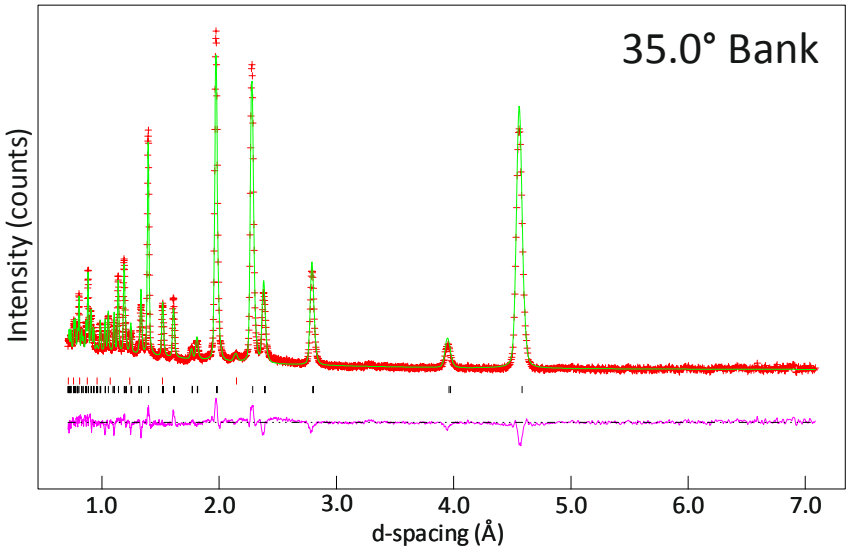


Figure 5.6 Neutron powder diffraction data collected from $Sr_2ReLi_{0.64}Co_{0.36}O_{5.5}$ at 5 K using the GEM Instrument

5.3.4 Magnetic Characterisation

Magnetisation data were collected from a sample of $Sr_2ReLi_{0.64}Co_{0.36}O_{5.5}$ in an applied field of 100 Oe in the temperature range 5 < T / K < 300 (Chapter 2, Section 2.11). Magnetisation-field isotherm plots collected at 300 K and 5 K shown in Figure 5.7

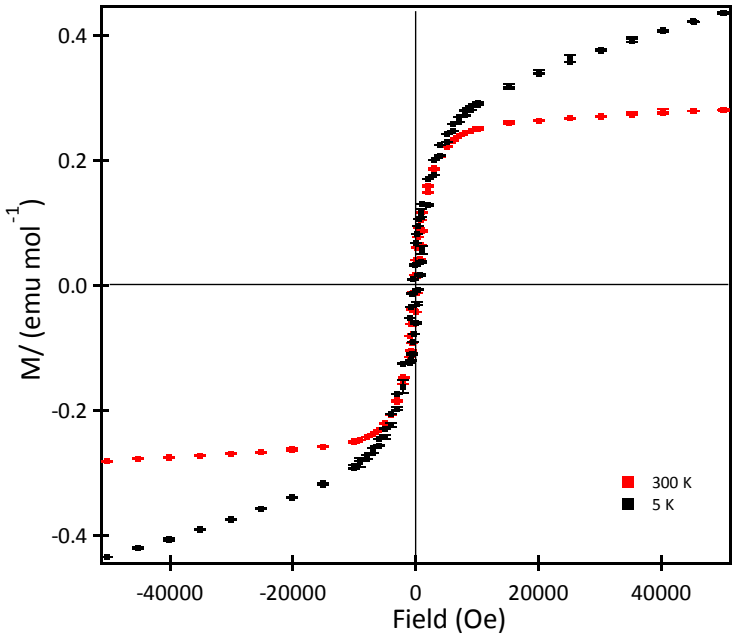


Figure 5.7 Magnetisation-field isotherms collected from $Sr_2ReLi_{0.64}Co_{0.36}O_{5.5}$

The saturated ferromagnetic moment at room temperature was taken as convincing evidence of elemental cobalt present in the sample. At a saturated moment of 0.25 μ_B, only ~10% of the magnetic moment from elemental cobalt is expressed in the magnetisation readings. This is consistent with the assumption that all of the ferromagnetic moment comes from the impurity and not the bulk phase. At 5 K the added contribution from the main phase is apparent.

Presence of a ferromagnetic impurity necessitated a ferrosubtraction measurement to be conducted (Chapter 2, Section 2.11.2). The plots of the paramagnetic susceptibility and

saturated ferromagnetic moment data extracted from the measurement are shown in Figure 5.8 and Figure 5.9 respectively.

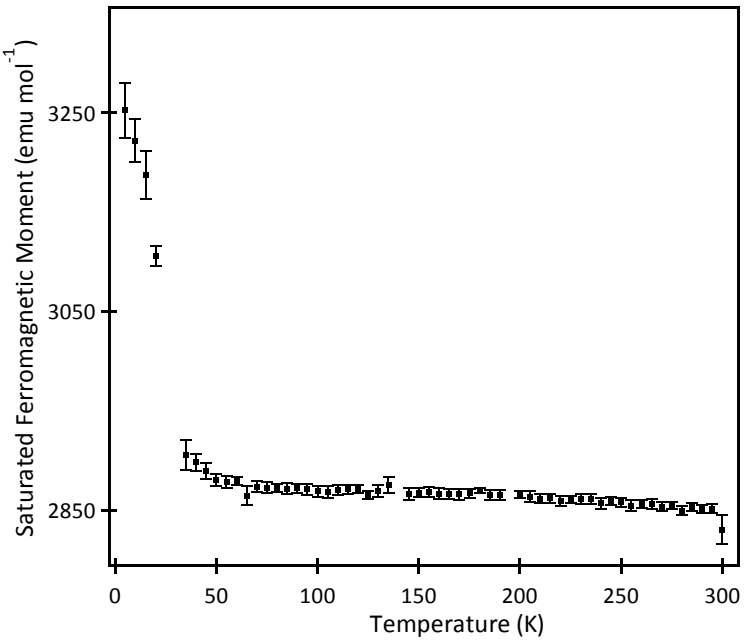


Figure 5.8 Saturated ferromagnetic moment extracted from a ferrosubtraction measurement carried out on $Sr_2ReLi_{0.64}Co_{0.36}O_{5.5}$.

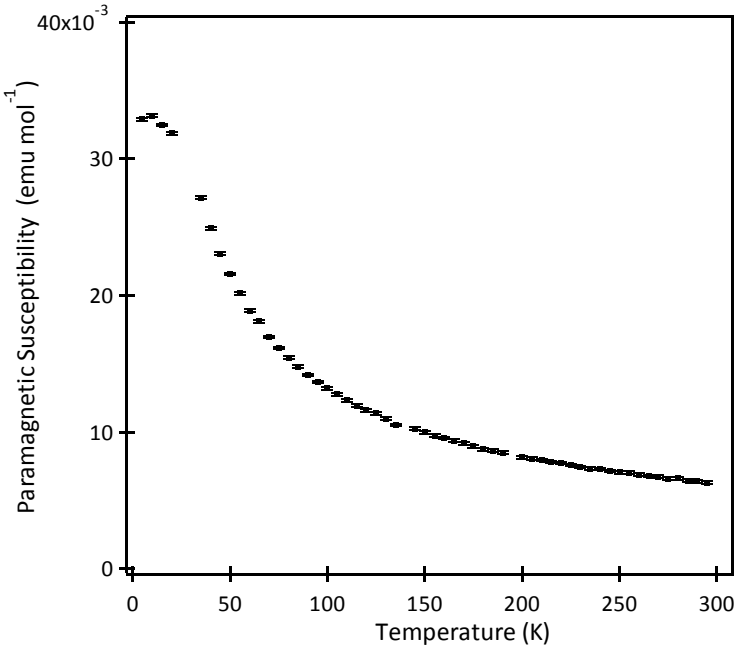


Figure 5.9 Paramagnetic susceptibility extracted from a ferrosubtraction measurement carried out on $Sr_2ReLi_{0.64}Co_{0.36}O_{5.5}$

The paramagnetic susceptibility readings show that $Sr_2ReLi_{0.64}Co_{0.36}O_{5.5}$ behaves like a conventional paramagnet in the temperature range 35 < T / K < 300. The susceptibility plot indicates an onset of magnetic ordering at T ≈ 20 K but the number of data points are too few to conclude this with certainty. Furthermore, neutron diffraction data collected at 5 K do not show any reflections that could be assigned to a magnetic unit cell. A straight line could be fit to the most linear range of the data in the temperature range of 35 < T / K < 300 as shown in Figure 5.10 . Curie-Weiss fit to the data range gives a Curie constant value C = 1.25(2) cm^3 K mol^{-1} and Weiss constant value θ = -15(1) K and a magnetic moment of μ^2 = 10.0(3) μ_B^2. There is near doubling in the Curie constant from unreduced $Sr_2ReLi_{0.64}Co_{0.36}O_6$ which expectedly indicates a larger presence of unpaired electrons introduced via reduction.

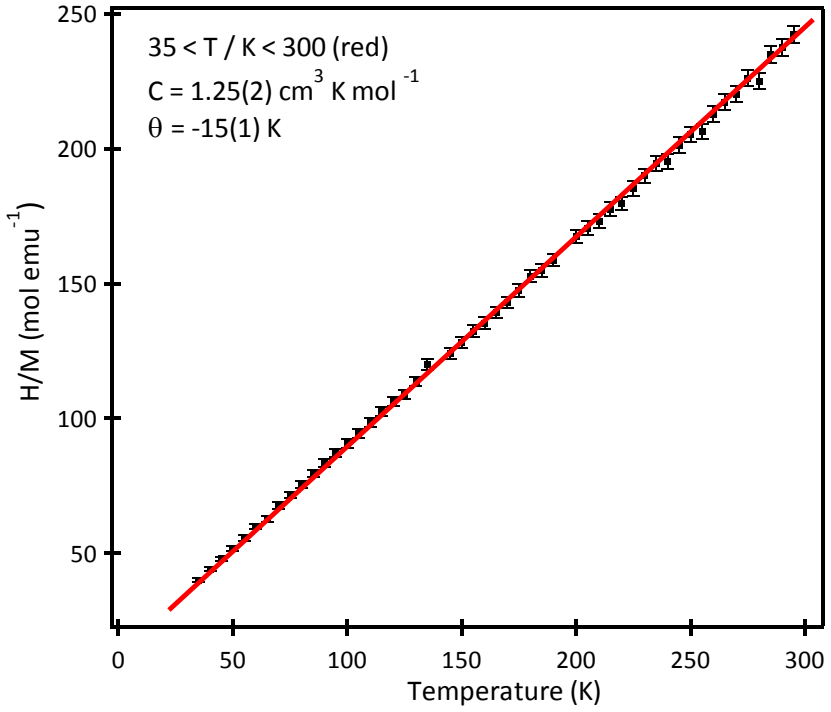


Figure 5.10 Fit to the Curie–Weiss law in the temperature range 35 < T / K < 300

5.4 Discussion

5.4.1 Reduction Chemistry

The reaction of $Sr_2ReLi_{0.64}Co_{0.36}O_6$ in 5% H_2 gas results in a gradual deintercalation of O atoms from the lattice as evidenced by a continuous change in lattice parameters across heating cycles. Structural refinements show that $Sr_2ReLi_{0.64}Co_{0.36}O_{5.5}$ retains the *I*4/*m* space group symmetry but undergoes a ~0.5% expansion in *a*, a minor contraction in *c* and an increase in volume.

The reduction profile of $Sr_2ReLi_{0.64}Co_{0.36}O_6$ can be contrasted to that of Sr_2ReLiO_6 where both can be reduced using H_2 gas but undergo different structural transformations. As shown in Chapter 4, the reduction of Sr_2ReLiO_6 results in deintercalation of oxygen from alternate layers and a lowering of symmetry to become metrically orthorhombic and the reduced phase $Sr_2ReLiO_{5.5}$ shows partial anion-vacancy order. Conversely, in a reducing environment $Sr_2ReLi_{0.64}Co_{0.36}O_6$ undergoes a structural transformation to become 'metrically' cubic in the same space symmetry and oxygen deintercalation happens in a disordered way and at random from both equatorial and axial sites.

Compound	*a* / Å	*b* / Å	*c* / Å	*a*√2 / *c*	Vol / Å³	Ref
$Sr_2ReLiO_{5.5}$	5.5213(1)	5.5213(1)	8.1133(1)	0.9624	247.09(3)	This work
Sr_2ReLiO_6	5.5467(2)	5.5467(2)	7.9197(4)	0.9905	244.29(1)	100
$Sr_2ReLi_{0.64}Co_{0.36}O_6$	5.5574(3)	5.5574(3)	7.9252(5)	0.9917	244.77(4)	This work
$Sr_2ReLi_{0.64}Co_{0.36}O_{5.5}$	5.5831(3)	5.5831(3)	7.9110(2)	0.9981	246.52(6)	This work
Sr_2ReCoO_6	5.5631(1)	5.5631(1)	7.9516(2)	0.9894	246.09(1)	96

Table 5.3 Unit cell parameters of reference Re materials and materials made in this research work.

The differences in reduction profile between Sr_2ReLiO_6 and $Sr_2ReLi_{0.64}Co_{0.36}O_6$ are likely to be a result of Li/Co disorder on the B'-site. It is reasonable to assume that the inclusion of

a 3*d* metal into the lattice removed the structural flexibility allowed by a Re/Li coordination system (detailed discussion in Chapter 4, Section 3.4.3). It is worth noting that attempts to topochemically reduce Sr_2ReCoO_6 using various reduction methods were unsuccessful. It is probable that Li acts a strong stabilising force for oxygen deintercalation and complex structural transformation seen in $Sr_2ReLiO_{5.5}$. This observation opens the possibility to make a wide range of topochemically reduced mixed-metal Li based perovskites.

5.4.2 Structural Characterisation

Refinements of synchrotron powder X-ray powder diffraction data and neutron powder diffraction data (Sections 5.3.3.1 and 5.3.3.2) show that the structure of $Sr_2ReLi_{0.64}Co_{0.36}O_{5.5}$ is best described by a body-centred tetragonal unit cell with *I*4*/m* space group symmetry (Figure 5.5) and lattice parameters of a = 5.5831(3) Å and c = 7.9110(2) Å. Rietveld refinement fitting statistics of χ^2 = 4.203; *wRp* = 4.33%; *Rp* = 3.39% suggest an excellent fit the collected diffraction data. The bond lengths listed in Table 5.2 suggest the octahedra deviate slightly from an O_h symmetry which is expected as the extracted data represent an averaged structure which does not account for the local geometry of 5-coordinate polyhedra.

5.4.3 Magnetic Characterisation

Magnetisation data collected from $Sr_2ReLi_{0.64}Co_{0.36}O_{5.5}$ (Section 5.3.4) show a magnetic hysteresis at 300 K strongly suggesting a small amount of elemental Co was made a result of reduction of remnant CoO found in $Sr_2ReLi_{0.64}Co_{0.36}O_6$ (Chapter 4, Section 5.3.3.2). To determine the bulk magnetic behaviour of $Sr_2ReLi_{0.64}Co_{0.36}O_{5.5}$, a ferrosubtraction

measurement was conducted (Chapter 2, Section 2.11.2). The paramagnetic susceptibility and ferromagnetic moment plots are shown in Section 5.3.4.

Paramagnetic susceptibility plot shows standard paramagnetic behaviour in the 35 < T / K < 300 temperature range. Below T ≈ 35 K the slope of the magnetisation plot inverts, suggesting the onset of a magnetically ordered state that is difficult to characterise but the calculated Weiss constant of θ = -15(1) K imply weakly antiferromagnetic interactions. Neutron powder diffraction data collected at 5 K do not show extra magnetic Bragg peaks so it's not possible to characterise the structure of this antiferromagnetic state. For similar reasons it is not possible to ascertain the spin coupling regimes in both reduced and parent phases discussed here and Chapter 4 respectively.

With a composition of $Sr_2Re^{6.65+}Li_{0.64}Co^{2+}{}_{0.36}O_6$ of the parent phase, oxygen deintercalation upon reduction can result in electrons being added only to Re centres or both to the Re or Co centres.

The values extracted from the Curie-Weiss fit described in Section 5.3.4 help clarify the oxidation state combination. The oxidation state combination would be $Re^{5.64+}/Co^{2+}$ for the all Re reduction case. For a mixed reduction case the oxidation state combination would be Re^{6+}/Co^{1+}. Inverse magnetisation fit to the Curie–Weiss law in the temperature range 35 < T / K < 200 yields a Curie constant of C = 1.25(2) $cm^3\ K\ mol^{-1}$ and a magnetic moment of μ^2 = 10.0(3) $\mu_B{}^2$. The expected spin-only Curie constant for the $Re^{5.64+}/Co^{2+}$ combination is C = 1.25 $cm^3\ K\ mol^{-1}$ (μ^2 = 10 $\mu_B{}^2$). Therefore, the observed moment is 100% of the expected spin-only moment for this oxidation state combination. The expected spin-only Curie constant for Re^{6+}/Co^{1+} combination is C = 1.863 $cm^3\ K\ mol^{-1}$ (μ^2 = 14.9 $\mu_B{}^2$).

Therefore, the observed moment is 67% of the expected spin-only moment for this oxidation state combination.

Results therefore strongly suggest the oxidation state combination is $Re^{5.64+}/Co^{2+}$ and reduction takes place only on Re centres. Furthermore, given the observation made in Chapter 4, the Re empty *d*-orbitals can be readily reduced in the presence of hydrogen gas but the reduction of Co^{2+} to Co^{1+} has been repeatedly shown to be challenging. $LaCoO_3$ and $SrCoO_{3-\delta}$ cannot be reduced to $ACoO_2$ while $LaNiO_3$ and $SrFeO_{3-\delta}$ can both be reduced to AMO_2 analogues[58, 113]. In cases where Co^{1+} has been made, only a fraction of sites are found to be Co(I) and the materials are made using heavily reducing metal hydrides[92, 104].

It is not surprising to see the observed moment coincident with the expected spin-only moment for this system. Although all three magnetic cation, Re^{5+}, Re^{6+} and Co^{2+} undergo strong spin-orbit coupling in individually or in high symmetry environments, deintercalation of O atoms from the lattice lowers the local symmetry of ReO_x and CoO_x centres significantly which likely quenches orbital contributions to the moment.

Compound	**SG**	**μ_{eff} / μ_B**	**μ_{exp} / μ_B**	**θ (K)**	**Re-O bond length (Å)**	**Ref.**
Ba_2CaReO_6	$Fm\bar{3}m$	0.744(2)	1.73	-39	2.092(1)	[52]
Sr_2CaReO_6	$I4/m$	1.72(9)	1.73	-426	1.926(8)/1.9101(4)	[53]
Sr_2MgReO_6	$P21/n$	1.659(6)	1.73	-443	1.899(5)/1.908(4)/1.925(5)	[109]
$Sr_2ReLiO_{5.5}$	$P4/m$	0.505(4)	1.73	-8.6(4)	1.846(2)/ 1.820(5) 1.875(5) 1.878(2)/ 1.959(2)	This work
$Sr_2ReLi_{0.64}Co_{0.36}O_{5.5}$	$I4/m$	3.16(1)	3.16	-15(1)	1.901(6)/ 1.875(3)	This work

Table 5.4 Magnetic behaviour and local symmetry of some rhenium double perovskites

5.5 Conclusion

The reaction of $Sr_2ReLi_{0.64}Co_{0.36}O_6$ with 5%/95% H_2/N_2 results in the deintercalation of oxygen and formation of $Sr_2ReLi_{0.64}Co_{0.36}O_{5.5}$. Magnetisation data collected from $Sr_2ReLi_{0.64}Co_{0.36}O_{5.5}$ show that the zero-field-cooled and field-cooled measurements are coincident $35 < T / K < 300$ temperature range and the material behaves like a Curie-Weiss paramagnet. Below $T \approx 30$ K the zero-field-cooled and field-cooled diverge signalling a transition to an ordered magnetic state but neutron powder diffraction data do not show magnetic Bragg peaks that would describe an antiferromagnetic unit cell. A Curie-Weiss fit to the magnetisation data yields a Curie constant of C = 1.25(2) cm^3 K mol^{-1} and a magnetic moment of μ^2 = 10.0(3) μ_B^2 which is ~100% of the expected spin-only value for the expected $Re^{5.64+}/Co^{2+}$ composition.

Chapter 6 Synthesis and Characterisation of $La_{0.5}Sr_{0.5-x}Ca_xMn_{0.5}Rh_{0.5}O_3$

6.1 Introduction

Synthesis, characterisation, and reactions of 4*d* transition-metal oxides have been widely explored. Notably, the 4*d* transition-metal Ru has been stabilised in interesting solid-oxide frameworks using solid-state reducing agents[59, 94, 114]. Despite being significantly more expensive than Ru, Rh has also been a subject of interest particularly for its superconductivity in polycrystalline form[115]. Since then it has been stabilised in various metal oxide frameworks coupled with 3*d* metals, primarily Mn, Fe, Ni, Cu, that stabilise Rh^{3+} and Rh^{4+} oxidation states[112, 116-118].

Recently a number of Rh-containing oxide-hydride phases have been made showing the ability of rhodium to stabilise oxyhydride lattices and reinforcing the concept of covalent stabilisation of complex metal-oxyhydrides[23]. Doping of mixed-metal manganese perovskites has been of particular interest given the wide range of physical behaviours shown in $La_xCa_{1-x}MnO_3$[65, 119, 120] with particular interest in stabilisation of Mn^{3+}/Mn^{4+} frameworks[121].

To further expand the understanding of the complex magnetism in 4*d*/3*d* transition-metal oxides, the synthesis and A-site doping of $La_{0.5}Sr_{0.5}Mn_{0.5}Rh_{0.5}O_3$ is herein reported.

6.2 Synthesis

6.2.1 Synthesis of $La_{0.5}Sr_{0.5-x}Ca_xMn_{0.5}Rh_{0.5}O_3$, (x = 0.125, 0.25)

Samples of composition $La_{0.5}Sr_{0.5-x}Ca_xMn_{0.5}Rh_{0.5}O_3$ (x = 0.125, 0.25) were prepared using a high-temperature ceramic synthesis method. Suitable stoichiometric ratios of La_2O_3

(99.999%, dried at 900 °C), $SrCO_3$ (99.994%), $CaCO_3$ (99.999%), Rh_2O_3 (99.99%, dried at 800 °C) and MnO_2 (99.997%) were ground together using an agate mortar and pestle, moved to an alumina crucible and heated to 1000 °C at 1 °C min^{-1} decompose the carbonates. The resulting samples were reground thoroughly, pressed into pellets, and heated for 4 periods of 48 hours at 1300 °C in air. The reaction progress was monitored using laboratory X-ray powder diffraction and the final samples were confirmed to be phase pure using synchrotron X-ray powder diffraction.

6.3 Results

6.3.1 Structural Characterisation

6.3.1.1 Space Group Determination of $La_{0.5}Sr_{0.5}Mn_{0.5}Rh_{0.5}O_3$

Synchrotron X-ray powder diffraction data were collected from a sample of $La_{0.5}Sr_{0.5}Mn_{0.5}Rh_{0.5}O_3$ (Chapter 2, Section 2.5.3) using the I11 instrument at the Diamond Light Source Ltd. A structural model was built based on the reported structure of $LaSrMnRuO_6$[122-124]. There had been an ambiguity over the correct structure of $LaSrMnRuO_6$ so the diffraction data collected from $La_{0.5}Sr_{0.5}Mn_{0.5}Rh_{0.5}O_3$ was refined against two orthorhombic models based on the *Imma*[125] and *Pnma*[122-124] space groups. The diffraction data were also refined against a model in the $P2_1/n$ space group to test for cation ordering. Table 6.1 shows the fitting statistics for each model. Figure 6.1 shows the structural depictions of the three possible models. The observed, calculated, and difference plots for the *Pnma, Imma,* and $P2_1/n$ refinements are shown in Figure 6.2.

The refinement of the *Pnma* model against collected data gives the best Rietveld refinement statistics. The model described in space group *Imma* did not account for a series of peaks observed in the diffraction data as seen in Figure 6.2. The model in space

group $P2_1/n$ allows for Mn/Rh ordering. However when the fractional occupancies of Mn and Rh were allowed to vary freely across the two possible cation sites, the best fit was obtained by a 1:1 ratio of Mn/Rh on both sites, indicating no B-site cation order is present in $La_{0.5}Sr_{0.5}Mn_{0.5}Rh_{0.5}O_3$. When an ordered arrangement of Mn and Rh was imposed, a poor fit to the data was observed as shown in Figure 6.2.

Space Group	χ^2	***wRp* (%)**	***Rp* (%)**
Pnma (#62)	25.98	3.11	1.96
Imma (#74)	53.84	4.47	2.82
$P2_1/c$ (#14) forced cation order	77.89	5.38	3.05

Table 6.1 Fitting statistics from the structural refinement of $La_{0.5}Sr_{0.5}Mn_{0.5}Rh_{0.5}O_3$

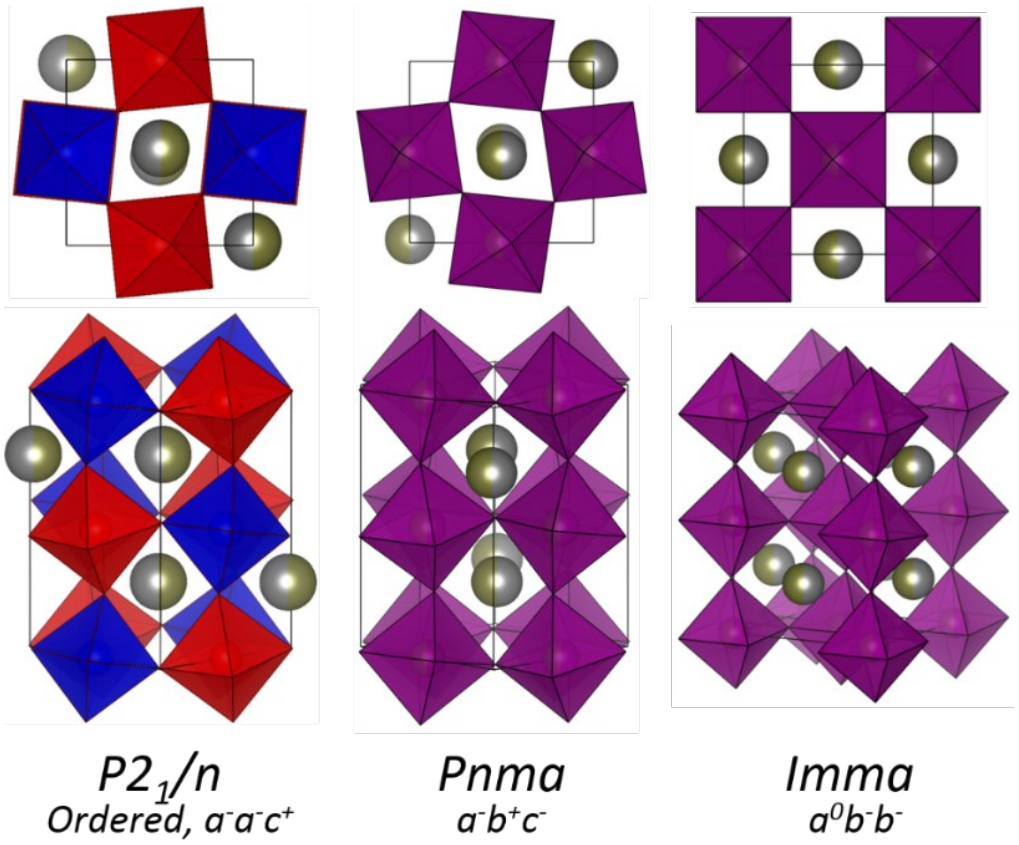


Figure 6.1 Structural models of the three possible structures of $La_{0.5}Sr_{0.5}Mn_{0.5}Rh_{0.5}O_3$ (purple spheres represent manganese/rhodium sites and red and blue spheres represent manganese and rhodium sites respectively).

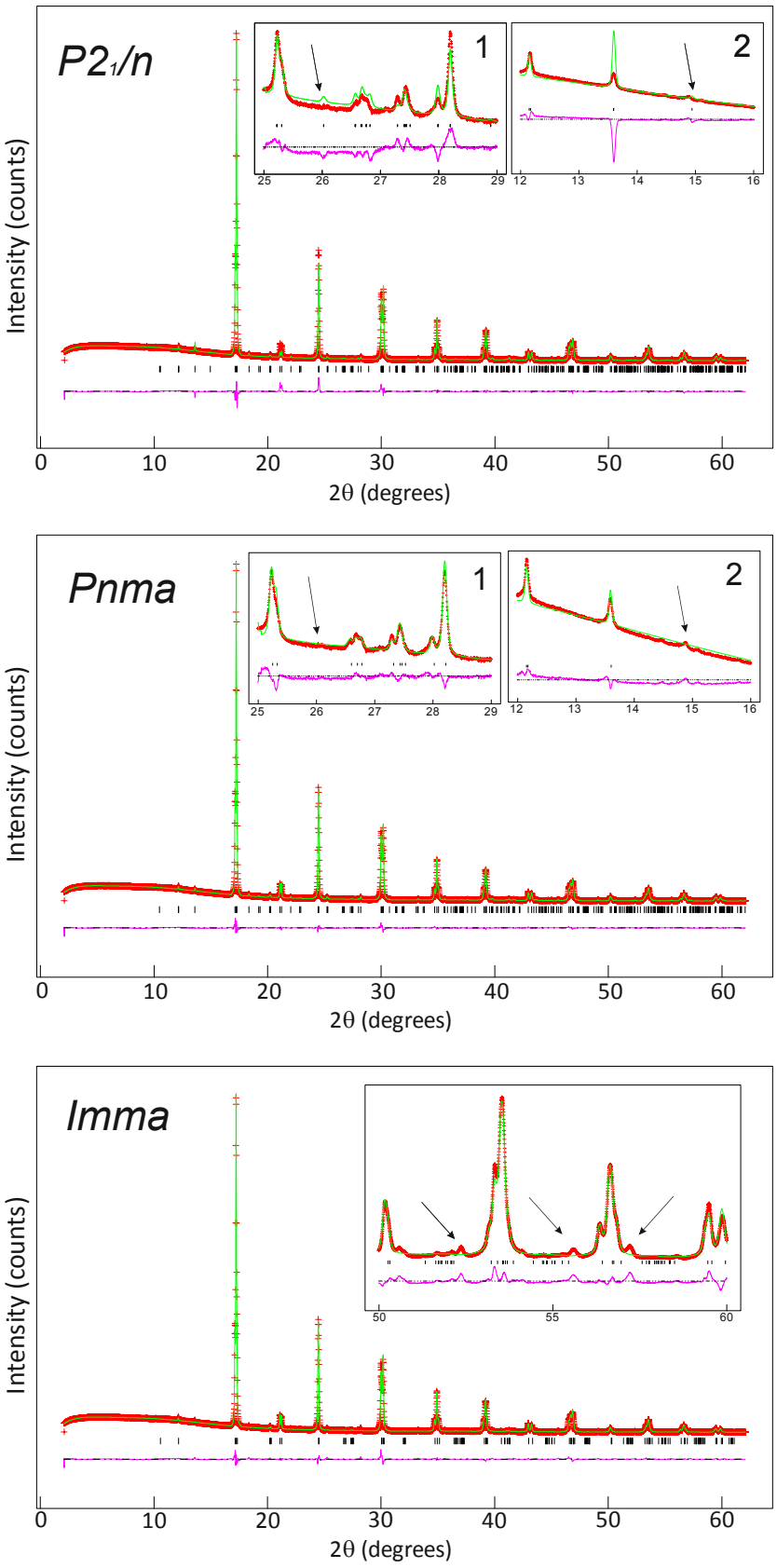


Figure 6.2 Observed, calculated, and difference plots from the refinement of three possible structural models against synchrotron X-ray powder diffraction data (λ = 0.82626(1) Å). Insets show selected angle reflections.

6.3.1.2 Synchrotron X-ray powder diffraction

Synchrotron X-ray powder diffraction data (Chapter 2, Section 2.5.3) were collected from a samples of $La_{0.5}Sr_{0.5-x}Ca_xMn_{0.5}Rh_{0.5}O_3$ (x = 0.125, 0.25). The diffraction data collected from all samples could be indexed using a primitive orthorhombic unit cell with extinction conditions consistent with the *Pnma* space group. The cell was built based on the published structure of $LaSrMnRuO_6$[124] with a 1:1 ratio of La/Sr on the A-site and a 1:1 ratio of Mn/Rh on the B-site. The model was refined against synchrotron X-ray powder diffraction data collected at room temperature from all samples. A single-phase refinement converged to give a good statistical fit for all samples and the structures for doped samples were only marginally different from the un-doped phase. Table 6.2 shows the lattice parameters of all three samples and the values are consistent with the expected lattice distortions.

Composition	***a* / Å**	***b* / Å**	***c* / Å**	**Vol / Å^3**
$La_{0.5}Sr_{0.5}Mn_{0.5}Rh_{0.5}O_3$	5.48323(3)	7.77780(5)	5.53677(3)	236.130(3)
$La_{0.5}Sr_{0.375}Ca_{0.125}Mn_{0.5}Rh_{0.5}O_3$	5.47935(3)	7.76555(5)	5.51703(3)	234.751(4)
$La_{0.5}Sr_{0.25}Ca_{0.25}Mn_{0.5}Rh_{0.5}O_3$	5.47776(4)	7.75272(6)	5.50131(4)	233.627(4)

Table 6.2 Lattice parameters obtained from X-ray powder diffraction data. Full breakdown given later in the section

Observed, calculated, and difference plots from Rietveld refinements against synchrotron X-ray data are presented in Figure 6.3 - Figure 6.5. Detailed structural parameters obtained from the refinements are given in Table 6.2 - Table 6.5. Selected bond lengths and angles are presented in Table 6.6.

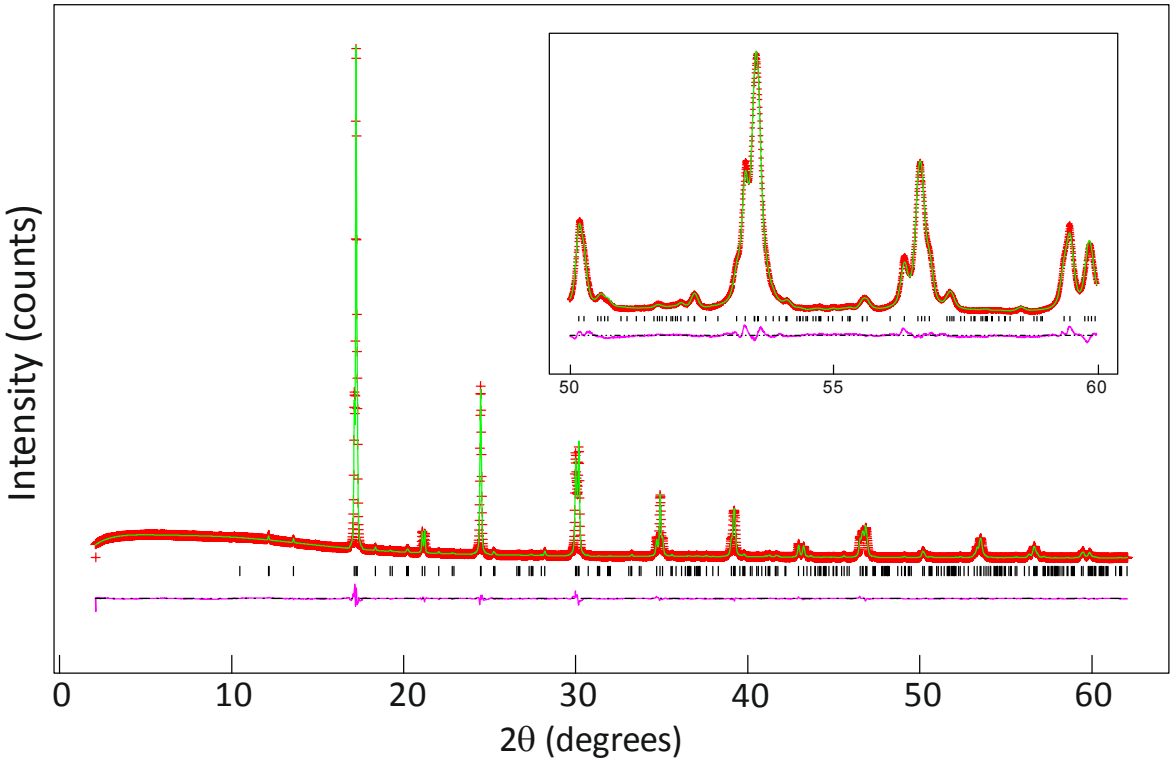


Figure 6.3 Observed, calculated, and difference plots from the refinement of the *Pnma* structural model of $La_{0.5}Sr_{0.5}Mn_{0.5}Rh_{0.5}O_3$ against synchrotron X-ray powder diffraction data

Atom	x	y	z	Fraction	U_{iso} (Å^2)
La/Sr	0.01805(7)	0.25	1.0017(2)	0.5	0.088(1)
Rh/Mn	0	0	0.5	0.5	0.043(3)
O(1)	0.4973(7)	0.25	0.9458(7)	1	0.178(8)
O(2)	0.2242(7)	0.5302(4)	0.7864(5)	1	0.178(8)
$La_{0.5}Sr_{0.5}Mn_{0.5}Rh_{0.5}O_3$ – Space group *Pnma* (#62) Formula mass = 240.19 gmol^{-1} *a* = 5.48323(3) Å, *b* = 7.77780(5) Å and *c* = 5.53677(3) Å, Vol = 236.130(3) Å^3 Radiation source: Synchrotron X-ray, λ = 0.82626(1) Å χ^2 = 25.91, *wRp* = 3.11%, and *Rp* = 1.96%					

Table 6.3 Parameters from the structural refinement of $La_{0.5}Sr_{0.5}Mn_{0.5}Rh_{0.5}O_3$

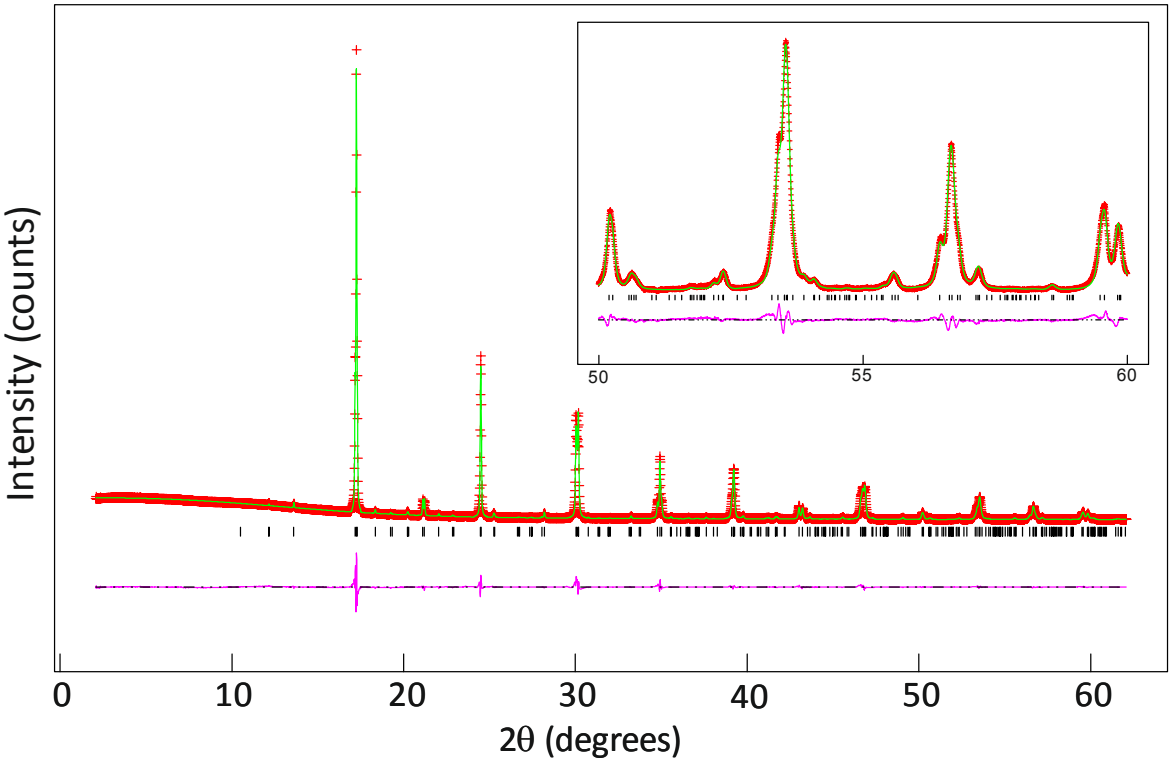


Figure 6.4 Observed, calculated, and difference plots from the refinement of the *Pnma* structural model of $La_{0.5}Sr_{0.375}Ca_{0.125}Mn_{0.5}Rh_{0.5}O_3$ against synchrotron X-ray powder diffraction data

Atom	x	y	z	Fraction	U_{iso} (Å^2)
La/Sr/Ca	0.02178(9)	0.25	1.0021(3)	0.5/0.375/0.125	0.018(1)
Rh/Mn	0	0	0.5	0.5	0.020(3)
O(1)	0.4952(7)	0.25	0.948(1)	1	0.089(8)
O(2)	0.2769(9)	0.4678(6)	0.2897(7)	1	0.089(8)
$La_{0.5}Sr_{0.375}Ca_{0.125}Mn_{0.5}Rh_{0.5}O_3$ – Space group *Pnma* (#62)					
Formula mass = 234.25 gmol^{-1}					
a = 5.47935(3) Å, b = 7.76555(5) Å and c = 5.51703(3) Å, Vol = 234.751(4) Å^3					
Radiation source: Synchrotron X-ray, λ = 0.82626(1) Å					
χ^2 = 41.3, wRp = 4.16%, and Rp = 2.76%					

Table 6.4 Parameters from the structural refinement of $La_{0.5}Sr_{0.375}Ca_{0.125}Mn_{0.5}Rh_{0.5}O_3$

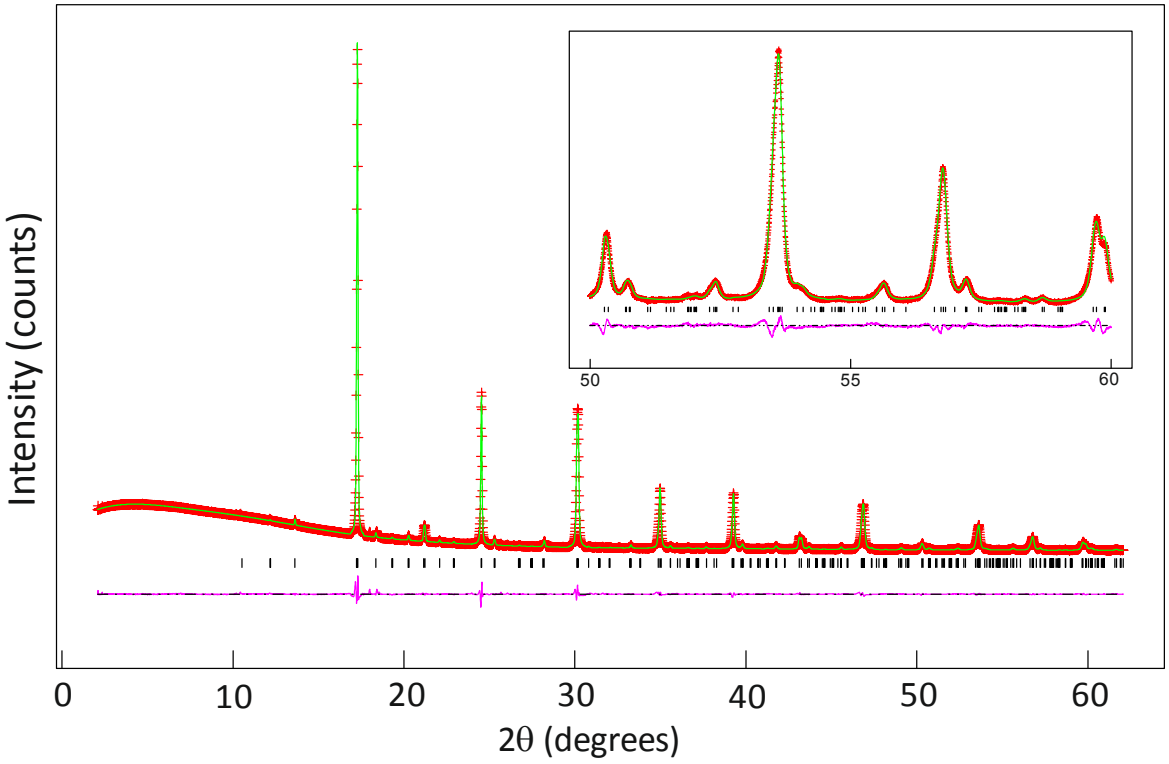


Figure 6.5 Observed, calculated, and difference plots from the refinement of the *Pnma* structural model of $La_{0.5}Sr_{0.25}Ca_{0.25}Mn_{0.5}Rh_{0.5}O_3$ against synchrotron X-ray powder diffraction data

Atom	x	y	z	Fraction	U_{iso} (Å^2)
La/Sr/Ca	0.0246(1)	0.25	1.0028(2)	0.5/0.25/0.25	0.060(1)
Rh/Mn	0	0	0.5	0.5	0.037(3)
O(1)	0.4975(7)	0.25	0.934(1)	1	0.150(4)
O(2)	0.217(4)	0.5285(6)	0.7875(9)	1	0.150(4)
$La_{0.5}Sr_{0.25}Ca_{0.25}Mn_{0.5}Rh_{0.5}O_3$ – Space group *Pnma* (#62) Formula mass = 228.305 gmol^{-1} a = 5.47775(4) Å, b = 7.75272(2) Å and c = 5.50130(4) Å, Vol = 233.627(4) Å^3 Radiation source: Synchrotron X-ray, λ = 0.82626(1) Å χ^2 = 27.58, wRp = 2.59%, and Rp = 1.39%					

Table 6.5 Parameters from the structural refinement of $La_{0.5}Sr_{0.25}Ca_{0.25}Mn_{0.5}Rh_{0.5}O_3$

Parameter	$La_{0.5}Sr_{0.5}Mn_{0.5}Rh_{0.5}O_3$	$La_{0.5}Sr_{0.375}Ca_{0.125}Mn_{0.5}Rh_{0.5}O_3$	$La_{0.5}Sr_{0.25}Ca_{0.25}Mn_{0.5}Rh_{0.5}O_3$
Vol ($Å^3$)	236.130(3)	234.751(4)	233.627(4)
B – O_{ax} (x2) (Å)	1.96755(7)	1.96335(10)	1.9724(11)
B – O_{eq} (x2) (Å)	1.934(4)	1.926(5)	1.951(6)
B – O_{eq} (x2) (Å)	2.020(4)	2.028(5)	1.993(6)
<Mn/Rh – O> (Å)	1.974(4)	1.972(8)	1.9723(2)
10^4 Δd	3.21	4.56	0.75
A – O_{ax} (Å)	2.4803(5)	2.4832(18)	2.406(6)
A – O_{ax} (Å)	2.647(4)	2.612(4)	2.618(4)
A – O_{eq} (x2) (Å)	2.462(4)	2.445(5)	2.457(6)
A – O_{eq} (x2) (Å)	2.721(4)	2.708(5)	2.680(5)
A – O_{eq} (x2) (Å)	2.730(4)	2.719(5)	2.719(6)
<Sr/La –O> (Å)	2.651(4)	2.637(5)	2.627(6)
M – O_{eq} – M (°)	160.3(2)	159.0(3)	159.5(3)
M – O_{ax} – M (°)	162.42(3)	162.84(4)	158.6(4)
O_{eq} – O_{ax} – O_{eq}	164.41(3)	164.33(3)	162.51(3)

Table 6.6 Bond lengths and other selected refinement parameters

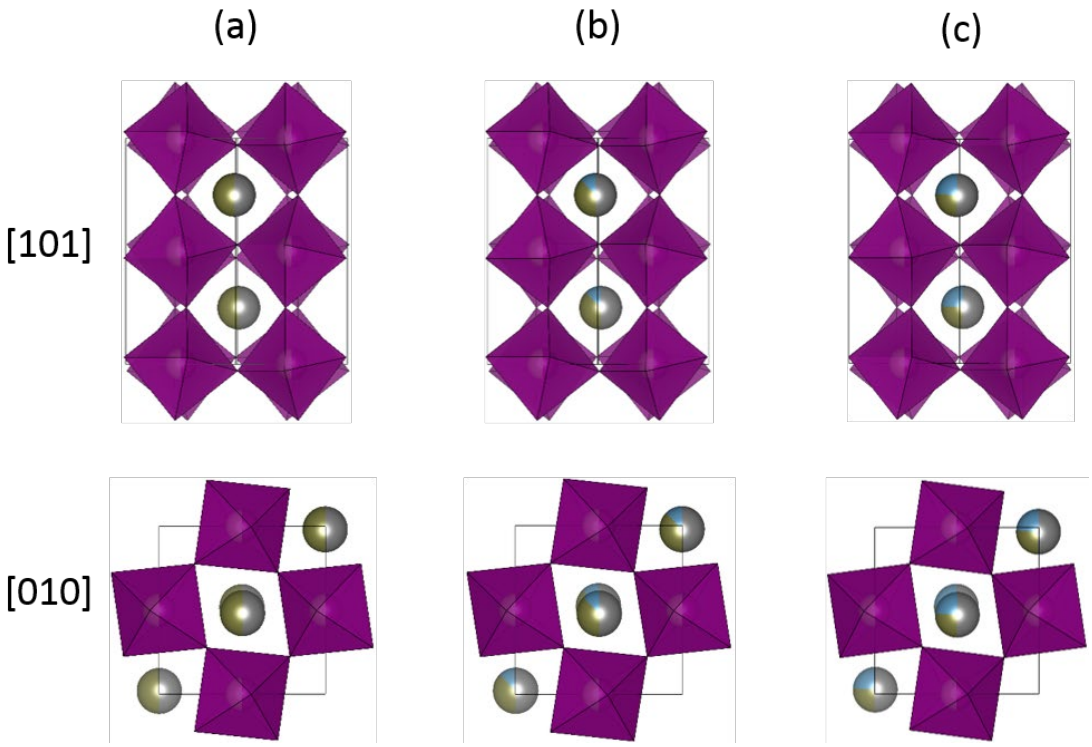


Figure 6.6 Crystal structures of the all $La_{0.5}Sr_{0.5-x}Ca_xMn_{0.5}Rh_{0.5}O_3$ where a) x = 0, b) x = 0.125, c) x = 0.25 in the *Pnma* space group showing views down the [101] and [010] directions highlighting the $a^-b^+c^-$ tilt system. Purple octachedra denote the Mn/Rh site and gray, yellow, blue spheres represent La, Sr, Ca-sites respectively

6.3.2 Magnetic Characterisation

Magnetisation data were collected from $La_{0.5}Sr_{0.5-x}Ca_xMn_{0.5}Rh_{0.5}O_3$ samples on a MPMS SQUID magnetometer in the temperature range 5 < T / K < 300 (Chapter 2, Section 2.11). Zero-field-cooled (ZFC) and field-cooled (FC) magnetisation data and magnetisation-field isotherms for all samples are given in Figure 6.7 and shown individually in Figure 6.8

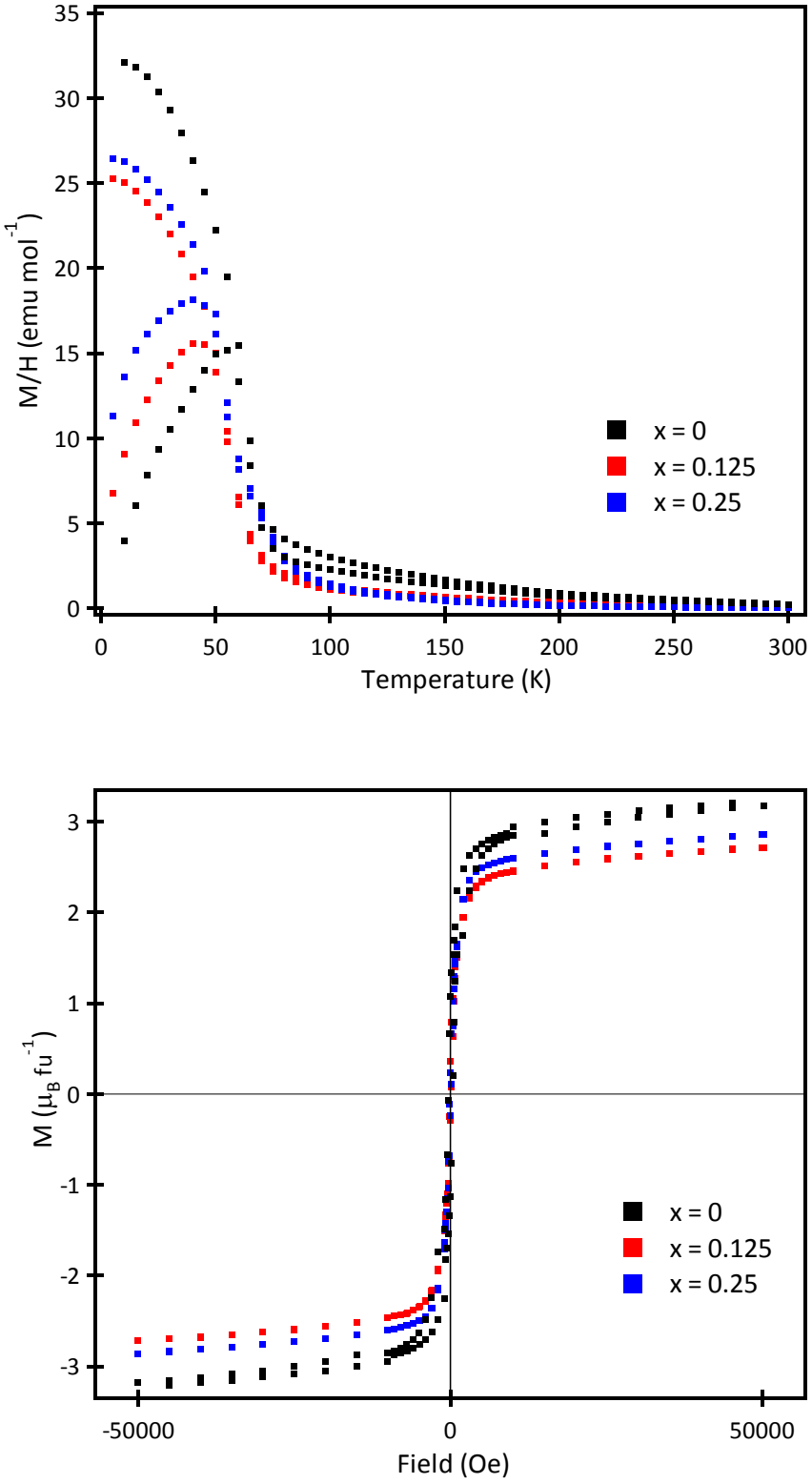


Figure 6.7 Top: Zero-field cooled and field cooled magnetisation data collected from $La_{0.5}Sr_{0.5-x}Ca_xMn_{0.5}Rh_{0.5}O_3$ in an applied field of 100 Oe. Bottom: Magnetisation-field isotherms collected from $La_{0.5}Sr_{0.5-x}Ca_xMn_{0.5}Rh_{0.5}O_3$ at 5 K.

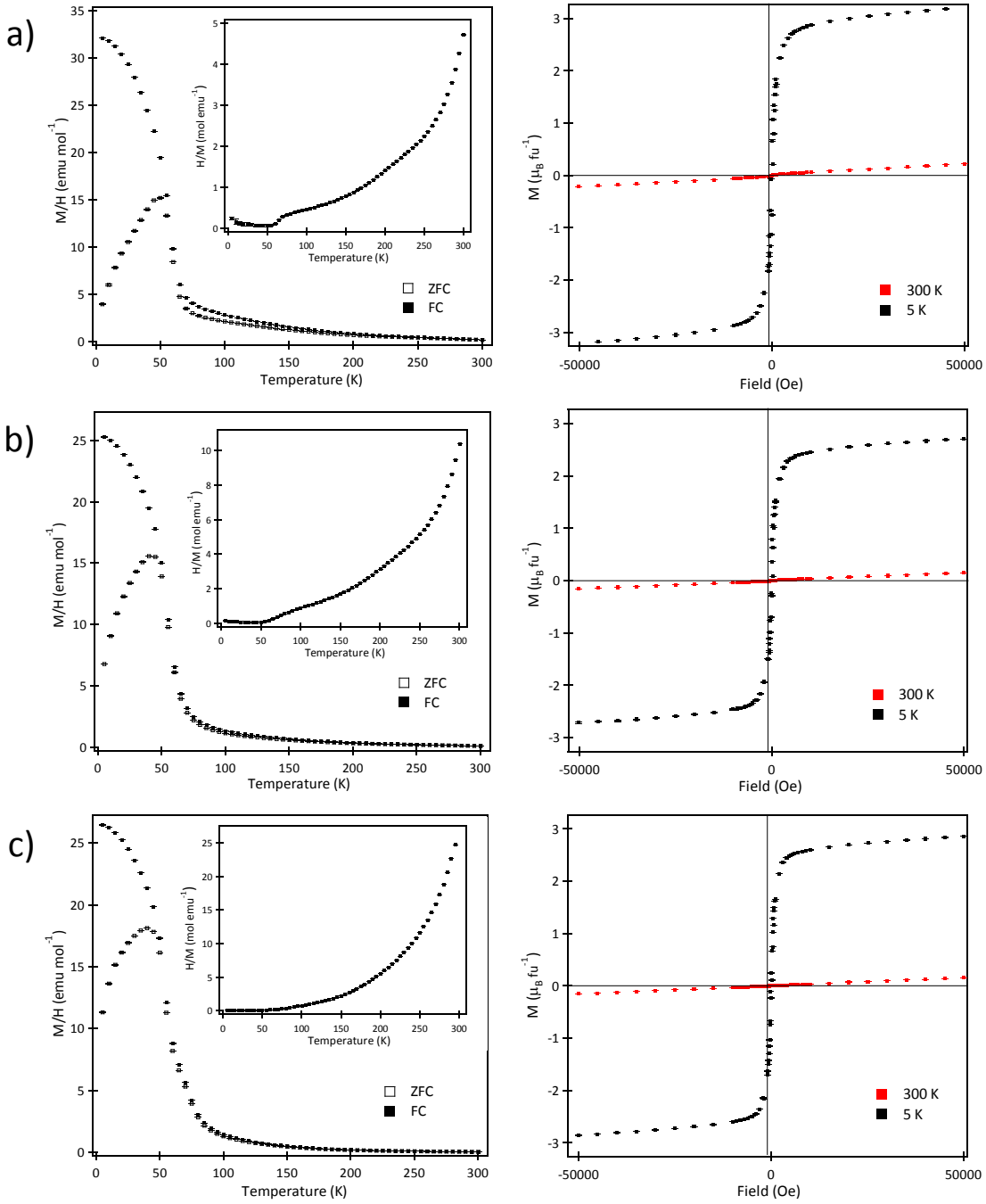


Figure 6.8 Individual ZFC and FC and magnetisation-field isotherms collected from a) $La_{0.5}Sr_{0.5}Mn_{0.5}Rh_{0.5}O_3$, b) $La_{0.5}Sr_{0.375}Ca_{0.125}Mn_{0.5}Rh_{0.5}O_3$ c) $La_{0.5}Sr_{0.25}Ca_{0.25}Mn_{0.5}Rh_{0.5}O_3$ at 5 K. Insets show inverse magnetisation plots.

The magnetic susceptibility data could not be fitted to the Curie-Weiss law over any significant temperature range and Figure 6.8 insets show how inverse magnetisation plots show non-linear behaviour at all temperatures. A straight line fit to the most linear section at 250 < T / K < 290 gives unrealistic Curie constant and Weiss constant values. Below T ≈

50 - 55 K, the ZFC and FC curves for all samples diverge, signalling a transition to a ferromagnetically ordered state. Magnetisation-field isotherms collected at 300 K show linear behaviour at all temperatures for all samples. Magnetisation-field isotherms for all samples collected at 5 K show a saturated ferromagnetic behaviour with moments in the range of $\mu \approx 2.9 - 3.2\ \mu_B$ per formula unit.

6.3.3 Conductivity Measurements

Conductivity data (Chapter 2, Section 2.13) were collected from $La_{0.5}Sr_{0.5-x}Ca_xMn_{0.5}Rh_{0.5}O_3$ samples using a voltammeter and a cryostat installed in the laboratory. The results are presented in terms of absolute conductivity across a ~13 mm bar of material. All samples show semiconducting behaviour and no anomalies were observed in the temperature range studied that would indicate a presence of electronically driven phase transitions. The resistance of all samples increased with decreasing temperature until the voltammeter was unable to record a value. A minimal current was used to reach temperatures down to 10 K but no anomalies in the transport behaviour were observed. The specific conductivity is relatively low ($\sigma_{300} = 0.05 - 0.6$ S). Figure 6.9 shows a sample conductivity data set for $La_{0.5}Sr_{0.5}Mn_{0.5}Rh_{0.5}O_3$.

The electric transport data collected from all samples were fitted using three possible disordered conduction mechanisms as described in Chapter 2 Section 1.3.3. The temperature dependence of the conductivity is inconsistent with Arrhenius semiconductor ($\log(\sigma)/T^{-1}$) and hopping polaron models ($\log(\sigma/T)/T^{-1}$). However, transport measurements were linearized when fit to the Mott's Variable Range Hopping conduction model. Figure 6.10 shows the linear dependence of log (σ) with regards to the three-dimensional temperature parameter $T^{-1/4}$.

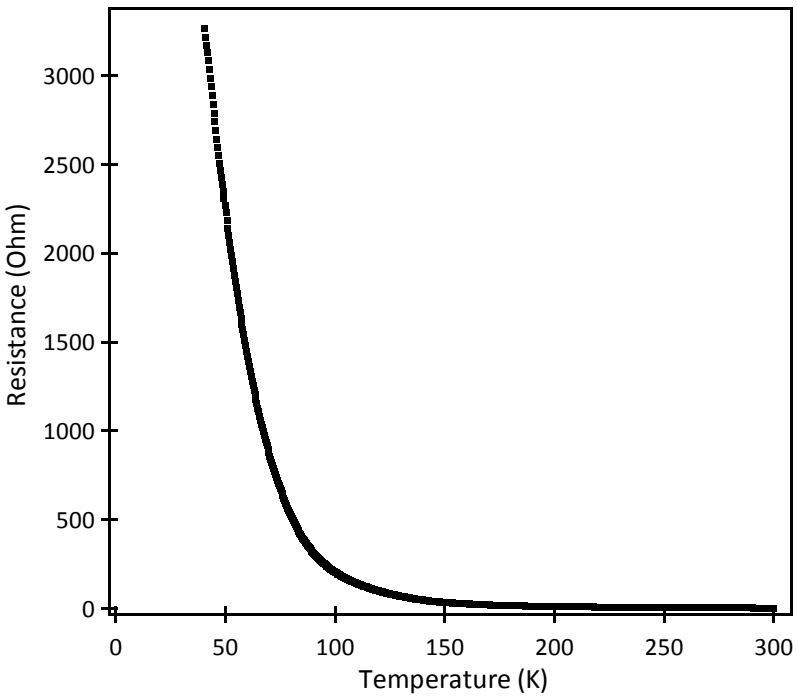


Figure 6.9 Resistance against temperature data collected from $La_{0.5}Sr_{0.5}Mn_{0.5}Rh_{0.5}O_3$ in the 40 < T / K < 300 range

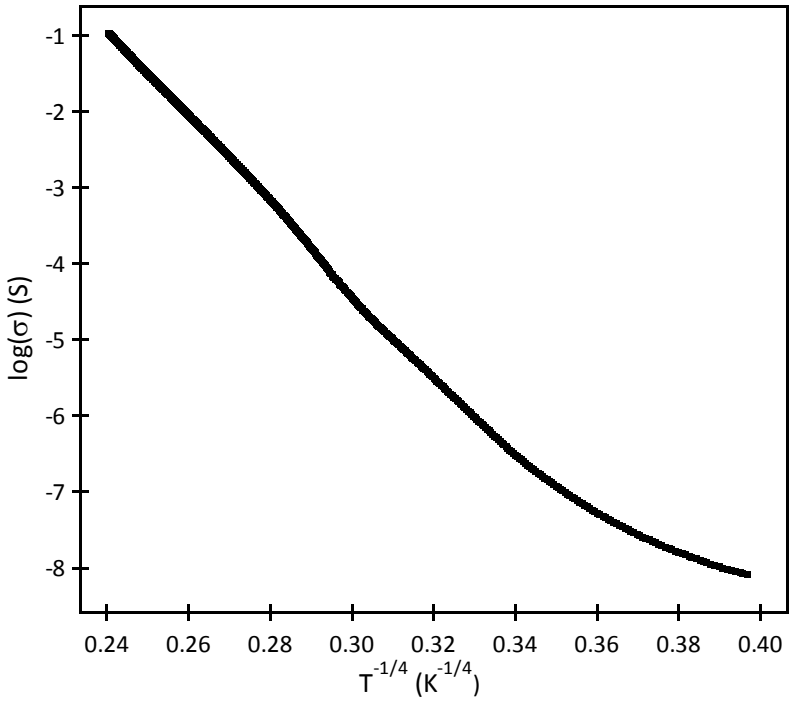


Figure 6.10 Conductivity (σ) as a function of temperature for $La_{0.5}Sr_{0.5}Mn_{0.5}Rh_{0.5}O_3$ in coordinates that linearize the Mott Variable Range Hopping model in three dimensions

6.4 Discussion

6.4.1 Structural Characterisation

Refinements of synchrotron X-ray powder diffraction data collected from samples of $La_{0.5}Sr_{0.5-x}Ca_xMn_{0.5}Rh_{0.5}O_3$ (x = 0.125, 0.25) as described in Section 6.3.1.2 show that all materials adopt a cation disordered perovskite structure with a orthorhombic *Pnma* space group. Unit cell parameters of the samples show an expected contraction of the unit cell as Sr^{2+} is replaced by Ca^{2+} with lattice parameters of all samples given in Table 6.2. Rietveld refinement fitting statistics suggest excellent fits to the collected diffraction data. The materials are B-site cation disordered with a 1:1 ratio of Mn and Rh on the 6-coordinate sites and A-site disordered with statistical mixtures of La, Sr^{2+} and Ca^{2+} on the A-site for undoped and doped samples.

The structures of analogous compounds to $La_{0.5}Sr_{0.5}Mn_{0.5}Rh_{0.5}O_3$ have been a topic of some debate in literature. Notably, the similar phase $LaSrMnRuO_6$ has been interchangeably characterised using both structures by Bune *et al.* (*Imma*)[125] and Dass *et al.* (*Pnma*)[123]. The difference was the use of neutrons in the latter so *Pnma* is accepted as the correct structure of $LaSrMnRuO_6$. The orthorhombic *Imma* and *Pnma* structures differ only in the details of the octahedral tilting so it is unsurprising to find the goodness of fit parameters comparable as discussed in Section 6.3.1.1. In the current $La_{0.5}Sr_{0.5}Mn_{0.5}Rh_{0.5}O_3$ case, these two refinements were expected to be comparable but the use of the I11 beamline synchrotron is a marked improvement on laboratory diffraction data used by Bune.

Typically, as X-rays are scattered by electrons and thus are less sensitive to the positions of light atoms like oxygen, neutron diffraction data are often presented for determining

the subtly distorted structures of perovskites. However, as seen in Table 6.7, the oxide ions in $La_{0.5}Sr_{0.5}Mn_{0.5}Rh_{0.5}O_3$ make up a significant fraction of the total electrons in the system ($O^{(1)}$ = 9%, $O^{(2)}$ = 19%) allowing the structure to be determined by X-ray powder diffraction data alone.

Atom	Multiplicity	Electron count of ion	No. of electrons per site	% of total
La^{3+}	2	54	108	25%
Sr^{2+}	2	36	72	17%
Mn^{3+}	2	22	44	10%
Rh^{4+}	2	41	82	19%
$O_{ax}(1)^{2-}$	4	10	40	9%
$O_{eq}(2)^{2-}$	8	10	80	19%

Table 6.7 Relative electron count of the ions in $La_{0.5}Sr_{0.5}Mn_{0.5}Rh_{0.5}O_3$

The La/Sr and Mn/Rh sites have closely comparable contributions to the intensity and their positions are mostly fixed by symmetry. The oxygen atoms contribute ~30% of the intensity to the diffraction pattern with the equatorial O atoms contributing twice as much as the axial O atoms but the error bar on the axial O atoms is lower as it lies in special positions.

Overall, the structural differences between the doped and un-doped samples are minor. There is a decrease in volume as Sr^{2+} is replaced with Ca^{2+} and a minor shortening in bond lengths and bond angles as expected. Nevertheless, this highlights the need to verify the reliability of conclusions presented here with respect to minor octahedral distortions that define $La_{0.5}Sr_{0.5}Mn_{0.5}Rh_{0.5}O_3$ and the doped analogues.

6.4.2 Oxidation States

The reporting of the $La_{0.5}Sr_{0.5}Mn_{0.5}Rh_{0.5}O_3$ compounds builds on the extensive work done on mixed-metal manganates based on which some of the most interesting physical

properties like colossal magnetoresistance have been previously reported[25]. The ferromagnetic state in these manganese oxides has notably been a long-standing prototypical example of the double-exchange interaction[126]. Pioneering work by Zener[46] and Jonker[127] among others described how antiferromagnetic $LaMn^{3+}O_3$ can be hole doped by mixing with crystals like $SrMnO_3$ and $CaMnO_3$ to make a ferromagnetic metal. The exchange of the itinerant Mn^{3+} ($t_{2g}^3 e_g^1$) e_g-electron to a Mn^{4+} ($t_{2g}^3 e_g^0$) site via O^{2-} *p*-orbitals is a notable pathway for metallic ferromagnetism (Chapter 1, Section 1.5.2).

Previous work on Rh compounds is not as widely available but key contributions by Bakowski et al[128] and later Smith[112] and Hayward[23] make up a significant body of literature on mixed-metal Rh oxides. The key considerations in the study of Rh materials have been the stability of two different Rh electronic configurations. The diamagnetic Rh^{3+} ($t_{2g}^6 e_g^0$) is generally accepted as the more stable configuration for electronic reasons. By simple analysis, Rh^{4+} ($t_{2g}^5 e_g^0$) configuration can be considered less stable in comparison to the diamagnetic type. For example, Schinzer[129] argued this saying M^{2+}/Rh^{4+} is subject to many competing effects and is not *a priori* valid and Battle argued that Rh in $La_{1.5}Sr_{0.5}RhMnO_6$ is present solely as Rh^{3+} ($t_{2g}^6 e_g^0$).

It is reported herein that $La_{0.5}Sr_{0.5}Mn_{0.5}Rh_{0.5}O_3$ crystallises with a Mn^{3+}/Rh^{4+} valence combination and is ferromagnetic with a saturated moment of μ = 3.2 μ_B below T_c = 50 K. It will be argued in the discussion section below and in further two chapters that Rh^{4+} can be considered a stable configuration for Rh. The arguments are corroborated by observing structural, magnetic, and electric transport behaviours of the materials.

6.4.3 Unit-cell and Jahn-Teller Distortion

As described in Section 6.3.1.2, $La_{0.5}Sr_{0.5}Mn_{0.5}Rh_{0.5}O_3$ and its doped analogues show a degree of octahedral distortion. The BO_6 octahedra are irregular with a three pairs of *trans* bonds. This type of distortion is denoted as Q_2 and is a common observation in ternary perovskites like $LaMnO_3$ or $KCuF_3$[21] that contain Jahn-Teller active ions.

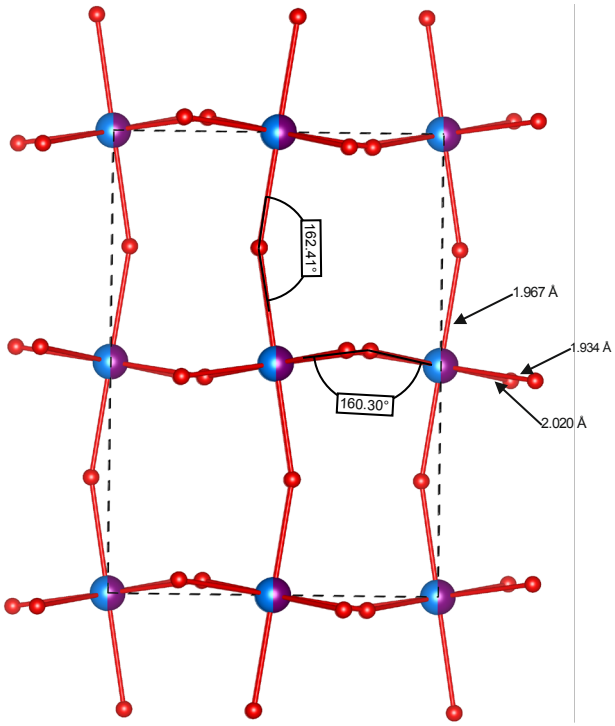


Figure 6.11 Selected bond angles and bond lengths for $La_{0.5}Sr_{0.5}Mn_{0.5}Rh_{0.5}O_3$

The observed BO_6 distortion of $La_{0.5}Sr_{0.5}Mn_{0.5}Rh_{0.5}O_3$ provides some support for the Mn^{3+}/Rh^{4+} oxidation state combination but the degree of the octahedral distortion in $La_{0.5}Sr_{0.5}Mn_{0.5}Rh_{0.5}O_3$ is considerably smaller than for the all Mn^{3+} phase, $LaMnO_3$. However, there have been cases of Mn^{3+} compounds with partial or complete suppression of the J-T distortion e.g. in $LaSrMnRuO_6$[122] or $LaSrMnSnO_6$[130]. Notable observation is made in the case A_2MnGaO_6 (A = La, Nd) where the Nd analogue shows significant J-T distortion as expected, but the distortion parameter Δd (Chapter 1, Section 1.6.3) is suppressed for $La_2Mn^{3+}GaO_6$. Therefore, a smaller octahedral distortion in $La_{0.5}Sr_{0.5}Mn_{0.5}Rh_{0.5}O_3$

compared to $LaMnO_3$ does not rule out the possibility of majority Mn^{3+}, but it does suggest that the degree of orbital ordering has been inhibited by the presence of Rh. It is also worth noting that Mn^{4+} ($t_{2g}^3 e_g^0$) does not undergo energy stabilisation via a Jahn-Teller distortion, and Rh^{4+} would also not undergo a strong Jahn-Teller distortion.

Table 6.8 list the Mn-O bond lengths from a range of reported Mn-containing perovskite oxides. The distortion parameter of $La_{0.5}Sr_{0.5}Mn_{0.5}Rh_{0.5}O_3$ is between $CaMn^{4+}O_3$ and $LaMn^{3+}O_3$. Other materials like $LaMnGaO_6$ and Nd_2MnGaO_6 show that the degree of J-T distortion for Mn^{3+} can depend on many factors and take a range of values. Whether the moderate degree of octahedral distortion observed in $La_{0.5}Sr_{0.5}Mn_{0.5}Rh_{0.5}O_3$ is strong evidence for presence of Mn^{3+} is unclear but it is certainly not compatible with the Mn^{4+} ($t_{2g}^3 e_g^0$) and Rh^{3+} ($t_{2g}^6 e_g^0$) oxidation state combination

Compound	**M–X (l)**	**M–X (m)**	**M–X (s)**	**10^4 Δd**
$CaMn^{4+}O_3$[21]	1.904	1.9	1.897	0.025
$LaMn^{3+}GaO_6$[22]	1.9898	1.982	1.978	0.06
$La_{0.5}Sr_{0.5}Mn_{0.5}Rh_{0.5}O_3$[15]	**2.02**	**1.96755**	**1.934**	**3.21**
$Nd_2Mn^{3+}GaO_6$[22]	2.101	1.9703	1.935	12.7
$LaMn^{3+}O_3$[20]	2.178	1.968	1.907	33
$La_2Mn^{3+}Rh^{3+}O_6$[23]	2.21	1.98	1.88	47

Table 6.8 Crystallographic information for a range of reported Mn-containing perovskite oxides.

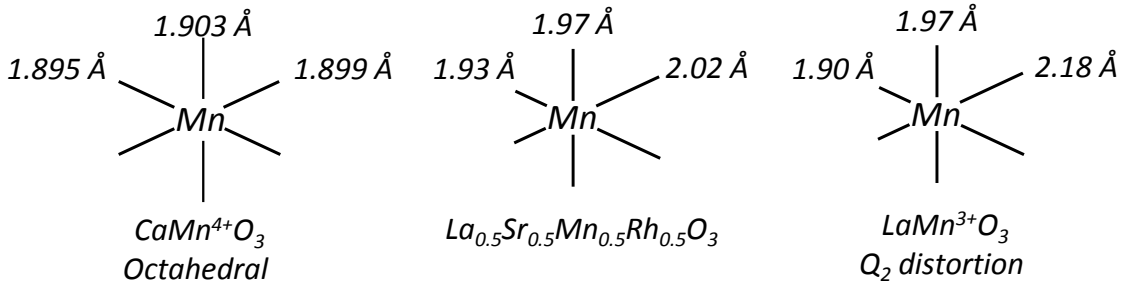


Figure 6.12 Schematics of octahedra for $CaMnO_3$, $La_{0.5}Sr_{0.5}Mn_{0.5}Rh_{0.5}O_3$ and $LaMnO_3$ highlighting the bonds lengths

6.4.4 Magnetic Characterisation

$La_{0.5}Sr_{0.5}Mn_{0.5}Rh_{0.5}O_3$ undergoes a transition to a ferromagnetic state below $T_C \approx 55$ K where a sharp drop is observed in the ZFC plot while the FC plot continues to increase. The magnetisation-field isotherm collected at 5 K shows a saturated ferromagnetic moment with a magnetic moment of 3.2 μ_B per formula unit. The magnetisation data do not follow the Curie-Weiss law over any temperature range as the inverse susceptibility data show large deviation from linearity. This indicates that above the transition temperature, the magnetism is dominated by complex magnetic interactions and $La_{0.5}Sr_{0.5}Mn_{0.5}Rh_{0.5}O_3$ is not a regular spin-only paramagnet.

Magnetic characterisation of Mn-containing perovskite oxides has often been made in light of colossal magnetoresistance exhibited by $La_{0.67}Ca_{0.33}MnO_3$ and similar materials (Chapter 2, Section 1.5.2). The key issue has always been to understand the complex magnetic interactions that describe the ground state, which in the case of CMR materials happens via Mn^{3+}/Mn^{4+} double exchange of an itinerant e_g electron. Conductivity measurement shown in Figure 6.10 indicate that $La_{0.5}Sr_{0.5}Mn_{0.5}Rh_{0.5}O_3$ is highly insulating over the whole temperature range measured. If double exchange was the source of the low-temperature ferromagnetic behaviour, there should be a corresponding insulator-

metal phase transition, which is not observed. Therefore the magnetic behaviour of $La_{0.5}Sr_{0.5}Mn_{0.5}Rh_{0.5}O_3$ needs to be explained on the basis of superexchange interactions.

Magnetisation-field isotherm collected at 5 K shows a saturated moment of 3.2 μ_B/f_u, which exceeds the maximum expected value for a Mn^{4+}/Rh^{3+} oxidation state combination. It is likewise difficult to devise a model for a ferromagnetic coupling in a Mn^{4+}/Rh^{3+} system. The Mn^{4+} ($t_{2g}^3 e_g^0$) electrons will not couple strongly to the fully occupied t_{2g} or empty e_g orbitals on diamagnetic Rh^{3+}. A minor π character interaction between full Rh and half-full Mn orbitals would be too small to account for the full ferromagnetic moment observed, as it would require a Mn-O-Rh-O-Mn coupling pathway. A Mn^{4+} - Mn^{4+} coupling mechanism would yield an antiferromagnetic ground state.

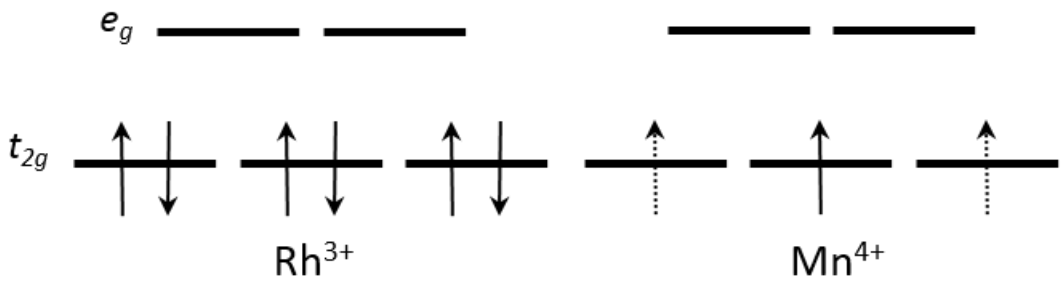


Figure 6.13 No allowed magnetic coupling mechanisms for Mn^{4+}/Rh^{3+} combination

In contrast it is possible to rationalise a ferromagnetic state from a Mn^{3+}/Rh^{4+} oxidation state combination. The Goodenough-Kanomori rules[131] can explain the ferromagnetic σ-superexchange between the half-filled Mn^{3+} e_g orbitals. Figure 6.14 shows an illustration of the allowed Goodenough-Kanomori type ferromagnetic superexchange pathway that can explain the ferromagnetism observed in $La_{0.5}Sr_{0.5}Mn_{0.5}Rh_{0.5}O_3$

Support for an Mn^{3+}/Rh^{4+} combination can further be found by observing that in $La_2Mn^{3+}Ga^{3+}O_6$, a disordered combination Mn^{3+} and diamagnetic Ga^{3+} is ferromagnetically

ordered[132], while Sr_2MnTiO_6, a disordered combination of Mn^{4+} and diamagnetic Ti^{4+} is not[133]. In fact, the magnetic behaviour of $La_{0.5}Sr_{0.5}Mn_{0.5}Rh_{0.5}O_3$ is qualitatively similar to $La_2Mn^{3+}Ga^{3+}O_6$ where a suppression of J-T is also observed possibly allowing magnetic coupling to take place between degenerate e_g Mn^{3+} half-filled orbitals.

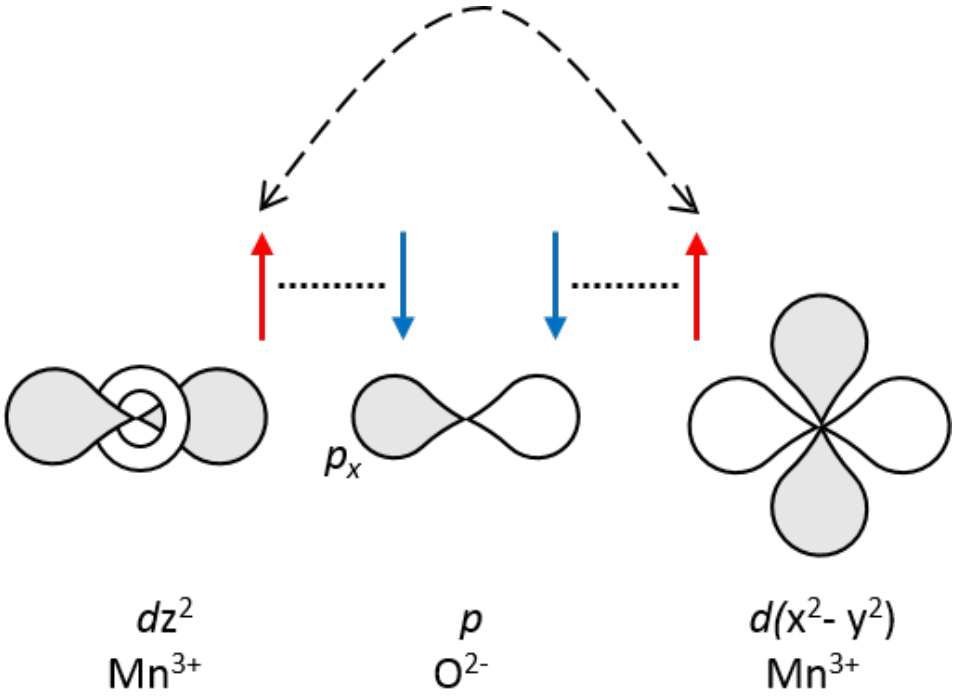


Figure 6.14 Ferromagnetic coupling mechanisms for Mn^{3+}/Rh^{4+} framework

A further possibility is a mixed-valent $Mn^{3+/4+}$ $Rh^{3+/4+}$ scenario, where double exchange between Mn^{3+} and Mn^{4+} would simply explain the observed ferromagnetic moment. Indeed the ferromagnetic order in $La_{1.5}Sr_{0.5}MnRhO_6$ has been explained on the basis of mixed valent $Mn^{3+/4+}$ centres[128]. However in such a scenario, as mentioned earlier metallic conductivity or at least a change in conductivity at the onset of magnetic order would be expected. As shown in Section 6.3.3 and described below, this behaviour is not observed in conductivity measurements.

6.4.5 Transport Properties

Conductivity measurements on the samples suggest the materials are Mott's Variable Range Hopping (VRH) semiconductors. This type of electronic behaviour is inherent for strongly disordered systems with localized charge-carrier states and no anomalies were observed that would suggest an electronically driven phase transition. The recorded room temperature conductivity indicates the materials are typical semiconductors even if the readings were not scaled for bar dimensions.

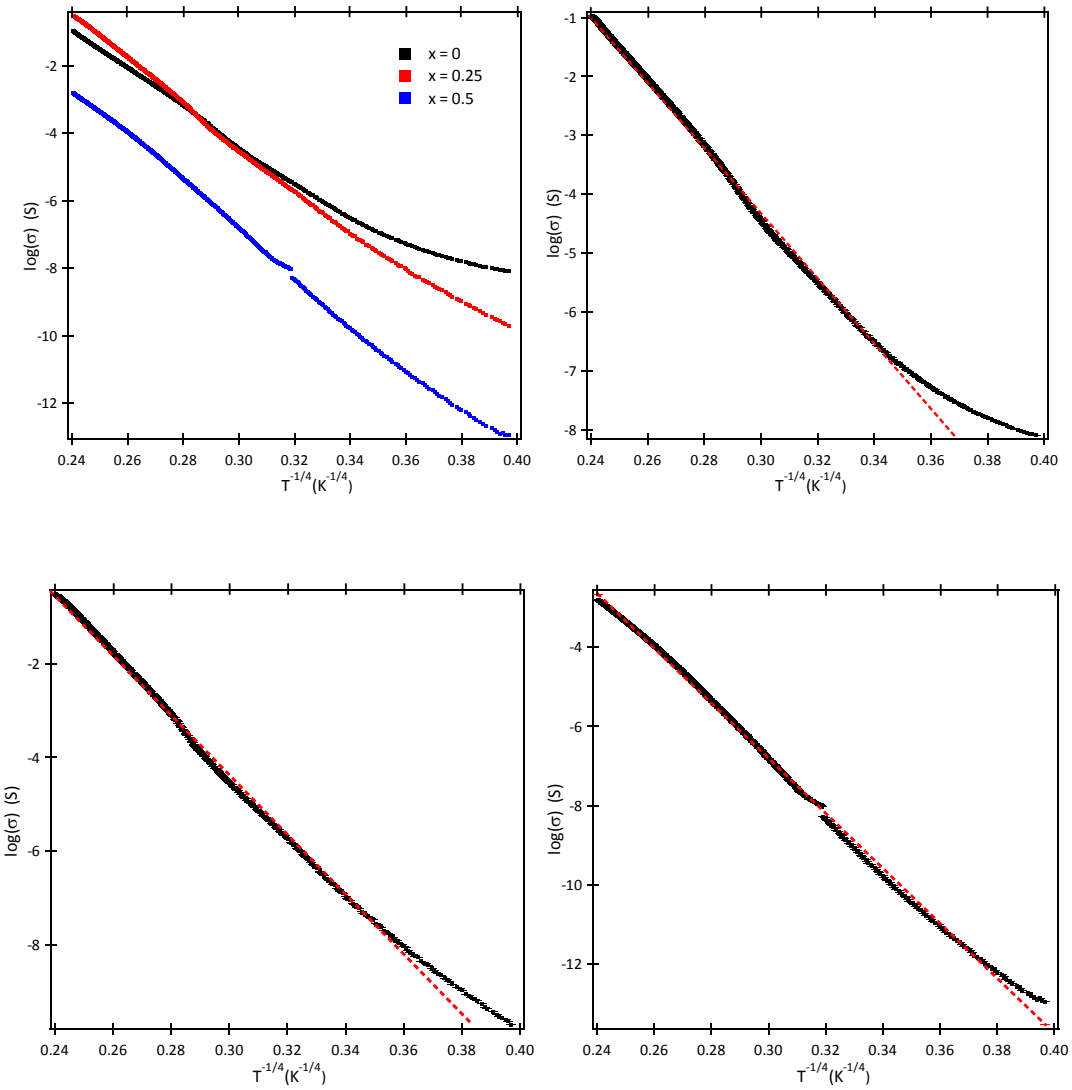


Figure 6.15 Electrical conductivity (σ) as a function of temperature for $La_{0.5}Sr_{0.5-x}Ca_xMn_{0.5}Rh_{0.5}O_3$ in coordinates that linearize the Mott's VRH model in three dimensions. a) combined, b) x = 0, c) x = 0.125, d) x = 0.25.

Figure 6.15 displays the conductivity data for all samples where the three dimensional conductance is displayed in a log $(\sigma)/T^{-1/4}$ plot. A straight line can be fitted to all the samples while a deviation is observed for the x = 0, 0.125 samples at low temperatures. The fits to other conduction mechanism do not show linearity.

A VRH conduction mechanism confirms the absence of any band formation in the material and imply that the hopping of charged electrons in random pathways results in an insulating behaviour. In contrast to the behaviour of $A_xA_{1-x}MnO_3$ perovskites, the onset of magnetic ordering is not accompanied by an abrupt change in electrical transport properties. A similar observation was made in the case of $LaSrMnRuO_6$, which qualitatively resembles $La_{0.5}Sr_{0.5}Mn_{0.5}Rh_{0.5}O_3$ in many ways. The lack of magnetically driven electronic transition can be taken as further evidence of a lack of Mn^{3+}/Mn^{4+} double exchange. It will also be important to follow up with magnetotransport measurements to measure the materials electronic response in a magnetic field.

6.4.6 Effects of A-site Doping

A-site doping $La_{0.5}Sr_{0.5}Mn_{0.5}Rh_{0.5}O_3$ is accompanied by minor structural distortions but no significant changes are observed in the magnetic or electric transport behaviour or these materials. A-site doping has been widely explored in an attempt to fine-tune desirable physical properties in functional materials. It has been repeatedly shown that varying the A-site cation composition or by applying external pressure, the magnetic and transport properties can be significantly varied in analogous compounds[24, 25, 134]. While a metal-insulator transition has previously been induced by decreasing the average A-site cation radius below a certain value, a metallic regime is not observed in any of the samples being

investigated in this study. Replacing Sr^{2+} with Ca^{2+} decreases the average bond length but $<r_A>$ does not reach the previously determined critical value of 1.18 Å.

The most relevant finding has been that hole doping of $La_{1-x}Ca'_xMnO_3$ and the average cation radius $<r_A>$ are the key variables that control the transition temperature. The random distribution of different A-site cations, size variance σ^2 across the cations, is an effective way of quantifying the various effects being imposed on the material. The variance can be calculated using the equation

$$\sigma^2 = \Sigma y_i r_i^2 - < r_A >^2$$

Where 'σ^2' is variance; 'y_i' is respective fractional occupancies ($\Sigma y_i = 1$); 'r_i' is ionic radii and '$<r_A>$' is mean ionic radii. The table below summarises the variance values and variation of cell parameters and key physical properties.

A-site	σ^2 / Å^2	*a* / Å	*b* / Å	*c* / Å	Vol / Å^3	$10^4 \Delta d$	T_C / K	E_A / meV
$La_{0.5}Sr_{0.5}$	0.00220	5.4832	7.7778	5.5367	236.13	3.21	55	0.86
$La_{0.5}Sr_{0.325}Ca_{0.125}$	0.00253	5.4793	7.7655	5.5170	234.75	4.56	52	1.29
$La_{0.5}Sr_{0.25}Ca_{0.25}$	0.00232	5.4777	7.7527	5.5013	233.62	0.75	50	1.87

Table 6.9 Variance, variation of cell parameters, volume, Curie temperature and activation energies

A-site Ca^{2+} doping of $La_{0.5}Sr_{0.5}Mn_{0.5}Rh_{0.5}O_3$ at 12.5% and 25% results in a compression of the cell but no major changes are observed across the set of parameters. The lattice parameters follow an expected pattern coincident with the inclusion of a smaller A-cation into the lattice. The most doped sample has the smallest unit cell volume and therefore the most compressed of the three. The variance increases from x = 0 to x = 0.125 and decreases to x = 0.25 given that Ca^{2+} ionic radius is very close to La. This does not have significant implications on the unit cell but helps describe the unusual pattern in the

octahedral distortion parameters. The distortion parameters given in Table 6.9 suggest the degree of J-T distortion increases from 0% Ca^{2+} to 12.5% Ca^{2+} but sharply decreases for 25% Ca^{2+} doped sample. This is in agreement with previous findings where Attfield *et al*[24] note that when mixtures of very large and very small cations are used, the strain field induced by the cation size disorder destabilizes the J-T distortions, effectively increasing the parameter $E_{J\text{-}T}$. At x = 0.25 the distribution of different A-site cations is at its highest and therefore it is unsurprising to see that the degree of J-T distortion would be suppressed as a result of this.

Table 6.9 also highlights the decrease of T_C and an increase in E_A as a result of Ca^{2+} doping. A relatively smaller M – O – M bond angle for x = 0.25 would effectively lead to minimisation of magnetic super-exchange lead to lowest T_C. Figure 6.16 highlights this by displaying the first derivative plots for all three samples clearly showing the small but evident change in T_c as a result of doping. The intermediate $La_{0.5}Sr_{0.375}Ca_{0.125}Mn_{0.5}Rh_{0.5}O_3$ has the most uneven transition indicative of a large variance in cation size with addition of Ca^{2+}.

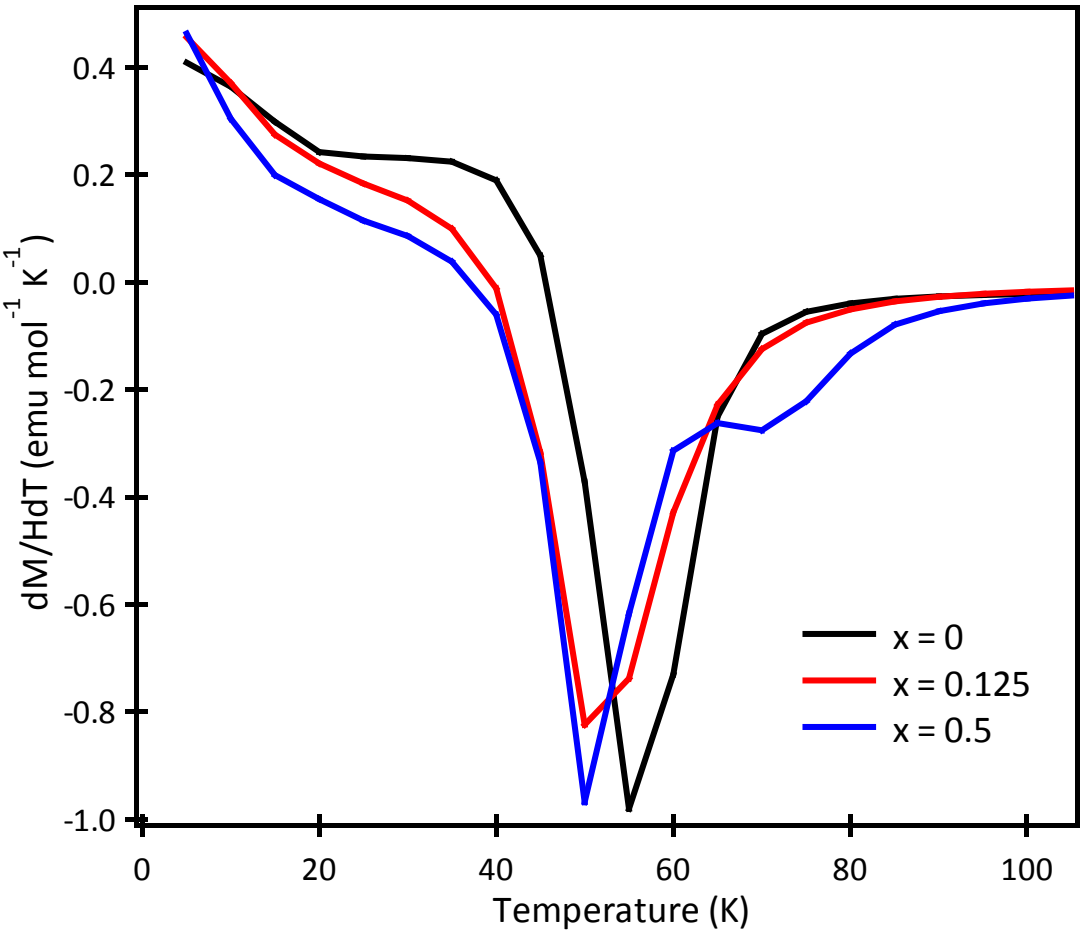


Figure 6.16 First derivative plots of susceptibility measurements for all three samples.

6.5 Conclusions

Cation disordered perovskites of composition $La_{0.5}Sr_{0.5-x}Ca_xMn_{0.5}Rh_{0.5}O_3$ (x = 0.125, 0.25) were prepared using a high-temperature ceramic synthesis method. X-ray powder diffraction data collected from the samples could be readily indexed using an orthorhombic unit cell with exclusion parameters most consistent with the *Pnma* space group. X-ray powder diffraction results confirmed stoichiometric La/Sr/Ca compositions on the A-site and a 1:1 ratio Mn/Rh on the B-site. Unit-cell parameters show a minor degree of cooperative Jahn-Teller distortion that falls between undistorted $CaMn^{4+}O_3$ and J-T distorted $LaMn^{3+}O_3$. All materials undergo a transition to a ferromagnetic state below

their T_C in the range of T ≈ 50 – 55 K and the magnetisation-field isotherms at 5 K show a saturated ferromagnetic state with a magnetic moment in the range of 2.8-3.2 μ_B/f_u. The magnetisation data do not follow the Curie-Weiss law indicative of strong and complex local magnetic interactions. It is proposed that the magnetic ordering arises via σ-superexchange coupling mechanism between Mn^{3+} half-filled e_g orbitals while Rh^{4+} electrons do not contribute to the magnetic moment. Electrical conductivity data show all materials are Mott's Variable Range Hopping semiconductors (insulators) and a transition to an electronically ordered state is not observed suggesting the absence of band formation. A-site doping with Ca^{2+} results in an expected compression of the cell, a bending of the bond-angles and a decrease in T_C as Sr^{2+} is replaced by Ca^{2+}. The most Ca^{2+} doped sample shows lower absolute conductivity, magnetic ordering temperature and the degree of Jahn-Teller distortion suggesting the presence of three different cations in the A-site affects the physical properties of the material.

Chapter 7 Oxygen Non-Stoichiometry in $La_{0.5}Sr_{1.5}Mn_{0.5}Rh_{0.5}O_4$

7.1 Introduction

The n = 1 Ruddlesden-Popper phase $La_{0.5}Sr_{1.5}Mn_{0.5}Rh_{0.5}O_4$ was investigated in detail to build on previous studies of manganese-rhodium oxides. The perovskite analogue $La_{0.5}Sr_{0.5}Mn_{0.5}Rh_{0.5}O_3$ (Chapter 6) shows ferromagnetic behaviour as a result of Mn^{3+} – Mn^{3+} superexchange coupling while the material is insulating. Recently Jin *et al* has reported a range of 4*d*/5*d* based oxyhydride phases made by topochemical reduction[23, 61] and the detailed analysis of $La_{0.5}Sr_{1.5}Mn_{0.5}Rh_{0.5}O_4$ herein is also intended to grow the list of parent phases available for topochemical reduction. This chapter describes three different samples of $La_{0.5}Sr_{1.5}Mn_{0.5}Rh_{0.5}O_4$ encountered in this work that show different levels of oxygen stoichiometry.

7.2 Synthesis

Samples A and B of $La_{0.5}Sr_{1.5}Mn_{0.5}Rh_{0.5}O_4$ were prepared via a high-temperature ceramic synthesis method. Suitable stoichiometric ratios of La_2O_3 (99.999%, dried at 900 °C), $SrCO_3$ (99.994%), Rh_2O_3 (99.99%, dried at 800 °C) and MnO_2 (99.997%) were finely ground together using an agate mortar and pestle and transferred into alumina crucibles. The mixtures were heated at a rate of 5 °C min^{-1} to 1000 °C to decompose the carbonates. The resulting powders were reground and pressed into pellets. The pellets were heated in air at 1300 °C for 3 periods of 48 hours with intermediate grinding. The reaction progress was monitored using laboratory X-ray diffractometers. Sample A was characterised using X-ray and neutron diffraction methods and Sample B was characterised using synchrotron X-ray powder diffraction.

Sample C was prepared by pressing a 13 mm pellet of Sample B and heating under O_2 flow at 1300 °C for 48 hours. The pellet was reground and characterised using synchrotron X-ray powder diffraction.

7.3 Structural Characterisation

'Sample A' of $La_{0.5}Sr_{1.5}Mn_{0.5}Rh_{0.5}O_4$ was made in air and the structure could be indexed using a single phase *I*4*/mmm* space group model. Magnetic susceptibility data collected from Sample A (Section 7.4.1) showed a magnetic event characterised by a sharp change in the inverse magnetisation slope at the high temperature range. Later, 'Sample B' was made under identical synthetic conditions to make a better sample. Magnetisation plots of Sample B showed a similar magnetic event but the overall magnetic behaviour was different. Furthermore, X-ray powder diffraction data collected from both samples showed inconsistencies with single phase *I*4*/mmm* models upon closer inspection. To test for oxygen deficiency, a portion of Sample B was heated in O_2 to make 'Sample C'. Sample C was identified as single-phase and stoichiometric $La_{0.5}Sr_{1.5}Mn_{0.5}Rh_{0.5}O_4$ revealing oxygen non-stoichiometry in Sample A and B. An overview of structural differences between samples are given below in Table 7.1.

$La_{0.5}Sr_{1.5}Mn_{0.5}Rh_{0.5}O_4$ Samples	**Conditions**
Sample A	48 hours at 1300 °C in air (x3)
Sample B	48 hours at 1300 °C in air (x3)
Sample C	48 hours at 1300 °C under O_2 flow (x1)

Table 7.1 Synthesis conditions for the samples discussed in this chapter

7.3.1 Synchrotron X-ray Powder Diffraction of Sample A

Sample A of $La_{0.5}Sr_{1.5}Mn_{0.5}Rh_{0.5}O_4$ was made in air over three heating cycles. Laboratory X-ray powder diffraction data suggested a majority phase n = 1 Ruddlesden-Popper phase with disordered Mn/Rh on the B-site. Synchrotron X-ray powder diffraction data (Chapter 2, Section 2.5.3) collected from Sample A could be indexed using a body centred tetragonal unit cell (a = 3.87439(6) Å, c = 12.4868(2) Å) consistent with a cation disordered, n = 1 Ruddlesden-Popper phase. A structural model was built on the basis of the reported structure of $LaSr_3NiRuO_8$[94]. The observed, calculated, and difference plots for the *I4/mmm* refinement are shown in Figure 7.1. Upon closer analysis an uncharacteristic peak broadening was observed. The model based on the *I4/mmm* space group could not account for the peak broadening and asymmetry despite the refinement of large number of variables.

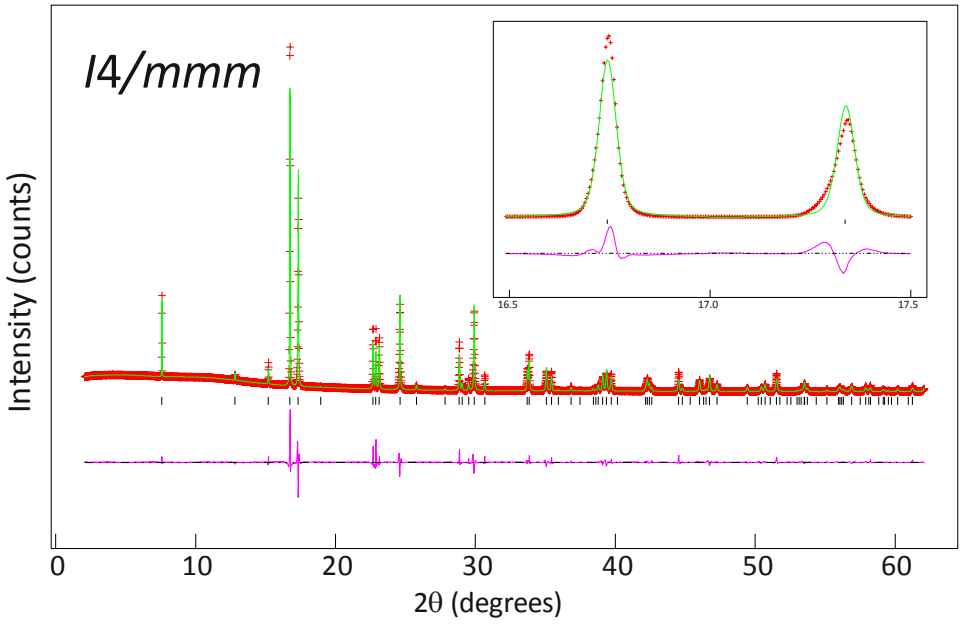


Figure 7.1 Observed, calculated, and difference plots from the refinement of *I4/mmm* structural model against synchrotron X-ray powder diffraction data collected from Sample A. (λ = 0.82595(1) Å)

7.3.2 Synchrotron X-ray Powder Diffraction of Sample B

Sample B was synthesised under identical synthetic conditions to Sample A in an attempt to make a better sample of $La_{0.5}Sr_{1.5}Mn_{0.5}Rh_{0.5}O_4$. Synchrotron X-ray powder diffraction data (Chapter 2, Section 2.5.3) collected from Sample B could be indexed using a body centred tetragonal unit cell (a = 3.87270(1) Å, c = 12.48162(8) Å) consistent with a cation disordered, n = 1 Ruddlesden-Popper phase. The observed, calculated, and difference plots for the *I*4*/mmm* refinement are shown in Figure 7.2. Sample B displayed similar peak characteristics as Sample A but subtly different magnetic behaviour. Figure 7.1 and Figure 7.2 insets highlight the characteristic Ruddlesden-Popper peaks that show significant asymmetricity and broadening. Elsewhere in the diffraction pattern many observed peaks are systematically poorly fitted. One hypothesis was that synthesis in air results in poor metal mixing resulting in Mn and Rh rich phases which could have significant implications for the structures of the topochemically reduced analogues of this material. An alternative reason is inhomogeneous oxygen stoichiometry, so a portion of Sample B was heated under flowing O_2 to make Sample C.

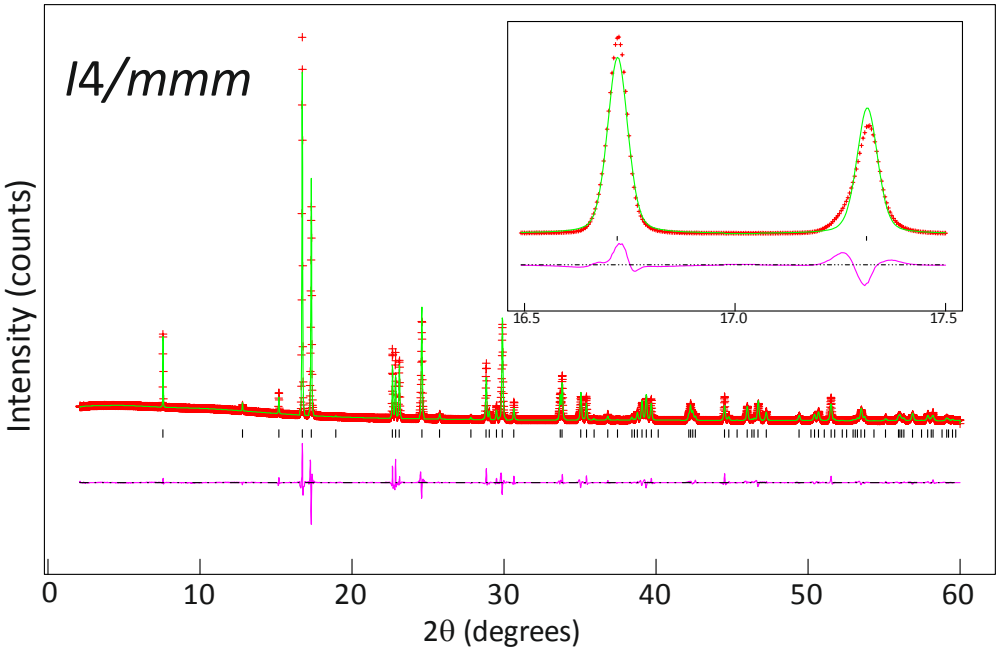


Figure 7.2 Observed, calculated, and difference plots from the refinement of *I4/mmm* structural model against synchrotron X-ray powder diffraction data collected from Sample B. (λ = 0.82595(1) Å)

7.3.3 Synchrotron X-ray Powder Diffraction of Sample C

A single-phase refinement against an *I4/mmm* space group based model gives a significantly improved fit to the diffraction data collected from Sample C. A two-phase refinement gives a negligible scaling factor for a minority phase and there was no evidence of oxygen non-stoichiometry. Synchrotron X-ray powder diffraction data (Chapter 2, Section 2.5.3) collected from Sample C could be indexed using a body-centred tetragonal unit cell (a = 3.872250(1) Å, c = 12.47664(4) Å) consistent with a cation disordered, n = 1 Ruddlesden-Popper phase with the tetragonal *I4/mmm* space group. A model was constructed based on the reported structure of $LaSr_3NiRuO_8$[61]. The model converged to an excellent statistical fit with fitting parameters χ^2 = 8.412, *wRp* = 2.08%, *Rp* = 1.14%. The refined structure given below is considered to be an accurate description of a stoichiometric $La_{0.5}Sr_{1.5}Mn_{0.5}Rh_{0.5}O_4$. The observed, calculated, and difference plots for

the *I4/mmm* refinement are shown in Figure 7.3. Full details of structural refinement parameters are given in Table 7.2 and Table 7.3.

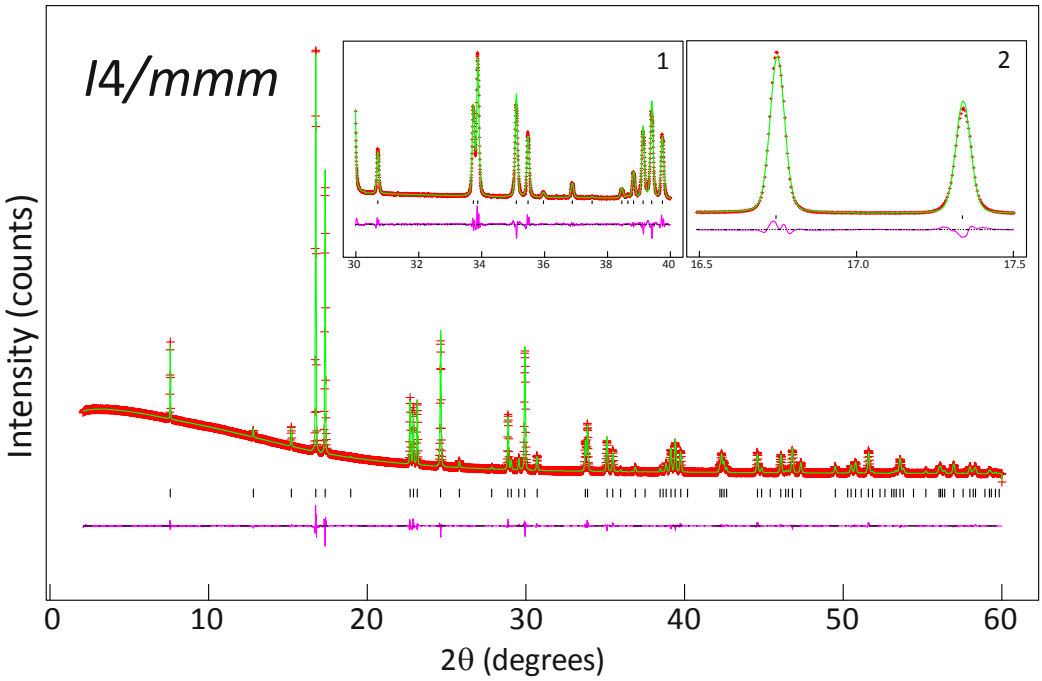


Figure 7.3 Observed, calculated, and difference plots from the refinement of single phase *I4/mmm* structural model against synchrotron X-ray powder diffraction data collected from Sample C. Insets show alternate angle ranges

Atom	***x***	***y***	***z***	**Fraction**	**U_{iso} (Å^2)**
La/Sr	0	0	0.3580(2)	0.25/0.75	0.00365(8)
Mn/Rh	0	0	0	0.5/0.5	0.00142(1)
O(1)	0	0.5	0	1	0.00777(3)
O(2)	0	0	0.1627(1)	1	0.00777(3)
$La_{0.5}Sr_{1.5}Mn_{0.5}Rh_{0.5}O_4$ – Space group *I4/mmm* (#139) Formula mass = 343.81 g mol^{-1} *a* = 3.87250(1) Å, *c* = 12.47664(4) Å, Vol = 187.103(2) Å^3 Radiation source: Synchrotron X-ray, λ = 0.82595(1) Å χ^2 = 8.412, *wRp* = 2.08%, and *Rp* = 1.14%					

Table 7.2 Structural parameters from the refinement of Sample C, $La_{0.5}Sr_{1.5}Mn_{0.5}Rh_{0.5}O_4$

Parameter	Length (Å)
Mn/Rh – O_{eq} (x4) (Å)	1.936(3)
Mn/Rh – O_{ax} (x2) (Å)	2.030(2)
<Mn/Rh – O> (Å)	1.938(5)
La/Sr – O(1) (x4) (Å)	2.6244(2)
La/Sr – O(2) (x4) (Å)	2.7505(2)
La/Sr – O(2) (x1) (Å)	2.436(1)
<La/Sr – O> (Å)	2.6595(5)

Table 7.3 Selected structural parameters from the refined structure of $La_{0.5}Sr_{1.5}Mn_{0.5}Rh_{0.5}O_4$

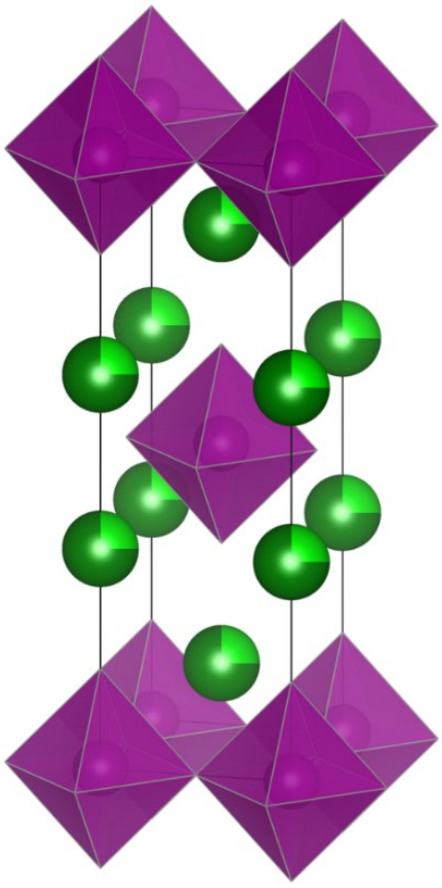


Figure 7.4 Illustration of the refined structure of $La_{0.5}Sr_{1.5}Mn_{0.5}Rh_{0.5}O_4$.

7.3.4 Structural Characterisation of Sample B

If Sample C is taken to be stoichiometric $La_{0.5}Sr_{1.5}Mn_{0.5}Rh_{0.5}O_4$, Samples A and B were considered to be oxygen non-stoichiometric and oxygen deficiency was assumed to be

the cause of poor refinement fits described in Sections 7.3.1 and 7.3.2. Two outcomes of oxygen non-stoichiometry were investigated: a cooperative octahedral distortion and a two-phase disproportionation.

Table 7.4 gives a list of allowed orthorhombic distortions of the n = 1 Ruddlesden-Popper structure. These models were refined against synchotron X-ray powder diffraction data collected from Sample B and the fitting statistics for each refinement are given in Table 7.4. The fitting statistics of the refinement against the undistorted model, *I4/mmm*, are significantly worse (20%) than the best distorted model, *Pmab*. However the peak shape fitting was not found to be satisfactory. Close inspection off all refinements showed poor peak fitting across the diffraction patterns and the fitting statistics were too poor.

Twist	Space group	χ^2	wRp (%)	Rp (%)	Ref
ΦΦ0/ΦΦ0	***Pmab* (#57)**	**102.6**	**7.95**	**4.46**	[135]
ΦΦ0/ ΦΦ0	*Bmab* (#64)	102.8	7.96	4.42	[136]
ΦΦΦ/ΦΦΦ	*Pbca* (#61)	102.7	7.96	4.42	[137]
Φ00/0Φ0	*Pccn* (#56)	103.2	7.97	4.45	[138]
ΦΦ0/ΦΦ0	*Pmcb* (#55)	116.5	8.47	4.72	[139]
000/000	***I4/mmm* (#139)**	**129.2**	**8.92**	**4.94**	[140]
Φ00/0Φ0	$P4_2/ncm$ (#138)	129.6	8.94	4.98	[141]

Table 7.4 Fitting statistics of refinements of distorted models against X-ray powder diffraction data from Sample B

To test for a two-phase split, the diffraction data collected from Sample B was concurrently refined using a two-phase model where two identical unit-cells of $La_{0.5}Sr_{1.5}Mn_{0.5}Rh_{0.5}O_4$ were allowed to freely refine with damped lattice and scaling parameters. Profile factors and atomic parameters were fixed to be equal.

Figure 7.5 and Figure 7.6 show the refinement plots for the distorted model with best fitting statistics and the two-phase refinement respectively. Table 7.5 shows the fitting statistics for both refinements.

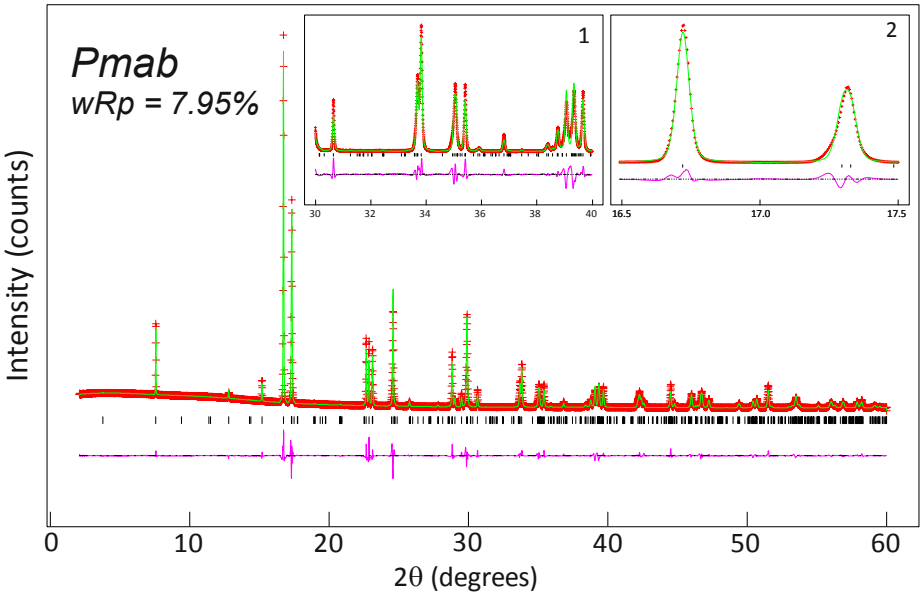


Figure 7.5 Observed, calculated, and difference plots from the refinement of single phase *Pmab* structural model against synchrotron X-ray powder diffraction data collected from Sample B. (λ = 0.82595(1) Å)

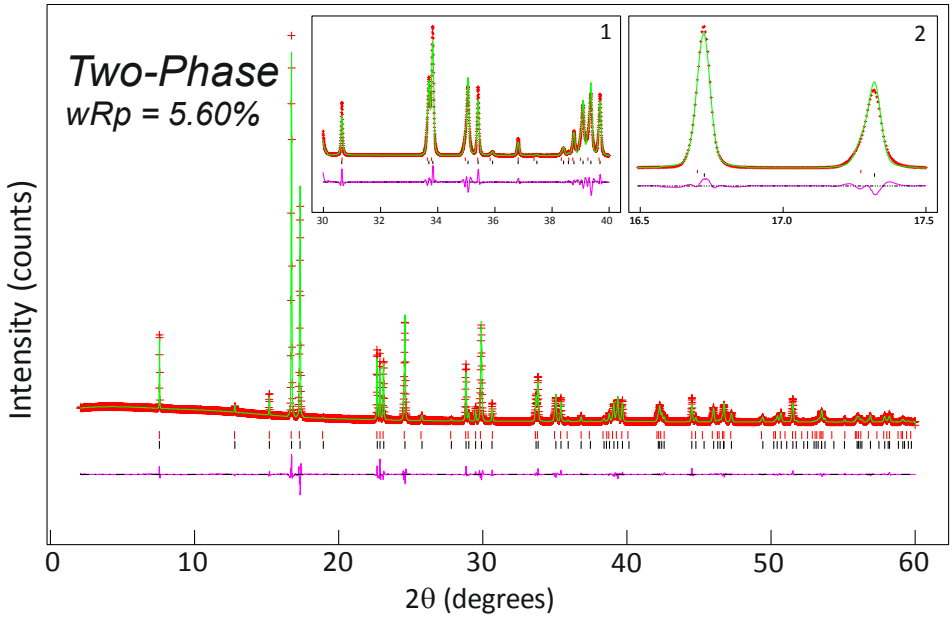


Figure 7.6 Observed, calculated, and difference plots from the refinement of two-phase I4/*mmm* structural model against synchrotron X-ray powder diffraction data collected from Sample B (λ = 0.82595(1) Å). Black tick marks – majority phase; red tick marks – minority phase

Refinement	Space group	χ^2	wRp (%)	Rp (%)
Distorted	*Pmab* (#57)	102.6	7.95	4.46
Two-Phase	*I4/mmm* (#139) (x2)	50.94	5.60	3.21

Table 7.5 Fitting statistics of *Pmab* and two-phase *I4/mmm* refinements

The two refinements provide convincing evidence for a two-phase model rather than a single distorted phase. Full details of structural refinement parameters of Sample B of $La_{0.5}Sr_{1.5}Mn_{0.5}Rh_{0.5}O_4$ are given in Table 7.6. The phase fraction parameters indicate only ~20% of the Sample B is the second phase. The fractional occupancies of O atoms were constrained to full occupancy as X-ray powder diffraction is generally not good at detecting individual O atomic positions accurately unless the relative contribution of oxide ions to the diffraction pattern is high. A two-phase refinement against synchrotron X-ray and neutron diffraction data collected from Sample A confirmed this.

Atom	*x*	*y*	*z*	Fraction	U_{iso} (Å^2)
La/Sr	0	0	0.35808(2)	0.25/0.75	0.00421(3)
Mn/Rh	0	0	0	0.5/0.5	0.00034(1)
O(1)	0	0.5	0	1	0.0081(3)
O(2)	0	0	0.1627(1)	1	0.0120(3)
$La_{0.5}Sr_{1.5}Mn_{0.5}Rh_{0.5}O_4$ – Space group *I4/mmm* (#139) *a* = 3.87719(1) Å, *c* = 12.49996(8) Å, Vol = 187.908(2) Å^3 Phase fraction = 79.57(3) weight %					
Atom	***x***	***y***	***z***	**Fraction**	**U_{iso} (Å^2)**
La/Sr	0	0	0.35808(2)	0.25/0.75	0.00421(3)
Mn/Rh	0	0	0	0.5/0.5	0.00034(1)
O(1)	0	0.5	0	1	0.0081(3)
O(2)	0	0	0.1627(1)	1	0.0120(3)
$La_{0.5}Sr_{1.5}Mn_{0.5}Rh_{0.5}O_4$ – Space group *I4/mmm* (#139) *a* = 3.88765(4) Å, *c* = 12.4956(4) Å, Vol = 188.858(5) Å^3 Phase fraction = 20.4(1) weight %					
Radiation source: Synchrotron X-ray, λ = 0.82595(1) Å χ^2 = 50.94, *wRp* = 5.60%, and *Rp* = 3.21%					

Table 7.6 Parameters from the two-phase refinement of Sample B, $La_{0.5}Sr_{1.5}Mn_{0.5}Rh_{0.5}O_4$ against synchrotron X-ray powder diffraction data

7.3.5 Structural Characterisation of Sample A

Synchrotron X-ray powder diffraction data collected from Sample A was refined against the two-phase model extracted from the refinement of diffraction data collected from Sample B as described in Section 7.3.4. The refinement fitting statistics extracted from single phase (described in Section 7.3.1) and two-phase models are given in Table 7.7. The two-phase model significantly improves the refinement statistics with a χ^2 = 20.82. Figure 7.7 shows the refinement plot for two-phase Sample A.

Model	χ^2	wRp (%)	Rp (%)
Single Phase Model	39.13	7.96	4.38
Two-Phase Model	20.82	5.74	3.42

Table 7.7 Fitting statistics for single phase and two-phase structural refinements against synchrotron X-ray powder diffraction data collected from Sample A

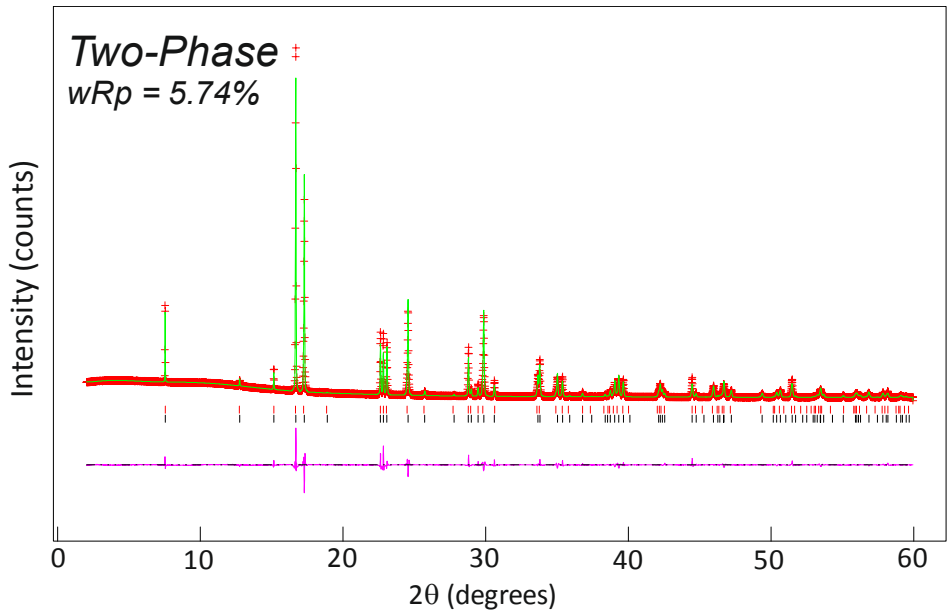


Figure 7.7 Observed, calculated, and difference plots from the refinement of two-phase *I4/mmm* structural model against synchrotron X-ray powder diffraction data collected from Sample A (λ = 0.82595(1) Å) .Black tick marks – majority phase; red tick marks – minority phase

Neutron powder diffraction data were collected from Sample A using the D2B diffractometer at the ILL neutron source (Chapter 1, Section 2.6.2) in Grenoble, France. Neutron powder diffraction data gives better indication of atomic positions so O fractional occupancies were refined**.** Table 7.8 shows the fitting statistics for both single and two-phase refinements where a ~10% improvement is seen in the two-phase regime. Nevertheless this improvement is not significant enough given the extra number of variables in the refinement but it is likely that neutrons would not be able to distinguish between the two regimes to a large confidence level. However taken together with synchrotron refinements, a 10% improvement can be considered to be significant enough to establish a difference between the two fits. Figure 7.8 shows the refinement plot for the two-phase refinement.

Model	χ^2	***wRp* (%)**	***Rp* (%)**
Single-Phase Model	2.065	3.37	2.62
Two-Phase Model	1.834	3.19	2.50

Table 7.8 Fitting statistics for single phase and two-phase structural refinements against neutron diffraction data collected from Sample A

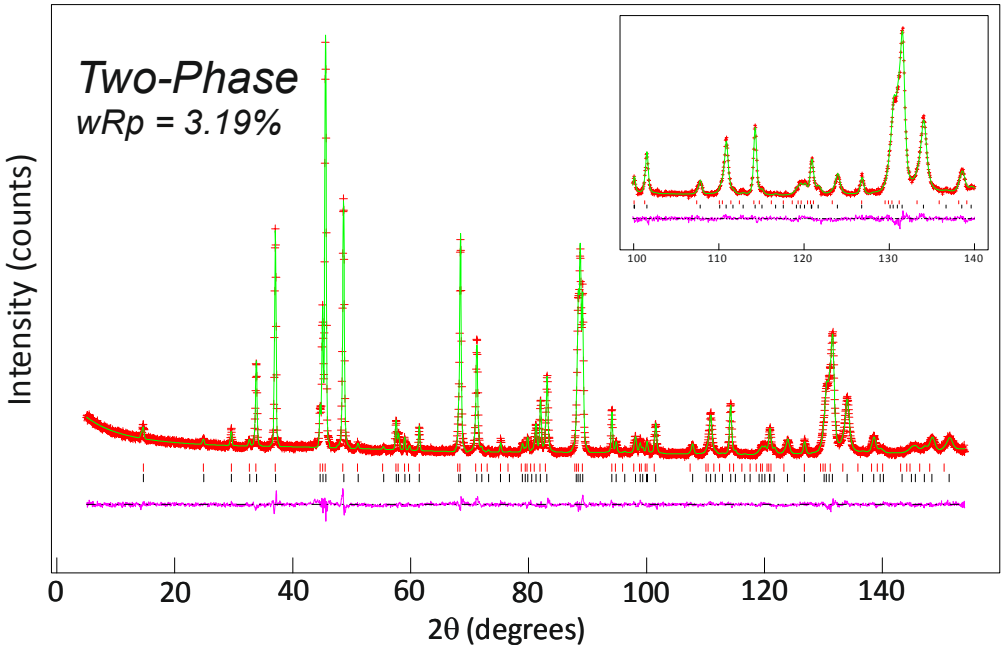


Figure 7.8 Observed, calculated, and difference plots from the refinement of two-phase *I4/mmm* structural model against neutron diffraction data collected from Sample A (λ = 1.59432(1) Å). Inset shows low angle reflections. Black tick marks – majority phase; red tick marks – minority phase

To test for oxygen non-stoichiometry, the fractional occupancy of each O site in both phases were allowed to refine with heavy damping. The equatorial O on the minority phase was the only site that converged to a non-uniform fractional occupancy of 0.88(3). Neutron powder diffraction data further corroborates the hypothesis that when synthesis of $La_{0.5}Sr_{1.5}Mn_{0.5}Rh_{0.5}O_4$ is performed in air, this results in inhomogeneous oxygen stoichiometry and an oxygen deficient phase.

Full details of structural refinement parameters of Sample A are given in Table 7.9. Given that Sample A and B displayed comparable features in the diffraction patterns, both were considered to have a two-phase split with oxygen vacancies on one site of the minority phase. These features are not seen in Sample C which is assumed to be stoichiometric.

Atom	*x*	*y*	*z*	Fraction	U_{iso} (Å^2)
La/Sr	0	0	0.35779(2)	0.25/0.75	0.00417(3)
Mn/Rh	0	0	0	0.5/0.5	0.0017(1)
O(1)	0	0.5	0	1	0.0086(3)
O(2)	0	0	0.16259(8)	1	0.0101(2)
$La_{0.5}Sr_{1.5}Mn_{0.5}Rh_{0.5}O_4$ – Space group *I4/mmm* (#139) *a* = 3.87362(8) Å, *c* = 12.4860(2) Å, Vol = 187.35(1) Å^3 Phase fraction = 88.3(9) weight %					
Atom	***x***	***y***	***z***	**Fraction**	**U_{iso} (Å^2)**
La/Sr	0	0	0.35779(2)	0.25/0.75	0.00417(3)
Mn/Rh	0	0	0	0.5/0.5	0.0017(1)
O(1)	0	0.5	0	0.85(3)	0.0101(3)
O(2)	0	0	0.16259(8)	1	0.017(2)
$La_{0.5}Sr_{1.5}Mn_{0.5}Rh_{0.5}O_4$ – Space group *I4/mmm* (#139) *a* = 3.8840(4) Å, *c* = 12.486(4) Å, Vol = 188.37(3) Å^3 Phase fraction = 11.5(8) weight %					
Radiation source: Fixed wavelength neutrons, λ = 1.59432(1) Å χ^2 = 1.834, *wRp* = 3.19%, and *Rp* = 2.50%					

Table 7.9 Parameters from a concurrent two-phase refinement of Sample C against synchrotron X-ray and neutron diffraction data

7.3.6 Thermogravimetric Analysis

Sample B and Sample C were heated under 5% H_2 gas to 1000 °C in a controlled reductive TGA measurement (Chapter 2, Section 2.4) on the Mettler Toledo TGA/DSC 1 STARe system. X-ray powder diffraction data were collected from the resulting powders and both products had decomposed to the subsequent oxides, La_2O_3, $SrCO_3$, MnO_x, and Rh metal. To allow for comparable analysis, the final product in both cases was assumed to be the same and used as the starting point in the mass-% change against temperature plot shown in Figure 7.9. Assuming that Sample C had the stoichiometric composition of $La_{0.5}Sr_{1.5}Mn_{0.5}Rh_{0.5}O_4$, the change in mass from decomposition to starting mass would be indicative of 'δ' in Sample B $La_{0.5}Sr_{1.5}Mn_{0.5}Rh_{0.5}O_{4-\delta}$.

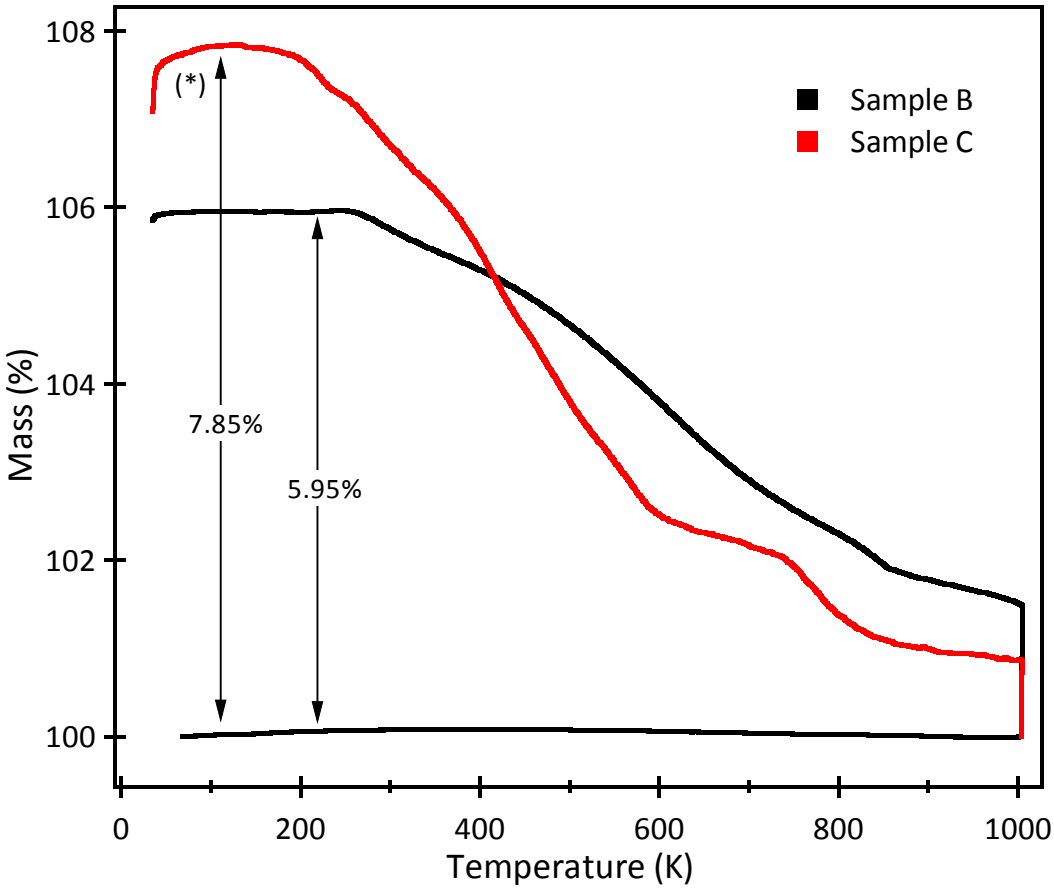


Figure 7.9 TGA plots for Sample B (black) and Sample C (red) heated under H_2 gas up to 1000 °C to decompose into constituent oxides. (*) buoyancy error as m < 10 mg mass used.

Assuming that Sample C has the stoichiometric composition $La_{0.5}Sr_{1.5}Mn_{0.5}Rh_{0.5}O_4$ with molar mass of 343.81 $gmol^{-1}$, a 7.85% reduction in mass indicates decomposition into constituent starting materials with a combined mass of 316.82 $gmol^{-1}$. The original composition of Sample B is calculated by adding back a 5.95% increase in mass to give a composition of $La_{0.5}Sr_{1.5}Mn_{0.5}Rh_{0.5}O_{3.50(5)}$. The key assumption made was that both samples decompose to the same starting materials with a varying MnO_x levels as it continues to reduce under H_2 gas. These results show that the two samples have different oxygen contents.

7.4 Magnetic Characterisation

Magnetisation data were collected from all three samples on an MPMS SQUID magnetometer in the temperature range 5 < T / K < 300 (Chapter 2, Section 2.11). Zero-field-cooled (ZFC) and field-cooled (FC) magnetisation data collected in an applied field of 100 Oe are shown in Figure 7.10. Inverse magnetisation plots are shown in Figure 7.11. Magnetisation-field isotherms collected are shown in Figure 7.12.

The ZFC – FC curves show standard temperature dependence of paramagnetic materials for Sample C and Sample B but a major deviation of ZFC and FC curves T ≈ 75 K is observed for Sample A. Next, inverse magnetisation plots are presented to show linear behaviour for Sample C in the 70 < T / K < 300 temperature range indicating Curie-Weiss type paramagnetism. Samples A and B show two change of slope events one at high temperature and one at low temperature ranges. Inverse magnetisation plots show attempted fits of all linear sections to the Curie-Weiss law. Finally, magnetisation-field isotherms are given showing no significant difference between the samples. The field-dependence of these materials at 5 K shows an unusual type of hysteresis that is difficult to characterise. It has been assumed that this is an instrumental error and that field dependence at 5 K is close to linear for all samples.

7.4.1 Magnetisation Plots

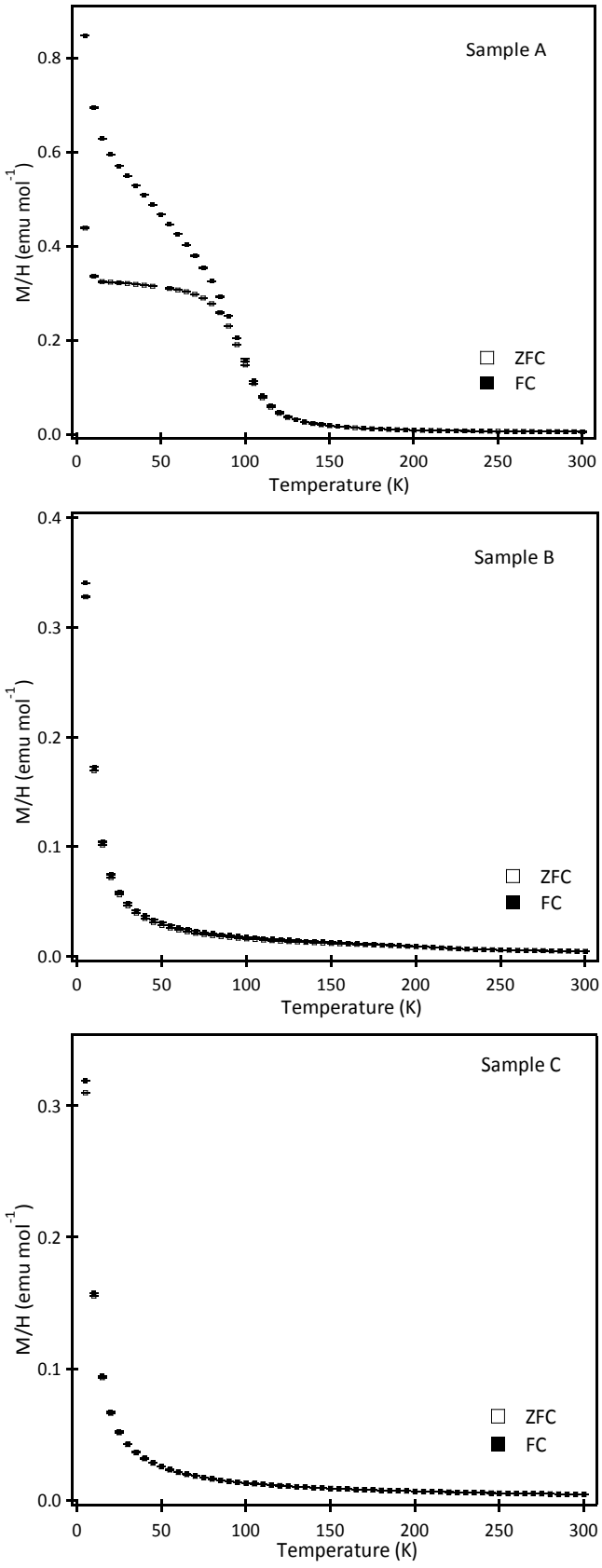


Figure 7.10 ZFC and FC magnetisation and magnetisation-field isotherms collected from all the samples

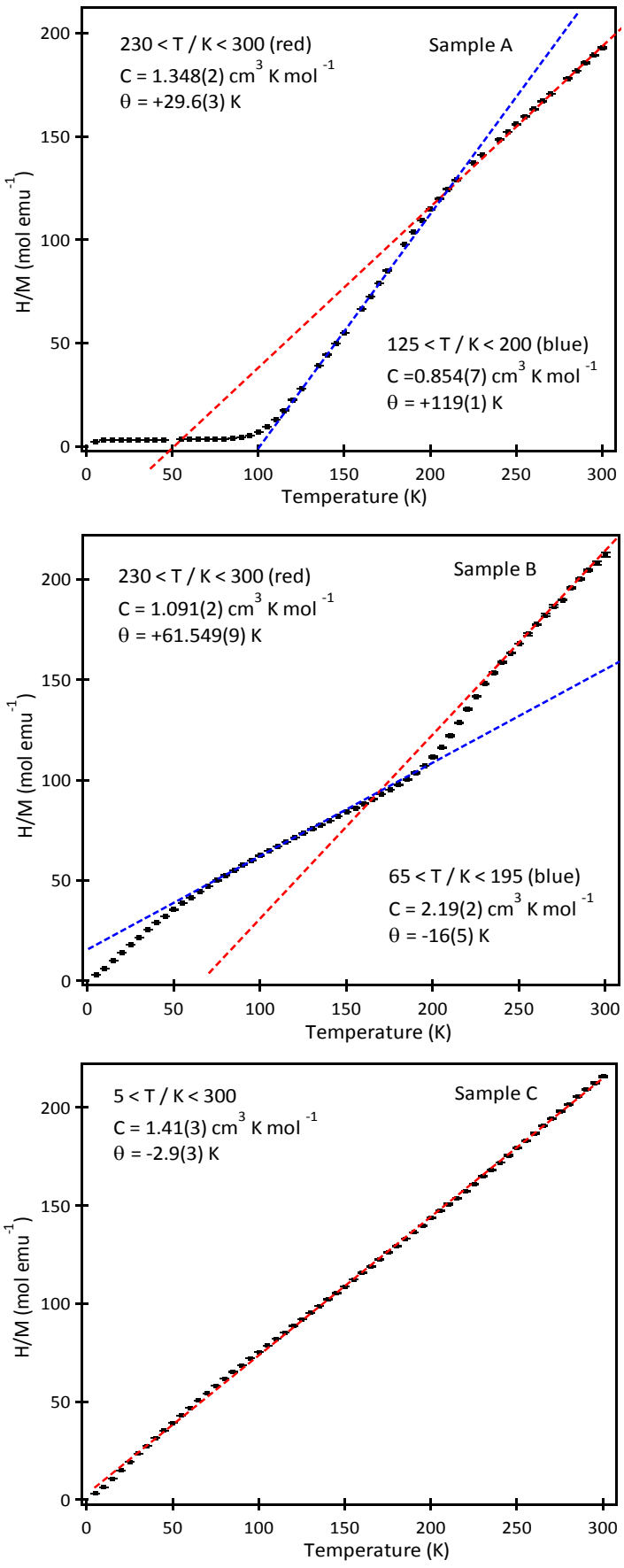


Figure 7.11 Inverse magnetisation plots for all samples

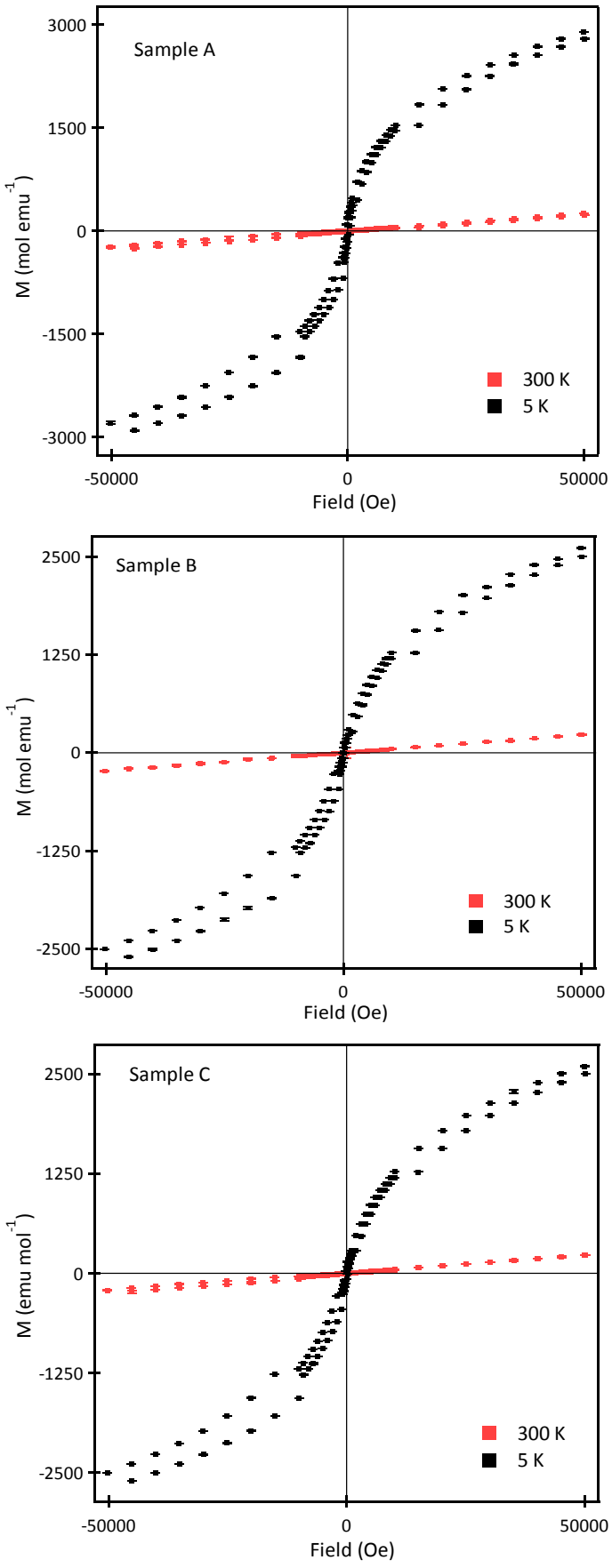


Figure 7.12 Magnetisation-field isotherms collected from all samples

7.4.2 Magnetic Characterisation of Sample C, $La_{0.5}Sr_{1.5}Mn_{0.5}Rh_{0.5}O_4$

Magnetisation data collected from Sample C indicate the material behaves as a standard Curie-Weiss paramagnet in the measured temperature range. As seen in Figure 7.10 (C), the ZFC – FC plots diverge slightly at T ≈ 100 K and the inverse ZFC magnetisation plot deviates from linearity around this temperature. Nevertheless a straight line can be fit to the inverse magnetisation plot given in Figure 7.11 (C) to extract the Curie and Weiss constants.

The inverse magnetisation data can be fit to the Curie–Weiss law in the temperature range $10 < T / K < 300$ to yield values of $C = 1.41(3)$ cm^3 K mol^{-1}, $\theta = -2.9(3)$ K and $\mu^2 = 11.32\ \mu_B^2$. The observed magnetic moment exceeds the expected value for the Mn^{4+}/Rh^{3+} valence combination where $C_{exp} = 0.937$ cm^3 K mol^{-1} ($\mu^2_{exp} = 7.5\ \mu_B^2$). The observed moment is 83.8% of expected moment for a Mn^{3+}/Rh^{4+} valence combination where $C_{exp} = 1.687$ cm^3 K mol^{-1} ($\mu^2_{exp} = 13.5\ \mu_B^2$). The results are in good agreement with the high-spin d^4 Mn^{3+} and low-spin d^5 Rh^{4+} electronic configuration. In the case where Rh^{4+} unpaired electron is not expressed in the magnetism, the observed moment would be ~95% of the expected moment for the Mn^{3+} d^4 electronic configuration. The Weiss constant of $\theta = -2.9(3)$ K suggests negligible or weakly antiferromagnetic interactions between the unpaired electrons. Magnetisation-field isotherms given in Figure 7.12 (C) show linear field dependence at room temperature. At low temperatures field-dependence shows weak hysteresis that is uncharacteristic for perfectly paramagnetic materials.

7.4.3 Magnetic Characterisation of Samples A and B

Magnetic behaviour of Samples A and B are different from stoichiometric Sample C. Both samples have a magnetic event T ≈ 200 K characterised with a sharp change in the inverse

magnetisation plot as seen in Figure 7.11 (A and B). The events are not characterised by a change in electrical conductivity (Sample B resistance-temperature plot shown in Figure 7.13). Variable temperature synchrotron X-ray powder diffraction measurements for both samples in the 100 < T / K < 300 range do not show a structural parameter change event.

Sample B is assumed to have the configuration $La_{0.5}Sr_{1.5}Mn_{0.5}Rh_{0.5}O_{3.5}$ as calculated in Section 7.3.6. The ZFC – FC plot given in Figure 7.10 (B) shows Sample B ZFC – FC curves are coincident with a minor divergence below T ≈ 100 K. Inverse magnetisation plot shown in Figure 7.11 (B) reveals two linear regions in the ranges of 65 < T / K < 195 and 230 < T / K < 300. Data in both ranges are fitted to the Curie-Weiss law independently with Curie constant, Weiss constant and magnetic moment values given as in inset in Figure 7.11 (B). The inverse magnetisation data in the high temperature range 230 < T / K < 300 can be fit to the Curie–Weiss law to yield values of C = 1.091(2) $cm^3\,K\,mol^{-1}$, θ = +61.549(9) K and μ^2 = 8.73. The fit to the low temperature range 65 < T / K < 195 yields values of C = 2.19(2) $cm^3\,K\,mol^{-1}$, θ = -16(5) K and $\mu^2 = 17.52\ \mu_B^2$. Weiss constants extracted from the fits suggest ferromagnetic and weakly antiferromagnetic interactions in the high and low temperature ranges respectively. Magnetisation-field isotherm shows identical behaviour to Sample C.

The oxygen stoichiometry of Sample A cannot be accurately calculated as the sample was used up in characterisation and could not analysed on a TGA machine. Neutron powder diffraction data collected on the D2B diffractometer was not accepted as a reliable test for oxygen content. The ZFC – FC plot given in Figure 7.10 (A) shows Sample A ZFC – FC curves are coincident until T ≈ 120 K where the two curves diverge strongly. Inverse magnetisation plot shown Figure 7.11 (A) reveals two linear regions in the ranges of 125 < T / K < 200 and 230 < T / K < 300. Data in both ranges are fitted to the Curie-Weiss law

independently with Curie constant, Weiss constant and magnetic moment values given as in inset in Figure 7.11 (A). The data in the 230 < T / K < 300 temperature range can be fitted to the Curie-Weiss law to yield values of C = 1.348(2) cm^3 K mol^{-1}, θ = +29.6(3) K and μ^2 = 10.78 μ_B^2. The data in the 125 < T / K < 200 temperature range can be fitted to the Curie-Weiss law to yield values of C = 0.854(7) cm^3 K mol^{-1}, θ = +119(1) K and μ^2 = 6.83 μ_B^2. Magnetisation-field isotherms are identical to the other samples.

Whether the fits represent a real magnetic state is debatable. Various inconclusive explanations such as valence transition and speculation on which cation is being reduced have been considered but were ruled out as there wasn't enough evidence.

7.5 Conductivity Measurements

Electrical conductivity data were collected from Sample B as described in Chapter 2, Section 2.13. Conductivity measurements on a cut-out bar of Sample B suggest the material is a Mott's Variable Range Hopping (VRH) semiconductor (Chapter 2, Section 1.3.3). The conductivity dependence on temperature under thermal semiconductor and hopping polaron models did not show linear behaviour. Transport measurements were linearized when fit to the Mott's Variable Range hopping conduction model. Figure 7.14 shows the linear dependence of log (σ) with regards to the three-dimensional temperature parameter $T^{-1/4}$. This type of electronic behaviour is inherent for disordered systems with localized charge-carrier states. No anomalies were observed that would suggest an electronically driven phase transition.

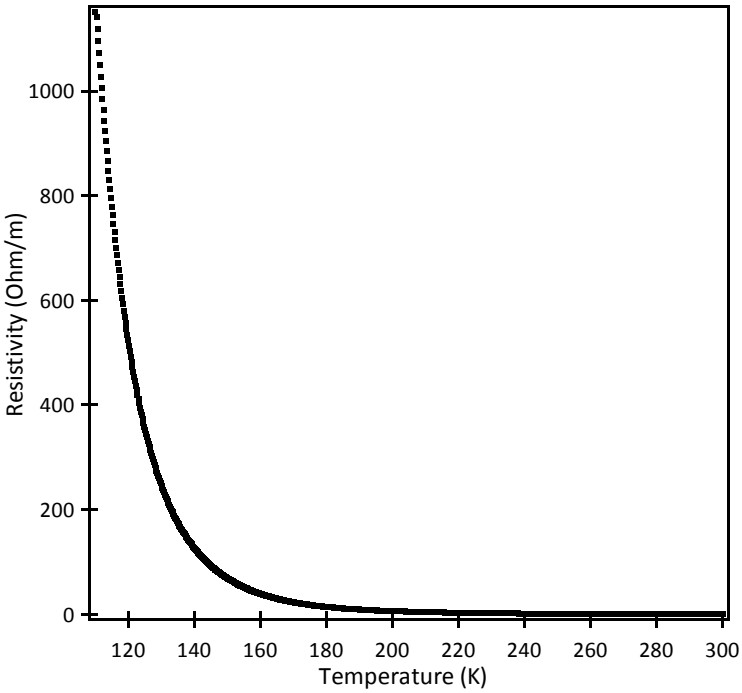


Figure 7.13 Resistivity-temperature data collected from B-$La_{0.5}Sr_{1.5}Mn_{0.5}Rh_{0.5}O_4$ in the 110 < T / K < 300 range

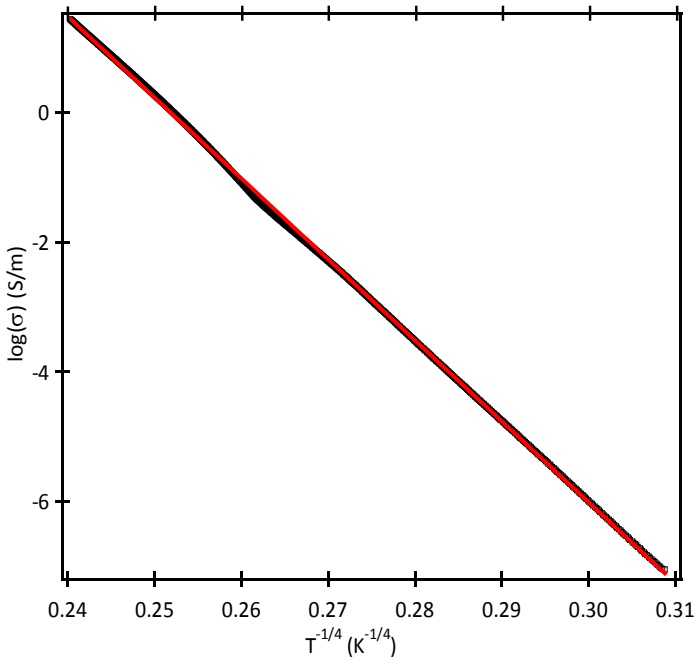


Figure 7.14 Electrical conductance (σ) as a function of temperature for Sample B in coordinates that linearize the Mott variable-range model in three dimensions.

7.6 Discussion

7.6.1 Structural Characterisation of $La_{0.5}Sr_{1.5}Mn_{0.5}Rh_{0.5}O_4$, Sample C

The refinement of synchrotron X-ray powder diffraction data collected from $La_{0.5}Sr_{1.5}Mn_{0.5}Rh_{0.5}O_4$ (Sample C) as described in Section 7.3.3 shows that the material adopts the archetypal n = 1 Ruddlesden-Popper structure with a tetragonal *I4/mmm* space group as shown in Figure 7.4. Rietveld refinement results indicate the material crystallizes with a body-centred unit cell with lattice parameters of a = 3.872250(1) Å, c = 12.47664(4) Å, disordered 1:1 ratio of Mn^{3+} and Rh^{4+} on the B-site and a disordered 1:3 ratio of La/Sr respectively on the A-site. Cations tend to order when the oxidation state difference between them is 2 or more and/or there is a size difference of more than 0.10 Å[28], so it is unsurprising to see an absence of cation order. Refinement fitting statistics of χ^2 = 8.412, *wRp* = 2.08%, and *Rp* = 1.14% suggest an excellent fit the collected diffraction data.

The refined structural parameters shown in Table 7.3 suggest a minor Jahn-Teller elongation along the *c*-axis where two axial bonds lengthen (O_{ax} = 2.030(2) Å) and four equatorial bonds shorten (O_{eq} = 1.936(3) Å). This is expected from Mn^{3+} ($t_{2g}^3e_g^1$) as it is a Jahn-Teller ion and can undergo a J-T distortion (Chapter, Section 1.6.3) where the orbital degeneracy is broken to achieve an energetically favourable configuration of $(d_{xz}^1d_{yz}^1)(d_{xy}^1)/(d_{z2}^1)(d_{x2-z2})^0$. Likewise low-spin Rh^{4+} d^5 ($t_{2g}^5e_g^0$) can undergo weak J-T distortion where the orbital degeneracy is broken to achieve an energetically favourable configuration of $(d_{xz}/d_{yz})_4(d_{xy})_1$. An accurate characterisation of oxygen positions would however require neutron diffraction data to be collected.

Magnetic characterisation described in Section 7.4.2 suggests that $La_{0.5}Sr_{1.5}Mn_{0.5}Rh_{0.5}O_4$ adopts the Mn^{3+}/Rh^{4+} valence combination. But unlike the perovskite analogue described

in Chapter 6, ferromagnetic ordering is not observed. This can simply be explained with respect to breakage of the perovskite connectivity and disruption of the ferromagnetic coupling backbone observed in the perovskite analogue.

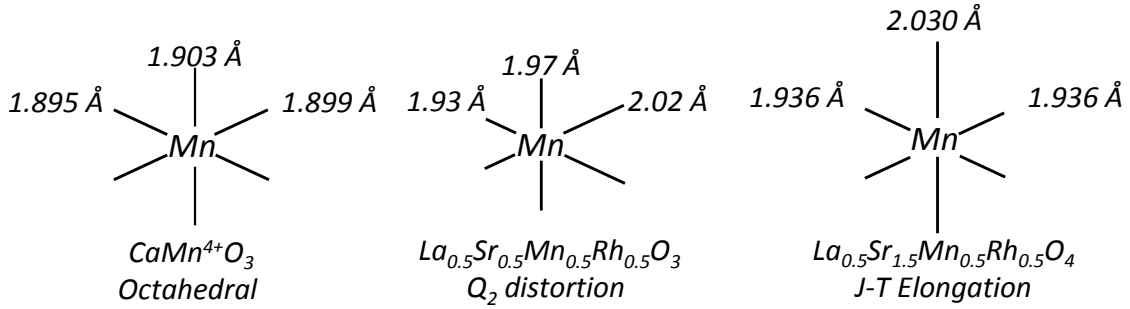


Figure 7.15 Illustrations of bonds lengths for undistorted $CaMnO_3$, Q_2 type distorted $La_{0.5}Sr_{0.5}Mn_{0.5}Rh_{0.5}O_3$ and $La_{0.5}Sr_{1.5}Mn_{0.5}Rh_{0.5}O_4$

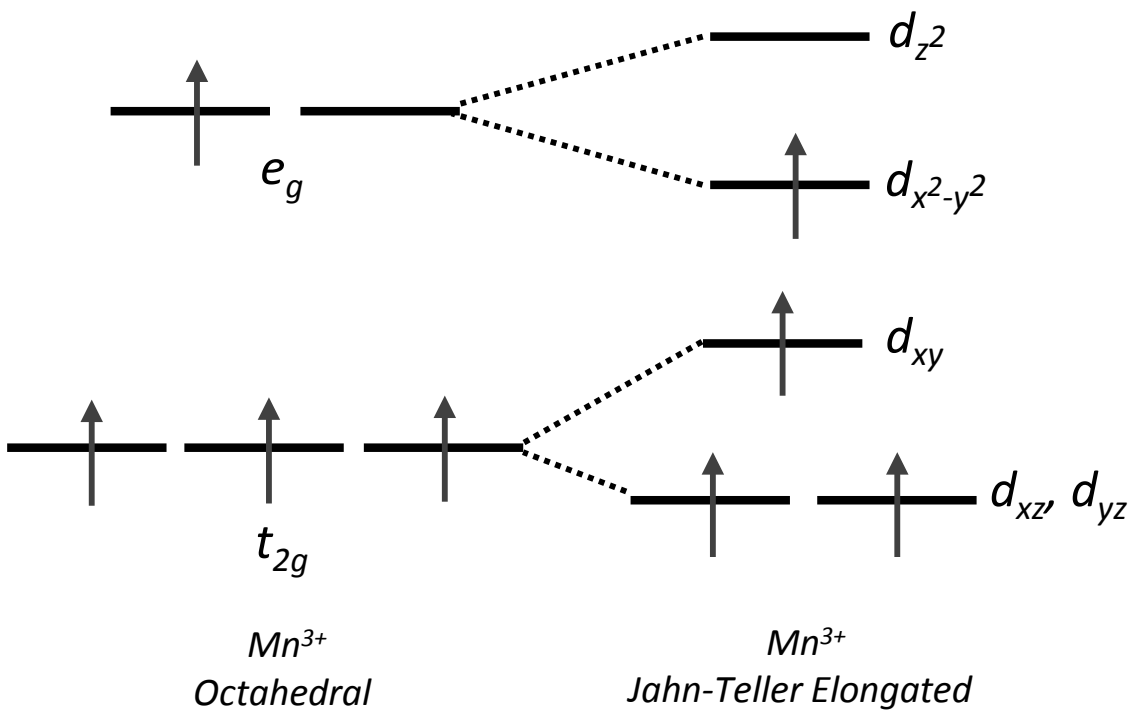


Figure 7.16 Illustration of the splitting of Mn^{3+} d^4 orbitals as a result of J-T compression

7.6.2 Two-Phase Split in Oxygen Deficient Samples A and B

X-ray powder diffraction data reveals that attempts to make $La_{0.5}Sr_{1.5}Mn_{0.5}Rh_{0.5}O_4$ in air results in a phase split between stoichiometric and oxygen deficient analogues. Heating the same material under flowing O_2 gas recovers the missing oxygen to make the stoichiometric $La_{0.5}Sr_{1.5}Mn_{0.5}Rh_{0.5}O_4$ confirmed by X-ray powder diffraction data and thermogravimetric analysis.

A literature review suggests that analogous Ruddlesden-Popper materials like $LaSr_3BB'O_8$[61] (B = Cu, Zn, Ni, B' = Sb, Ru)[61, 142], among others are conventionally synthesised in air. Made under similar synthetic conditions, the initial characterisation of the $La_{0.5}Sr_{1.5}Mn_{0.5}Rh_{0.5}O_4$ showed a poor peak profile fits across the diffraction pattern. A closer look revealed peak broadening and asymmetricity that could be attributed to two-phase mixture of oxygen in homogenous phases.

In homogenous O stoichiometry implies the minority phase is reduced either on Mn or Rh centres but it is challenging to characterise these oxidation states. However this helps understand the magnetic behaviour of Samples A and B. The sharp decrease in the slope of inverse magnetisation plots shown in Figure 7.11 (A and B) could be interpreted in many ways e.g. a possible charge transfer. Two-phase split helps explain the magnetism given that stoichiometric $La_{0.5}Sr_{1.5}Mn_{0.5}Rh_{0.5}O_4$ is a conventional Curie-Weiss paramagnet. The mixed contribution from stoichiometric and oxygen deficient to the magnetic susceptibility plots likely results in the complex behaviour observed.

7.7 Conclusions

The refinement of synchrotron X-ray powder diffraction data collected from $La_{0.5}Sr_{1.5}Mn_{0.5}Rh_{0.5}O_4$ (Sample C) shows that the material adopts the archetypal n = 1 Ruddlesden-Popper structure with a tetragonal *I*4*/mmm* space group. Magnetisation data collected from $La_{0.5}Sr_{1.5}Mn_{0.5}Rh_{0.5}O_4$ indicate the material behaves as a standard Curie-Weiss paramagnet in the measured temperature range and the results are in good agreement with the high-spin d^4 Mn^{3+} and low-spin d^5 Rh^{4+} electronic configuration. Attempts to synthesise $La_{0.5}Sr_{1.5}Mn_{0.5}Rh_{0.5}O_4$ in air results in a two-phase split with in homogenous oxygen stoichiometry that was detected using synchrotron X-ray powder diffraction and neutron diffraction.

Chapter 8 Synthesis and Characterisation of $La_{0.5}Sr_{0.5}Fe_{0.5}Rh_{0.5}O_3$

8.1 Introduction

Following on from the study of disordered rhodium-manganese oxides, the synthesis of $La_{0.5}Sr_{0.5}Fe_{0.5}Rh_{0.5}O_3$ is reported. Iron-containing perovskites have been extensively studied, as Fe can be stabilised in multiple coordination environments and oxidation states. Notable examples include $Sr_2MFe^{3+}O_6$ (M = Mo, Re)[5] that are spin-polarised and high T_C ferromagnets respectively. Likewise, Fe has been shown to stabilise novel coordination environments, as seen in $Sr_2IrFe^{2+}O_4$ which consists of ordered, infinite sheets of apex-linked $Fe^{2+}O_4$ and $Ir^{2+}O_4$ squares[64]. Here the structure and physical properties of A-site and B-site disordered $La_{0.5}Sr_{0.5}Fe_{0.5}Rh_{0.5}O_3$ are reported.

8.2 Synthesis

A sample of $La_{0.5}Sr_{0.5}Fe_{0.5}Rh_{0.5}O_3$ was prepared via a high-temperature ceramic synthesis method. Suitable stoichiometric ratios of La_2O_3 (99.999%, dried at 900 °C), $SrCO_3$ (99.994%), Rh_2O_3 (99.99%, dried at 800 °C) and Fe_2O_3 (99.997%) were finely ground together using an agate mortar and pestle and transferred into an alumina crucible. The mixture was heated at a rate of 5 °C min^{-1} to 1000 °C to decompose the carbonates. The resulting powder was reground and pressed into a pellet. The pellet was heated at 1300 °C under flowing O_2 for 3 periods of 48 hours with intermediate grinding. Reaction progress was monitored using laboratory X-ray powder diffraction. The sample was characterised using synchrotron X-ray powder diffraction and ^{57}Fe Mössbauer spectroscopy.

8.3 Results

8.3.1 Structural Characterisation

Synchrotron X-ray powder diffraction data (Chapter 2, Section 2.5.3) were collected from a sample of $La_{0.5}Sr_{0.5}Fe_{0.5}Rh_{0.5}O_3$. The diffraction data could be indexed using a primitive orthorhombic unit cell with extinction conditions consistent with the *Pnma* (#62) space group with lattice parameters a = 5.5784(2) Å, b = 7.8585(2) Å, c = 5.5579(1) Å. A structural model was constructed based on the refined structure of $La_{0.5}Sr_{0.5}Mn_{0.5}Rh_{0.5}O_3$ described in Chapter 6, with a 1:1 ratio of La/Sr on the A-site and a 1:1 ratio of Fe/Rh on the B-site. The model was refined against synchrotron X-ray powder diffraction data collected at room temperature. A single-phase refinement converged to a good statistical fit where χ^2 = 14.32, *wRp* = 2.05%, *Rp* = 1.18%. The observed, calculated, and difference plots for the *Pnma* refinement are shown in Figure 8.1. Full details of structural refinement parameters are given in Table 8.1 and Table 8.2.

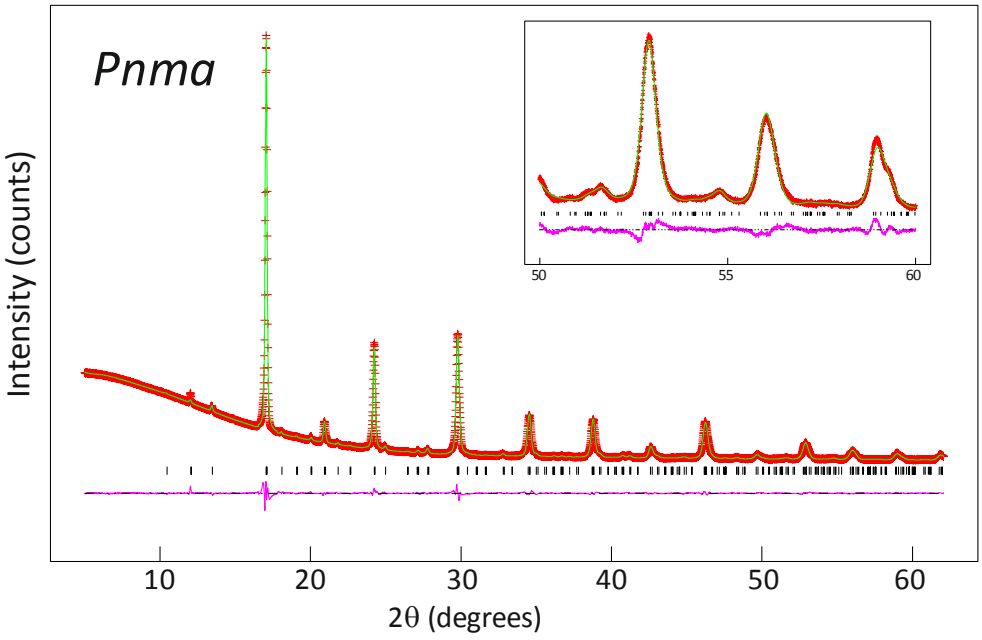


Figure 8.1 Observed, calculated, and difference plots from the refinement of single-phase *Pnma* structural model against synchrotron X-ray powder diffraction data collected from $La_{0.5}Sr_{0.5}Fe_{0.5}Rh_{0.5}O_3$. Inset shows high angle fit.

Atom	x	y	z	Fraction	U_{iso} (Å^2)
La/Sr	0.0222(1)	0.25	0.9922(2)	0.5/0.5	0.024(1)
Rh/Fe	0	0	0.5	0.5/0.5	0.066(1)
O(1)	0.4967(6)	0.25	0.9622(4)	1	0.089(8)
O(2)	0.2294(3)	0.5397(1)	0.7800(2)	1	0.081(1)
$La_{0.5}Sr_{0.5}Fe_{0.5}Rh_{0.5}O_3$ – Space group *Pnma* (#62)					
Formula mass = 481.29 gmol^{-1}					
a = 5.5784(4) Å, b = 7.8585(5) Å and c = 5.5579(4) Å, Vol = 241.59(3) Å^3					
Radiation source: Synchrotron X-ray, λ = 0.82595(1) Å					
χ^2 = 14.32, *wRp* = 2.05%, and *Rp* = 1.18%					

Table 8.1 Parameters from the structural refinement of $La_{0.5}Sr_{0.5}Fe_{0.5}Rh_{0.5}O_3$ against X-ray powder diffraction data

Refinement Parameters	
Fe/Rh – O_{ax} (x2) (Å)	1.9750(3)
Fe/Rh – O_{eq} (x2) (Å)	1.957(2)
Fe/Rh – O_{eq} (x2) (Å)	2.033(1)
<Fe/Rh – O> (Å)	1.986(4)
La/Sr – O(1) (x1) (Å)	2.673(4)
La/Sr – O(1) (x1) (Å)	2.570(5)
La/Sr – O(1) (x1) (Å)	2.867(4)
La/Sr – O(2) (x2) (Å)	2.460(3)
La/Sr – O(2) (x2) (Å)	2.842(2)
La/Sr – O(2) (x2) (Å)	2.679(3)
<La/Sr – O> (Å)	2.678(5)
M – O_{eq} – M (°)	158.62(6)
M – O_{ax} – M (°)	167.7(1)

Table 8.2 Selected structural parameters from the refined structure of $La_{0.5}Sr_{0.5}Fe_{0.5}Rh_{0.5}O_3$

Synchrotron X-ray powder diffraction data suggest the Mn/Rh octahedra deviate from perfect O_h symmetry and the bond angles deviate strongly from 180°. However, since X-rays are poor at detecting subtle distortions in the oxygen lattice, neutron diffraction data would need be collected to quantify the degree of distortion and Jahn-Teller effects.

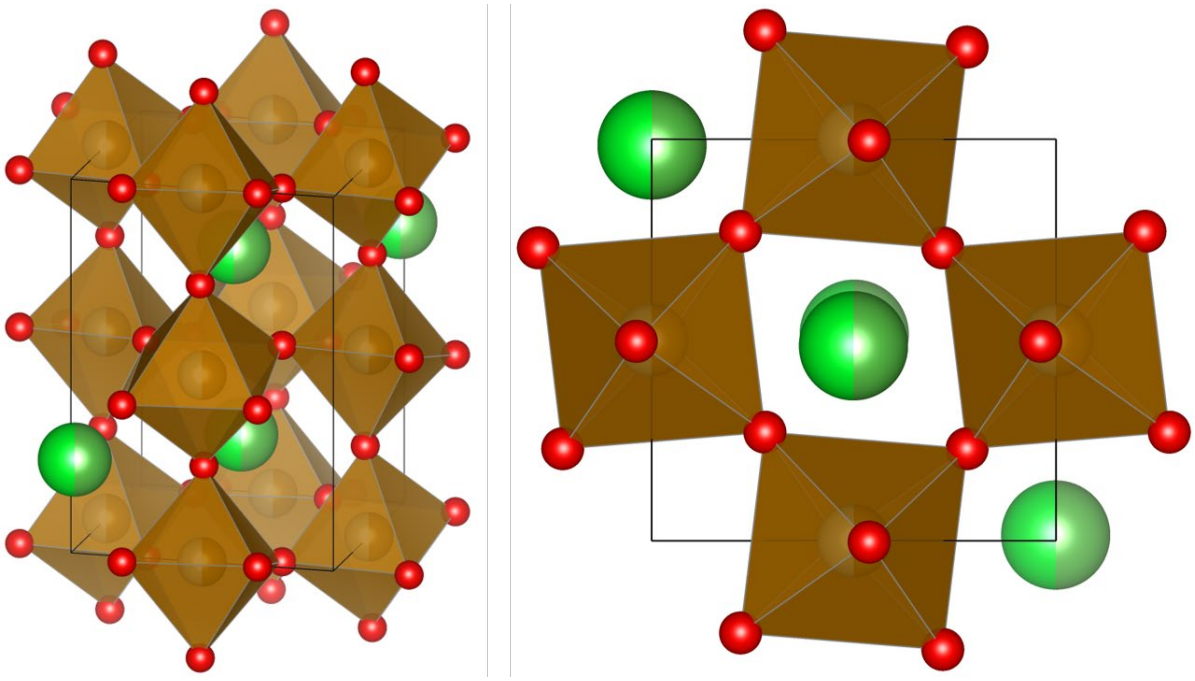


Figure 8.2 The structure of $La_{0.5}Sr_{0.5}Fe_{0.5}Rh_{0.5}O_3$ with *Pnma* space group symmetry viewed along [101] (left) and [010] (right) directions.

8.3.2 ^{57}Fe Mössbauer Spectroscopy

A ^{57}Fe Mössbauer spectrum was collected from a sample of $La_{0.5}Sr_{0.5}Fe_{0.5}Rh_{0.5}O_3$ at 293 K by Dr Paul A. Bingham at Sheffield Hallam University (Chapter 2, Section 2.9). At 293 K, the spectrum shows a complex signal with an observed linewidth that is broader than expected. The signal could not be fitted as a single doublet so it was deconvoluted as two doublets with an 88% - 12% site population, as shown in Table 8.3. Figure 8.3 shows the ^{57}Fe Mössbauer spectrum collected from $La_{0.5}Sr_{0.5}Fe_{0.5}Rh_{0.5}O_3$ where a broad signal is observed and fitted to one wide and one narrow doublet.

If the chemical shifts of both doublets are consulted, it is evident that neither of the signals are consistent with Fe^{4+} centres. In a systematic ^{57}Fe Mössbauer study of Fe-containing perovskite oxides, Adler *et al*[143] have reported the chemical shifts of Fe^{4+} and Fe^{3+} signals in samples of $SrFeO_{3-\delta}$ ($\delta = 0 - 0.3$). The reported results suggest Fe^{4+} signals have chemical

shifts in the range -0.03 < CS / mm s^{-1} < 0.05 at 299 K. As per Table 8.3, the chemical shifts of the two contributing doublets are far outside the Fe^{4+} signal range. The observed chemical shifts are more compatible with the range 0.24 < CS / mm s^{-1} < 0.35 reported by Adler *et al* for Fe^{3+} signals[143]. Both doublets are therefore assigned to Fe^{3+} centres.

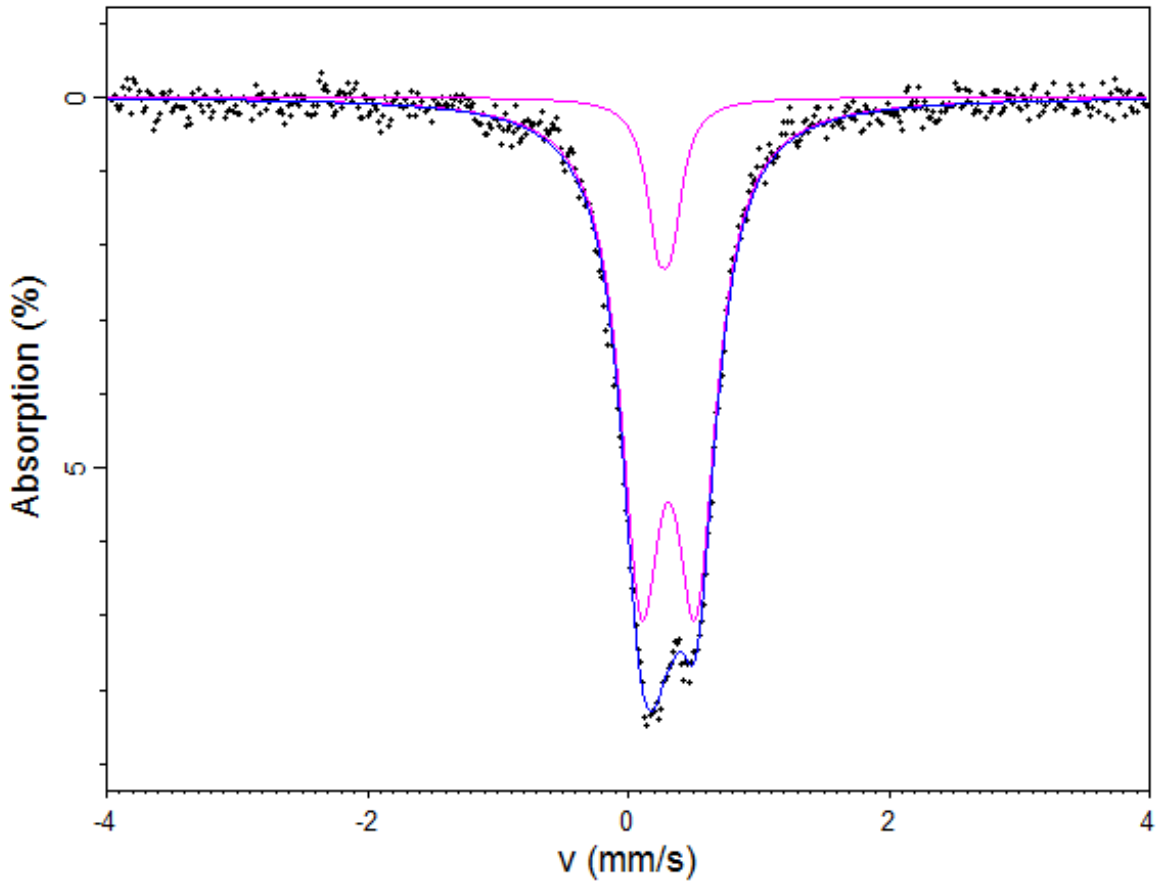


Figure 8.3 ^{57}Fe Mössbauer spectrum collected at 293 K

	CS / mm s^{-1}	Δ / mms^{-1}	HWHM / mm s^{-1}	Site Population	χ^2
Doublet 1	0.2782(99)	0.107(31)	0.107(63)	11.8(82)	0.735213
Doublet 2	0.3103(41)	0.420(20)	0.1923(63)	88.2(86)	

Table 8.3 Fitting statistics extracted from the ^{57}Fe Mössbauer spectra collected at 293 K

8.3.3 Magnetic Characterisation

Magnetisation data were collected from a sample of $La_{0.5}Sr_{0.5}Fe_{0.5}Rh_{0.5}O_3$ on a MPMS SQUID (Chapter 2, Section 2.11) magnetometer in the temperature range 5 < T / K < 300. All magnetisation data were scaled to the $La_{0.5}Sr_{0.5}Fe_{0.5}Rh_{0.5}O_3$ configuration. Zero-field-cooled (ZFC) and field-cooled (FC) magnetisation data in an applied field of 100 Oe are given in Figure 8.4. The molar magnetic susceptibility and inverse molar magnetic susceptibility data collected from $La_{0.5}Sr_{0.5}Fe_{0.5}Rh_{0.5}O_3$ show a divergence of ZFC and FC curves below T ≈ 50 K. With the temperature-independent part subtracted, the inverse magnetisation plot displays linearity above the transition temperature. Magnetisation data can be fit to the Curie–Weiss law in the temperature range 50 < T / K < 300 to yield values of C = 1.047(3) $cm^3\,K\,mol^{-1}$, θ = −22.5(8) K and K = 4.74 x 10^{-5} $cm^3\,mol^{-1}$. The Weiss constant of θ = −22.5(8) K is consistent with the expected weakly antiferromagnetic interactions.

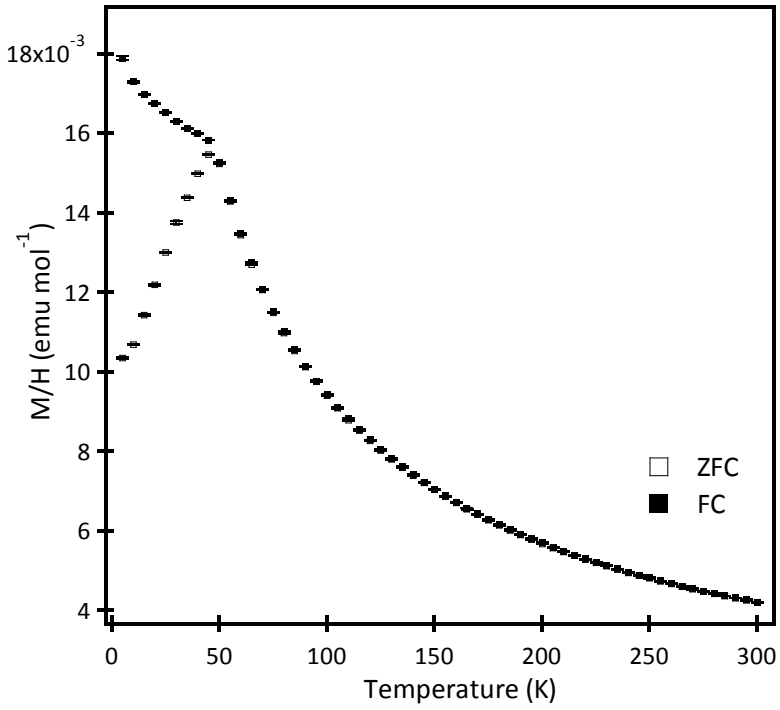


Figure 8.4 Zero-field and field cooled magnetisation data collected from $La_{0.5}Sr_{0.5}Fe_{0.5}Rh_{0.5}O_3$ in 100 Oe.

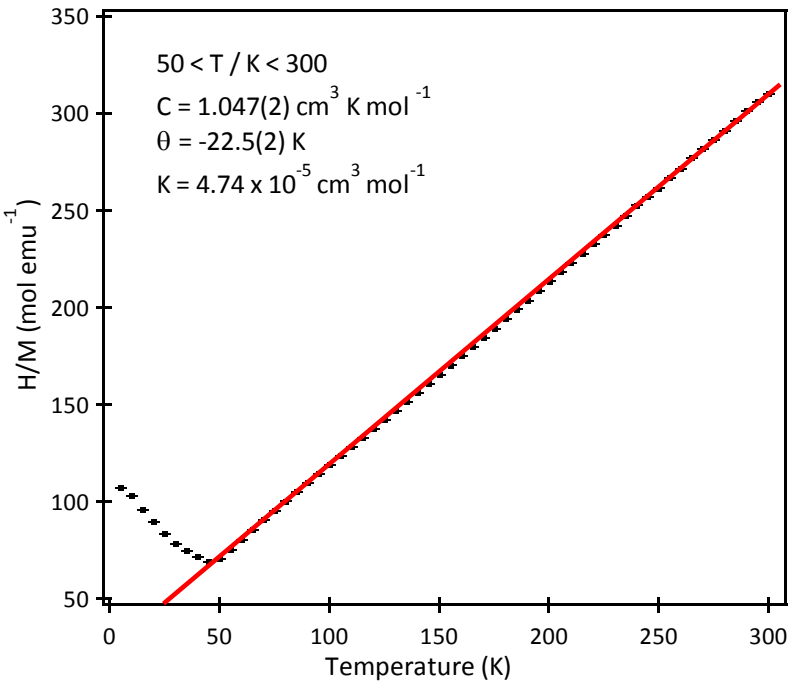


Figure 8.5 Curie–Weiss law fit in the temperature range 50 < T / K < 300 to data collected from $La_{0.5}Sr_{0.5}Fe_{0.5}Rh_{0.5}O_3$

The magnetisation data has the mathematical form of the Curie-Weiss law but large temperature-independent (~25% at 300 K) value indicates that $La_{0.5}Sr_{0.5}Fe_{0.5}Rh_{0.5}O_3$ is not a simple paramagnet. The observed Curie constant yields a magnetic moment that can be expressed in terms of $\mu^2 = 8.59(2)\ \mu_B^2$. The expected Curie constant of the Fe^{3+}/Rh^{4+} valence combination is $C = 2.375\ cm^3\ K\ mol^{-1}$ ($\mu^2 = 19\ \mu_B^2$) and the expected moment for the Fe^{4+}/Rh^{3+} valence combination is $C = 1.50\ cm^3\ K\ mol^{-1}$ ($\mu^2 = 12\ \mu_B^2$). The observed value deviates from the expected spin-only values for both oxidation state combinations. ^{57}Fe Mössbauer spectroscopy findings strongly suggest the presence of Fe^{3+} and the suppressed moment is likely the result of a combination of effects such as spin-orbit coupling from Rh^{4+} ($t_g^5 e_g^0$) centres and local magnetic couplings. It will be argued in the discussion section that a suppressed magnetic moment is common among disordered mixed-metal Fe^{3+} and Rh^{4+} perovskites.

Magnetisation-field isotherms show that field dependence of $La_{0.5}Sr_{0.5}Fe_{0.5}Rh_{0.5}O_3$ at 300 K is linear. The magnetisation-field isotherm collected at 5 K shows a small amount of hysteresis that deviates from the origin which is the characteristic behaviour of a spin-glass material. The lines on the Figure 8.6 highlight the offset of the magnetisation-isotherms from the origin.

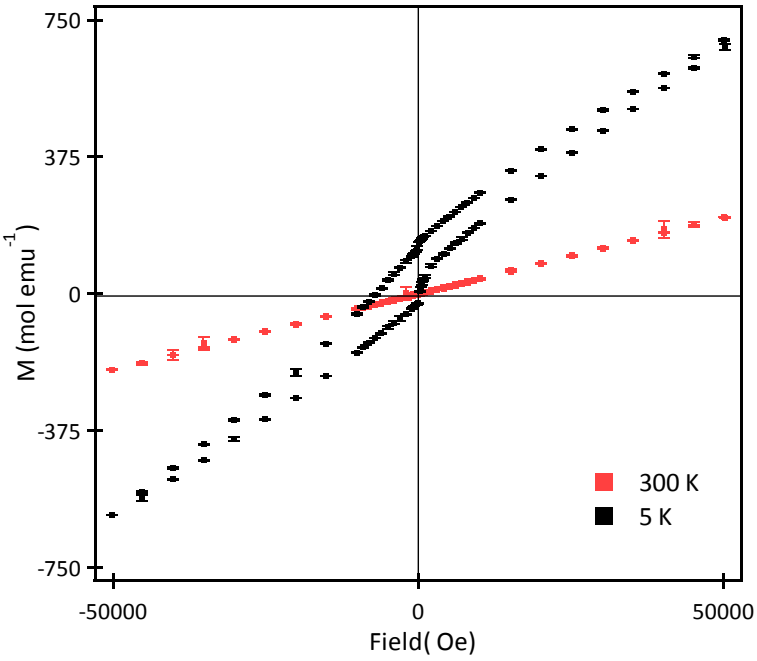


Figure 8.6 Magnetisation-field isotherms collected from $La_{0.5}Sr_{0.5}Fe_{0.5}Rh_{0.5}O_3$

8.3.4 Conductivity Measurements

Conductivity data were collected from a sample of $La_{0.5}Sr_{0.5}Fe_{0.5}Rh_{0.5}O_3$ as described in Chapter 2, Section 2.13. Figure 8.7 shows the dependence of electrical resistance to temperature, indicating semiconductor behaviour. No events are observed at the transition temperature that would indicate the formation of a metallic or an electronically driven state. Below T ≈ 40 K the resistance of the material is too high to be recorded with available currents. The resistance of the material increases smoothly past the magnetic

transition temperature of T ≈ 50 K, indicating a lack of correlated magnetic and electric transport behaviour.

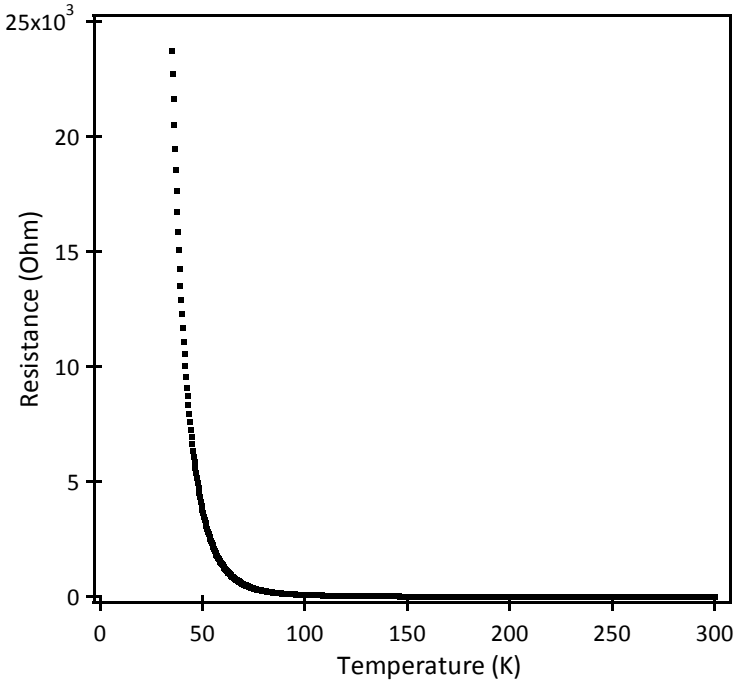


Figure 8.7 Resistance against temperature data collected from $La_{0.5}Sr_{0.5}Fe_{0.5}Rh_{0.5}O_3$ in the 30 < T / K < 300 range

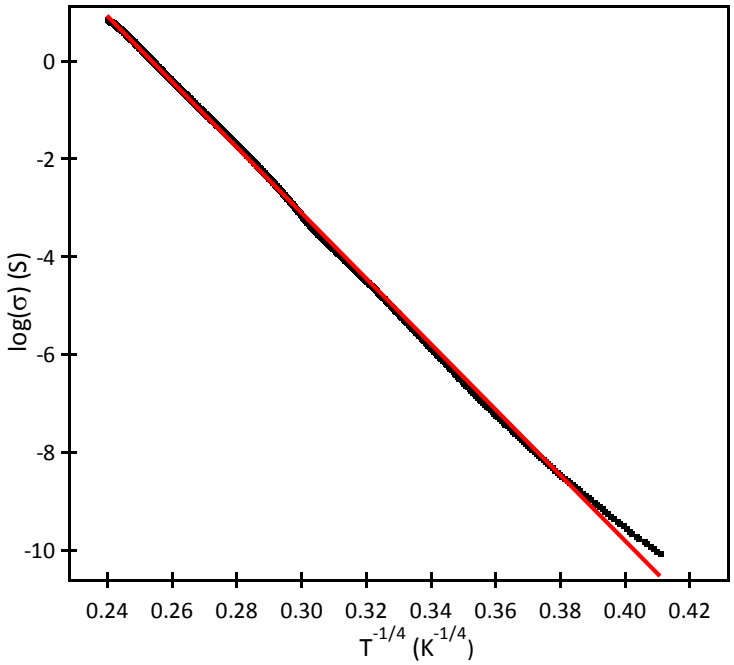


Figure 8.8 Conductivity (σ) as a function of temperature for $La_{0.5}Sr_{0.5}Fe_{0.5}Rh_{0.5}O_3$ in coordinates that linearize the Mott's Variable-Range Hopping model in three dimensions

The electric transport measurements were fit to three possible disordered conduction mechanisms as described in Chapter 2 Section 1.3.3. The temperature dependence of conductivity is inconsistent with Arrhenius semiconductor and hopping-polaron models. However, transport measurements were linearized when fit to the Mott's Variable Range Hopping conduction model. Figure 8.8 shows the linear dependence of log (σ) with regards to the three-dimensional temperature parameter $T^{-1/4}$.

8.4 Discussion

8.4.1 Structural Characterisation

The refinement of synchrotron X-ray powder diffraction data collected from $La_{0.5}Sr_{0.5}Fe_{0.5}Rh_{0.5}O_3$ as described in Section 8.3.1 shows that the material adopts a cation disordered perovskite structure with an orthorhombic *Pnma* space group. Rietveld refinement results indicate the material crystallizes with a primitive unit cell with lattice parameters of a = 5.5784(4) Å, b = 7.8585(5) Å and c = 5.5579(4) Å and the refinement fitting statistics of χ^2 = 14.32, wRp = 2.05%, and Rp = 1.18% suggest an excellent fit to the collected diffraction data. $La_{0.5}Sr_{0.5}Fe_{0.5}Rh_{0.5}O_3$ is B-site cation disordered with a 1:1 ratio of Fe^{3+} and Rh^{4+} on the B-site site, and A-site disordered with a 1:1 ratio of La/Sr and no cation order is observed. Cations tend to order when the oxidation state difference between them is 2 or more and/or there is a size difference of more than 0.10 Å[28], so it is unsurprising to see an absence of cation order.

8.4.2 Oxidation State Determination

The ^{57}Fe Mössbauer spectrum of $La_{0.5}Sr_{0.5}Fe_{0.5}Rh_{0.5}O_3$ recorded at 293 K shows a signal with a chemical shift that strongly indicates the presence of all Fe^{3+} centres without any evidence of Fe^{4+} centres. Qualitatively, the signal could be fitted by two doublets with site

populations of 88% - 12% and chemical shifts of 0.3103(41) mm s^{-1} and 0.2782(99) mm s^{-1} respectively. Citing literature sources[143-145], it was concluded that these chemical shifts indicate that $La_{0.5}Sr_{0.5}Fe_{0.5}Rh_{0.5}O_3$ contains a Fe^{3+}/Rh^{4+} valence combination.

The observed signal is uncharacteristically broad and deviates from a signal expected from a Fe^{3+} centre in perfect cubic symmetry. The line profile is a compound shape and comes from many contributing signals. The shoulder seen in Figure 8.3 was not characteristic of quadrupole splitting, so two other possibilities were considered for the unexpected broadening. One possibility was that $La_{0.5}Sr_{0.5}Fe_{0.5}Rh_{0.5}O_3$ has two different Fe sites as was observed in A_2FeSbO_6 (A = Sr, Ba, Ca)[145] where at least a 75%:25% site split is observed between doublets. The other explanation was an intrinsic broadening of the signal as a result of A- and B-site disorder as observed in $SrLaFeSnO_6$[144].

An analysis of the signal does not give convincing evidence of a B-site split. While the signal can be fitted as two doublets, it is unlikely that the shoulder represents an entirely different site. Primary evidence for this is that the solved structure for $La_{0.5}Sr_{0.5}Fe_{0.5}Rh_{0.5}O_3$ described in Section 8.3.1 shows no evidence of a split-site. Quantitatively, the site population of the minority doublet is 11.8% as per Table 8.3 compared to 22% in Sr_2FeSbO_6 or 50% in Ba_2FeSbO_6, where a site split is established unambiguously. Qualitatively, Figure 8.3 does not show asymmetricity or wide shoulder formations as was observed in the ^{57}Fe Mössbauer spectra of in the split-site A_2FeSbO_6 (A = Sr, Ba, Ca) series[145]. The broadening is more likely a result of the superposition of many different local Fe^{3+} – Rh^{4+} cation environments, as illustrated in Figure 8.9. Analogous observation is made in $BaLaFeSnO_6$[144], where an unambiguous Fe^{3+} signal deviates from a cubic isomer shift, and the random distribution of Ba/La and Fe/Sn atoms on the A- and B-sites in

$BaLaFeSnO_6$ generates local electric field gradients at the Fe site that can appear as doublets on the spectrum[145, 146].

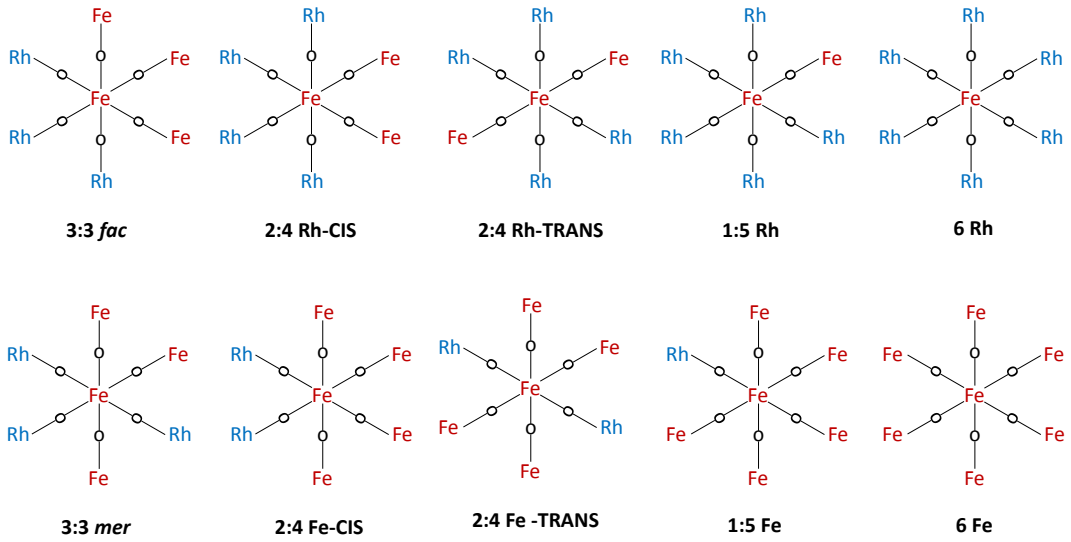


Figure 8.9 The different local Fe environments in a disordered arrangement

Following from the discussion above, it can be concluded with certainty that $La_{0.5}Sr_{0.5}Fe_{0.5}Rh_{0.5}O_3$ crystallises with a Fe^{3+}/Rh^{4+} valence combination. Lack of cation order results in a multitude of different local Fe cation environments that create localised electric field gradients that appear as line profile broadening on the ^{57}Fe Mössbauer spectrum. These findings will be important when magnetic and electrical conductivity properties of $La_{0.5}Sr_{0.5}Fe_{0.5}Rh_{0.5}O_3$ are discussed.

Material	**CS (mm s^{-1})**	**Δ / mm s^{-1}**	**Ref**
$SrFeO_3$ (Fe^{4+})	0.07	0	143
$SrFeO_{2.69}$ (Fe^{3+})	0.35	1.35	143
$La_{0.5}Sr_{0.5}Fe_{0.5}Rh_{0.5}O_3$	**0.3103(41)**	**0.420(20)**	**This work**
$Sr_2Fe^{3+}NbO_6$	0.382	0.517	145
$SrLaFe^{3+}SnO_6$	0.385	0.318	144
$Ba_2Fe^{3+}TaO_6$	0.432	0.552	144
$Sr_2Fe^{3+}RuO_6$ (ordered)	0.51	0	144

Table 8.4 Mössbauer spectrum-fitting parameters for a list of Fe-containing perovskite oxides.

8.4.3 Magnetic Characterisation

8.4.3.1 Magnetic Susceptibility Measurements

Magnetisation data collected from $La_{0.5}Sr_{0.5}Fe_{0.5}Rh_{0.5}O_3$ (Section 8.3.3) show that the zero-field-cooled and field-cooled measurements are weakly divergent at all temperatures, and the curves undergo a significant divergence event at T ≈ 50 K, signalling a transition to a magnetically ordered state. The material behaves like a paramagnet in the 50 < T / K < 300 range if temperature-independent contributions are excluded and the inverse magnetisation plot displays linearity above the transition temperature. The temperature-independent moment corresponded to ~25% of the measured magnetisation at 300 K indicating significant local magnetic interactions. Inverse magnetisation fit to the Curie–Weiss law in the temperature range 50 < T / K < 300 yields a Curie constant of C = 1.047(3) $cm^3\ K\ mol^{-1}$ (μ^2 = 8.376 μ_B^2) and a Weiss constant of θ = −22.5(8) K. The Weiss constant of θ = −22.5(8) K is consistent with the expected weakly antiferromagnetic interactions. The expected Curie constant for Fe^{3+}– Rh^{4+} valence combination is C = 2.375 $cm^3\ K\ mol^{-1}$ (μ^2 = 19 μ_B^2). Therefore, the observed moment is 44% of the expected value for Fe^{3+}– Rh^{4+} system. The observed moment is likewise smaller than the spin-only moment for a Fe^{4+}–Rh^{3+}.

The suppression of the magnetic moment is not surprising to see, given that $La_{0.5}Sr_{0.5}Fe_{0.5}Rh_{0.5}O_3$ has many competing magnetic interactions. There are several contributions to the suppressed moment, but the most obvious one is that Rh^{4+} undergoes a significant degree of spin-orbit coupling, meaning that the spin-only value no longer applies. This is evidenced by the large observed temperature-independent part. Without Rh electrons, the observed moment is still ~50% of the expected moment for a Fe^{3+}

($t_{2g}^3 e_g^2$) system. A significant suppression of the magnetic moment is relatively common among disordered Fe^{3+} systems. A study of Fe^{3+} perovskite oxides coupled with a diamagnetic cation on the B-site by Battle *et al* shows a supressed moment for all samples[145]. A follow up study of Ga dilution to make $Sr_2Fe_{1-x}Ga_xTaO_6$ showed that at the point where Fe content is 5% the magnetic moment is fully expressed for the Fe^{3+} species indicating that the reduction in magnetic moment was due to cooperative effects between metal centres[147]. In all cases, it appears to be a result of complex competing neighbour exchange interactions between magnetic centres. As Table 8.5 and Table 8.6 suggest, both Fe^{3+} and Rh^{4+} compounds have been known to show this behaviour.

Material	**Spin-glass freezing T / K**	**Θ / K**	**μ_{obs}^2 / μ_B^2 (μ^2_{exp})**	**Ref**
$La_{0.5}Sr_{0.5}Fe_{0.5}Rh_{0.5}O_3$	**50(1)**	**-23**	**8.4 (19)**	This Work
$Sr_2Fe^{3+}TaO_6$	23(1)	-55	10.9 (17.5)	[145]
$Ca_2Fe^{3+}TaO_6$	23(1)	-19	13.0 (17.5)	[145]
$Ba_2Fe^{3+}NbO_6$	25(1)	-55	12.3(17.5)	[145]

Table 8.5 Selected magnetic parameters from a series of Fe based spin-glass disordered perovskites

Material	**C / cm^3 K mol^{-1}**	**Θ / K**	**μ_{obs}^2 / μ_B^2**	**μ_{exp}^2 (Rh^{4+})**	**μ_{exp}^2 (Rh^{3+})**	**Ref**
$La_{0.5}Sr_{0.5}Fe_{0.5}Rh_{0.5}O_3$	1.047	**-23**	**8.37**	**19.00**	**17.5**	This Work
$La_2CoRh^{4+}O_6$	1.677	-109	13.40	17.97	24.01	[112]
$La_2NiRh^{4+}O_6$	1.038	-136	8.29	10.99	2.99	[112]
$La_2CuRh^{4+}O_6$	3.455	-32.1	2.16	5.98	7.99	**[112]**
$La_2MgRh^{4+}O_6$	0.163	-21	1.30	3.00	-	[148]
$La_2ZnRh^{4+}O_6$	0.174	-17.3	1.392	3.00	-	[148]

Table 8.6 Selected list of Rh^{4+} based perovskites where a magnetic moment suppression is observed

The formation of spin-glass phases is understood to be a common occurrence when compounds contain more than one magnetic species[149] or when the crystal structure shows high degree of atomic disorder as in $Sr_2Fe^{3+}MO_6$ (M = Ta, Nb, Sb) [41, 150]. This can be contrasted with long-range antiferromagnetic ordering observed in $LaFe^{3+}O_3$ at temperatures as high as 750 K and the fall in T_N is observed when the Fe^{3+} concentration falls to 50% at *ca.* 550 K[151]. More generally it is not uncommon for frustrated spin systems to show spin-glass behaviour at low temperatures. The origins of this frustration are described below.

8.4.3.2 Origins of magnetic frustration

Magnetisation plots suggest that $La_{0.5}Sr_{0.5}Fe_{0.5}Rh_{0.5}O_3$ undergoes a transition to a spin-glass below T ≈ 55 K where ZFC and FC curves diverge. The magnetisation-field isotherm collected at 5 K (Section 8.3.3, Figure 8.6) is not symmetric and displaced from the origin, indicating a significant degree of magnetic frustration that can be characterised as a spin-glass type behaviour. Spin-glass behaviour is seen in materials that satisfy the following two criteria; chemical disorder and magnetic frustration. Structural characterisation of $La_{0.5}Sr_{0.5}Fe_{0.5}Rh_{0.5}O_3$, discussed in Section 8.3.1, shows that the material is A- and B-site disordered with random cation distribution across the sites so it is not surprising to see a high degree of magnetic frustration.

One way to rationalise the origin of magnetic frustration is to consider the relative strength of competing superexchange interactions in $La_{0.5}Sr_{0.5}Fe_{0.5}Rh_{0.5}O_3$. This explanation follows the reasoning proposed by Battle *et al* and corroborated by Hayward *et al* regarding magnetically frustrated Fe/Ru systems[152, 153]. If simple Goodenough-Kanomori[131] superexchange couplings are considered, the spin-glass $Sr_3(Fe_{0.5}Ru_{0.5})_2O_7$

should be antiferromagnetic and should not be magnetically frustrated. Battle suggested that the observed frustrated magnetic behaviour is a result of competing exchange interaction pairings of Fe^{3+} ($t_{2g}^3e_g^2$) 3*d* and Ru^{5+} ($t_{2g}^3e_g^0$) 4*d* centres. This reasoning follows that $|J^{nn}_{Fe/Fe}| >> |J^{nn}_{Fe/Ru}| \approx |J^{nn}_{Ru/Ru}| \approx |J^{nnn}_{Fe/Fe}|$ or simply that the relative strength of next-nearest neighbour exchange interactions between Fe centres is comparable to the relative strength of any exchange interactions of Ru centres. The same rationalisation can be applied to the current Fe^{3+} ($t_{2g}^3e_g^2$) Rh^{4+} ($t_{2g}^5e_g^0$) system, where four competing interactions are present. Similar to an ideal G-type antiferromagnetic Fe^{3+} perovskite, the coupling between nearest neighbour Fe^{3+} – O – Fe^{3+} is antiferromagnetic ($J^{nn}_{Fe/Fe} < 0$). The Rh^{4+} – O – Rh^{4+} interactions are likewise expected to be antiferromagnetic ($J^{nn}_{Rh/Rh} < 0$). Finally the Fe^{3+} – O – Rh^{4+} interactions are expected to be ferromagnetic ($J^{nn}_{Fe/Rh}$). A simple interpretation of these interactions would imply that the system should be antiferromagnetic. This is not the case in $La_{0.5}Sr_{0.5}Fe_{0.5}Rh_{0.5}O_3$. Instead, it is proposed that next-nearest-neighbour interactions between Fe^{3+} centres contribute to magnetic frustration because the strength of these interactions is comparable to antiferromagnetic Rh^{4+} – O – Rh^{4+} and ferromagnetic Fe^{3+}– O – Rh^{4+} interactions. Figure 8.10 illustrates the competing magnetic interactions. It is worth contrasting the magnetic behaviour observed here with that of $La_{0.5}Sr_{0.5}Mn_{0.5}Rh_{0.5}O_3$ described in Chapter 6. While structurally very similar, $La_{0.5}Sr_{0.5}Fe_{0.5}Rh_{0.5}O_3$ is a spin-glass while $La_{0.5}Sr_{0.5}Mn_{0.5}Rh_{0.5}O_3$ undergoes ferromagnetic ordering to reach a saturated moment of μ = 3.2 μ_B. In the former case it is assumed that while nearest neighbour antiferromagnetic interactions between Fe^{3+} – Fe^{3+} and Rh^{4+} – Rh^{4+} centres are strong, the competing interactions are comparably strong to create magnetic frustration. In the latter case σ-superexchange coupling between Mn^{3+} – Mn^{3+} cations dominate.

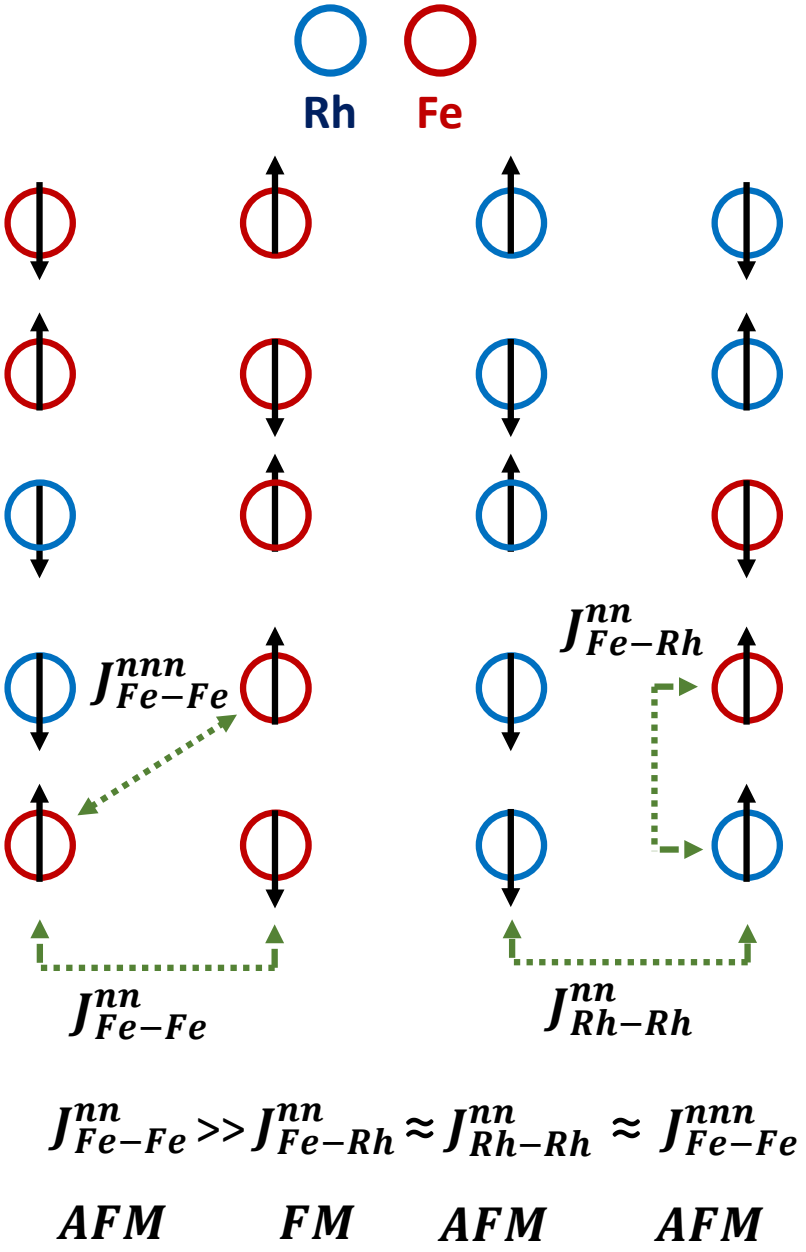


Figure 8.10 The nearest-neighbour (n-n) and next-nearest-neighbour (n-n-n) coupling regimes in $La_{0.5}Sr_{0.5}Fe_{0.5}Rh_{0.5}O_3$ and the magnetic frustration that leads to a spin glass state

8.4.4 Rhodium Coordination Chemistry

The reporting of an A- and B-site disordered perovskite $La_{0.5}Sr_{0.5}Fe_{0.5}Rh_{0.5}O_3$ follows on from the work described in Chapter 6, where a disordered manganese-rhodium perovskite is reported. Structurally these two phases are very similar as both contain a trivalent 3*d* transition-metal and Rh^{4+} in the B-site. In both cases, there was ambiguity

over the oxidation state combination because Rh^{3+} ($t_{2g}^6 e_g^0$) had conventionally been regarded to be more energetically stable than the Rh^{4+} ($t_{2g}^5 e_g^0$) coordination. ^{57}Fe Mössbauer spectroscopy allowed for an unambiguous determination of the oxidation state of Fe in $La_{0.5}Sr_{0.5}Fe_{0.5}Rh_{0.5}O_3$, which further corroborates the conclusions made earlier that $La_{0.5}Sr_{0.5}Mn_{0.5}Rh_{0.5}O_3$ contains a Mn^{3+}/Rh^{4+} valence combination. Both materials are disordered in A- and B-sites which adds to the relatively wide body of literature work on mixed-metal 3*d* - 4*d* (3d = Fe, Mn; 4*d* = Rh, Ru) perovskites conducted by Battle *et al*[145], Gibb *et al*[144], and Subramanian *et al*[112], among others. Table 8.7 shows a selected list of known disordered 3*d* – 4*d* mixed metal perovskites. While ordered analogues have been reported, there are few compared to the disordered ones. Table 8.7 suggests that these tend to crystallise with the orthorhombic *Pnma* space group and are non-metallic, but show a wide range of magnetic and electric transport behaviour.

Material	**SG**	**Disorder**	***a* (Å)**	***b* (Å)**	***c* (Å)**	**Magnetism**	**Conductivity**	**Ref**
$LaSrMn^{3+}RuO_6$	*Pnma*	A-, B-sites	5.53	7.81	5.56	FM, T_c = 200	SPH, SC	122
$LaSrFe^{3+}SnO_6$	*Pbnm*	A-, B-sites	5.65	5.65	7.99	SG, T = 40 K	-	146
$LaSrMn^{3+}Rh^{4+}O_6$	*Pnma*	A-, B-sites	5.48	7.78	5.54	FM, T_c = 53 K	VRH, SC	This work
$LaSrFe^{3+}Rh^{4+}O_6$	*Pnma*	A-, B-sites	5.57	7.85	5.56	SG, T = 50 K	VRH, SC	This work
$La_2Mn^{3+}Rh^{3+}O_6$	*Pnma*	B-site	5.58	7.84	5.55	FM, T_c = 65 K	Arrhenius SC	154
$LaFe^{3+}Rh^{3+}O_6$	*Pbnm*	B-site	5.57	5.60	7.87	FM, T_c = 25 K	Arrhenius SC	112
$LaCuRh^{4+}O_6$	*Pbnm*	B-site	5.55	5.71	7.84	PM	Arrhenius SC	112

Table 8.7 Selected list of known disordered 3*d*-4*d* mixed-metal perovskite oxides. SPH - Small Polaron Hopping Semiconductor, VRH - Variable Range Hopping Semiconductor

8.5 Conclusions

A mixed-metal perovskite oxide of composition $La_{0.5}Sr_{0.5}Fe_{0.5}Rh_{0.5}O_3$ was prepared using a high-temperature ceramic synthesis method. X-ray powder diffraction data collected from the sample could be readily indexed using an orthorhombic unit cell with exclusion parameters most consistent with the *Pnma* space group. Structural characterisation showed a 1:1 ratio of La/Sr on the A-site and a 1:1 ratio of Fe/Rh on the B-site. ^{57}Fe Mössbauer spectrum of $La_{0.5}Sr_{0.5}Fe_{0.5}Rh_{0.5}O_3$ collected at 293 K shows a single peak with a complex line profile and a chemical shift consistent with the presence of Fe^{3+} centres. The line profile of the signal is broadened and is experimentally fit as two doublets in order to account for the disturbance of the electric field gradient, due to cation disorder. Magnetic susceptibility measurements show that $La_{0.5}Sr_{0.5}Fe_{0.5}Rh_{0.5}O_3$ undergoes a transition to a spin-glass state at $T \approx 50$ K and the magnetisation-field isotherm collected at 5 K shows a weak magnetic hysteresis with significant off-centring. The inverse magnetic susceptibility plot with the temperature-independent part subtracted shows that in the $50 < T / K < 300$ temperature region $La_{0.5}Sr_{0.5}Fe_{0.5}Rh_{0.5}O_3$ shows Curie-Weiss behaviour, with the Weiss constant suggesting weak antiferromagnetic interactions. The observed magnetic moment is 44% of the calculated spin-only moment for a Fe^{3+}/Rh^{4+} valence combination. The high suppression of the magnetic moment is proposed to be a result of magnetic cluster formation and possible delocalisation of Rh electrons. Electrical conductivity data shows that $La_{0.5}Sr_{0.5}Fe_{0.5}Rh_{0.5}O_3$ is a Mott's Variable Range Hopping semiconductor, and a transition to an electronically ordered state is not observed.

Chapter 9 Conclusions

In this thesis, a diverse range of work has been demonstrated covering the chemistry of 4*d* rhodium and 5*d* rhenium metals. The oxide chemistry of these elements is relatively poorly understood due to high costs and synthetic challenges faced by solid-state chemists. Overall, the findings in this thesis open the possibility a wide range of future work on both metals.

The first part of this thesis focuses on rhenium chemistry. One of the key findings in this part is the new pathways for rhenium metastable phases using topochemical reduction with H_2 gas. This method has led to the first reported case of a topochemically reduced metastable Re^{6+} perovskite oxide that contains unusual structural transformations and magnetic behaviour. The formed phase, $Sr_2ReLiO_{5.5}$ exhibits a partially anion-vacancy ordered structure with extensive microstructural twinning to minimize crystallographic strain. Despite the breakage of local symmetry at Re centres, the material shows a very small-moment paramagnetism that suggest large orbital contributions to the magnetic moment as would be expected from a high symmetry Re^{6+} environment. This finding contradicts the widely accepted understanding that orbital contributions are necessarily quenched in low symmetry environments.

Building on this, it has been shown that the reduction behaviour of $Sr_2ReLiO_{5.5}$ is partly a result of structural flexibility allowed by a Re/Li coordination environment. It had been shown previously that 4*d*/5*d* transition-metals are hard to reduce topochemically as they tend to be unstable with respect to reduction, instead favouring a decomposition to elements. Conventional belief states that 3*d* transition-metals need to be included to stabilise the reduced lattice of a 4*d*/5*d* system. While this is shown to be true for some

metals, Re appears to behave differently. Work presented in this thesis showed that a mixed-valent 3*d* and diamagnetic Li material $Sr_2ReCo_{0.36}Li_{0.64}O_6$ reduces in a H_2 flow, clearly suggesting that lithium helps stabilise these reduction reactions. It is therefore interesting that lithium appears to be playing role of 3*d* metals in these rhenium systems, suggesting a range of novel topochemically reduced A_2MLiO_{6-x} (M = 4*d*/5*d* transition metal) phases could be prepared and stabilized in this manner.

More generally, this behaviour is interesting to observe, as it has not been seen in reduction chemistry of other 5*d* and 4*d* transition-metal perovskite oxides. So far, these factors are unique to Re and have not been seen for other late 5*d* elements. The topochemical behaviour of 5*d* systems remains poorly understood so it would be useful to continue the research work Re compounds in an attempt to stabilise novel materials like Re oxyhydrides, oxyfluorides or other anion-vacancy ordered meta-stable phases.

The second avenue of research pursued in this thesis is chemistry and physical properties of mixed-metal rhodium perovskite oxides. This work builds on a relatively wide range of literature on perovskite manganates that show colossal magnetoresistance among other interesting physical properties and combines with the relatively unexplored Rh metal.

The key findings of this part of the thesis concern the oxidation states adopted by Rh in perovskite oxides and the implications for correlated magnetic behaviour. Previous work on Rh oxides has been ambiguous over the stable oxidation-state that Rh can adopt. Low-spin Rh^{3+} ($t_{2g}^6e_g^0$) is diamagnetic and has been assumed to be the preferred stable oxidation state for Rh. In this thesis, with respect to several mixed-metal oxides it has been shown that the Rh^{4+} ($t_{2g}^5e_g^0$) is likewise a very possible valence for Rh if synthesised in an oxidative environments like flowing O_2 gas. The synthesis of $La_{0.5}Sr_{0.5}Mn_{0.5}Rh_{0.5}O_3$

was carried out successfully to make an A- and B-site cation disordered perovskite that shows a saturated ferromagnetic moment below its T_C = 55 K but is an insulator. The elucidation of the physical behaviour $La_{0.5}Sr_{0.5}Mn_{0.5}Rh_{0.5}O_3$ required an analysis of possible superexchange pathways that could lead to ferromagnetic interactions and it has been argued that the only possible valence combination that would result in this behaviour is Mn^{3+}/Rh^{4+} and the Mn^{3+} – Mn^{3+} σ-superexchange interactions are suggested to be a valid pathway for a ferromagnetically ordered state. Furthermore, magnetic characterisation of the material in the high-temperature state yields a Curie constant and magnetic moment values that are inconsistent with a Mn^{4+}/Rh^{3+} valence combination as these exceed the spin-only moment. Finally, the classic Mn^{3+} – Mn^{4+} double-exchange pathway is ruled out as the material is observed to be an insulator. This is followed by the synthesis of the n = 1 Ruddlesden-Popper oxide analogue, $La_{0.5}Sr_{1.5}Mn_{0.5}Rh_{0.5}O_4$. Magnetic characterisation of the material also suggests a Mn^{3+}/Rh^{4+} valence combination but no ferromagnetic ordering is observed. This is simply explained with respect to breakage of the perovskite connectivity and disruption of the ferromagnetic coupling backbone observed in the perovskite analogue.

Finally the synthesis and magnetic characterisation of $La_{0.5}Sr_{0.5}Fe_{0.5}Rh_{0.5}O_3$ is described. This material shows spin-glass behaviour with a freezing temperature of T = 50 K at low temperatures and Curie-Weiss type behaviour in the high temperatures. The extracted magnetic moment is observed to be lower than the expected spin-only moment for both Mn^{4+}/Rh^{3+} and Mn^{3+}/Rh^{4+} valence combinations, but a key observation is made using ^{57}Mössbauer spectroscopy, which shows a signal with a chemical shift that can be unambiguously assigned to Fe^{3+} centres. This confirms that $La_{0.5}Sr_{0.5}Fe_{0.5}Rh_{0.5}O_3$ has the

Fe^{3+}/Rh^{4+} valence combination. The line profile of the signal is observed to be a complex shape of multiple individual signals and this is attributed to the local random distribution of Fe coordination environments, which is found to be consistent with spin-glass behaviour.

A contrast and comparison of manganese-rhodium and iron-rhodium mixed-metal oxides described in this thesis answers some critical questions regarding this class of materials but also open the possibility for further work. The fact that both crystallize with Rh^{4+} is in an interesting observation in the context that $LaRh^{3+}O_3$[155], $SrMn^{4+}O_3$[156] and $SrFe^{3.6}O_{2.8}$[157] all can be made in ambient conditions but switch oxidation states when combined. Crucially, all rhodium materials presented here are B-site disordered which has serious implications for their electrical transport and magnetic properties. Attempts should be made to synthesise cation ordered double perovskites, which would open new pathways for correlated electrical transport and magnetic behaviour. Likewise, the reduction chemistry of these materials should be explored in an attempt to make novel meta-stable phases like $Sr_2ReLiO_{5.5}$.

Appendix 1 List of Figures

Figure 1.1 Left: Aristotype ABX_3 *Pm*-3*m* (221) $SrTiO_3$[19]; Right: *Pbnm* (62) $CaTiO_3$[27] 4

Figure 1.2 Left: B-site rock-salt ordered Ba_2MgWO_6[29] Middle: B-stie layered ordered La_2CuSnO_6[30] Right: A-site columnar ordereed $CaFeTi_2O_6$[31] 5

Figure 1.3 Left: *Fm*-3*m* (225) B-site ordered Sr_2WMnO_6[28] Right: *C2/m* (12) doubly ordered $NaLaMgWO6_6$[32]6

Figure 1.4 Left: The perovskite $KNiF_3$. Centre: The aristotype $KNiF_4$, n = 1 Ruddlesden-Popper structure. Right: $K_3Ni_2F_7$, n = 2 Ruddlesden-Popper structure[35]. 7

Figure 1.5 Illustrations of (a) atomic orbital, (b) molecular orbitals, (c) a large molecule, (d) distinct bands[36] 8

Figure 1.6 Illustrations for different electronic behaviour. E_g is the bang gap in electron volts (eV) 9

Figure 1.7 The Hubbard model: Electron hopping from filled (black) to empty sites (white). Hopping to a filled site has an on-site Coulomb interaction, *U*, penalty.[39] 10

Figure 1.8 Hubbard sub-bands as a function of bandwidth, *W*. 11

Figure 1.9 Spin alignment in an external field 13

Figure 1.10 Standard superexchange mechanisms in transition-metal oxides 14

Figure 1.11 Schematic DOS for 100% spin-polarisation. The minority spin is insulating and majority spin is metallic 16

Figure 1.12 Simplified phase diagram of $La_{1-x}Ca_xMnO_3$[3] 17

Figure 1.13 Left: I4*/m* (87) Sr_2ReFeO_6[48]; Right: *Pnma* (62) $La_{0.7}Ca_{0.3}MnO_3$[49] 18

Figure 1.14 An illustration of orbital arrangements of Re^{6+} in free ion, octahedral coordination and in spin-orbit coupling regimes 20

Figure 1.15 The most common Jahn-Teller distortions of an octahedral Cu^{2+} complex[56]. 21

Figure 1.16 Topochemical reduction of $SrFe_{0.5}Ru_{0.5}O_3$ to $SrFe_{0.5}Ru_{0.5}O_2$ 23

Figure 1.17 Topochemical reduction of $CaMnO_3$ to $CaMnO_{2.5}$ under H_2 gas[66] 24

Figure 2.1 Set-up for the flowing hydrogen gas reaction. 27

Figure 2.2 A depiction of Bragg's Law of diffraction 29

Figure 2.3 Air sensitive X-ray slide holder 32

Figure 2.4 Schematic representation of I11 X-ray source and the diffractometer[69]. 33

Figure 2.5 ISIS neutron and Muon facility schematic 36

Figure 2.6 GEM Instrument at the ISIS Facility[71] 36

Figure 2.7 D2B diffractometer at ILL, Grenoble, France[74] 37

Figure 2.8 Quadrupole splitting from a 3/2 to 1/2 transition. Δ is the magnitude of quadrupole splitting. . 42

Figure 2.9 Schematic of a STEM-EELS[30] 45

Figure 2.10 Principal component of a Superconducting Quantum Interference Device magnetometer[88] ... 46

Figure 3.1 X-ray powder diffraction data collected from Sr_2ReLiO_6 heated up to 800 °C 5% H_2 in N_2. (* = impurity peaks) (** = signs of reduction) 53

Figure 3.2 Progression of reduction of Sr_2ReLiO_6 at consecutive heatings (* = splitting peaks, ** = [001] peak) 54
Figure 3.3 Thermogravimetric data collected during the reoxidation of $Sr_2ReLiO_{5.47(4)}$ to Sr_2ReLiO_6 55
Figure 3.4 (a) EELS measurement of the Re $O_{2,3}$ edge of $Sr_2ReLiO_{5.5}$ (sample) compared with La_2ReLiO_6 (Re^{5+}), Sr_2ReCoO_6 (Re^{6+}) and Sr_2ReLiO_6 (Re^{7+}). For better visualisation, the reference patterns for Re^{5+}, Re^{6+} and Re^{7+} were compared separately to the sample spectrum in (b), (c) and (d). 56
Figure 3.5 Zero-field and field cooled magnetisation data collected from $Sr_2ReLiO_{5.5}$ in an applied field of 1000 Oe 58
Figure 3.6 Curie–Weiss law linear fit in the temperature range 50 < T / K < 300 to data collected from $Sr_2ReLiO_{5.5}$ 58
Figure 3.7 Magnetisation-field isotherms collected from $Sr_2ReLiO_{5.5}$ 59
Figure 3.8 Observed, calculated, and difference plots from the refinement of the *P4/m* structural model of $Sr_2ReLiO_{5.5}$ against synchrotron X-ray powder diffraction data (λ = 0.82626(1) Å) 61
Figure 3.9 Electron diffraction patterns (a–c) and dark field TEM image (e) showing extensive twinning of $Sr_2ReLiO_{5.5}$ particles. Indices of the different twin components are given in bold versus italic. The schematic representation (d) visualises the twins as seen along the [$\mathbf{110}$] zone as in (c), blue and purple layers represent stoichiometric $ReLiO_4$ and reduced $ReLiO_3$ layers respectively. Indices with subscript 'p' indicate the lattice vectors of the 'single perovskite' lattice. Light and dark bands in (e) indicate domains related by 90° rotation around the [$\mathbf{110}$] axis, imaged by selecting only the 201 reflection in a [$\mathbf{112}$]/[$\mathbf{221}$] electron diffraction pattern (inset). 63
Figure 3.10 Observed, calculated, and difference plots from the refinement of *P4/m* and *Pmmm* models (bottom) against neutron powder diffraction data collected from $Sr_2ReLiO_{5.5}$ at 300 K. 65
Figure 3.11 Observed, calculated, and difference plots from the of the *Pnma* structural model of $Sr_2ReLiO_{5.5}$ against neutron powder diffraction data collected at 300 K using the GEM instrument. 67
Figure 3.12 (a) the refined structure of $Sr_2ReLiO_{5.5}$ viewed in projection approximately along [100]. (b) The anion-deficient $ReLiO_3$ layered viewed down [001]. Anion-vacancy ordered arrangements of the $ReLiO_3$ layer with (c) 4- and 6-fold coordinate metal cations, (d) and (e) 5-fold coordinate metal cations. Light grey, dark grey and purple spheres represent Sr, Li and Re cations respectively. Red spheres represent fully occupied anion sites (O(1) O(3)), blue and green spheres represent partially occupied O(4) and O(5) anion sites respectively. 72
Figure 3.13 Possible crystal field splittings of Re 5-coordinate polyhedra 78
Figure 4.1 Observed, calculated, and difference plots from the refinement of the *I4/m* structural model of $Sr_2ReLi_{0.64}Co_{0.36}O_6$ against synchrotron X-ray powder diffraction data 82
Figure 4.2 Observed, calculated, and difference plots from the refinement of $Sr_2ReLi_{0.64}Co_{0.36}O_6$ against neutron powder diffraction data collected at 298 K (black = $Sr_2ReLi_{0.64}Co_{0.36}O_6$, red = vanadium, blue = CoO) 85
Figure 4.3 The structure $Sr_2ReLi_{0.64}Co_{0.36}O_6$ with *I4/m* space group symmetry viewed along [101] (left) and [010] (right) directions (blue octahedra = Co/Li, grey octahedra = Re, green spheres = Sr). 86

Figure 4.4 Neutron powder diffraction data collected from $Sr_2ReLi_{0.64}Co_{0.36}O_6$ at 5 K using the GEM Instrument (black = $Sr_2ReLi_{0.64}Co_{0.36}O_6$, red = vanadium; blue = CoO, green = CoO magnetic cell). 87
Figure 4.5 Zero-field cooled and field-cooled magnetisation data collected from $Sr_2ReLi_{0.64}Co_{0.36}O_6$ 88
Figure 4.6 Magnetisation-field isotherms collected from $Sr_2ReLi_{0.64}Co_{0.36}O_6$ 89
Figure 4.7 Fit to the Curie–Weiss law in the temperature range 20 < T / K < 200 89
Figure 5.1 Progression of reduction of $Sr_2ReLi_{0.64}Co_{0.36}O_6$ during consecutive heatings. (* = converging peaks) 94
Figure 5.2 Thermogravimetric data collected during the reoxidation of $Sr_2ReLi_{0.64}Co_{0.36}O_6$ to $Sr_2ReLi_{0.64}Co_{0.36}O_{5.52(3)}$ 95
Figure 5.3 Observed, calculated, and difference plots from the refinement of the *I4/m* structural model of $Sr_2ReLi_{0.64}Co_{0.36}O_{5.5}$ against synchrotron X-ray powder diffraction data (λ = 0.82596(1) Å) 96
Figure 5.4 Observed, calculated, and difference plots from the refinement of $Sr_2ReLi_{0.64}Co_{0.36}O_{5.5}$ against neutron powder diffraction data collected at 298 K (black = $Sr_2ReLi_{0.64}Co_{0.36}O_{5.5}$, red = vanadium can, blue = cobalt) 98
Figure 5.5 The averaged structure $Sr_2ReLi_{0.64}Co_{0.36}O_{5.5}$ with *I4/m* space group symmetry viewed along [101] (left) and [010] (right) directions. The blue octahedra = Co/Li site, grey octahedra = Re site, green spheres = Sr site. The oxygen positions are assigned occupancies consistent with the structural refinement 100
Figure 5.6 Neutron powder diffraction data collected from $Sr_2ReLi_{0.64}Co_{0.36}O_{5.5}$ at 5 K using the GEM Instrument 100
Figure 5.7 Magnetisation-field isotherms collected from $Sr_2ReLi_{0.64}Co_{0.36}O_{5.5}$ 101
Figure 5.8 Saturated ferromagnetic moment extracted from a ferrosubtraction measurement carried out on $Sr_2ReLi_{0.64}Co_{0.36}O_{5.5}$. 102
Figure 5.9 Paramagnetic susceptibility extracted from a ferrosubtraction measurement carried out on $Sr_2ReLi_{0.64}Co_{0.36}O_{5.5}$ 102
Figure 5.10 Fit to the Curie–Weiss law in the temperature range 35 < T / K < 300 103
Figure 6.1 Structural models of the three possible structures of $La_{0.5}Sr_{0.5}Mn_{0.5}Rh_{0.5}O_3$ (purple spheres represent manganese/rhodium sites and red and blue spheres represent manganese and rhodium sites respectively). 111
Figure 6.2 Observed, calculated, and difference plots from the refinement of three possible structural models against synchrotron X-ray powder diffraction data (λ = 0.82626(1) Å). Insets show selected angle reflections. 112
Figure 6.3 Observed, calculated, and difference plots from the refinement of the *Pnma* structural model of $La_{0.5}Sr_{0.5}Mn_{0.5}Rh_{0.5}O_3$ against synchrotron X-ray powder diffraction data 114
Figure 6.4 Observed, calculated, and difference plots from the refinement of the *Pnma* structural model of $La_{0.5}Sr_{0.375}Ca_{0.125}Mn_{0.5}Rh_{0.5}O_3$ against synchrotron X-ray powder diffraction data 115
Figure 6.5 Observed, calculated, and difference plots from the refinement of the *Pnma* structural model of $La_{0.5}Sr_{0.25}Ca_{0.25}Mn_{0.5}Rh_{0.5}O_3$ against synchrotron X-ray powder diffraction data 116

Figure 6.6 Crystal structures of the all $La_{0.5}Sr_{0.5-x}Ca_xMn_{0.5}Rh_{0.5}O_3$ where a) x = 0, b) x = 0.125, c) x = 0.25 in the *Pnma* space group showing views down the [101] and [010] directions highlighting the $a^-b^+c^-$ tilt system. Purple octachedra denote the Mn/Rh site and gray, yellow, blue spheres represent La, Sr, Ca-sites respectively.....118
Figure 6.7 Top: Zero-field cooled and field cooled magnetisation data collected from $La_{0.5}Sr_{0.5-x}Ca_xMn_{0.5}Rh_{0.5}O_3$ in an applied field of 100 Oe. Bottom: Magnetisation-field isotherms collected from $La_{0.5}Sr_{0.5-x}Ca_xMn_{0.5}Rh_{0.5}O_3$ at 5 K.....119
Figure 6.8 Individual ZFC and FC and magnetisation-field isotherms collected from a) $La_{0.5}Sr_{0.5}Mn_{0.5}Rh_{0.5}O_3$, b) $La_{0.5}Sr_{0.375}Ca_{0.125}Mn_{0.5}Rh_{0.5}O_3$ c) $La_{0.5}Sr_{0.25}Ca_{0.25}Mn_{0.5}Rh_{0.5}O_3$ at 5 K. Insets show inverse magnetisation plots.....120
Figure 6.9 Resistance against temperature data collected from $La_{0.5}Sr_{0.5}Mn_{0.5}Rh_{0.5}O_3$ in the 40 < T / K < 300 range.....122
Figure 6.10 Conductivity (σ) as a function of temperature for $La_{0.5}Sr_{0.5}Mn_{0.5}Rh_{0.5}O_3$ in coordinates that linearize the Mott Variable Range Hopping model in three dimensions 122
Figure 6.11 Selected bond angles and bond lengths for $La_{0.5}Sr_{0.5}Mn_{0.5}Rh_{0.5}O_3$ 126
Figure 6.12 Schematics of octahedra for $CaMnO_3$, $La_{0.5}Sr_{0.5}Mn_{0.5}Rh_{0.5}O_3$ and $LaMnO_3$ highlighting the bonds lengths 128
Figure 6.13 No allowed magnetic coupling mechanisms for Mn^{4+}/Rh^{3+} combination.....129
Figure 6.14 Ferromagnetic coupling mechanisms for Mn^{3+}/Rh^{4+} framework 130
Figure 6.15 Electrical conductivity (σ) as a function of temperature for $La_{0.5}Sr_{0.5-x}Ca_xMn_{0.5}Rh_{0.5}O_3$ in coordinates that linearize the Mott's VRH model in three dimensions. a) combined, b) x = 0, c) x = 0.125, d) x = 0.25. 131
Figure 6.16 First derivative plots of susceptibility measurements for all three samples. 135
Figure 7.1 Observed, calculated, and difference plots from the refinement of *I4/mmm* structural model against synchrotron X-ray powder diffraction data collected from Sample A. (λ = 0.82595(1) Å).....139
Figure 7.2 Observed, calculated, and difference plots from the refinement of *I4/mmm* structural model against synchrotron X-ray powder diffraction data collected from Sample B. (λ = 0.82595(1) Å).....141
Figure 7.3 Observed, calculated, and difference plots from the refinement of single phase *I4/mmm* structural model against synchrotron X-ray powder diffraction data collected from Sample C. Insets show alternate angle ranges.....142
Figure 7.4 Illustration of the refined structure of $La_{0.5}Sr_{1.5}Mn_{0.5}Rh_{0.5}O_4$. 143
Figure 7.5 Observed, calculated, and difference plots from the refinement of single phase *Pmab* structural model against synchrotron X-ray powder diffraction data collected from Sample B. (λ = 0.82595(1) Å)...145
Figure 7.6 Observed, calculated, and difference plots from the refinement of two-phase I4*/mmm* structural model against synchrotron X-ray powder diffraction data collected from Sample B (λ = 0.82595(1) Å). Black tick marks – majority phase; red tick marks – minority phase 145

Figure 7.7 Observed, calculated, and difference plots from the refinement of two-phase *I4/mmm* structural model against synchrotron X-ray powder diffraction data collected from Sample A (λ = 0.82595(1) Å) .Black tick marks – majority phase; red tick marks – minority phase 147
Figure 7.8 Observed, calculated, and difference plots from the refinement of two-phase *I4/mmm* structural model against neutron diffraction data collected from Sample A (λ = 1.59432(1) Å). Inset shows low angle reflections. Black tick marks – majority phase; red tick marks – minority phase 149
Figure 7.9 TGA plots for Sample B (black) and Sample C (red) heated under H_2 gas up to 1000 °C to decompose into constituent oxides. (*) buoyancy error as m < 10 mg mass used..... 151
Figure 7.10 ZFC and FC magnetisation and magnetisation-field isotherms collected from all the samples 153
Figure 7.11 Inverse magnetisation plots for all samples 154
Figure 7.12 Magnetisation-field isotherms collected from all samples 155
Figure 7.13 Resistivity-temperature data collected from B-$La_{0.5}Sr_{1.5}Mn_{0.5}Rh_{0.5}O_4$ in the 110 < T / K < 300 range..... 159
Figure 7.14 Electrical conductance (σ) as a function of temperature for Sample B in coordinates that linearize the Mott variable-range model in three dimensions. 159
Figure 7.15 Illustrations of bonds lengths for undistorted $CaMnO_3$, Q_2 type distorted $La_{0.5}Sr_{0.5}Mn_{0.5}Rh_{0.5}O_3$ and $La_{0.5}Sr_{1.5}Mn_{0.5}Rh_{0.5}O_4$ 161
Figure 7.16 Illustration of the splitting of Mn^{3+} d^4 orbitals as a result of J-T compression 161
Figure 8.1 Observed, calculated, and difference plots from the refinement of single-phase *Pnma* structural model against synchrotron X-ray powder diffraction data collected from $La_{0.5}Sr_{0.5}Fe_{0.5}Rh_{0.5}O_3$. Inset shows high angle fit. 165
Figure 8.2 The structure of $La_{0.5}Sr_{0.5}Fe_{0.5}Rh_{0.5}O_3$ with *Pnma* space group symmetry viewed along [101] (left) and [010] (right) directions. 167
Figure 8.3 ^{57}Fe Mössbauer spectrum collected at 293 K 168
Figure 8.4 Zero-field and field cooled magnetisation data collected from $La_{0.5}Sr_{0.5}Fe_{0.5}Rh_{0.5}O_3$ in 100 Oe. 169
Figure 8.5 Curie–Weiss law fit in the temperature range 50 < T / K < 300 to data collected from $La_{0.5}Sr_{0.5}Fe_{0.5}Rh_{0.5}O_3$ 170
Figure 8.6 Magnetisation-field isotherms collected from $La_{0.5}Sr_{0.5}Fe_{0.5}Rh_{0.5}O_3$ 171
Figure 8.7 Resistance against temperature data collected from $La_{0.5}Sr_{0.5}Fe_{0.5}Rh_{0.5}O_3$ in the 30 < T / K < 300 range..... 172
Figure 8.8 Conductivity (σ) as a function of temperature for $La_{0.5}Sr_{0.5}Fe_{0.5}Rh_{0.5}O_3$ in coordinates that linearize the Mott's Variable-Range Hopping model in three dimensions 172
Figure 8.9 The different local Fe environments in a disordered arrangement 175
Figure 8.10 The nearest-neighbour (n-n) and next-nearest-neighbour (n-n-n) coupling regimes in $La_{0.5}Sr_{0.5}Fe_{0.5}Rh_{0.5}O_3$ and the magnetic frustration that leads to a spin glass state..... 180

Appendix 2 Bibliography

1. Cox, P. A., *Transition Metal Oxides: An Introduction to their Electronic Structure and Properties* OUP Oxford: 2020.
2. Aylett, B. J., Transition Metal Oxides: Structure, Properties and Synthesis of Ceramic Oxides. *Applied Organometallic Chemistry* **1999,** *13* (6), 476-477.
3. Spaldin, N. A., *Magnetic Materials: Fundamentals and Applications*. 2nd ed.; Cambridge University Press: Cambridge, 2010.
4. Norman, M. R.; Pepin, C., The electronic nature of high temperature cuprate superconductors. *Reports on Progress in Physics* **2003,** *66* (10), 1547-1610.
5. Kobayashi, K. I.; Kimura, T.; Tomioka, Y.; Sawada, H.; Terakura, K.; Tokura, Y., Intergrain tunneling magnetoresistance in polycrystals of the ordered double perovskite Sr_2FeReO_6. *Physical Review B* **1999,** *59* (17), 11159-11162.
6. Coey, J. M. D.; Chien, C. L., Half-Metallic Ferromagnetic Oxides. *MRS Bulletin* **2003,** *28* (10), 720-724.
7. Eerenstein, W.; Mathur, N. D.; Scott, J. F., Multiferroic and magnetoelectric materials. *Nature* **2006,** *442* (7104), 759-765.
8. Moreau, J. M.; Michel, C.; Gerson, R.; James, W. J., Ferroelectric $BiFeO_3$ X-ray and neutron diffraction study. *Journal of Physics and Chemistry of Solids* **1971,** *32* (6), 1315-1320.
9. Asahi, R.; Morikawa, T.; Ohwaki, T.; Aoki, K.; Taga, Y., Visible-Light Photocatalysis in Nitrogen-Doped Titanium Oxides. *Science* **2001,** *293* (5528), 269-271.
10. Ishihara, T., *Perovskite Oxide for Solid Oxide Fuel Cells*. Springer US: 2009.
11. Dawber, M.; Rabe, K. M.; Scott, J. F., Physics of Thin-Film Ferroelectric Oxides. *Reviews of Modern Physics* **2005,** *77* (4), 1083-1130.
12. Hosono, H.; Ueda, K., Transparent Conductive Oxides. In *Springer Handbook of Electronic and Photonic Materials*, Springer International Publishing: Cham, 2017; pp 1-1.
13. Peña, M. A.; Fierro, J. L. G., Chemical Structures and Performance of Perovskite Oxides. *Chemical Reviews* **2001,** *101* (7), 1981-2018.
14. von Helmolt, R.; Wecker, J.; Holzapfel, B.; Schultz, L.; Samwer, K., Giant negative magnetoresistance in perovskitelike $La_{2/3}Ba_{1/3}MnO_x$. *Physical Review Letters* **1993,** *71* (14), 2331-2333.
15. Brown, B. W.; Banks, E., Conductivity of the Sodium Tungsten Bronzes. *Physical Review* **1951,** *84* (3), 609-610.
16. Jonker, G. H.; Van Santen, J. H., Ferromagnetic compounds of manganese with perovskite structure. *Physica* **1950,** *16* (3), 337-349.
17. Jonker, G. H.; Van Santen, J. H., Magnetic compounds wtth perovskite structure III. ferromagnetic compounds of cobalt. *Physica* **1953,** *19* (1), 120-130.
18. Goldschmidt, V. M., Die Gesetze der Krystallochemie. *Naturwissenschaften* **1926,** *14* (21), 477-485.
19. Abramov, Y. A.; Tsirelson, V. G.; Zavodnik, V. E.; Ivanov, S. A.; Brown I. D., The chemical bond and atomic displacements in $SrTiO_3$ from X-ray diffraction analysis. *Acta Crystallographica Section B* **1995,** *51* (6), 942-951.
20. Goodenough, J. B.; Kafalas, J. A.; Longo, J. M., High-Pressure Synthesis. In *Preparative Methods in Solid State Chemistry*, Hagenmuller, P., Ed. Academic Press: 1972; pp 1-69.

21. Lufaso, M. W.; Woodward, P. M., Jahn-Teller distortions, cation ordering and octahedral tilting in perovskites. *Acta Crystallographica Section B* **2004,** *60* (1), 10-20.
22. Zhang, R.; Senn, M. S.; Hayward, M. A., Directed Lifting of Inversion Symmetry in Ruddlesden–Popper Oxide–Fluorides: Toward Ferroelectric and Multiferroic Behavior. *Chemistry of Materials* **2016,** *28* (22), 8399-8406.
23. Jin, L.; Hayward, M. A., Rhodium-containing oxide-hydrides: covalently stabilized mixed-anion solids. *Chem Commun (Camb)* **2019,** *55* (33), 4861-4864.
24. Rodriguez-Martinez, L. M.; Attfield, J. P., Cation disorder and size effects in magnetoresistive manganese oxide perovskites. *Physical Review B* **1996,** *54* (22), R15622-R15625.
25. Urushibara, A.; Moritomo, Y.; Arima, T.; Asamitsu, A.; Kido, G.; Tokura, Y., Insulator-metal transition and giant magnetoresistance in $La_{1-x}Sr_xMnO_3$. *Physical Review B* **1995,** *51* (20), 14103-14109.
26. Goodenough, J. B., Theory of the Role of Covalence in the Perovskite-Type Manganites $(La,M^{2+})MnO_3$. *Physical Review* **1955,** *100* (2), 564-573.
27. Buttner, R. H.; Maslen, E. N., Electron difference density and structural parameters in $CaTiO_3$. *Acta Crystallographica Section B* **1992,** *48* (5), 644-649.
28. King, G.; Woodward, P. M., Cation ordering in perovskites. *Journal of Materials Chemistry* **2010,** *20* (28).
29. Patwe, S. J.; Achary, S. N.; Mathews, M. D.; Tyagi, A. K., Synthesis, phase transition and thermal expansion studies on M_2MgWO_6 ($M=Ba^{2+}$ and Sr^{2+}) double perovskites. *Journal of Alloys and Compounds* **2005,** *390* (1), 100-105.
30. Anderson, M. T.; Poeppelmeier, K. R., Lanthanum copper tin oxide (La_2CuSnO_6): a new perovskite-related compound with an unusual arrangement of B cations. *Chemistry of Materials* **1991,** *3* (3), 476-482.
31. Leinenweber, K.; Parise, J., High-Pressure Synthesis and Crystal Structure of $CaFeTi_2O_6$, a New Perovskite Structure Type. *Journal of Solid State Chemistry* **1995,** *114* (1), 277-281.
32. Knapp, M. C.; Woodward, P. M., A-site cation ordering in $AA'BB'O_6$ perovskites. *Journal of Solid State Chemistry* **2006,** *179* (4), 1076-1085.
33. Ruddlesden, S. N.; Popper, P., New compounds of the K_2NiF_4 type. *Acta Crystallographica* **1957,** *10* (8), 538-539.
34. Ruddlesden, S. N.; Popper, P., The compound $Sr_3Ti_2O_7$ and its structure. *Acta Crystallographica* **1958,** *11* (1), 54-55.
35. Ricart, J. M.; Dovesi, R.; Roetti, C.; Saunders, V. R., Electronic and magnetic structure of $KNiF_3$ perovskite. *Physical Review B* **1995,** *52* (4), 2381-2389.
36. Cox, P. A., *The Electronic Structure And Chemistry Of Solids* Oxford Science Publications: Oxford, UK, 1987.
37. Kuiper, P.; Kruizinga, G.; Ghijsen, J.; Sawatzky, G. A.; Verweij, H., Character of Holes in $Li_xNi_{1-x}O$ and Their Magnetic Behavior. *Physical Review Letters* **1989,** *62* (2), 221-224.
38. Hubbard, J., Electron Correlations in Narrow Energy Bands. *Proceedings of the Royal Society of London. Series A, Mathematical and Physical Sciences* **1963,** *276* (1365), 238-257.
39. Leon, G. Study of the Hall effect in two different strongly correlated fermion systems. 2009.

40. Mott, N. F., Conduction in non-crystalline materials. *The Philosophical Magazine: A Journal of Theoretical Experimental and Applied Physics* **1969,** *19* (160), 835-852.
41. Cussen, E.; Vente, J.; Battle, P.; Gibb, T., Neutron diffraction study of the influence of structural disorder on the magnetic properties of Sr_2FeMO_6 (M=Ta, Sb). *Journal of Materials Chemistry* **1997,** *7* (3), 459-463.
42. Felser, C.; Fecher, G. H.; Balke, B., Spintronics: A Challenge for Materials Science and Solid-State Chemistry. *Angewandte Chemie International Edition* **2007,** *46* (5), 668-699.
43. de Groot, R. A.; Mueller, F. M.; Engen, P. G. v.; Buschow, K. H. J., New Class of Materials: Half-Metallic Ferromagnets. *Physical Review Letters* **1983,** *50* (25), 2024-2027.
44. Kobayashi, K. I.; Kimura, T.; Sawada, H.; Terakura, K.; Tokura, Y., Room-temperature magnetoresistance in an oxide material with an ordered double-perovskite structure. *Nature* **1998,** *395* (6703), 677-680.
45. Kato, H.; Okuda, T.; Okimoto, Y.; Tomioka, Y.; Takenoya, Y.; Ohkubo, A.; Kawasaki, M.; Tokura, Y., Metallic ordered double-perovskite Sr_2CrReO_6 with maximal Curie temperature of 635 K. *Applied Physics Letters* **2002,** *81* (2), 328-330.
46. Zener, C., Interaction between the d-Shells in the Transition Metals. II. Ferromagnetic Compounds of Manganese with Perovskite Structure. *Physical Review* **1951,** *82* (3), 403-405.
47. Searle, C. W.; Wang, S. T., Studies of the ionic ferromagnet $LaPbMnO_3$. V. Electric transport and ferromagnetic properties. *Canadian Journal of Physics* **1970,** *48* (17), 2023-2031.
48. Retuerto, M.; Martínez-Lope, M. J.; García-Hernández, M.; Alonso, J. A., Curie temperature enhancement in partially disordered Sr_2FeReO_6 double perovskites. *Materials Research Bulletin* **2009,** *44* (6), 1261-1264.
49. Wang, L. M.; Lai, J.-H.; Wu, J.-I.; Kuo, Y.-K.; Chang, C. L., Effects of Ru substitution for Mn on $La_{0.7}Sr_{0.3}MnO_3$ perovskites. *Journal of Applied Physics* **2007,** *102* (2), 023915.
50. Ohanian, H. C., What is spin? *American Journal of Physics* **1986,** *54* (6), 500-505.
51. Goodenough, J. B., Spin-Orbit-Coupling Effects in Transition-Metal Compounds. *Physical Review* **1968,** *171* (2), 466-479.
52. Yamamura, K.; Wakeshima, M.; Hinatsu, Y., Structural phase transition and magnetic properties of double perovskites Ba_2CaMO_6 (M=W, Re, Os). *Journal of Solid State Chemistry* **2006,** *179* (3), 605-612.
53. Wiebe, C. R.; Greedan, J. E.; Luke, G. M.; Gardner, J. S., Spin-glass behavior in the S=1/2 fcc ordered perovskit Sr_2CaReO_6. *Physical Review B* **2002,** *65* (14), 144413.
54. Kanamori, J., Crystal Distortion in Magnetic Compounds. *Journal of Applied Physics* **1960,** *31* (5), S14-S23.
55. Burdett., V. J. K., *Molecular Shapes*. John Wiley & Sons: New York 1981; Vol. 93, p 718-718.
56. Halcrow, M. A., Jahn–Teller distortions in transition metal compounds, and their importance in functional molecular and inorganic materials. *Chemical Society Reviews* **2013,** *42* (4), 1784-1795.
57. Pechini, M. P. US Patent. No. 3330697, 1967.
58. Hayward, M. A.; Green, M. A.; Rosseinsky, M. J.; Sloan, J., Sodium Hydride as a Powerful Reducing Agent for Topotactic Oxide Deintercalation: Synthesis and Characterization of the Nickel(I) Oxide $LaNiO_2$. *Journal of the American Chemical Society* **1999,** *121* (38), 8843-8854.

59. Denis Romero, F.; Burr, S. J.; McGrady, J. E.; Gianolio, D.; Cibin, G.; Hayward, M. A., $SrFe_{0.5}Ru_{0.5}O_2$: square-planar Ru^{2+} in an extended oxide. *J Am Chem Soc* **2013,** *135* (5), 1838-44.
60. Amano Patino, M.; Zeng, D.; Blundell, S. J.; McGrady, J. E.; Hayward, M. A., Extreme Sensitivity of a Topochemical Reaction to Cation Substitution: $SrVO_2H$ versus $SrV_{1-x}Ti_xO_{1.5}H_{1.5}$. *Inorg Chem* **2018,** *57* (5), 2890-2898.
61. Jin, L.; Lane, M.; Zeng, D.; Kirschner, F. K. K.; Lang, F.; Manuel, P.; Blundell, S. J.; McGrady, J. E.; Hayward, M. A., $LaSr_3NiRuO_4H_4$: A 4d Transition-Metal Oxide–Hydride Containing Metal Hydride Sheets. *Angewandte Chemie International Edition* **2018,** *57* (18), 5025-5028.
62. Page, J. E. Topochemical Reduction and Doping of Some Complex Iridum Oxides. Oxford University, Oxford, UK, 2018.
63. Page, J. E.; Hayward, M. A., Structure and Magnetism of $(La/Sr)_2M_{0.5}Ir^{(V)}_{0.5}O_4$ and Topochemically Reduced $(La/Sr)_2M_{0.5}Ir^{(II)}_{0.5}O_3$ (M = Fe, Co) Complex Oxides. *Inorg Chem* **2019,** *58* (9), 6336-6343.
64. Page, J. E.; Morgan, H. W. T.; Zeng, D.; Manuel, P.; McGrady, J. E.; Hayward, M. A., Sr_2FeIrO_4: Square-Planar Ir(II) in an Extended Oxide. *Inorg Chem* **2018,** *57* (21), 13577-13585.
65. Poeppelmeier, K. R.; Leonowicz, M. E.; Scanlon, J. C.; Longo, J. M.; Yelon, W. B., Structure determination of $CaMnO_3$ and $CaMnO_{2.5}$ by X-ray and neutron methods. *Journal of Solid State Chemistry* **1982,** *45* (1), 71-79.
66. Chiang, C. C. K.; Poeppelmeier, K. R., Structural investigation of oxygen-deficient perovskite $CaMnO_{2.75}$. *Materials Letters* **1991,** *12* (1), 102-108.
67. Clegg, W.; Blake , A. J.; Gould, R. O., *Crystal Structure Analysis Principles and Practice*. Oxford Science Publications: New York, 2001.
68. Judith Milledge, H., E. J. W. Whittaker Crystallography: an Introduction for Earth Science (and Other Solid State) Students. *Mineralogical Magazine* **1983,** *47* (343), 262-262.
69. Thompson, S. P.; Parker, J. E.; Potter, J.; Hill, T. P.; Birt, A.; Cobb, T. M.; Yuan, F.; Tang, C. C., Beamline I11 at Diamond: A new instrument for high resolution powder diffraction. *Review of Scientific Instruments* **2009,** *80* (7), 075107.
70. Tartoni, N.; Thompson, S. P.; Tang, C. C.; Willis, B. L.; Derbyshire, G. E.; Wright, A. G.; Jaye, S. C.; Homer, J. M.; Pizzey, J. D.; Bell, A. M. T., High-performance X-ray detectors for the new powder diffraction beamline I11 at Diamond. *Journal of Synchrotron Radiation* **2008,** *15* (1), 43-49.
71. Williams, W. G.; Ibberson, R. M.; Day, P.; Enderby, J. E., GEM — General materials diffractometer at ISIS. *Physica B: Condensed Matter* **1997,** *241-243*, 234-236.
72. ISIS ISIS Neutron and Muon Source. https://www.isis.stfc.ac.uk/Pages/How-ISIS-works--in-depth.aspx.
73. Sears, V. F., Neutron scattering lengths and cross sections. *Neutron News* **1992,** *3* (3), 26-37.
74. Lebon, A. ILL How D2B Works. https://www.ill.eu/users/instruments/instruments-list/d2b/how-it-works/simulated-experiment/.
75. Rietveld, H., A profile refinement method for nuclear and magnetic structures. *Journal of Applied Crystallography* **1969,** *2* (2), 65-71.
76. Larson, A. C.; Von Dreele, R. B., GSAS Manual. *Los Alamos National Laborotory Report LAUR* **1994,** *86*.

77. Brese, N. E.; Okeeffe, M., Bond-Valence Parameters for Solids. *Acta Crystallographica Section B-Structural Science* **1991,** *47* (2), 192-197.
78. Brown, I. D.; Altermatt, D., Bond-valence parameters obtained from a systematic analysis of the Inorganic Crystal Structure Database. *Acta Crystallographica Section B* **1985,** *41* (4), 244-247.
79. Murad, E., Mössbauer spectroscopy and its applications. *Clay Minerals* **1986** *21* (1), 107-107.
80. Glaser, T., Mössbauer Spectroscopy and Transition Metal Chemistry. Fundamentals and Applications. . *Angewandte Chemie International Edition* **2011,** *50* (43), 10019-10020.
81. Williams, D. B.; Carter, C. B., *Transmission Electron Microscopy*. Springer US: 2009.
82. Bonnamy, S.; Oberlin, A., Chapter 4 - Transmission Electron Microscopy. In *Materials Science and Engineering of Carbon*, Inagaki, M.; Kang, F., Eds. Butterworth-Heinemann: 2016; pp 45-70.
83. Egerton, R. F., Electron energy-loss spectroscopy in the TEM. *Reports on Progress in Physics* **2009,** *72* (1).
84. Egerton, R. F.; Malac, M., EELS in the TEM. *Journal of Electron Spectroscopy and Related Phenomena* **2005,** *143* (2), 43-50.
85. Egerton, R. F., *Electron Energy-Loss Spectroscopy in the Electron Microscope*. Springer: New York, 2011; Vol. 3rd ed.
86. Tan, H.; Verbeeck, J.; Abakumov, A.; Van Tendeloo, G., Oxidation state and chemical shift investigation in transition metal oxides by EELS. *Ultramicroscopy* **2012,** *116*, 24-33.
87. Ewels, P.; Sikora, T.; Serin, V.; Ewels, C. P.; Lajaunie, L., A Complete Overhaul of the Electron Energy-Loss Spectroscopy and X-ray Absorption Spectroscopy Database. *Microscopy and Microanalysis* **2016,** *22* (3), 717-724.
88. Clarke, J., SQUIDs. *Scientific American* **1994,** *271* (2), 46-53.
89. Bardeen, J.; Cooper, L. N.; Schrieffer, J. R., Theory of Superconductivity. *Physical Review* **1957,** *108* (5), 1175-1204.
90. Dixon, E.; Hadermann, J.; Ramos, S.; Goodwin, A. L.; Hayward, M. A., Mn(I) in an extended oxide: the synthesis and characterization of $La_{1-x}Ca_xMnO_{2+\delta}$ (0.6 </ = x </ 1). *J Am Chem Soc* **2011,** *133* (45), 18397-405.
91. Hayward, M. A.; Green, M. A.; Rosseinsky, M. J.; Sloan, J., Sodium Hydride as a Powerful Reducing Agent for Topotactic Oxide Deintercalation: Synthesis and Characterization of the Nickel(I) Oxide $LaNiO_2$. *Journal of the American Chemical Society* **1999,** *121* (38), 8843-8854.
92. Seddon, J.; Suard, E.; Hayward, M. A., Topotactic reduction of $YBaCo_2O_5$ and $LaBaCo_2O_5$: square-planar Co(I) in an extended oxide. *J Am Chem Soc* **2010,** *132* (8), 2802-10.
93. Dixon, E.; Hayward, M. A., The topotactic reduction of $Sr_3Fe_2O_5Cl_2$ - square planar Fe(II) in an extended oxyhalide. *Inorg Chem* **2010,** *49* (20), 9649-54.
94. Patino, M. A.; Zeng, D.; Bower, R.; McGrady, J. E.; Hayward, M. A., Coupled Electronic and Magnetic Phase Transition in the Infinite-Layer Phase $LaSrNiRuO_4$. *Inorg Chem* **2016,** *55* (17), 9012-6.
95. Aharen, T.; Greedan, J. E.; Ning, F.; Imai, T.; Michaelis, V.; Kroeker, S.; Zhou, H.; Wiebe, C. R.; Cranswick, L. M. D., Magnetic properties of the S = 3/2 geometrically

frustrated double perovskites La_2LiRuO_6 and Ba_2YRuO_6. *Physical Review B* **2009,** *80* (13), 134423.
96. Retuerto, M.; Martínez-Lope, M. J.; García-Hernández, M.; Fernández-Díaz, M. T.; Alonso, J. A., Crystal and Magnetic Structure of Sr_2MReO_6 (M = Ni, Co, Zn) Double Perovskites: A Neutron Diffraction Study. *European Journal of Inorganic Chemistry* **2008,** *2008* (4), 588-595.
97. Kato, H.; Okuda, T.; Okimoto, Y.; Tomioka, Y.; Oikawa, K.; Kamiyama, T., Structural and electronic properties of the ordered double perovskites A_2MReO_6 (A = Sr, Ca; M = Mg, Sc, Cr, Mn, Fe, Co, Ni, Zn) *Phys. Rev*. **2004**, 6, 1-8.
98. Thompson, C. M.; Chi, L.; Hayes, J. R.; Hallas, A. M.; Wilson, M. N.; Munsie, T. J.; Swainson, I. P.; Grosvenor, A. P.; Luke, G. M.; Greedan, J. E., Synthesis, structure, and magnetic properties of novel B-site ordered double perovskites, $SrLaMReO_6$ (M = Mg, Mn, Co and Ni). *Dalton Trans* **2015,** *44* (23), 10806-16.
99. Marjerrison, C. A.; Thompson, C. M.; Sala, G.; Maharaj, D. D.; Kermarrec, E.; Cai, Y.; Hallas, A. M.; Wilson, M. N.; Munsie, T. J. S.; Granroth, G. E.; Flacau, R.; Greedan, J. E.; Gaulin, B. D.; Luke, G. M., Cubic Re^{6+} $5d^1$ Double Perovskites, Ba_2MgReO_6, Ba_2ZnReO_6, and $Ba_2Y_{2/3}ReO_6$: Magnetism, Heat Capacity, muSR, and Neutron Scattering Studies and Comparison with Theory. *Inorg Chem* **2016,** *55* (20), 10701-10713.
100. Bharathy, M.; Loye, H. Ã., Journal of Solid State Chemistry Crystal growth and structural investigation of A_2BReO_6 (A ¼ Sr , Ba ; B ¼ Li , Na). **2008,** *181*, 2789-2795.
101. Aharen, T.; Greedan, J. E.; Bridges, C. A.; Aczel, A. A.; Rodriguez, J.; MacDougall, G.; Luke, G. M.; Michaelis, V. K.; Kroeker, S.; Wiebe, C. R.; Zhou, H.; Cranswick, L. M. D., Structure and magnetic properties of the S = 1 geometrically frustrated double perovskites La_2LiReO_6 and Ba_2YReO_6. *Physical Review B* **2010,** *81* (6).
102. Verbeeck, J.; Van Aert, S., Model based quantification of EELS spectra. *Ultramicroscopy* **2004,** *101* (2-4), 207-24.
103. Hansteen, O. H.; Fjellvåg, H.; Hauback, B. C., Crystal Structure and Magnetic Properties of $La_2Co_2O_5$. *Journal of Solid State Chemistry* **1998,** *141* (2), 411-417.
104. Hayward, M. A.; Rosseinsky, M. J., Anion Vacancy Distribution and Magnetism in the New Reduced Layered Co(II)/Co(I) Phase $LaSrCoO_{3.5-x}$. *Chemistry of Materials* **2000,** *12* (8), 2182-2195.
105. Leonowicz, M. E.; Poeppelmeier, K. R.; Longo, J. M., Structure determination of Ca_2MnO_4 and $Ca_2MnO_{3.5}$ by X-ray and neutron methods. *Journal of Solid State Chemistry* **1985,** *59* (1), 71-80.
106. Gillie, L. J.; Wright, A. J.; Hadermann, J.; Van Tendeloo, G.; Greaves, C., Synthesis and Characterization of the Reduced Single-Layer Manganite $Sr_2MnO_{3.5+x}$. *Journal of Solid State Chemistry* **2002,** *167* (1), 145-151.
107. James, M.; Avdeev, M.; Barnes, P.; Morales, L.; Wallwork, K.; Withers, R., Orthorhombic superstructures within the rare earth strontium-doped cobaltate perovskites: $Ln_{1-x}Sr_xCoO_{3-\delta}$ (Ln=Y^{3+}, Dy^{3+}–Yb^{3+}; (0.750 < x < 0.875). *Journal of Solid State Chemistry* **2007,** *180* (8), 2233-2247.
108. Hayward, M. A., Topochemical reactions of layered transition-metal oxides. *Semiconductor Science and Technology* **2014,** *29* (6), 064010.
109. Wiebe, C. R.; Greedan, J. E.; Kyriakou, P. P.; Luke, G. M.; Gardner, J. S.; Fukaya, A.; Gat-Malureanu, I. M.; Russo, P. L.; Savici, A. T.; Uemura, Y. J., Frustration-driven spin freezing in the S=1/2 fcc perovskite Sr_2MgReO_6. *Physical Review B* **2003,** *68* (13), 134410.

110. Greenwood, N. N.; Earnshaw, A., *Chemistry of the Elements* 2nd ed.; Butterworth-Heinemann: 1997.
111. Charles, K., *Introduction to Solid State Physics*. 8th ed.; Wiley: 2004.
112. Smith, A. E.; Sleight, A. W.; Subramanian, M. A., Electrical and magnetic properties of new rhodium perovskites: La_2MRhO_6, M=Cr, Fe, Cu. *Materials Research Bulletin* **2010,** *45* (4), 460-463.
113. Tsujimoto, Y.; Tassel, C.; Hayashi, N.; Watanabe, T.; Kageyama, H.; Yoshimura, K.; Takano, M.; Ceretti, M.; Ritter, C.; Paulus, W., Infinite-layer iron oxide with a square-planar coordination. *Nature* **2007,** *450*, 1062.
114. Denis Romero, F.; Burr, S. J.; McGrady, J. E.; Gianolio, D.; Cibin, G.; Hayward, M. A., $SrFe_{0.5}Ru_{0.5}O_2$: Square-Planar Ru^{2+} in an Extended Oxide. *Journal of the American Chemical Society* **2013,** *135* (5), 1838-1844.
115. Buchal, C.; Pobell, F.; Mueller, R. M.; Kubota, M.; Owers-Bradley, J. R., Superconductivity of Rhodium at Ultralow Temperatures. *Physical Review Letters* **1983,** *50* (1), 64-67.
116. Segal, N.; Vente, J. F.; Bush, T. S.; Battle, P. D., Structural and magnetic properties of Sr_4MIrO_6 (M = Ca, Zn, Cd, Li, Na). *Journal of Materials Chemistry* **1996,** *6* (3), 395-401.
117. Jung, D.-Y.; Demazeau, G., Structural and magnetic study on the perovskite rhodium(III) oxides, $Sr_2MRh^{3+}O_6$ (M=Nb, Ta). *Solid State Communications* **1995,** *94* (12), 963-967.
118. Battle, P. D.; Vente, J. F., Structural and Magnetic Characterization of La_2NiRhO_6. **1999,** *146*, 163-167.
119. Parsons, T. G.; D'Hondt, H.; Hadermann, J.; Hayward, M. A., Synthesis and Structural Characterization of $La_{1-x}A_xMnO_{2.5}$(A = Ba, Sr, Ca) Phases: Mapping the Variants of the Brownmillerite Structure. *Chemistry of Materials* **2009,** *21* (22), 5527-5538.
120. Gillie, L. J.; Wright, A. J.; Hadermann, J.; Van Tendeloo, G.; Greaves, C., Synthesis and characterization of the reduced double-layer manganite $Sr_3Mn_2O_{6+x}$. *Journal of Solid State Chemistry* **2003,** *175* (2), 188-196.
121. Moritomo, Y.; Asamitsu, A.; Kuwahara, H.; Tokura, Y., Giant magnetoresistance of manganese oxides with a layered perovskite structure. *Nature* **1996,** *380* (6570), 141-144.
122. Woodward, P. M.; Goldberger, J.; Stoltzfus, M. W.; Eng, H. W.; Ricciardo, R. A.; Santhosh, P. N.; Karen, P.; Moodenbaugh, A. R., Electronic, Magnetic, and Structural Properties of Sr_2MnRuO_6 and $LaSrMnRuO_6$ Double Perovskites. *Journal of the American Ceramic Society* **2008,** *91* (6), 1796-1806.
123. Dass, R. I.; Yan, J. Q.; Goodenough, J. B., Ruthenium double perovskites: Transport and magnetic properties. *Physical Review B* **2004,** *69* (9), 094416.
124. Bashir, J.; Shaheen, R.; Khan, M. N., Structural characterization of $SrLaMnRuO_6$ by synchrotron X-ray powder diffraction and X-ray absorption spectroscopy. *Solid State Sciences* **2008,** *10* (5), 638-644.
125. Bune, R. O.; Lobanov, M. V.; Popov, G.; Greenblatt, M.; Botez, C. E.; Stephens, P. W.; Croft, M.; Hadermann, J.; Van Tendeloo, G., Crystal Structure and Properties of Ru-Stoichiometric $LaSrMnRuO_6$. *Chemistry of Materials* **2006,** *18* (10), 2611-2617.
126. Kubo, K.; Ohata, N., A Quantum Theory of Double Exchange. I. *Journal of the Physical Society of Japan* **1972,** *33* (1), 21-32.
127. Jonker, G. H., Magnetic compounds with perovskite structure IV Conducting and non-conducting compounds. *Physica* **1956,** *22* (6), 707-722.

128. Bakowski, B.; Battle, P. D.; Cussen, J. E.; Noailles, D. L.; Rosseinsky, J. M.; Coldea, I. A.; Singleton, J., Ferromagnetic ordering in the perovskite $La_{1.5}Sr_{0.5}RhMnO_6$. *Chemical Communications* **1999,** (21), 2209-2210.
129. Schinzer, C., Spin-glass behaviour of disordered perovskite $LaNi_{1/2}Rh_{1/2}O_3$. *J. of Alloys and Compounds* **1999,** *288*, 65-75.
130. Tao Y.; Perkisas, T.; Hadermann, J.; Croft, M.; Ignatov, A.; Van Tendeloo, G.; Greenblatt, M., Synthesis and structure determination of ferromagnetic semiconductors $LaAMnSnO_6$ (A = Sr, Ba). *J. Mater. Chem.* **2011,** *21* (1), 199-205.
131. Goodenough, J. B., *Magnetism and the Chemical Bond*. Wiley: New York, **1963**.
132. Cussen, E. J.; Rosseinsky, M. J.; Battle, P. D.; Burley, J. C.; Spring, L. E.; Vente, J. F.; Blundell, S. J.; Coldea, A. I.; Singleton, J., Control of Magnetic Ordering by Jahn−Teller Distortions in Nd_2GaMnO_6 and La_2GaMnO_6. *Journal of the American Chemical Society* **2001,** *123* (6), 1111-1122.
133. Lamsal, J.; Mondal, R.; Kumar, A.; Bharathi, K. K.; Santhosh, P. N.; Nirmala, R.; Nigam, A. K.; Yelon, W. B.; Quezado, S.; Malik, S. K., Magnetization and neutron diffraction studies on Sr_2TiMnO_6. *Journal of Applied Physics* **2011,** *109* (7), 07E329.
134. Hwang, H. Y.; Cheong, S. W.; Radaelli, P. G.; Marezio, M.; Batlogg, B., Lattice Effects on the Magnetoresistance in Doped $LaMnO_3$. *Physical Review Letters* **1995,** *75* (5), 914-917.
135. Simonov, V. I.; Bagdasarov, K. S., Atomic structures of $(La_{1-x}Sr_x)_2CuO_4$ with various strontium content. *Kristallografiya* **1990,** *35*, p861-p868.
136. Medarde, M.; Rodríguez-Carvajal, J., Oxygen vacancy ordering in $La_{2-x}Sr_xNiO_{4-\delta}$ ($0 \le x \le 0.5$): the crystal structure and defects investigated by neutron diffraction. *Zeitschrift für Physik B Condensed Matter* **1997,** *102* (3), 307-315.
137. Braden, M.; André, G.; Nakatsuji, S.; Maeno, Y., Crystal and magnetic structure of Ca_2RuO_4 Magnetoelastic coupling and the metal-insulator transition. *Physical Review B* **1998,** *58* (2), 847-861.
138. Fu, W.; Visser, D.; Ijdo, D., High-resolution neutron powder diffraction study on the structure of Sr_2SnO_4. *Journal of Solid State Chemistry* **2002,** *169*, 208-213.
139. Kajitani, T.; Hosoya, S.; Hiraga, K.; Fukuda, T., Tetragonal-Orthorhombic Phase Transition of La_2CoO_{4-x}. *Journal of the Physical Society of Japan* **1990,** *59* (2), 562-570.
140. Ghorbani-Moghadam, T.; Kompany, A.; Bagheri-Mohagheghi, M. M.; Abrishami, M. E., Cobalt spin states investigation of Ruddlesden-Popper $La_{2-x}Sr_xCoO_4$, using X-ray diffraction and infrared spectroscopy. *Journal of Magnetism and Magnetic Materials* **2018,** *465*, 768-774.
141. Kajitani, T.; Hosoya, S.; Hirabayashi, M.; Fukuda, T.; Onozuka, T., Crystal Structure of Tetragonal Form of La_2NiO_{4+x}. *Journal of the Physical Society of Japan* **1989,** *58* (10), 3616-3623.
142. Attfield, M. P.; Battle, P. D.; Bollen, S. K.; Kim, S. H.; Powell, A. V.; Workman, M., Structural and electrical studies of mixed copper/ruthenium oxides and related compounds of zinc and antimony. *Journal of Solid State Chemistry* **1992,** *96* (2), 344-359.
143. Adler, P.; Lebon, A.; Damljanović, V.; Ulrich, C.; Bernhard, C.; Boris, A. V.; Maljuk, A.; Lin, C. T.; Keimer, B., Magnetoresistance effects in $SrFeO_{3-y}$: Dependence on phase composition and relation to magnetic and charge order. *Physical Review B* **2006,** *73* (9), 094451.
144. Gibb, T. C.; Whitehead, R. J., Order–disorder and magnetic clusters in some mixed-metal perovskites. *Journal of Materials Chemistry* **1993,** *3* (6), 591-596.

145. Battle, P. D.; Gibb, T. C.; Herod, A. J.; Kim, S.-H.; Munns, P. H., Investigation of magnetic frustration in A_2FeMO_6 (A = Ca, Sr, Ba; M = Nb, Ta, Sb) by magnetometry and Mössbauer spectroscopy. *Journal of Materials Chemistry* **1995,** *5* (6), 865-870.
146. Gibb, T. C., Study of magnetic relaxation in the perovskite $SrLaFeSnO_6$ by Mössbauer spectroscopy. *Journal of Materials Chemistry* **1992,** *2* (4), 415-422.
147. Cussen, E. J.; Battle, P. D., The influence of structural disorder on the magnetic properties of $Sr_2Fe_{1-x}Ga_xTaO_6$ ($0 \le x \le 1$). *Journal of Materials Chemistry* **2003,** *13* (5), 1210-1214.
148. Schinzer, C.; Demazeau, G., Structure and properties of new perovskites La_2MRhO_6 (M = Mg, Zn). *J. Of Mat Science* **1999,** *34*, 251-256.
149. Kim, S. H.; Battle, P. D., Structural and Electronic Properties of the Mixed Co/Ru Perovskites AA'$CoRuO_6$ (A, A' = Sr, Ba, La). *Journal of Solid State Chemistry* **1995,** *114* (1), 174-183.
150. Tao, S.; Canales-Vázquez, J.; Irvine, J. T. S., Structural and Electrical Properties of the Perovskite Oxide Sr_2FeNbO_6. *Chemistry of Materials* **2004,** *16* (11), 2309-2316.
151. Koehler, W. C.; Wollan, E. O., Neutron-diffraction study of the magnetic properties of perovskite-like compounds $LaBO_3$. *Journal of Physics and Chemistry of Solids* **1957,** *2* (2), 100-106.
152. Battle, P. D.; Bollen, S. K.; Powell, A. V., Spin glass behavior in Sr_3FeRuO_7 and Sr_4FeRuO_8. *Journal of Solid State Chemistry* **1992,** *99* (2), 267-275.
153. Romero, F. D.; Bingham, P. A.; Forder, S. D.; Hayward, M. A., Topochemical Fluorination of $Sr_3(M_{0.5}Ru_{0.5})_2O_7$ (M = Ti, Mn, Fe), n = 2, Ruddlesden–Popper Phases. *Inorganic Chemistry* **2013,** *52* (6), 3388-3398.
154. Haque, M. T.; Kamegashira, N., Synthesis, structure and properties of $LnMn_{1/2}Rh_{1/2}O_3$ (Ln=rare earth). *Journal of Alloys and Compounds* **2005,** *395* (1), 220-226.
155. Gysling, H. J.; Monnier, J. R.; Apai, G., Synthesis, characterization, and catalytic activity of $LaRhO_3$. *Journal of Catalysis* **1987,** *103* (2), 407-418.
156. Daoud-Aladine, A.; Martin, C.; Chapon, L. C.; Hervieu, M.; Knight, K. S.; Brunelli, M.; Radaelli, P. G., Structural phase transition and magnetism in hexagonal $SrMnO_3$ by magnetization measurements and by electron, X-ray, and neutron diffraction studies. *Physical Review B* **2007,** *75* (10), 104417.
157. Schmidt, M.; Campbell, S. J., In situ neutron diffraction study 300 – 1273 K of non-stoichiometric strontium ferrite $SrFeO_x$. *Journal of Physics and Chemistry of Solids* **2002,** *63* (11), 2085-2092.